Author:
Li, Xiangqian

Title:
Modelling Stress and Damage Interaction in Fibre Reinforced Composite Laminates

Modelling Stress and Damage Interaction in Fibre Reinforced Composite Laminates

Xiangqian Li

Supervised by: Dr. Stephen R. Hallett

Professor Michael R. Wisnom

A dissertation submitted to the University of Bristol in accordance with the requirements of the degree of Doctor of Philosophy in the Faculty of Engineering, Department of Aerospace Engineering. September 2009.

Word count: 49,217

Abstract

Due to the complex nature of composite materials, a complete and validated methodology for predicting the behaviour of composite structures including the effects of damage has not yet been fully achieved despite years of extensive research around the world.

The aim of this research was to explicitly model the representative damage modes: splitting, delamination and fibre breakage in composite laminates and investigate how these damages initiated and interacted with each other to influence the damage propagation in laminates and lead to the ultimate failure of specimens. This was done using finite element analysis with splitting and delamination failure modes modelled using cohesive interface elements and the fibre breakage formulation was implemented in a solid element which also accounted for the influence of thermal residual stress, nonlinear shear behaviour, the orientation of the reinforcement and the size effect on the properties of the laminates. A novel interface element failure criteria considering the effect of through-thickness compression were proposed and a progressive fibre-dominated element failure model that accounts for size effects and could be applied in more general configurations of composites were raised. Formulations and failure criteria of the interface elements and solid elements were implemented in the explicit finite element code LS-Dyna using user defined material subroutines. All models in this thesis were analysed in LS-Dyna.

The tests of single-lap shear, cut-ply and dropped ply , four point bending and open hole tension from other researchers were modelled to verify the new interface element failure criteria and progressive fibre-dominated element failure models. The models gave excellent prediction of both delamination stresses for single-lap shear, cut-ply and dropped-ply tests and fibre failure stresses for four point bending and open hole tension tests. However, in all the cases that failed by fibre failure this was sudden and catastrophic. This gives little opportunity to study the influence of the sub-critical damage on the progression of fibre failure. To examine progressive failure Overheight Compact Tension (OCT) tests on eight different lay-ups of laminates were carried out and models on the tests were also built in this thesis. The advantage of the OCT test is that it allows the stable formation of a process zone ahead of the crack tip and subsequent crack growth, thus making it possible to investigate the development of sub-critical fibre damage and its influence on the final failure modes of the laminates. Ultrasonic C-scan and X-ray were used to examine the splitting, delamination and fibre breakage damages within OCT specimens. The obtained damage information was compared with model predictions and show good correlation.

Declaration

I declare that the work in this dissertation was carried out in accordance with the Regulations of the University of Bristol. The work is original, except where indicated by special reference in the text, and no part of the dissertation has been submitted for any other academic award. Any views expressed in the dissertation are those of the author:

SIGNED:: Le Xiangqian DATE:: 16 Sep 2010

Acknowledgement

I would like to thank for the invaluable support and advice from my supervisors Dr Stephen R. Hallett and Professor Michael R. Wisnom in finishing this thesis. Thanks for their insightful teaching and instruction on expanding my knowledge in composites related fields and giving me the chance to grasp experimental skills of manufacturing, testing and inspecting composite laminates and the chance to be a part of the collaborative work with University of British Columbia (UBC) – without these I would not be where I am now.

I would also like to thank for the financial support of Oversea Research Scholarship(ORS) from Universities UK, Studentship from University of Bristol and funding from Dr Stephen R. Hallett and Professor Michael R. Wisnom in my PhD research and the travel to UBC.

Professor Anoush Poursartip, Professor Reza Vaziri and Dr Navid Zobeiry at University of British Columbia helped me greatly when I carried out Over-height Compact Tension (OCT) experiments in UBC. Nicola Latham and Dr Richard Trask gave me the major help in X-ray scanning the specimens. Dr Jonathan Scholey and Adam Pickard instructed me on the C-scan technique. Ian Chorley and Mike Jones at University of Bristol helped me a lot in preparing and stacking the IM7/8552 laminates. I would like to express my genuine thanks for all their time and warm instructions

Finally I would like to give my thanks to my wife and all members in the Advanced Composites Centre for Innovation and Science (ACCIS) at the University of Bristol for their support, encouragement and compassion during the course of my PhD work.

Table of Contents

List of Figures

List of Tables

Chapter 1 Introduction

1.1 Background and Aim of the Research

Fiber Reinforced(FR) composite materials have unique advantages over monolithic materials, such as high strength, high stiffness, long fatigue life, low density, and adaptability to the intended function of the structure. The behavior of a composite material is complicated by the fact that it is not only anisotropic, but, on the macro scale, is also inhomogeneous. The properties of a FR composite material not only depend on the properties of the constituents but also on the volume fraction of reinforcement or fiber volume ratio, the geometry and orientation of the reinforcement, and the distribution of the constituents. These properties cause a variety of failure mechanisms associated with FR composite materials.

When a FR composite laminate is subjected to loading, the failure may happen at intra-laminar or inter-laminar level. At intra-laminar level, the matrix can develop cracks, or fibres can debond from the matrix and break. At inter-laminar level, plies may delaminate. These damages interact with each other, cause stress re-distribution and lead to a localised or global failure of the composite material involving one or more of many failure modes possible. The study of the failure modes and damage propagation is an integral part of the characterization of composite materials.

Despite years of extensive research around the world, a complete and validated methodology for predicting the behaviour of composite structures including the effects of damage has not yet been fully achieved. This is largely due to their complex nature, so that for any composite structure the performance and the development of damage leading to failure are dependent on a range of parameters including the geometry, material, lay-up, loading conditions, load history and failure modes.

The aim of this research was to explicitly model the representative damage modes: splitting, delamination and fibre breakage in composite laminates and investigate how these damages initiated and interacted with each other to influence the damage propagation in laminates and lead to the ultimate failure of specimens. This was done using finite

element analysis with splitting and delamination failure modes modelled using cohesive interface elements and the fibre breakage formulation was implemented in a solid element which also accounted for the influence of thermal residual stress, nonlinear shear behaviour, the orientation of the reinforcement and the size effect on the properties of the laminates. In the literature, most of interface element formulations and failure criteria ignored the enhancement effect of through-thickness compression on the delamination, size effects of fibre failure were only investigated in some simple configurations of composites and absent in most attempts to model progressive failure of composites. In this thesis, the interface element failure criteria considering the effect of through-thickness compression were proposed and a progressive fibre-dominated element failure model that accounts for size effects and could be applied in more general configurations of composites were raised. Formulations and failure criteria of the interface elements and solid elements were implemented in the explicit finite element code LS-Dyna using user defined material subroutines. All models in this thesis were analysed in LS-Dyna.

The tests of single-lap shear, cut-ply and dropped ply , four point bending and open hole tension from other researchers were modelled to verify the new interface element failure criteria and progressive fibre-dominated element failure models. The models gave excellent prediction of both delamination stresses for single-lap shear, cut-ply and dropped-ply tests and fibre failure stresses for four point bending and open hole tension tests. However, in all the cases that failed by fibre failure this was sudden and catastrophic. This gives little opportunity to study the influence of the sub-critical damage on the progression of fibre failure. To examine progressive failure Overheight Compact Tension (OCT) tests on eight different lay-ups of laminates were carried out and models on the tests were also built in this thesis. The advantage of the OCT test is that it allows the stable formation of a process zone ahead of the crack tip and subsequent crack growth, thus making it possible to investigate the development of sub-critical fibre damage and its influence on the final failure modes of the laminates. Ultrasonic C-scan and X-ray were used to examine the splitting, delamination and fibre breakage damages within OCT specimens. The obtained damage information was compared with model predictions and show good correlation.

1.2 Outline of the Thesis

Firstly a review of numerous composites failure theories proposed in various literature is presented in Chapter 2. Failure theories are divided in two parts, the first being the prediction of failure of a single lamina and the second dealing with prediction of first-ply-failure and damage progression leading to ultimate failure of a multi-directional laminate. Interface element failure theories and size effects of specimen strength are reviewed separately.

In chapter 3 the formulation and failure criteria of interface elements in forms of both discrete beam and eight-noded solid elements are presented. Pre-processor programs to generate these two types of interface elements are introduced. A set of new interface element failure criteria considering the influence of through thickness compressive stress on the interface shear strength and fracture energy is proposed. Tests of Double Cantilever Beam (DCB), End Notched Flexure(ENF), single-lap shear, two types of cut-ply and two types of dropped-ply were simulated and their results compared with theoretical and experimental results to validate the proposed interface element formulations and the new failure criteria.

Chapter 4 describes the formulation of an eight-noded solid element which can be used to model the non-linear shear behaviour, thermal stress and statistical fibre failure problems in laminates. Four-point bending tests on 16, 32 and 64ply laminates and open hole tension tests on six different layups of IM7/8552 laminates were modeled using interface elements and solid elements of this type. The simulated results are compared with experimental observations and show good correlations.

The first section of Chapter 5 reports experimental results of Over Height Compact Tension (OCT) tests conducted during a research visit to the University of British Columbia. Eight different layups of IM7/8552 laminates: $[45/90/135/0]_{2s}$, $[45/90/135/0]_{4s}$, $[45_2/90_2/135_2/0_2]_s$, $[45_4/90_4/135_4/0_4]_s$, $[0/90]_{4s}$, $[0/90]_{8s}$, $[0_2/90_2]_{2s}$ and $[0_4/90_4]_{2s}$ were tested in this program. Splitting and delamination damage in tested specimens were inspected using non destructive C-scan and X-ray techniques and reported in this chapter

as well. The influence of the layup on laminate toughness, failure modes and failure progression are discussed.

The second section of Chapter 5 is about the modeling of the above OCT tests using interface elements introduced in Chapter 3 and solid elements in Chapter 4. OCT tests on all eight lay-ups were simulated with models using the same material input properties and statistical fibre failure parameters as those for modelling open hole tests in Chapter 4. The numerical simulation and experimental results are compared in four aspects: load vs. pin opening displacement (POD) curves, surface failure appearance, delamination and splitting and fibre breakage. Good correlation between model predictions and tested results were achieved for all the eight lay-ups.

Chapter 6 summarizes and discusses the advantages and deficiencies of the composites failure theories proposed in this thesis. Further improvement of the statistic fibre failure theory and future work to verify the proposed failure theories is recommended.

Appendix A gives the detailed description about the data structure and algorithms for interface elements pre-processor programs which are introduced in Chapter 3.

Appendix B illustrates input cards for user defined materials in LS-Dyna, umat42 for discrete beam elements, umat49 for solid interface elements and umat44 for the solid ply element developed in Chapter 4.

Appendix C lists detailed OCT test results, C-scan and X-ray scan results of the specimens.

Chapter 2 Review of Composites Failure Theory

2.1 Introduction

A composite material is a material system which is composed of at least two phases on a macroscopic scale, whose mechanical properties are designed to be superior to those of the constituent materials acting independently. Elements of the two or more phases in a composite work together to produce material properties that are different to the properties of those elements on their own. In practice, most composites consist of a bulk material (the 'matrix', as shown in Fig 2.1-1), and a reinforcement of some kind, added primarily to increase the strength and stiffness of the matrix. This reinforcement is commonly in fibre form. Today, the most common man-made composites can be divided into three main groups: Polymer Matrix Composites, Metal Matrix Composites and Ceramic Matrix Composites. Polymer Matrix Composites are also known as Fibre Reinforced Polymers (or Plastics) (FRP) –these materials use a polymer-based resin as the matrix, and a variety of fibres such as glass, carbon and aramid as the reinforcement. Failure theories reviewed in this chapter are mainly concerning this type of composites. If there is no specific indication, composites discussed in this thesis exclusively refer to this type of FRP composites.

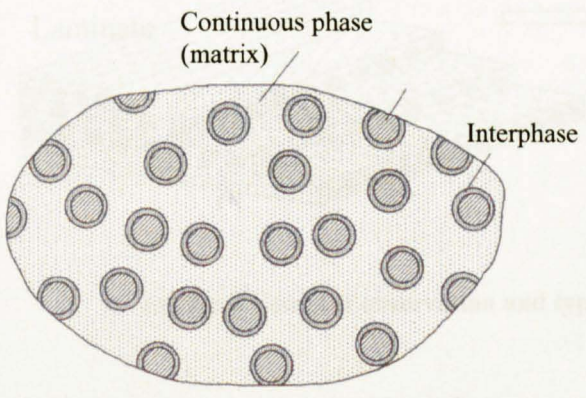

Fig 2.1-1 Schematic phases of a composite material[1]

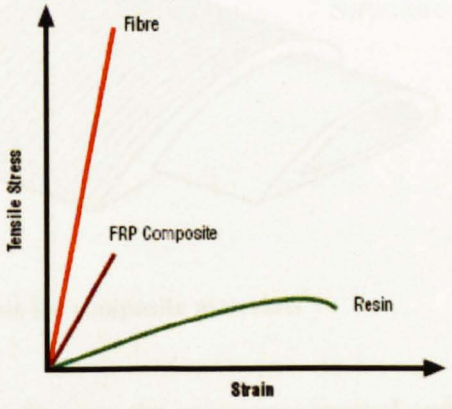

Fig 2.1-2 Typical longitudinal stress-strain curves for FRP composite and its constituents

The properties of a FRP composite material combine something of the properties of the resin on its own with that of the fibres on their own. Fig 2.1-2 gives an example of how the stress-strain properties of resin and fibre influence the property of FRP composite. In high-performance structural composites, the normally continuous fibre reinforcement is the backbone of the material, which determines its stiffness and strength in the fibre direction.

The matrix phase provides protection for the sensitive fibres, bonding support, and local stress transfer from one fibre to another. The interphase, although small in dimensions, can play an important role in controlling the failure mechanism, failure propagation, fracture toughness and the overall stress-strain behavior to failure of the material.

The basis for the superior structural performance of composite materials lies in the high specific strength (strength to density ratio) and high specific stiffness (modulus to density ratio) and in the anisotropic and heterogeneous character of the material.

Depending on the particular characteristics and behavior under consideration, composite materials can be viewed and analyzed at different levels and on different scales as shown in Fig 2.1-3.

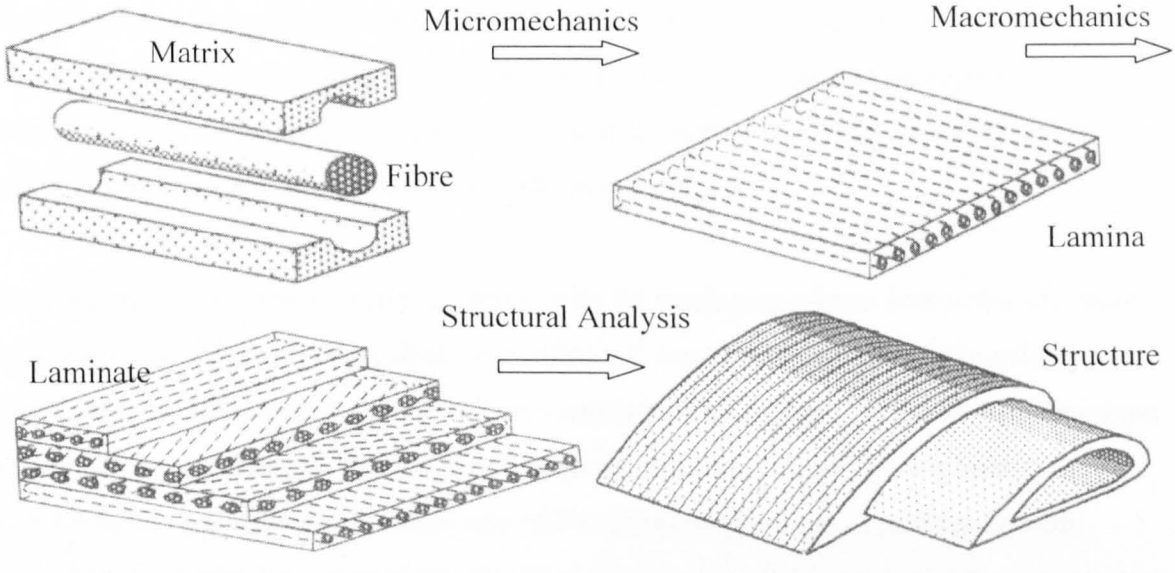

Fig 2.1-3 Levels of observation and types of analysis for composite materials[1]

The failure of composites has been investigated extensively from the micromechanical and macromechanical points of view. On the micromechanical scale, failure mechanisms and processes vary widely with type of loading and are intimately related to the properties of the constituent phases, i. e., matrix, reinforcement, and interface-interphase. The usually low fracture toughness of the fibre is enhanced by the matrix ductility and the energy dissipation at the fibre/matrix interface. The stress transfer capability of the matrix enables the development of multiple-site and multiple-path failure mechanisms. On the other hand,

the fibres exhibit a relatively high scatter in strength. Local stress concentrations around the fibres reduce the transverse tensile strength appreciably. In macromechanical analysis, the material is treated as quasi-homogenous and the average material behaviour can be controlled and predicted from the properties of the constituents.

These numerous composites failure theories can be divided in two parts, one being the prediction of failure of a single lamina and the second dealing with prediction of first-ply-failure and damage progression leading to ultimate failure of a multi-directional laminate. Theories at these two levels are reviewed separately in the following section 2.2 and 2.3.

Besides failure at lamina and laminate level, interlaminar failure is a special type of failure consisting of separation of contiguous layers, even when the layers themselves remain intact. This is a common form of failure at free edges or in regions of geometric or loading discontinuities. Cohesion elements are becoming widely used in prediction of this type of failure, which requires a three-dimensional stress and failure analysis including interlaminar strength and toughness properties of the laminate. Failure theories for the cohesion elements are reviewed individually in section 2.4.

The strength of composites tends to reduce with increasing specimen size under the same test conditions. This is the so-called 'size effect' of composite materials. Size effects are important from a fundamental point view in understanding failure. They are also important in practical sense since tests to establish values of material strength are normally performed on relatively small specimens. If the strength decreases significantly with increasing specimen size, potentially disastrous failures could occur if proper account were not taken of the size effect. An understanding of size effects is also required in order to be able to correctly interpret the results of scaled model tests on structures. The various factors influencing size effects are briefly discussed in section 2.5.

2.2 Failure theory at lamina level

The mechanisms for complete laminate failure are best understood by first considering failure of the individual lamina. Fibre orientations of adjacent laminae in a laminate may be different, thus, the apparent stiffness in specific directions may vary through the laminate, but the state of stress experienced by individual laminae can be correlated to the

effective stiffness of the lamina. Early efforts by researchers to predict failures in orthotropic materials led to current failure theories for composite materials.

Strength-based failure criteria are commonly used with the finite element method to predict failure events in composite structures. Numerous continuum-based criteria have been derived to relate internal stresses and experimental measures of material strength to the onset of failure. In general, such stress-based failure criteria can be categorized into two classes[2,3]: criteria not directly associated with failure modes and those associated with failure modes.

The former criteria are essentially derivatives from theories developed in the 1950s to describe yielding of metals (Hill), updated to account for material anisotropy and the sign-dependent (i.e. tensile or compressive) strength characteristics observed in FRPs. They are widely used in computer programs, as the theories can be reduced to simple equations which are easy to embody into efficient algorithms.

The common feature in the latter group of criteria is that specific modes of failure are defined, each mode being described by a unique equation within the theory. Failure of a unidirectional laminate begins on the microscopic level represented by these local failure modes. Typically, the criteria will differentiate between fibre failure and matrix failure (referring to Fig 2.2-1), and some provide further differentiation, such as between brittle and ductile matrix failure modes. Thus, in addition to predictions of strength, strain to failure etc, these criteria also provide predictions of mode of failure.

The failure theories not directly associated with failure modes include Hoffmann criterion[4], Tsai-Wu[6-8], Tsai-Hill [7-9], Modified Tsai-Wu[9], and all other polynomial, tensorial, or parametric criteria.

The most general polynomial failure criteria for composite materials, from which all other criteria can be obtained as special cases, is expressed in terms of a single tensor polynomial failure criterion proposed by Tsai and Wu[5]. Failure is assumed to occur if the following condition is satisfied[6,7].

$$F_i\sigma_{ii} + F_{ij}\sigma_{ii}\sigma_{ij} + F_{ijk}\sigma_{ii}\sigma_{jj}\sigma_{kk} + \ldots \geq 1 \qquad (2.2\text{-}1)$$

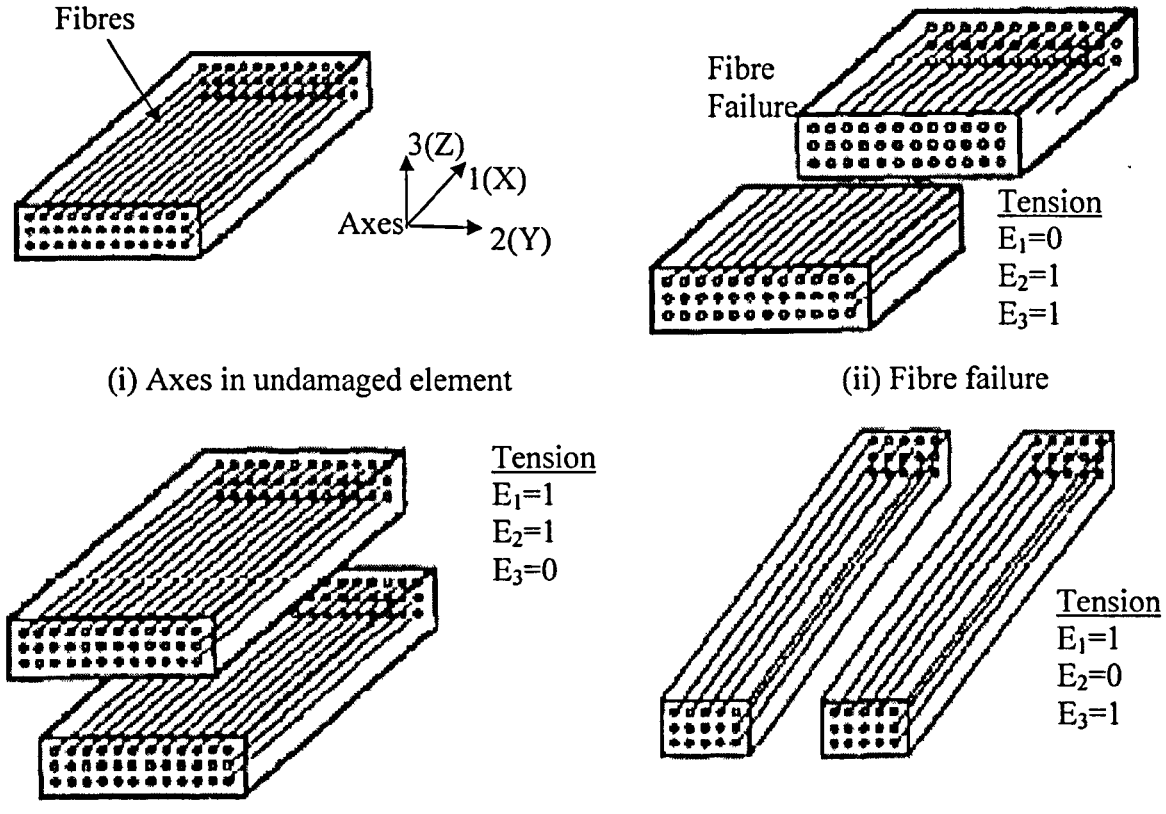

(i) Axes in undamaged element (ii) Fibre failure

(iii) Inter-ply matrix splitting-delamination mode (iv) Intra-ply matrix splitting

Fig. 2.2-1. Schematic representation of damage types included in composites [8]

The two-dimensional form of the above polynomial is expressed as[9,10]:

$$F_1\sigma_{11} + F_2\sigma_{22} + 2F_{12}\sigma_{11}\sigma_{22} + F_{11}\sigma_{11}^2 + F_{22}\sigma_{22}^2 + F_{66}\sigma_{12}^2 \geq 1 \qquad (2.2\text{-}2)$$

where, σ_{11}, σ_{22} and σ_{12} are the in-plane stresses in the material coordinate directions.

The three-dimensional form is[8]:

$$F_1\sigma_{11} + F_2\sigma_{22} + F_3\sigma_{33} + 2F_{12}\sigma_{11}\sigma_{22} + 2F_{13}\sigma_{11}\sigma_{33} + 2F_{23}\sigma_{22}\sigma_{33} + F_{11}\sigma_{11}^2 + F_{22}\sigma_{22}^2 + F_{33}\sigma_{33}^2 + F_{44}\sigma_{23}^2 + F_{55}\sigma_{13}^2 + F_{66}\sigma_{12}^2 \geq 1 \qquad (2.2\text{-}3)$$

where F_i and F_{ii} are the components of the experimentally determined strength tensors. σ_{i3} is the out-of-plane stress.

The failure criteria associated with failure modes include Maximum strain[11,12] and stress criterion[7, 9], Hashin[2,9,13], Yamada and Sun[14,15], Puck[2,14,16], and all other physically based and damage-mechanism based failure criteria such as Gamble et al's approach[4](3D), Chang and Chang criteria[2], Davila et al's LaRC03 criteria[17] (2D), and Cuntze and Freund's Failure Mode Concept(FMC) based criteria[18,19](3D).

Many comments have already been made about the different criteria of fibrous composites based on theclassification. Sun et al.[14] include an estimation of the use that people involved in the field of composites make of the different criteria. According to this information, around 70 percent of composite designers are not currently using Tsai-derived criteria. Also interesting is the clear preponderance of the maximum strain criterion.

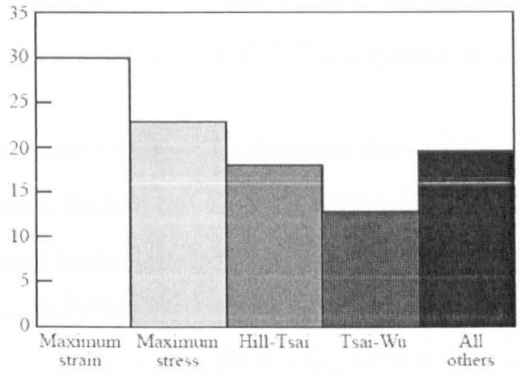

Fig 2.2-2. Rate of use for different failure criteria[2],[14]

The lesser use of Hashin and derived criteria, which are included in "others" in Fig. 2.2-2, might lie in the lesser attention composite textbooks pay to this type of criterion, whereas if composite research papers are reviewed, the majority of researchers do consider Hashin's criteria.

Paris[2] points out that many counter examples given in the literature have reported the inconsistencies to which tensorial criteria may lead. Especially, Hart-Smith[20] found that decreasing the transverse strength of a lamina of the material leads these types of criteria to over predict the resistance of the composite in submarine hulls subjected to bi-compressive stress states.

Maximum stress and maximum strain criteria are simple, direct ways to predict failure of composites. Their major limitation is that there is no interaction between the stresses/strains acting on the lamina, underpredicting the strength in the presence of combined actions of in-plane stresses.
For those criteria based on experimental observations and involving experimental parameters, there is the possibility that even starting from incorrect assumptions, the final conclusion can be correct (predicting things quite accurately) because adjusting parameters

are involved. Therefore, Paris[2] suggests to focus on failure criteria in a completely physically based manner.

Hinton and Soden[3] concluded that even at the lamina level of composites, there was a lack of evidence to show whether any of the criteria could provide accurate and meaningful predictions of failure over anything other than a very limited range of circumstances. They summarized and compared the similarities and the differences between predictive capabilities of 19 leading theories[21,22,23,24] (see Table 2.2-1) contributed by their originators to the World Wide Failure Exercise(WWFE)[3,25,26] completed in 2003.

Hinton and Soden's comparison of these 19 theories showed that on a lamina level, no two theories gave the same biaxial failure envelops for all the 3 test cases, and differences as great as 690% were observed in the strength predictions. Some theories (Huang, Bogetti, Hart-Smith, Eckold and Wolfe[21-24]) predicted uni-axial strength data of the lamina that were different to those measured and provided as input data. The largest deviation between measured and predicted uniaxial strength value (transverse tensile strength) was a factor of 3.2. This highlights some very significant problems within certain of these theories.

Table 2.2-1 Failure modes and criteria used by various researchers[21,23]

Mode of failure	Failure criterion	Theory
Fibre failure	$\pm\left(\frac{I_{1f}}{S_{11f}}\right)^2+\left(\frac{I_{4f}}{S_{12f}^2}\right)=1,$ I_{1f}, I_{4f} are fibre stress invariants	Mayes
	$\sigma_{eq}=\sigma_{11}, \sigma_{22}\le 0$ *and* $\left[\sigma_{11}^q+\sigma_{22}^q\right]^{1/q}, \sigma_{22}>0, 1<q\le\infty$	Huang
Fibre failure in tension and compression	$\left[\frac{\int_{\varepsilon_1}\sigma_1 d\varepsilon_1}{\int_{*_1}\sigma_1 d\varepsilon_1}\right]^{m1} / \sum_{i=1,2,6}\left[\frac{\int_{\varepsilon_i}\sigma_i d\varepsilon_i}{\int_{*_i}\sigma_i d\varepsilon_i}\right]^{mi} \ge 0.1$	Wolfe
Fibre failure in tension	$\frac{1}{\varepsilon_{1T}}(\varepsilon_1+\frac{\upsilon_{f12}}{E_{f1}}m_{\sigma f}\sigma_2)=1$	Puck
	$\sigma_{11}=X_T$	Zinoviev, Rotem, Sun, Edge, Hart-Smith and Cuntze
	$\varepsilon_1=\varepsilon_{1T}$ (*and Eckold's* $\varepsilon_1=0.004$)	Hart-Smith, Eckold and Bogetti
Fibre failure in compressive	$\frac{1}{\varepsilon_{1C}}\left\|\left(\varepsilon_1+\frac{\upsilon_{f12}}{E_{f1}}m_{\sigma f}\sigma_2\right)\right\|=1-(10\gamma_{21})^2$	Puck

	$\sigma_{11} = X_C (and \quad Eckold \quad \sigma_{11} = X_T$	Zinoviev, Edge, Rotem, Sun, Hart-Smith, Cuntze and Eckold
	$\varepsilon_1 = \varepsilon_{1C} (and \quad Eckold's \quad \varepsilon_1 = 0.004)$	Hart-Smith, Eckold and Bogetti
Fibre shear failure	Tresca type criterion	Hart-Smith
Fibre tension /compression & Matrix tension /compression /shear	$(\frac{\sigma_{11}}{X_T X_C})^2 + (\frac{\sigma_{22}}{Y_T Y_C})^2 + (\frac{1}{X_T} - \frac{1}{X_C})\sigma_{11} + (\frac{1}{Y_T} - \frac{1}{Y_C})\sigma_{22} + (\frac{2F_1 2\sigma_1\sigma_2}{\sqrt{X_T X_C Y_T Y_C}}) + (\frac{\tau_{12}}{S_{12}})^2 = 1$	Tsai
Matrix transverse tensile failure	$\sigma_{22} = Y_T$	Zinoviev, Edge, Eckold and Sun
	$\sigma + k\sigma t > \sqrt{\frac{4p\gamma}{\frac{1}{EA(2p)} - \frac{1}{EA(p)}}} + \bar{\sigma}_0$ 2γ is fracture energy	McCartney
	$\varepsilon_2 = \varepsilon_{2T} (and \quad Eckold's \quad \varepsilon_2 = 0.001)$	Hart-Smith, Eckold and Bogetti
	YT=XT/10 or XC/10 whichever is the greatest	Hart-Smith
Matrix transverse tensile failure (IFF1)	$\frac{\sigma_{22}}{Eff^{\perp\sigma} \cdot R_\perp^t} = 1$	Cuntze
Inter-fibre failure Mode A (transverse tension)	$\sqrt{\left(\frac{\tau_{21}}{S_{21}}\right)^2 + \left(1 - p_{\perp\parallel}^{(+)} \frac{Y_T}{S_{21}}\right)^2 \left(\frac{\sigma_{22}}{Y_T}\right)^2} + p_{\perp\parallel}^{(+)} \frac{\sigma_{22}}{S_{21}} = 1 - \frac{\sigma_{11}}{\sigma_{11D}}$	Puck
Matrix transverse compression	YC=XT/10 or XC/10 whichever is the greatest	Hart-Smith
	$\sigma_{22} = Y_C$	Zinoviev, Edge, Eckold, Sun and Huang
	$\varepsilon_2 = \varepsilon_{2C} (and \quad Eckold's \quad \varepsilon_2 = 0.001)$	Hart-Smith, Eckold and Bogetti
Inter-fibre failure Mode B(moderate transverse compression)	$\frac{1}{S_{21}}\left(\sqrt{\tau_{21}^2 + \left(p_{\perp\parallel}^{(-)}\sigma_{22}\right)^2} + p_{\perp\parallel}^{(-)}\sigma_{22}\right) = 1 - \frac{\sigma_{11}}{\sigma_{11D}}$	Puck
Inter-fibre failure Mode C(large transverse compression)	$\left[\left(\frac{\tau_{21}}{2(1 + p_{\perp\perp}^{(-)})S_{21}}\right)^2 + \left(\frac{\sigma_{22}}{Y_C}\right)^2\right]\frac{Y_C}{(-\sigma_{22})} = 1 - \frac{\sigma_{11}}{\sigma_{11D}}$	Puck

Wedge failure(IFF3)	$\frac{(b_{\perp}^{r}-1)(\sigma_{22}+\sigma_{33})}{Eff^{\perp r}\cdot R_{\perp}^{c}}+\frac{b_{\perp}^{r}(\sigma_{22}-\sigma_{33})^{2}+b_{\perp\parallel}^{r}\cdot\tau_{21}^{2}}{(Eff^{\perp r}\cdot R_{\perp}^{c})^{2}}=1$	Cuntze
Inter-fibre failure(IFF2)	$\frac{\tau_{21}^{3}+b_{\perp\parallel}2\sigma_{2}\cdot\tau_{21}^{2}}{(Eff^{\perp\parallel}\cdot R_{\perp\parallel})^{3}}=1$	Cuntze
In-plane shear failure	S12=XT/20 or XC/20 whichever is the greatest	Hart-Smith
	$\tau_{12}=S_{12}$	Zinoviev, Edge, Hart-Smith, and Sun
Combined transverse tension & shear	$\left(\frac{\sigma_{2}}{Y_{T}}\right)^{2}+\left(\frac{\tau_{12}}{S_{12}}\right)^{2}=1$	Edge
Combined longitudinal compression & shear	$\left(\frac{\sigma_{11}}{H_{1C}}\right)+\left\|\frac{\tau_{12}}{S_{12}}\right\|=1$	Edge
Delamination	$\tau_{12}\times t_{e}>\omega_{r}$	Edge
Matrix failure	$\frac{I_{3m}}{\pm S_{22m}^{2}\pm S_{33m}^{2}}+\left(\frac{I_{4m}}{S_{12m}^{2}}\right)=1,$ I_{3m},I_{4m} are matrix stress invariants as those in 1.3.11	Mayes
	$\left(\frac{\sigma_{22}}{Y}\right)^{2}+\left(\frac{\tau_{12}}{S_{12}}\right)^{2}=1$ (Chamis obtains Y and S12 from micromechanics)	Chamis and Sun
	$\left(\frac{E_{m}(\varepsilon_{1})\varepsilon_{1}}{Y_{m}}\right)^{2}+\left(\frac{\sigma_{22}}{Y}\right)^{2}+\left(\frac{\tau_{12}}{S_{12}}\right)^{2}=1$	Rotem
	$\left[\frac{\int_{\varepsilon_{1}}\sigma_{1}d\varepsilon_{1}}{\int_{\varepsilon_{1}^{u}}\sigma_{1}d\varepsilon_{1}}\right]^{m1}/\sum_{i=1,2,6}\left[\frac{\int_{\varepsilon_{i}}\sigma_{i}d\varepsilon_{i}}{\int_{\varepsilon_{i}^{u}}\sigma_{i}d\varepsilon_{i}}\right]^{mi}<0.1$	Wolfe
	$\sigma_{eq}=\sigma_{22},\sigma_{22}\le 0$ *and* $\left[\sigma_{11}^{q}+\sigma_{22}^{q}\right]^{1/q},\sigma_{22}>0,1<q\le\infty$	Huang

2.3 Failure theory at laminate level

At the laminate level, the composite failure problem is obviously more complicated because the problem involves the failure criterion of a lamina. The strength of a multidirectional laminate is a function of many factors, in addition to the fundamental lamina strengths. The varying lamina orientations, stiffnesses, strengths, and coefficients of thermal and moisture expansion affect the directional characteristics of laminate strength. The exact stacking sequence affects the bending and coupling stiffness and hence the stresses and strength of the laminate. Finally, the fabrication process affects the residual stresses, which influence the overall strength.

Failure in a laminate may be caused by failure of individual laminae or plies within the laminate (intralaminar failure) or by separation of contiguous laminae or layers (interlaminar failure). Failure of a laminate may be defined as the initial failure or the ultimate failure, depending on the degrees of conservatism applied. The initial failure of a laminate, also called first ply failure in most literature, means that the first layer (or group of layers) to fail in the laminate defines the failure point. In the case of ultimate laminate failure, there is no generally accepted definition of what constitutes such failure. It is typically taken to be that a laminate has failed when the maximum load level is reached. Other definitions of laminate failure include a prescribed stiffness degradation, failure of the principal load-carrying plies(0° plies), failure of all plies, or a prescribed level of strain.

Many researchers[21,27,28,29,30,31] choose to differentiate between the behaviour of an isolated lamina and that of a lamina embedded within a laminate. They argue that the embedded properties (particularly the transverse tensile and shear strengths) of a lamina would be substantially increased because of the constraining effect of the surrounding layers. For example, Sun[21,32] assumed that the new values for the shear and transverse tensile strengths of the laminate are 50% higher than those of the lamina. Following the findings of Rotem and Hashin[33], Rotem[19,21] assumed that, for all the laminate in the WWFE, the shear and transverse strengths, as well as the corresponding stiffness of the embedded laminae, increased by 20% above their values measured on isolated laminae. He took the measured isolated lamina strengths as being the cause of initial cracking in the constrained lamina and the modified strengths as controlling the onset of final failure. On the basis of his

experience with carbon/epoxy materials and their use in the aircraft industry, Hart-Smith[30,31] assumed theoretical limits to the transverse strengths of embedded laminae, which were much higher than those suggested by Rotem and Sun. In all the failure envelopes predicted by Hart-Smith, the transverse lamina strengths were raised to such an extent that the matrix tensile cracking (initial failure) mode never occurred. In Davila et al's LaRC03 criteria [17], they also distinguish the properties for general laminates from those for unidirectional lamina by considering the 'in situ' effects.

There are also some researchers arguing whether it is reasonable to consider the design of a laminate without having clarified the conditions under which a lamina fails. For instance, Hashin[3] did not believe that even the most complete information about failure of single plies is sufficient to predict the failure of a laminate, consisting of such plies. Paris[2] raised questions on whether the exact knowledge of what happens at the lamina level would be enough to predict the behavior of a laminate as below:

(a). A correct knowledge of the stress state in the lamina placed in the laminate would be required.
(b). The maintenance of just the same intralaminar mechanisms of failure or the appearance of new ones, when the lamina is subjected to the new state of stress, has to be clarified.
(c). The inclusion of delaminations in the mechanism of failure obviously has to be considered, since there is much more physical evidence that the phenomenon, in itself, is much more realistically controlled by the parameters associated with fracture mechanics theory instead of stresses.

However, Paris agreed with most of other researchers that it is a more realistic approach to assume a gradual degradation procedure in lamina properties after initial damage as a way to treat embedded lamina behavior as different from that of the isolated lamina.

Multi-directional laminates subjected to uni-axial or biaxial stresses may still be capable of carrying load beyond first-ply failure or initial failure occurrence. The modelling of post-failure behaviour of a laminate requires that assumptions be made regarding the properties of the degraded lamina. Material degradation within the damaged area was evaluated based on the mode of failure predicted by the failure criteria. Therefore, the residual stiffness and

strength of composites greatly depend on the mode of failure in each layer. The property degradation models for each layer can be separated into three idealized types of failure modes named as brittle, ductile and degrading[34],[35],[36]. For the brittle mode, the material is assumed to lose its entire stiffness and strength in the dominant stress direction, whereas for the ductile mode the material retains its load carrying capacity but loses all of its stiffness in the failure direction. And, for the degrading mode the material is assumed to lose its stiffness and strength gradually in the failure direction.

Hinton and Soden[21] and Paris[2] classifed the post-initial-failure models into two main groups: instantaneous or progressive degradation, referring to Table 2.3-1. The theories that gradually reduced ply properties, once either of the failure criteria is satisfied, usually give higher predictions of final failure loads than those that suddenly and simultaneously reduced two or more ply properties[21].

At present, the questions of whether the properties can be degraded instantaneously or progressively still requires some further studies, which will probably not be definitive until the lamina failure criteria are completely established.

The general flowchart for progressive failure analysis of a laminate is shown in Fig 2.3.1-1.

Table 2.3-1 Summary of post-initial-failure models used in literature[21],[23]

Name	Failure mode	Properties degraded
Eckold		No post failure
Hart-Smith		No post failure
Rotem	After final matrix failure	$E_2 = 0.0, G_{12} = 0.0, E_1 = E_1^0 \exp(-k\varepsilon_1)$ K is a large constant
McCartney	Lamina cracking	Detailed mathematical analysis for reducing stiffness
Puck	Cracking under tension Mode (A)	$E_2 = \eta E_2^0, G_{12} = \eta G_{12}^0, \nu_{12} = \eta \nu_{12}^0$ η is a parameter which varies with stress

	Cracking under compression Modes (B) and (C)	$G_{12} = \eta_1 G_{12}^0, \nu_{12} = \eta_1 \nu_{12}^0$ η_1 is smaller than η
Chamis	Matrix failure	E_m is replaced by a negligible value and $E_2, G_{12}, \nu_{12}, E_1$ are computed from micro-mechanics
Edge	Matrix failure	$E_2 = \beta_1 E_2^0, G_{12} = \beta_2 G_{12}^0, \nu_{12} = \beta_3 \nu_{12}^0$ $\beta_1, \beta_2, \beta_3$ are empirical parameters that decreases with increasing strain
Wolfe	Matrix failure	$E_2 = 0.0, G_{12} = 0.0, \nu_{12} = 0.0$
Sun (linear)	Shear matrix failure	$E_2 = 0.0, G_{12} = 0.0$
	Transverse matrix failure	$E_2 = 0.0$
Sun (NL)	Matrix shear failure	$E_2 = E_2^0 \exp(-\alpha_E \lambda), G_{12} = G_{12}^0 \exp(-\alpha_G \lambda)$ α_E, α_G are constants, λ is normalized crack density
	Transverse matrix failure	$E_2 = E_2^0 \exp(-\alpha_E \lambda)$
Tsai	Matrix failure ($\varepsilon_2 > 0$)	$E_m = 0.15 E_m^0, \nu_{12} = 0.15 \nu_{12}^0$ E_2, G_{12} are computed from micromechanics
	Matrix failure ($\varepsilon_2 \leq 0$)	$E_2 = 0.01 E_2^0, G_{12} = 0.01 G_{12}^0$ $\nu_{12} = 0.01 \nu_{12}^0, E_1 = 0.01 E_1^0$

Zinoviev	Open cracks $\sigma_2 > 0$	For $\lvert\gamma_{12}\rvert < \lvert\gamma_{12}^*\rvert$, when $(a)\varepsilon_2 < \varepsilon_2^* : E_2 = \psi_2 E_2^0, G_{12} = \psi_3 G_{12}^0$, ψ is a function of strain; $(b)\varepsilon_2 = \varepsilon_2^* : E_2 = 0.0, G_{12} = \psi_3 G_{12}^0$; For $\lvert\gamma_{12}\rvert = \lvert\gamma_{12}^*\rvert$, when $(a)\varepsilon_2 < \varepsilon_2^* : E_2 = \psi_2 E_2^0, G_{12} = 0.0$, $(b)\Delta\varepsilon_2 > 0 : E_2 = 0.0, G_{12} = 0.0$;
	Closed cracks $\sigma_2 < 0$	For $\Delta\varepsilon_2 < 0$: $(a)\lvert\gamma_{12}\rvert < \lvert\gamma_{12}^*\rvert : G_{12} = \psi_3 G_{12}^0$ $(b)\Delta\lvert\gamma_{12}\rvert > 0 : G_{12} = 0.0$
Bogetti	Shear failure	$G_{12} = 0.0$
Bogetti	Transverse strain failure	$E_2 = 0.0$
Cuntze	IFF1, IFF2 and IFF3	Curves describing 'softening' behavior
Huang	Matrix or fibre Failure	$E_m = E_f = 0.0$ or $E_2 = 0.0, G_{12} = 0.0, \nu_{12} = 0.0, E_1 = 0.0$
Mayes	Matrix failure	$E_m = 0.01 E_m^o$, E_2, G_{12} are computed from micromechanics

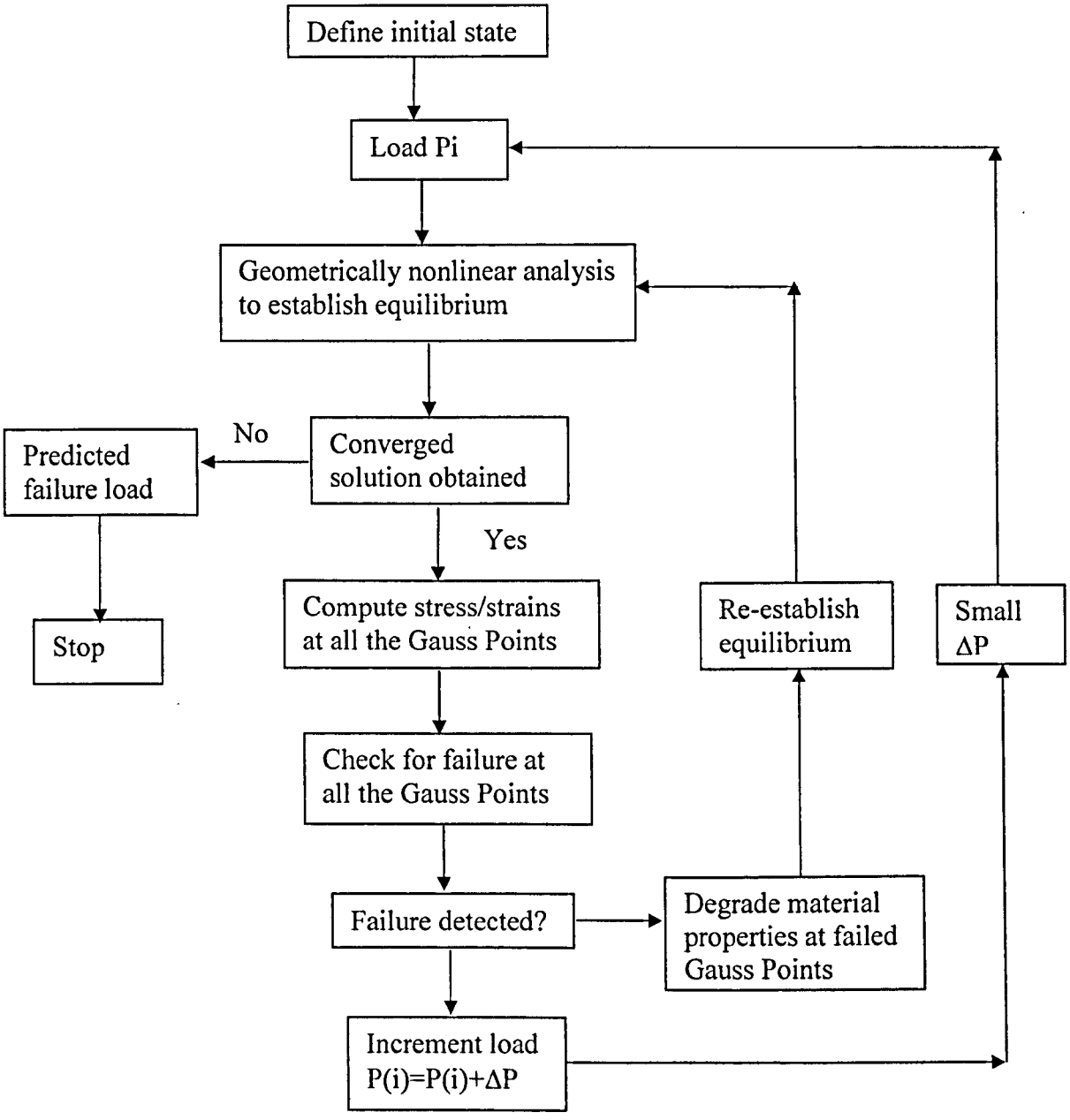

Fig 2.3.1-1 Flowchart of Progressive failure analysis of a Laminate[9]

2.4 Review of Delamination Modelling

Interlaminar damage (delamination) is one of the predominant forms of failure in many laminated composites systems, especially when there is no reinforcement in the thickness direction. Therefore, the theories regarding delamination problems are specially reviewed in this separate section. The delamination of composites may arise from various stress-concentrated circumstances including improper adhesion of layers, geometric discontinuities (such as matrix cracks, ply drop-offs, stiffener terminations and flanges, bonded and bolted joints, and access holes), the presence of free edges, or structures subject to transverse concentrated load such as low-velocity impacts. Delamination may lead to a significant reduction in the compressive load-carrying capacity of a structure, or trigger intra-ply damage mechanisms and cause a significant loss of structural integrity. In some cases delamination can provide stress relief and delay final failure of the structure. The ability to accurately predict the initiation and evolution of delamination is essential for predicting the performance of composite structures and developing reliable and safe designs.

2.4.1. Approaches applied in delamination problems

There are a large number of papers addressing the delamination problems. applied approaches include:

1. Fracture-mechanics-based approach

Fracture mechanics has been used to model delamination problems. It assumes the existence of initial defects or cracks and self-similar delamination growth and therefore cannot be applied directly without initial delaminations. In many applications[37],[38],[39], stress-based methods have to be used to predict the initiation of delaminations, following which fracture mechanics can be applied to evaluate energy release rates G for self-similar delamination growth[40,41,42,43,44,45,46]. The energy release rates are usually evaluated using the virtual crack closure technique (VCCT) proposed by Rybicki and Kanninen[47]. The VCCT technique is based on Irwin's assumption that when a crack extends by a small amount, the energy released in the process is equal to the work required to close the crack

to its original length. The Mode I, Mode II, and Mode III energy release rates, GI , GII and GIII respectively, can then be computed from the nodal forces and displacements obtained from the solution of a finite element model. Kreuger et al.[48],[49],[50] have shown that the VCCT is capable of predicting debonding of composite skin and stringer configurations. Kreuger has implemented VCCT subroutines to work together with the commercial FEA software ABAQUS[51]. Although valuable information concerning the onset and the stability of delamination can be obtained using the VCCT[52,53,54], its use in the simulation of delamination growth may require complex moving mesh techniques to advance the crack front when the local energy release rates reach a critical value[55]. Furthermore, an initial delamination must be defined and, for certain geometries and load cases, the location of the delamination front might be difficult to determine[56],[57],[58]. Also it is difficult to deal with multiple potential delamination sites.

2. Cohesive Zone Models (CZM)

The limitations of fracture-mechanics-based approaches, i.e. the assumption of an initial delaminated area and self-similar delamination growth can be overcome by the use of models having a cohesive or damage zone to simulate the fracture processes (see for example Geubelle and Baylor[59]; Petrossian and Wisnom[60]; Pinho et al[61],[62], Yang and Ravi-Chandar[63]; Needleman[64]; Espinosa et al.[65]; Mohammed and Liechti[66]; Pandol; et al.[67];Rahul-Kumar et al.[68]; Chen et al.[69]; Liechti and Wu[70]). This approach uses Cohesive Zone Models (CZM) and has been the focus of extensive research in recent years. Cohesion elements are based on a Dudgale-Barenblatt cohesive zone approach [71],[72], which can be related to Griffith's theory of fracture when the cohesive zone size is negligible when compared with characteristic dimensions, regardless of the shape of the constitutive equation[73]. In most of the CZM, either intralaminar or delamination damage mechanisms are considered. The cohesion elements relate traction to the relative displacement at an interface where a crack may occur. Crack/damage initiation is related to an interfacial strength, i.e. the maximum traction on the traction/relative displacement curve. When the area under this curve is equal to the critical fracture energy, the traction is reduced to zero and complete crack surfaces are formed. Indirect use of fracture mechanics is thus made in the model. A main advantage of the use of cohesion elements is the capability to predict both onset and propagation of delamination without previous knowledge of the crack

location and propagation direction. Moreover, with cohesion elements, the prediction of non-self similar delamination growth is possible.

Cohesion elements can be divided into two main groups:
1>.Continuous cohesion elements, including:
a.zero-thickness volumetric elements connecting solid elements[74],
b.finite-thickness volumetric elements connecting shell elements[75], and
c.line elements[76],[77].
2>Point cohesion elements.
Point cohesion elements are identical to non-linear spring elements connecting nodes[78],[79].

The resistance of delamination growth has been characterized by fracture toughness or critical energy release rates under modes I (crack opening), II (crack sliding or in plane shear), III(crack transverse shear) and mixed-mode loading conditions. For pure Mode I, II or III loading conditions, various traction/relative displacement curves, cubic/exponential (Needleman[80]; Xu and Needleman[81]), bilinear (Reedy et al.[82]; Mi et al.[83]), trapezoidal(Tvergaard and Hutchinson[84]) and elastic-perfectly plastic (Cui and Wisnom[78]), have been employed in the literature, as shown in Fig. 2.4.1-2. After the interfacial opening or shear tractions attain their respective interlaminar tensile or shear strengths, the stiffnesses are gradually reduced to zero. A damage parameter which is a function of the tracked maximum relative displacement and displacements corresponding to damage initiation and total decohesion of the elements is usually used to evaluate the damage evolution and degrade the stiffness[85]. The area under the stress-relative displacement curves is the respective (Mode I, II or III) fracture energy. The advantages of such models are their simplicity and the unification of crack initiation and growth within one model. They can also be easily implemented into an existing FE code via an "interface element".

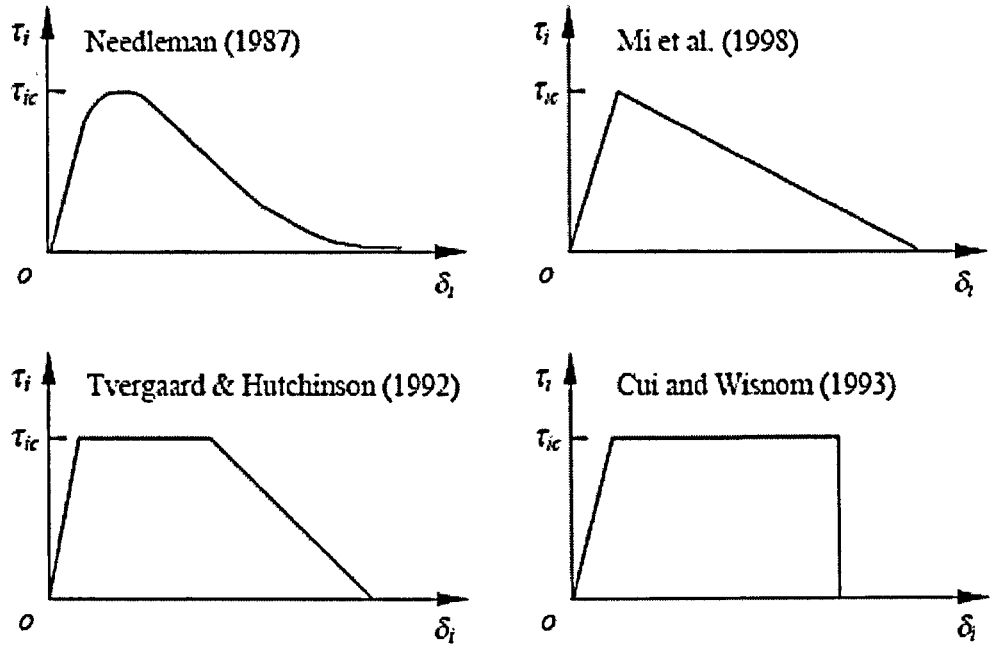

Fig. 2.4.1-2. Traction-relative displacement curves employed in various models in the literature[86]

2.4.2 Modelling delamination under mixed-mode loadings

In real loading conditions, it is very unlikely that pure mode I or mode II conditions will occur. Therefore, it is important to know how the delamination initiates and propagates under mixed-mode loading conditions. Similar to the pure mode loading, the delamination under mixed-mode loading conditions is also evaluated in two aspects: the onset and the propagation of the damage.

1. Delamination onset criteria under mixed-mode loadings

Most of the failure criteria summarized in Section 1(Failure Criteria associated with a Lamina) could be used as the onset criteria under mixed-mode loadings. Among them, the failure criterion presented by Brewer and Lagace[87] is the most widely applied one and has been successfully used to predict the onset of delamination in a large number of previous investigations[88],[89],[90]. Its form is described as:

$$\left(\frac{<\sigma_{33}>}{Z_{33}}\right)^2+\left(\frac{\tau_{13}}{S_{13}}\right)^2+\left(\frac{\tau_{23}}{S_{23}}\right)^2\geq 1 \qquad (2.4.2\text{-}1)$$

$$<x>=\begin{cases}x, x>0\\0, x<0\end{cases}$$

Usually, S_{13} is assumed to be equal to S_{23}[72,96], we then get the following form:

$$\left(\frac{<\sigma_{33}>}{Z_{33}}\right)^2+\left(\frac{\tau_{13}^2+\tau_{23}^2}{S^2}\right)\geq 1 \qquad (2.4.2\text{-}2)$$

$$<x>=\begin{cases}x, x>0\\0, x<0\end{cases}$$

When $\sigma_{33}<0$, some researchers assume that the shear strength S will be increased, with the representative modifications by Sun[91] and Puck[92] respectively as the below:

$$\left(\frac{<\sigma_{33}>}{Z_{33}}\right)^2+\left(\frac{\tau_{13}}{S_{13}+\eta_{13}<-\sigma_{33}>}\right)^2+\left(\frac{\tau_{23}}{S_{23}+\eta_{23}<-\sigma_{33}>}\right)^2\geq 1 \qquad (2.4.2\text{-}3)$$

There are also theories that consider the strengthening effect of compressive σ_{33} on shear strength S as a mixed-mode compression-shear failure, such as the criterion by Hou et al[93]:

$$\begin{cases}\left(\frac{\sigma_{33}}{Z_{33}}\right)^2+\frac{\sigma_{23}^2+\sigma_{13}^2}{S_{13}^2}\geq 1, \sigma_{33}>0\\ \frac{\sigma_{13}^2+\sigma_{23}^2-8\sigma_{33}^2}{S_{13}^2}\geq 1, -\sqrt{(\sigma_{13}^2+\sigma_{23}^2)/8}\leq\sigma_{33}<0\\ e_1^2\equiv 0, no\ \ dela\min ation, \sigma_{33}\leq-\sqrt{(\sigma_{13}^2+\sigma_{23}^2)/8}\end{cases} \qquad (2.4.2\text{-}4)$$

And the criterion by Christensen and Deteresa[94], which uses a linear instead of a quadratic interaction of σ_{33} :

$$\frac{\sigma_{33}}{T}+\frac{\sigma_{13}^2+\sigma_{23}^2}{S^2}\leq 1 \qquad (2.4.2\text{-}5)$$

2. Delamination propagation criteria under mixed-mode loadings

The criteria used to predict delamination propagation under mixed-mode loading conditions are usually established in terms of the energy release rates and fracture toughness. There are established test methods to obtain the Mode I and II interlaminar fracture toughness. The Double Cantilever Beam Specimen (DCB)[95],[96] is used for Mode I. The End Notched Flexure (ENF)[97] or the End Loaded Split (ELS)[98],[99] specimens are used for Mode II. For mixed-mode I and II, the Mixed-Mode Bending (MMB)[100] test specimen is normally used.

However, further research is required to assess the Mode III interlaminar fracture toughness, G_{IIIC}. Although some test methods have been suggested for the measurement of Mode III interlaminar fracture toughness, such as the Edge Crack Torsion[101],[102] (ECT), there are important issues that need clarification, such as the determination of the transverse shear modulus G_{23}, which is a parameter required for the analysis[103]. Furthermore, there is no reliable mixed-mode delamination failure criterion incorporating Mode III because there is no mixed-mode test method available incorporating Mode III loading. The distinction between mode II and III depends on the direction of the relative displacement between homologous points with respect to the orientation of the crack front. Without knowing how the crack front is oriented—and in a generic situation, with multiple crack growth, it might be difficult even to define it—it is impossible to distinguish between modes II and III. In most cohesion element formulations, the sliding mode uses a combined shear of both mode II and mode III based on mode II values and does not require a direct mode III input[62]. The sliding mode is usually considered to represent both modes II and III. Therefore the absence of G_{IIIC} can be overcome in modelling delamination problems.

A comprehensive study of failure criteria for mixed-mode delamination in brittle epoxy, tough epoxy and thermoplastic composites under the full mixed-mode range was performed by Reeder[104,105]. Some of the criteria evaluated are included in the table 2.4.2-1 below from Criterion 1 to 10. Table 2.4.2-1 summarizes the most commonly used delamination propagation criteria in the literature:

Table .2.4.2-1. Summary of delamination propagation criteria in literature[97-128]

Name	Criteria	Proposer	Comments
1.Linear Criterion[106,107,108,109,110,111]	$\left(\frac{G_I}{G_{IC}}\right)+\left(\frac{G_{II}}{G_{IIC}}\right)\geq 1$	Wu,E.M. Reuter Jr.R.C 1965	Good to predict failure of thermoplastic PEEK matrix composites and the response of epoxy composites.
2.Power Law Criterion[112] (α=2,β=2)[113],1981 (α=0.5,β=1)[106],1965 (α=1,β=1.5)[114],1987 (α=1.4,β=1.8)[115],1990 (α=0.64,β=0.8)[115]	$\left(\frac{G_I}{G_{IC}}\right)^{\alpha}+\left(\frac{G_{II}}{G_{IIC}}\right)^{\beta}\geq 1$	Whitcomb,J.D. 1984	Find optimum value of α and β by curve fitting through experimental data. Conservative, cannot account for the effect of load ratio on the mixed-mode fracture toughness in epoxy composites.
3.Polynomial Criterion[116]	$G_I+G_{II}=G_{IC}+\rho\left(\frac{G_{II}}{G_I}\right)+\tau\left(\frac{G_{II}}{G_I}\right)^2$	Yan, X.Q et al 1991	Unable to model low GII/GI ratios. Inappropriate as a general mixed-mode criterion.
4.KIC Criterion[117]	$G_I+G_{II}=G_{IIC}-(G_{IIC}-G_{IC})\sqrt{G_I/G_I}$	Hahn, H. T. 1983	If GIC=GIIC, reduces to Criterion 1; If GIC<<GIIC, reduces to Criterion 2, with α=0.5,β=1.
5. Hackle Criterion[118]	$G_I+G_{II}=(G_{IC}-\chi)+\chi\sqrt{1+\frac{G_{II}}{G_I}\sqrt{\frac{E_{11}}{E_{22}}}}$ χ is an arbitrary constant	Hahn, H. T. Johannesson, T 1983	Based on hackle angle parameter $\sqrt{1+(K_{II}/K_I)^2}$. Except for χ=0, this criterion always predicts an infinite GIIC, so not inappropriate as a general mixed-mode criterion either.
	$G_I+G_{II}=(G_{IC}-G_{IIC})e^{\gamma(1-N)}+G_{IIC}$ $N=\sqrt{1+\frac{G_{II}}{G_I}\sqrt{\frac{E_{11}}{E_{22}}}}$ γ is an arbitrary constant		

6.Exponential KIC/KIIC Criterion[119]	$G_I + G_{II} = (G_{IIC} - G_{IC})e^{\eta\sqrt{G_I/G_{II}}} + G_{IC}$ η is an arbitrary constant	White, Scott, R 1987	Can model the same types of responses modeled by Criterion 5 (2). But when η<=1
7.Critical Crack Opening Displacement(COD) Criterion[120]	$\frac{G_I}{G_{IC}} = 3\sqrt{\frac{E_{11}}{E_{22}}}\left(\left(\frac{G_{IIC}}{G_{IC}}\right)^2 \frac{G_{IC}}{G_{II}} - \frac{G_{II}}{G_{IC}}\right)$ $\frac{G_{II}}{G_{IIC}} = \frac{1}{3}\sqrt{\frac{E_{22}}{E_{11}}}\left(\frac{G_{IC}}{G_I} - \frac{G_I}{G_{IC}}\right)$	Hashemi, S. Et al 1987	Based on crack opening displacement, more appropriate for lower stiffness ratio.
8.Mode I & II Interaction Parameter Criterion[121]	$\left(\frac{G_I}{G_{IC}} - 1\right)\left(\frac{G_{II}}{G_{IIC}} - 1\right) - k\left(\frac{G_I}{G_{IC}}\right)\left(\frac{G_{II}}{G_{IIC}}\right) = 0$	Williams, J. G., & Hashemi, S. 1989	Material responses modeled by this criterion seem to be almost identical to those modeled by Criterion 2. k values from 0.26 to 3.12[122], 1990
9.Linear Mode I & II Interaction Criterion[123]	$\left(\frac{G_I}{G_{IC}} - 1\right)\left(\frac{G_{II}}{G_{IIC}} - 1\right) - \left[k + \varphi\frac{G_I}{G_I + G_{II}}\right]\left(\frac{G_I}{G_{IC}}\right)\left(\frac{G_{II}}{G_{IIC}}\right) = 0$	Hashemi, S. Et al 1991	(k,φ)=(3,-4);(4,-3) are suggested for different materials. But the criterion is a complicated implicit function of GIC and GIIC, which could make it difficult to use.
10. Bilinear Criterion[104]	$G_I = \xi G_{II} + G_{IC}$ $G_I = \varsigma G_{II} - \varsigma G_{IIC}$	J.R.Reeder 1993	Taking into account the modification of failure mechanisms near the one-to-one ratio of GI/GII, yields the best results when simulating epoxy matrix composites.
11.B-K Criterion[124]	$G_C = G_{IC} + (G_{IIC} - G_{IC})\left(\frac{G_{II}}{G_T}\right)^{\eta}$	Benzeggagh, M.L. and Kenane, M.	By determining the material parameter η from standard

	$G_T = G_I + G_{II}$ If Mode III loading occurs: $G_C =$ $G_{IC} + (G_{IIC} - G_{IC})\left(\frac{G_{shear}}{G_T}\right)^{\eta}$ $G_{shear} = G_{II} + G_{III}$ $G_T = G_I + G_{shear}$	1996	delamination tests, this criterion could represent the mixed-mode fracture toughness over large range of mode mixities. It can be applied for both tough and brittle epoxy, as well as thermoplastic composites by adjusting the η values. η~2.60 for E-glass/epoxy; η~1.56 for carbon/epoxy.
12. B-A Criterion[125]	$G_C =$ $2G_{IC} + (G_{IIC} - G_{IC})\left(\frac{G_{II}}{G_T}\right)^{\eta}$	Ben W.Kim Arnold H. Mayer 2002	More precisely fits the experimental data of multidirectional AS4-Carbon/Epoxy composites. η is related with fibre stacking orientation.
13. Piotr Criterion[126]	$\left(\frac{G_I}{G_{IC}}\right) + \left(\frac{G_{II}}{G_{IIC}}\right) + \gamma\left(\frac{G_I G_{II}}{G_{IC} \cdot G_{IIC}}\right) \geq 1$ $\gamma = a + b\left(\frac{G_{II}}{G_{IIC}}\right)$	Piotr Czarnocki 2003	Interaction coefficient γ is the function of Mode Ratio. a, b are related with relative fibre reinforcement orientation
14. Compression-Shear Criterion[127]	$G_{IIc} = G_{IIco} * (1 - \lambda \bar{\sigma}_2)$ G_{IIco} is the original critical fracture energy λ is enhancement factor $\bar{\sigma}_2$ is average compressive stress	Cui &Wisnom 1994	Accounts for enhancement of GIIC due to compression. Could well predict the shear failure of cut-ply and dropped ply tests. λ need data fit with experimental results.

2.5 Size Effect

Adequate design of structures may be carried out only on the basis of reliable information about properties of the materials used. The concept of material properties assumes that at a certain scale the material can be considered homogenous. The mechanical properties of composites are generally determined experimentally using small coupon tests. In these tests it is normally assumed that every part of the material behaves in the same way and so volume-averaged properties can be measured over the domain of material tested. A fundamental question about this assumption is: does the size of the specimen affect the value of the property measured?

For properties such as elastic modulus, Wisnom[128] concluded that its value should not vary with specimen size since variations of the elastic modulus at very small scales would average out over the volume at which typical engineering tests are carried out. Strength is different, however, because failure tends to initiate from defects or other weak points in the material. Defects in composites tend to be randomly distributed and larger volumes have a higher probability of containing a larger defect. There is, therefore, no reason to assume that volume averaged strengths will be independent of specimen size. Strengths will tend to be a function of the extreme values rather than the means of the distributions of local strengths, and can be expected to reduce with increasing volume of material being tested. This is called the 'size effect'.

There is significant experimental evidence for the existence of a size effect in composites[129-136]. Experimental analysis of the size effect of the laminated composite strength is a fairly complex problem because, by contrast with conventional materials, there are different modes of the size effect, associated with different dimensions and test configurations—thickness, length, width[130,131] and the well known hole(notch) size effect[131]. Moreover, the edge effect[132] and cracking of the weakest laminae[133] may influence the size effect performance. The problem of thickness scaling is further complicated by the fact that this can be achieved in different ways[134]: (a) ply-level scaling and (b) sublaminate-level scaling. The ply-level scaling was to increase laminate thickness by blocking multiple plies with the same orientation and the sublaminate level scaling was to increase laminate thickness by increasing the number of repeated ply stacks However, in spite of the differences of the considered reinforcement schemes, their geometrical

parameters, kinds of constituents, and ways of loading, the dependence of the mean strength characteristics on the composite thickness has been experimentally shown[130-135].

Factors influencing the size effect include statistical defects in stressed volumes, material microstructures, free edge effects, stress gradients, specimen manufacture and preparation and testing considerations[128]. In testing, the effect of stress concentration and gauge size can be avoided using scaled tests, which require the full test geometry to be scaled, including any tabs or loading fixtures. Material microstructures such as heterogeneities in the packing of fibres, fibre crimp in woven materials, fibre stitching damage in stitched composites may also give rise to size effects. The cure process, surface polishing and different ways in which large structures and small test coupons can be produced all may influence the size effect.

Experimental confirmation and estimation of the size effect is a fairly labor-intensive and expensive procedure, because the investigation of possible composite materials strength size effects concerns both a large number of pertinent variables and experimental data subject to considerable scatter[136],[137]. This type of problem requires an efficient experimental program and statistical analysis techniques in order to separately estimate the effects of each variable, and also to distinguish these effects from the random variation in the experimental data. It is necessary to conduct statistical analysis for a large sample of the test specimens. Consequently, it is very important to develop a detailed method that adequately accounts for the size effect of composites.

Among the above factors, the influence of statistical defects on the fibre tensile strength is especially important for the size effect and was extensively investigated using probabilistic failure models for its quantitative analysis[136,138,,139,140,]. The probabilistic models are usually based upon the weakest link theory also known as `Weibull theory'[138].This theory assumes brittle behaviour and has been found to satisfactorily describe the size effects seen for the strength of both ceramics and single constituent fibres of composite materials. The weakest link theory was extended in the literature for various specific configuration of fibre reinforced composites by using idealized load sharing rules and failure theories were derived by assuming simple tensile failure of unidirectional composites[141,-142,143,144,145,146]. However it is questionable whether these theories could be applied where more complex failure modes of laminates occur. In some cases the theories have only been presented as mathematical exercises without any reference to experimental data. The complexity of

some of the models becomes redundant when their parameters become difficult or impossible to estimate, and gross approximations are required. Also, the advantages of further refining the mathematical model must be balanced against the assumptions made in the derivation of the theory (especially concerning the uniformity of the microstructure). Regardless of the fact that the fibre statistic failure formulations proposed in the literature have analytical forms, their practical realization is also connected with the inevitable realization of computer-aided time-demanded numerical procedures. And this, in turn, creates complexities for introduction into engineering practice and restricts the application of the results obtained in various theories. To effectively implement a probabilistic theory in finite element analysis (FEA) for more general configuration of composites, it is expected that the parameters of the theory could be experimentally determined. For the consideration of computing efficiency, the formulation of the theory and the pertinent variables should be as concise as possible.

2.6 Summary and Conclusion

Failure analysis of a laminate is much more complex than that of a single lamina. The stresses in the individual laminae are fundamental and control failure initiation and progression in the laminate. Failure of a lamina does not necessarily imply total failure of the laminate, but is only the beginning of an interactive failure process. Laminate strength theories, like lamina strength theories, are macroscopic and are expressed in terms of the basic lamina strength parameters. The strength of each individual lamina is assessed separately by referring its stresses to its principal axes, which vary from lamina to lamina, and by applying a selected failure criterion. It is questionable to assume that a layer, or lamina, within the laminate has the same properties and behaves in the same manner as an isolated unidirectional lamina, because the in-situ properties of an embedded layer may be different from those of an isolated layer. Furthermore, a layer within the laminate is under a state of fabrication residual stresses, and its failure takes the form of dispersed damage (micro-cracking) rather than one major localized flaw or crack. Nevertheless, it is acceptable to use isolated lamina properties in existing lamina theories to predict first ply failure.

The numerous composites failure theories can be classified into three groups, *limit or non-interactive theories* (e.g. maximum stress, maximum strain); *interactive theories* (e.g. Tsai-Hill, Tsai-Wu); and *partially interactive or failure mode based theories* (e.g. Hashin-

Rotem, Puck). The validity and applicability of a given theory depends on the convenience of application and agreement with experimental results. The plethora of theories is accompanied by a dearth of suitable and reliable experimental data, which makes the selection of one theory over another rather difficult.

Kortschot and Beaumont[147,148,149,150] ever investigated the damage growth and strength of double-edge notched cross-ply laminates considering the blunting effect of splitting, delamination and the size effect of 0^{o} ply strength, which is highly relevant to the research in this thesis. They assumed self-similar growth of splitting and delamination to obtain the relation between stress and damage growth in cross-ply carbon/epoxy laminates and subsequently combined this with calibrated 0^{o} ply strength by a direct application of the weakest-link Weibull model to predict the remote failure stress of the notched laminate. The obvious deficiency of their approach is the lack of capability to accurately simulate the growth and interaction of splitting, delamination and fibre failure. Their method of determining the damage growth was complicated but not flexible and need empirical assumptions of the delamination areas and neglect of thermal stresses. The size effect of 0^{o} ply strength only considered a small volume subjected to a concentrated stress at the notch tip. Also the application of their research was limited to cross-ply layups of laminates.

The work in this thesis builds on this information available in the literature on composites failure modeling. It has taken the path of progressive damage modeling, using cohesion elements to model potential intralaminar cracks and connect laminae in a laminate. Laminae in the laminate are considered to behave individually in the same manner as a unidirectional lamina but interact with each other through interlaminar and intralaminar interface elements. Effects of thermal residual stress and fibre orientations in a laminate were included in this way. The influence of dispersed flaws on the tensile strength of the lamina was accounted for by applying Weibull statistical strength theories on fibre tensile failure.

Simulation of open hole tension tests on six layups of IM7/8552 carbon epoxy laminates and Over Height Compact Tension(OCT) tests on eight layups of laminates using the same materials showed that this technique of modelling stress and damage interaction in composite laminates can effectively capture the complex influence of factors: statistical flaws in laminae, stacking sequence of laminae, lamina orientations, stiffnesses, strengths and coefficient of thermal expansion on the strength of the laminate.

Chapter 3 Modelling Interface element failure in composites

3.1 Introduction

Initiation and propagation of delamination is often a precursor to ultimate failure in laminated composite structures. Knowledge of delamination and the ability to model this aspect of failure therefore deserve particular attention. Delamination in laminated composites is often localized in the resin rich layer between plies. The thickness of these layers is generally very small and they can therefore be modelled as interfaces where displacement discontinuities can take place in a mathematical model. This is a basic assumption of the widely-used interface element models, which are then characterized by suitable constitutive relationships between the stresses acting on the interface and the displacement discontinuities.

Interface elements which are located between adjacent laminae to simulate both initiation and non self-similar growth of delamination have been successfully applied to numerical simulation of interlaminar fracture in composite structures[66-95]. LS-Dyna is one of the explicit FE codes most widely used by the industry to model impact or crash situations in laminated composite materials. In this work, two types of interface elements: discrete beam element and eight-noded solid element were formulated and implemented in LS-Dyna. Solid elements in LS-Dyna cannot be zero thickness, therefore the solid interface elements are mainly used to model the resin-rich zones within a laminate. To model the very thin cohesive zones, zero-thickness beam interface elements need to be applied. The formulation of interface elements is based on published work[88-127] reviewed in Section 2.4 but includes the enhancement effect of through-thickness compression on the delamination, which was ignored in most interface element failure criteria in the literature

Interface elements are typically formulated in terms of a traction vs. relative displacement relationship instead of the traditional stress vs. strain relation. Generally, two surfaces (top and bottom) are considered, as shown in Fig 3.1-1. Each point in each of these surfaces has a corresponding point in the other surface, designated as homologous. A pair of homologous points is a pair of points that are in contact before the interface is loaded. The relative displacement between each pair of homologous points is projected in a local

reference system, which expresses the relative displacement in terms of an opening mode (mode I) and a sliding mode. Sliding can be due to modes II or III loading (or a combination of both). As discussed in Section 2.4.2, in a generic situation where the propagation orientation of the crack front is not known and multiple crack growth may exist, it is impossible to distinguish between modes II and III. Therefore the sliding mode usually uses a combined shear of both mode II and mode III based on mode II values and does not require a direct mode III input. In this case, the sliding mode is considered to represent both modes II and III. and the absence of G_{IIIC} can be overcome in modelling delamination problems.

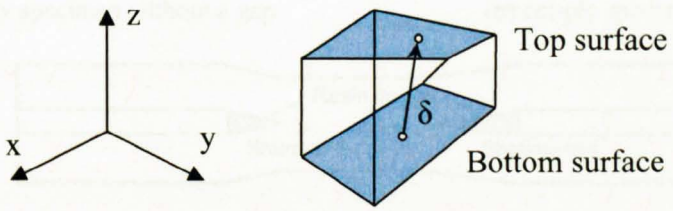

Fig 3.1-1 Schematic interface model

Prior to delamination onset, an elastic constitutive law relates the relative displacement of two homologous points with the traction (force per unit area) acting on both the top and bottom surfaces. For pure mode I or pure shear mode problems, the interface is usually considered to have an elastic behaviour (linear or not) until the respective maximum allowable stress is reached. Then, the stiffness is reduced in such a way that the energy absorbed per unit area is equal to the corresponding critical energy release rate (G_{Ic} or G_{Sc}, respectively.) G_{IC} is the mode I or opening mode critical fracture energy and G_{SC} is the shear mode critical fracture energy . For mixed-mode problems, the elastic relationship is valid until a stress-based initiation criterion is verified. From this stage onwards, the stiffness is reduced for each mode ratio in such a way that the energy absorbed in the mixed-mode situation is defined by a propagation criterion.

Formulation and implementation of both discrete beam and eight-node solid interface elements in LS-Dyna were validated by modelling the standard mode I delamination toughness test Double Cantilever Beam (DCB) and the generally used mode II End Notch Flexure (ENF) test.

In most interface element failure theories reviewed in Section 2.4, the effect of tensile through-thickness stress is normally taken into account in combination with interlaminar shear stress. When the through-thickness stress is compressive, however, its effect is usually ignored and the failure of the interface elements is considered to be pure mode II. Experiments on cut-ply and dropped-ply specimens[127] as shown in Fig 3.1-1 however show that the compressive through-thickness stress can greatly increase the delamination failure stress and cannot be simply neglected.

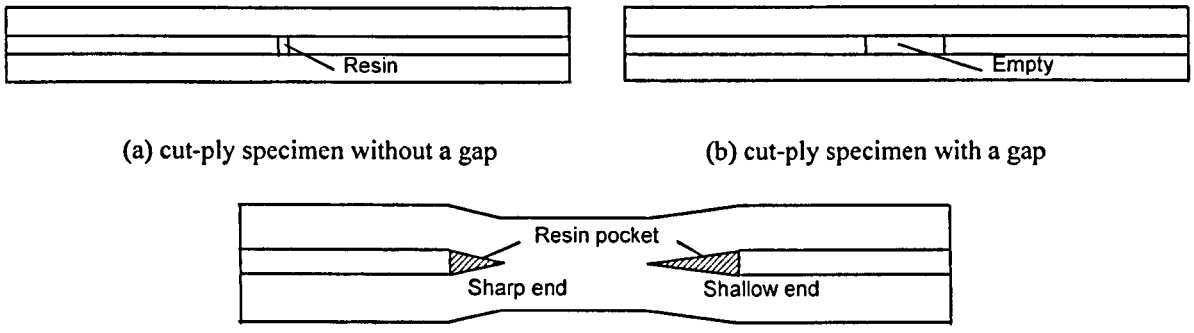

(a) cut-ply specimen without a gap

(b) cut-ply specimen with a gap

(c) Dropped-ply specimen with different taper angles

Fig 3.1-1 Schematic representation of cut-ply and dropped-ply specimens

The influence of compressive stress on mode II damage evolution was investigated numerically based on the cut-ply and dropped-ply experiments. A new interfacial failure model with modified failure initiation and propagation criteria was proposed to take the effect of compression on matrix shear strength and mode II critical fracture energy, G_{IIC}, into account. This new model uses only one independently determined parameter to relate the compression to the increase in interlaminar shear strength and G_{IIC}. With the new failure criterion applied, two types of cut-ply models and two types of dropped-ply models, using the same input parameter, all produce excellent correlation with experimental delamination stresses.

A single-lap shear test developed by Dong and Harding[151] was simulated using interface elements and a consistent mesh independent result was obtained, while the failure prediction of a traditional solid element based numerical model was seriously influenced by the mesh density due to the highly localised stress concentration in the specimen. As a validation case of the above theory about the influence of compressive stress on mode II damage evolution, the single-lap model was run with the new criterion and the same input parameters and this also achieved very good correlation with the experimental failure stress.

3.2 Constitutive Law Applied in Interface Elements

Although the constitutive model presented in this section has been published elsewhere[152], its details are of significant importance to this thesis and they are reproduced here for completeness.

3.2.1 Introduction

Various constitutive laws as shown in Fig 2.4.3-1 have been compared by Williams and Hadavinia[153] in analyzing a cantilever beam specimen using a beam on elastic foundation model. They concluded that the shape of the interfacial constitute law was not of extreme importance, provided the fracture toughness was correctly accounted for, and the initial stiffness and maximum traction were reasonably consistent with the stiffness and strength of the material being modeled. Therefore a simple bilinear softening cohesive-decohesive constitute law (as shown in Fig 3.2.1-1) which relates the interfacial traction components to the relative displacement components was adopted in this thesis to model interface element behaviour.

Consider a point in an interface like the one in Fig 3.2.1-1. The tractions σ_i between the top and bottom surfaces of the interface at that point are related to the relative displacement δ_i at the same point for i=1–3. The index value i=1 corresponds to an opening mode (mode I), while the index values i=2 and 3 correspond to a transverse shear mode (modes II and III).

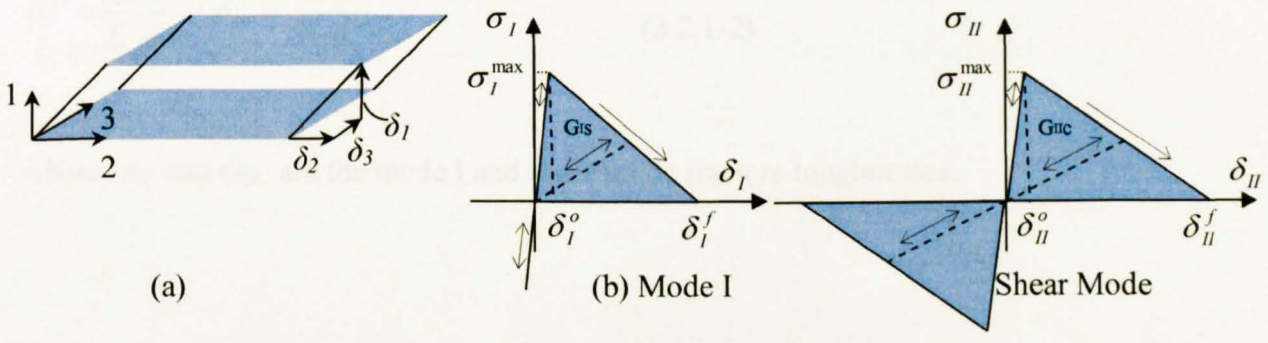

Fig 3.2.1-1 Bilinear constitutive law in single-mode loading

The relative displacements and tractions corresponding to the onset of damage are denoted as onset displacements and onset tractions respectively. The onset displacement is identified with the superscript 'o' and the onset traction is denoted as σ^{max}. The relative

displacements corresponding to complete decohesion are denoted final displacements and identified with the superscript 'f'.

Suppose a point is loaded such that a relative displacement δ_i is applied parallel to one of the local axes (i=1, 2 or 3). While the relative displacement has never exceeded its damage onset value, the point behaves elastically. Once the onset displacement is exceeded, some energy is absorbed. The total energy that can be absorbed at each point (per unit area of the interface) equals the critical energy release rate for the corresponding mode.

When the maximum traction σ_I^{max} or σ_{II}^{max} (according to the mode) is reached, the damage is assumed to start propagating. The corresponding onset displacements are, for the opening and shear modes, respectively

$$\delta_I^o = \frac{\sigma_I^{max}}{E_I}, \quad \delta_{II}^o = \frac{\sigma_{II}^{max}}{E_{II}} \qquad (3.2.1\text{-}1)$$

where σ_I^{max} and σ_{II}^{max} are the mode I and shear mode maximum allowable tractions, respectively. E_I and E_{II} are the initial tensile and shear stiffness of the interface. (The subscripts I and II on the onset displacements δ_I^o and δ_{II}^o indicate that these onset displacements correspond to the normal or shear traction acting alone, respectively.) When the traction reaches zero, the energy absorbed must equal the critical energy release rate. This leads directly to the definition of the final displacements in a pure-mode loading situation as

$$\delta_I^f = \frac{2G_{IC}}{E_I \delta_I^o}, \quad \delta_{II}^f = \frac{2G_{IIC}}{E_{II} \delta_{II}^o} \qquad (3.2.1\text{-}2)$$

where G_{IC} and G_{IIC} are the mode I and shear mode fracture toughnesses.

3.2.2 Mixed Mode Failure Criteria and Constitute Law

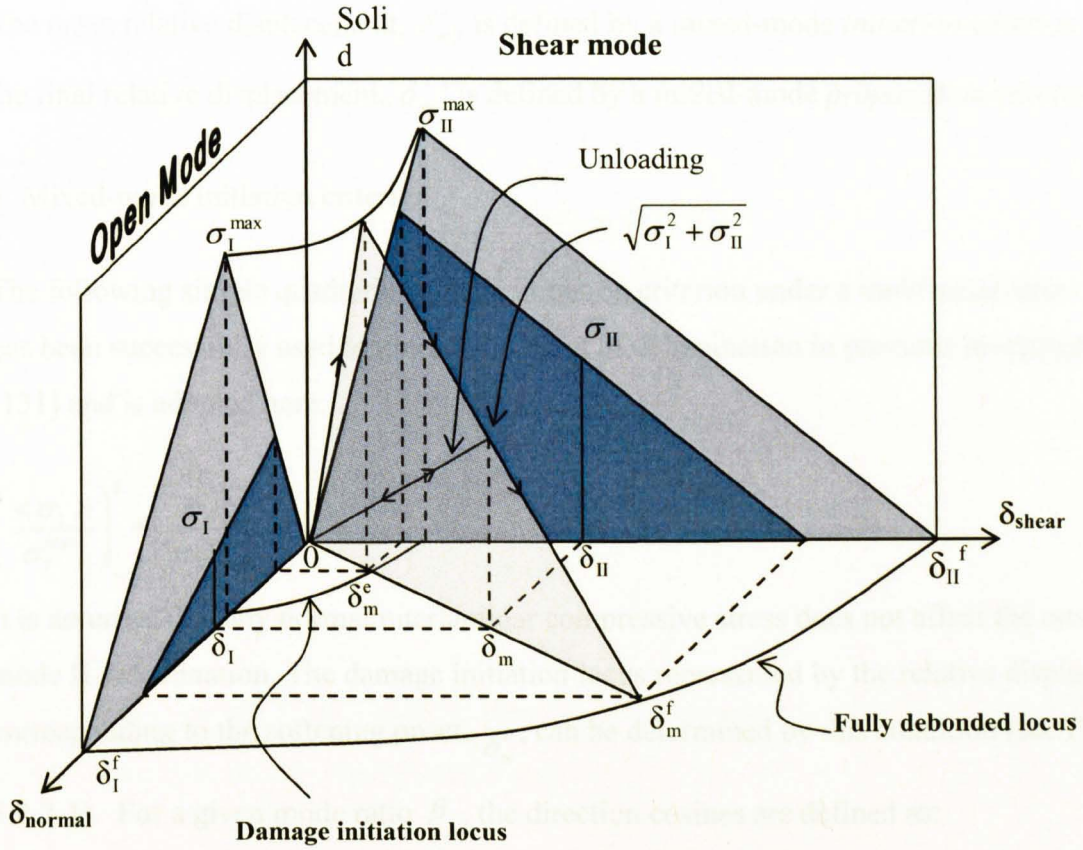

Fig 3.2.2-1 Mixed-mode behaviour for the bilinear constitutive law

In a situation where more than one mode acts simultaneously, the damage starts propagating even before one of the limit tractions for pure mode loading (Mode I or Mode II) is attained individually—as shown in Fig 3.2.2-1. In order to analyze this situation, the shear relative displacement, δ_{II}, and the magnitude of the relative displacement, δ_m, are defined as

$$\delta_{II} = \sqrt{(\delta_2)^2 + (\delta_3)^2}\ ,\quad \delta_m = \sqrt{<\delta_I>^2 + (\delta_{II})^2} \qquad (3.2.2\text{-}1)$$

where $<\delta_I> = \begin{cases} \delta_I & \delta_I \geq 0 \\ 0 & \delta_I < 0 \end{cases}$

The shear traction is defined as

$$\sigma_{II} = \sqrt{(\sigma_2)^2 + (\sigma_3)^2} \qquad (3.2.2\text{-}2)$$

and the participation of the different mode β, is defined as:

$$\beta = \max\left\{0, \frac{\delta_{II}}{\delta_I}\right\}$$

The onset relative displacement, δ_m^o, is defined by a mixed-mode *initiation* criterion and the final relative displacement, δ_m^f, is defined by a mixed-mode *propagation* criterion.

1. Mixed-mode initiation criterion

The following simple quadratic damage initiation criterion under a multi-axial stress state has been successfully used to predict the onset of delamination in previous investigations [131] and is adopted here:

$$\left(\frac{<\sigma_1>}{\sigma_I^{\max}}\right)^2 + \left(\frac{\sigma_{II}}{\sigma_{II}^{\max}}\right)^2 = 1 \qquad (3.2.2\text{-}3)$$

It is assumed that any normal interlaminar compressive stress does not affect the onset of mode II delamination. The damage initiation locus represented by the relative displacement corresponding to the softening onset, δ_m^o, can be determined by this condition (see Fig 3.2.2-1). For a given mode ratio β, the direction cosines are defined as:

$$\cos I = \delta_I / \delta_m \quad \text{and} \quad \cos II = \delta_{II} / \delta_m \qquad (3.2.2\text{-}4)$$

the relative displacement corresponding to softening onset(or damage initiation), δ_m^o,can be calculated using equation 3.2.2-3 as:

$$\delta_m^o = \begin{cases} \left[\sqrt{\left(\frac{\cos I}{\delta_I^o}\right)^2 + \left(\frac{E_{II}\cos II}{\delta_{II}^o}\right)^2}\right]^{-1} & \delta_I \geq 0 \\ \delta_{II}^o & \delta_I < 0 \end{cases} \qquad (3.2.2\text{-}5)$$

2. Mixed-mode propagation criterion

The mixed-mode propagation criterion establishes the state of complete decohesion for different ratios of applied mode I and shear mode energy release rates. There are several criteria that establish mixed-mode propagation, refer to the review in Table 2.4.3-1. One of these, the power law criterion[104-107], can be expressed as

$$\left(\frac{G_I}{G_{IC}}\right)^{\alpha}+\left(\frac{G_{II}}{G_{IIC}}\right)^{\alpha}=1 \qquad (3.2.2\text{-}6)$$

Where $\alpha \in (1.0,2.0)$ is an empirical parameter derived from mixed-mode tests. G_I and G_{II} are the energy absorbed up to the complete decohesion in a mixed-mode loading situation, for each mode. G_{IC} and G_{IIC} are critical energy release rates for pure mode I(opening) and pure mode II (shear) respectively. Experimental results indicate that a significant range of interface failure under mixed mode conditions can be covered by the power law. This failure criterion of the interface element is thus adopted in this thesis.

As the tractions are a function of the relative displacements, these energies may be expressed in terms of relative displacements. The energy absorbed by each mode in a mixed-mode loading is (refer to Fig 3.2.2-1)

$$G_I=\frac{E_I\delta_m^o\cos I\delta_m^f\cos I}{2} \quad \text{and} \quad G_{II}=\frac{E_{II}\delta_m^o\cos II\delta_m^f\cos II}{2} \qquad (3.2.2\text{-}7)$$

Introducing Equation 3.2.2-7 in the expression of the power law criterion, equation (3.2.2-6), the expression for δ_m^f can be obtained as

$$\delta_m^f=\begin{cases}\left(\left(\frac{E_I\delta_m^o\cos I^2}{2G_{IC}}\right)^{\alpha}+\left(\frac{E_{II}\delta_m^o\cos II^2}{2G_{IIC}}\right)^{\alpha}\right)^{-1/\alpha} & \delta_I\geq 0\\ \delta_{II}^f & \delta_I<0\end{cases} \qquad (3.2.2\text{-}8)$$

3. Constitutive Law

In order to account for irreversibility, the maximum over time value of the mixed-mode displacement is defined as, at time t

$$\delta^{\max}(t)=\max_{ti\leq t}\{\delta(ti)\}$$

A simple damage variable d is introduced to track the extent of damage accumulated at the interface:

$$d=\begin{cases}0 & \delta^{\max}\leq\delta_m^o\\ \dfrac{\delta^{\max}-\delta_m^o}{\delta_m^f-\delta_m^o} & \delta_m^o<\delta^{\max}<\delta_m^f\\ 1 & \delta_m^f\leq\delta^{\max}\end{cases} \qquad (3.2.2\text{-}9)$$

The damage state variable d is defined in such a way as to assure that the transition between load steps is smooth, even for the case of significant mode ratio change.

Unloading of the constitutive law is simply assumed to return linearly back to a zero stress state at the origin as shown in Fig 3.2.2-1. The Mode I (normal tensile) interface stress can be calculated as:

$$\sigma_I = (1-d)\delta_{ratio} E_I \delta_m^o \cos I \qquad \delta_I > 0 \qquad (3.2.2\text{-}10)$$

The resultant shear interface stress is:

$$\sigma_{II} = (1-d)\delta_{ratio} E_{II} \delta_m^o \cos II \qquad (3.2.2\text{-}11)$$

Where δ_{ratio} is a loading level factor with respect to the current maximum 'yield' limit in the current loading direction. If the current load step causes further damage, then $\delta_{ratio} = 1$, otherwise, the current load step is 'elastic' and δ_{ratio} is calculated as:

$$\delta_{ratio} = \frac{\delta_m}{\delta_m^o + d(\delta_m^f - \delta_m^o)} \qquad (3.2.2\text{-}12)$$

The shear stress components can then be decomposed as

$$\sigma_2 = \sigma_{II}\delta_2 / \delta_{II} \quad \text{and} \quad \sigma_3 = \sigma_{II}\delta_3 / \delta_{II} \qquad (3.2.2\text{-}13)$$

In order to avoid interpenetration for compression situations, a penalty contact stress is introduced:

$$\sigma_1 = E_1 \delta_1 \qquad \delta_1 < 0 \qquad (3.2.2\text{-}14)$$

It is worth mentioning that in many of the published works reviewed in Section 2.4, the stress degradation is considered via the degradation of initial stiffnesses. Typical conventional cohesive models calculate stresses via the damage variable using the following forms of equations:

$$\sigma_I = (1-d)E_I \delta_I \quad \text{and} \quad \sigma_{II} = (1-d)E_{II}\delta_{II} \qquad (3.2.2\text{-}15)$$

The corresponding damage parameter for monotonic loading is calculated as:

$$d = \frac{\delta_m^f(\delta_m - \delta_m^o)}{\delta_m(\delta_m^f - \delta_m^o)} \qquad (3.2.2\text{-}16)$$

This type of definition of damage variable is a highly nonlinear function of the relative displacement. Jiang et al[152] demonstrated in their work that such a damage variable could

grow from 0 to very close to 1 extremely quickly for very small values of the relative displacement and even varied with initial stiffness values, which might cause numerical instability and results inconsistency. Therefore the simple linear form of damage variable in equation 3.2.2-9 is preferred in this thesis.

3.3 Implementation of Interface Element Constitutive Law in LS-Dyna

The constitutive behaviour presented above has previously been implemented in LS-Dyna (v940.2) [ref]. In order to continue development in a more up to date version of the software (v970 +) this was reformulated within the framework of a user material model. This was done using Mat42 for discrete beam elements (similar to the original formulation) and user material Mat49 for a new solid element formulation. The discrete beam element as shown in Fig 3.3-1a is a one dimensional zero thickness element. The solid interface element as shown in Fig 3.3-1b is a three dimensional non-zero thickness eight-node constant stress element.

1. Discrete interface element

The user defined material input card for discrete beam interface elements in LS-Dyna is explained in Appendix A-1. Each beam in the model has an effective load-transferring area contributed by all the laminate elements around the beam, as shown in Fig 3.3-1. This effective area and the beam orientation vectors are automatically calculated when beam elements are generated by a custom written pre-processor program introduced in the following section 3.4.. Within the user material, the axial and transverse nodal displacement tensors of the beam elements are known, the nodal force tensors need to be calculated accordingly. Using the presented interface element formulation, beam nodal force tensors can be determined in a straightforward manner.

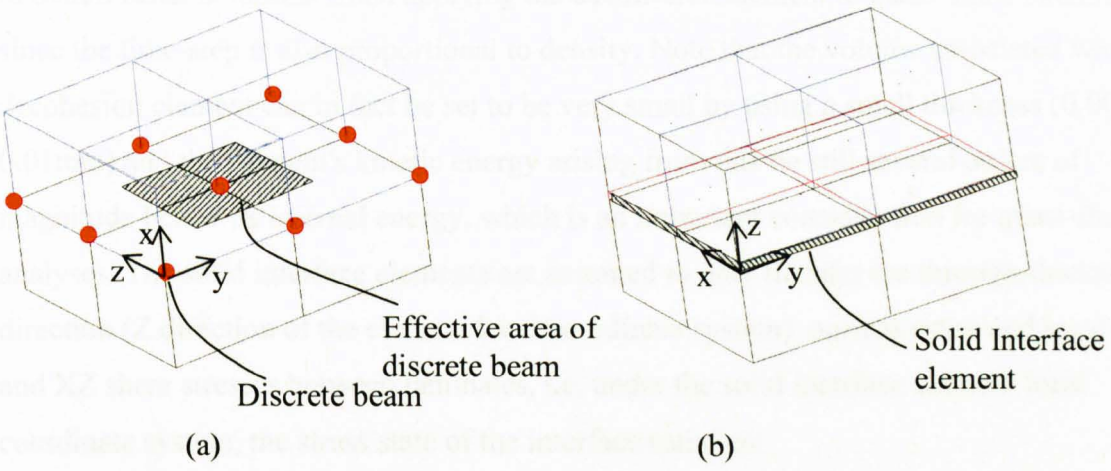

Fig 3.3-1 Implementation of (a) discrete beam and (b) solid interface elements

The difficulty in using discrete elements is that when the interface has a complex shape it requires a large number of coordinate systems in LS-Dyna for the different orientations of the discrete elements. Though the pre-processor program can automatically generate these coordinate systems, the resulting models are generally much larger and slower to run. When the dimensions of a model with discrete elements are changed in size by scaling or any other orienting method, it is usually required to re-run the pre-processor program to update effective areas of beam elements. Also if the interface in the model undergoes large rotations during the analysis the referenced coordinate systems are not rotated accordingly thus giving rise to potential error by incorrectly determining the mode ratio. Comparatively the solid element formulation takes its orientation directly from the nodal coordinates (which rotate correctly with the interface) and does not require external coordinate system definitions. Its area is internally calculated within LS-Dyna again from nodal coordinates and so does not require the use of the pre-processor program for this. It is further easier to extract the time history variable information from the solid elements through graphical post-processing of the results.

2. Solid interface element

The user defined material input card for solid interface elements in LS-Dyna is explained in Appendix A-2. The implementation of solid interface elements has the implication of requiring to model the resin rich layer (for the case of delaminations) with non-zero thickness. In reality the resin-rich layer has a finite thickness and so this is appropriate so long as this is kept small. The downside of this is that the time-step in the explicit analysis is controlled by element length thus resulting in long run times. Mass scaling can be used

to obtain faster solutions when applying the decohesion element to quasi-static situations since the time-step is also proportional to density. Note that the volume associated with the decohesion element can in fact be set to be very small by using a small thickness (0.001–0.01mm) and the element's kinetic energy arising from this be still several orders of magnitude below its internal energy, which is an important consideration for quasi-static analyses. The solid interface elements are assumed to only transfer the through-thickness direction (Z direction of the element local coordinate system) normal stress and local YZ and XZ shear stresses between laminates, i.e. under the solid interface element local coordinate system, the stress state of the interface satisfies:

$$\begin{cases} \sigma_{11} = 0 \\ \sigma_{22} = 0 \\ \sigma_{33} = local\_Z\_tension/compression \\ \tau_{12} = 0 \\ \tau_{32} = local\_ZY\_shear\_stress \\ \tau_{31} = local\_ZX\_shear\_stress \end{cases} \qquad (3.3\text{-}1)$$

Within the user material, the nodal displacements and the strains are known, the incremental displacements of the solid interface along three load-carrying directions are:

$$\begin{cases} \Delta\delta_{33,t+1} = (tk + \Delta\delta_{33,t}) * \Delta\varepsilon_{33,t+1} \\ \Delta\delta_{32,t+1} = (tk + \Delta\delta_{32,t}) * \Delta\varepsilon_{32,t+1} \\ \Delta\delta_{31,t+1} = (tk + \Delta\delta_{31,t}) * \Delta\varepsilon_{31,t+1} \end{cases} \qquad (3.3\text{-}2)$$

where, tk is the thickness of the solid interface element at $t=0$.

The non-zero components of the stress tensor correspond to the tractions, whose determination is straightforward using the presented formulation, which requires storing δ^{max} as a history variable.

3. Flowchart for the implementation

The flowchart for implementing the interface element constitutive law in LS-Dyna is given in Fig 3.3-2.

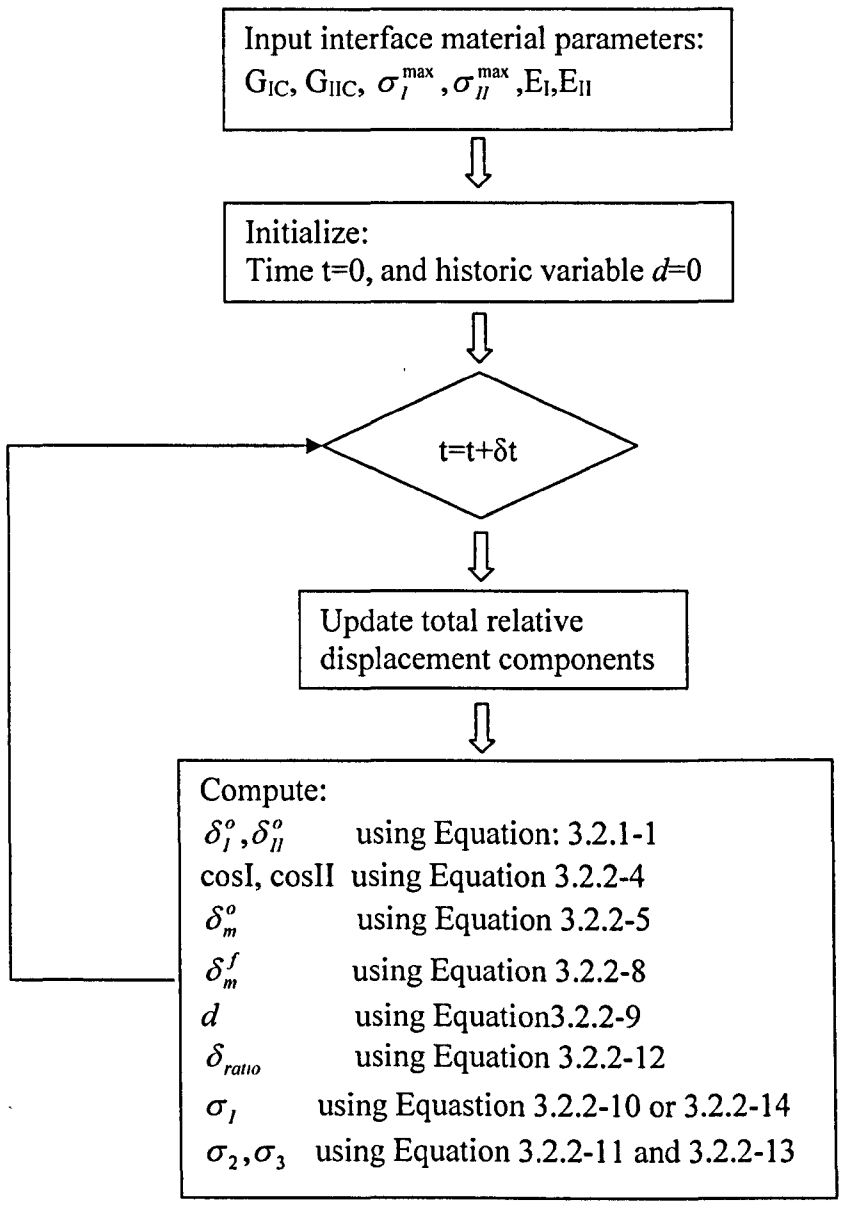

Fig 3.3-2 Flowchart for implementing interface element constitutive law in LS-Dyna

3.4 Pre-processing Programs for Interface Element Model

When applying beam interface elements in the models, the equivalent areas and orientation vectors of each beam need to be determined. This work cannot be done manually in any commercial pre-processing software so far. When the shape of a model is complicated, it is also difficult to create manually either beam or solid interface elements at pre-defined positions in the model using commercial pre-processing software. Therefore pre-processing programs specifically for automatically generating beam and solid interface elements in models were developed in this section. The pre-programs were designed to

generate interface elements along the pre-defined potential failure surfaces between laminates so that the interface failure criteria can be implemented in the model. According to the properties of interface elements, the pre-process programs are divided into two parts: one part is for generating two-node discrete-beam-element, the other part is for inserting eight-node solid element between laminates. The programs for discrete-beam-element and solid-element are respectively introduced in the following sections:

3.3.1 Program for discrete-beam element

This program is used to generate 'Discrete Beam Thickness' interface elements in Ls-Dyna FEM models. The main project file is named as 'model_builder.dsw', which includes 6 source files, respectively, 'area.for', 'beamvector.for', 'model_build.for', 'modify_node.for', 'modules.for' and 'utils.for'.

The function of main source file 'model_build.for' is to read in geometry data of Ls-Dyna models, then identify the outer faces of each ply of the model. By matching the outer faces of each laminate with outer faces of surrounding plies, interfaces between laminates can be figured out and the adjacent plies can be separated by duplicating the nodes on interfaces. Finally, it creates a new Ls-Dyna data file, which includes all the information in the original model, as well as the inserted 'Beam Thickness' interface elements and the duplicated nodes information.

The subroutine file 'area.for' is used to calculate the effective areas of each node on the interlaminar interface. 'beamvector.for' is to calculate the orientation vectors of discrete beams. File 'modify_node.for' is to modify the node number of elements in the higher ply when the interface is separated and a new node is generated by duplicating the old node. The 'moduls.for' defines the data structures applied in the program. The file 'utils.for' includes the file import and export subroutines.

Before using this pre-process program to generate interface elements, the user should create an original model with Ls-Dyna and define plies between which the user wishes to insert interface elements. Plies should be numbered with PID in the form of n*10000 (n=1,2,3..., means the n-th ply). Fig 3.3.1-1 demonstrates a typical process of creating

interface elements using this pre-process program. The model Fullcap_3 is shown in Fig 3.3.1-2a. Fig 3.3.1-2b is the effect of beam interface elements being put in the model by the program. To highlight the separation effect of three plies in the model, Fig 3.3.1-2c gives a view where three plies are translated apart. Elements of the FEM model can be either wedge or hexahedral or a mixture of both as those in the model Fullcap_3.

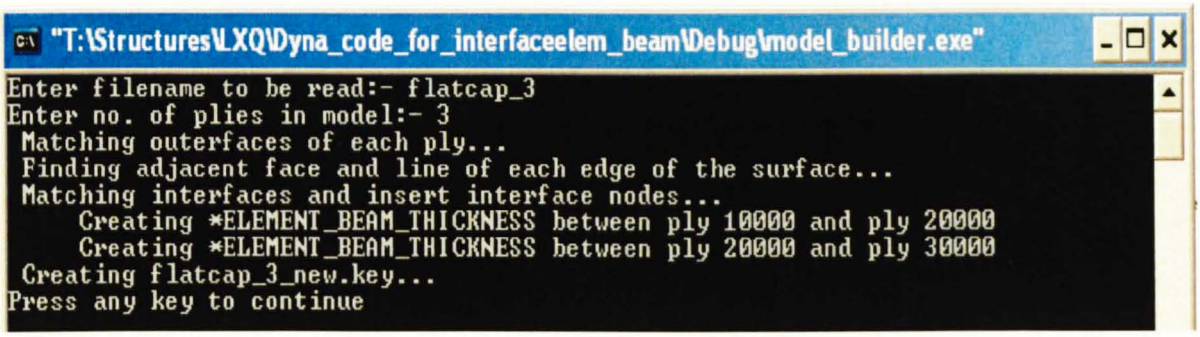

Fig 3.3.1-1 Running window of the discrete-beam pre-process program

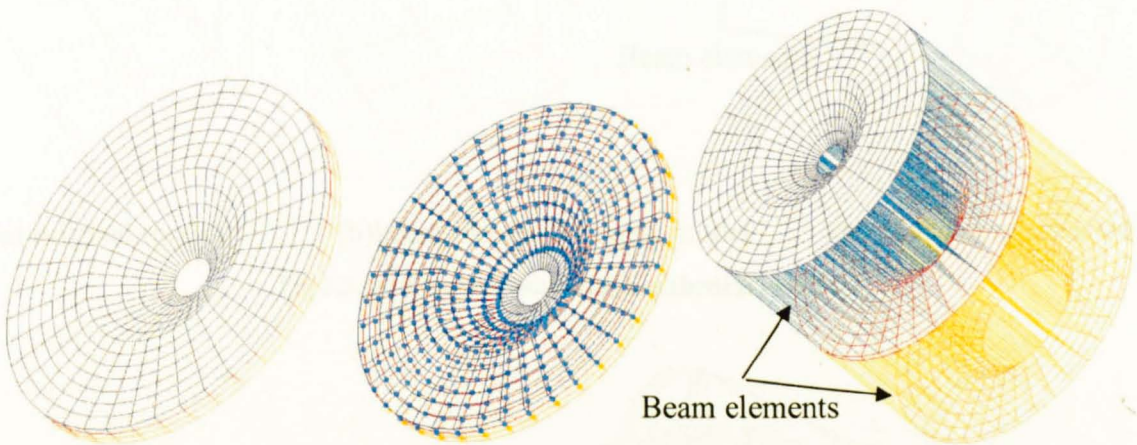

(a) original model (b) beam elements in the model (c)separation of 3 plies

Fig 3.3.1-2 Fullcap_3 model and the effect of beam interface elements being generated in the original model

From Fig 3.3.1-1, it can be seen that the user needs to input the file name of the original model and the number of plies in the model. The program displays the procedure of generating interface elements in turn as 'Matching outer faces of each ply...', ' Finding adjacent face and line of each edge of the surface...', 'Matching interface and insert interface nodes...', 'Creating *ELEMENT_BEAM_THICKNESS between plies...', and at last 'Creating' the new model file which includes inserted interface elements and all data information in the original model.

Fig 3.3.1-3a, 3.1-4a and 3.1-5a give examples of simple models meshed with hexahedral elements, wedge elements and the mixture of both types of elements. Fig 3.3.1-3b, 3.1-4b and 3.1-5b are their corresponding new models with discrete beam interface elements being inserted. The discrete beam is a twin-node and zero thickness element. Here in Fig 3.3.1-3c, 3.1-4c and 3.1-5c plies in the new models are moved apart to show the beam elements clearly.

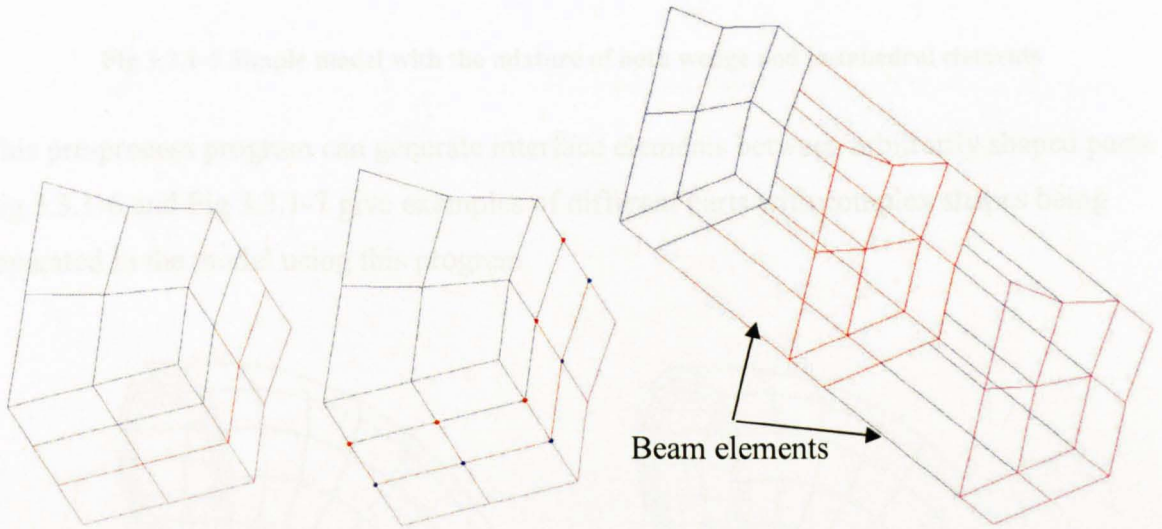

(a) original model (b)beam elements in new model (c) plies being separated

Fig 3.3.1-3 Simple model with hexahedral elements

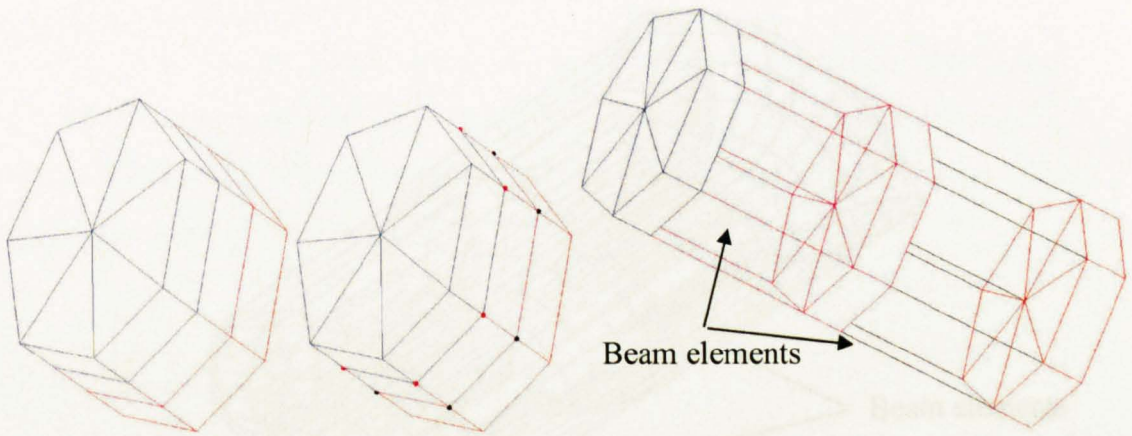

(a) original model (b)beam elements in new model (c) plies being separated

Fig 3.3.1-4 Simple model with wedge elements

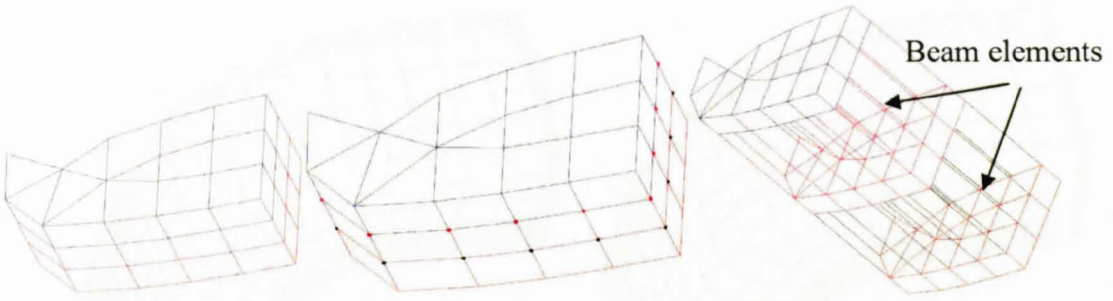

(a) original model (b)beam elements in new model (c) plies being separated

Fig 3.3.1-5 Simple model with the mixture of both wedge and hexahedral elements

This pre-process program can generate interface elements between arbitrarily shaped parts. Fig 3.3.1-6 and Fig 3.3.1-7 give examples of different parts with complex shapes being separated in the model using this program.

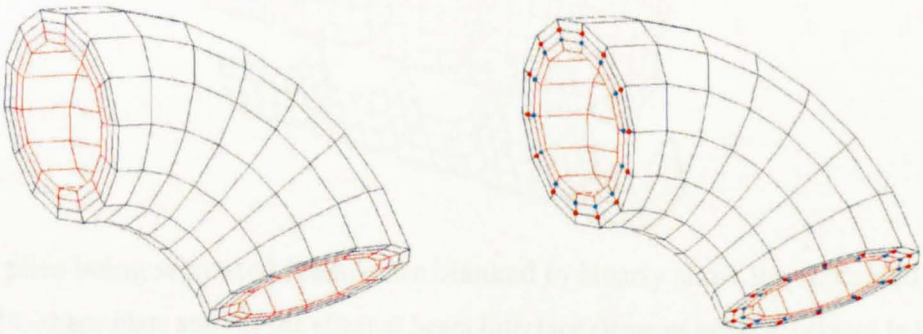

(a) original model (b) new model with beam interface elements

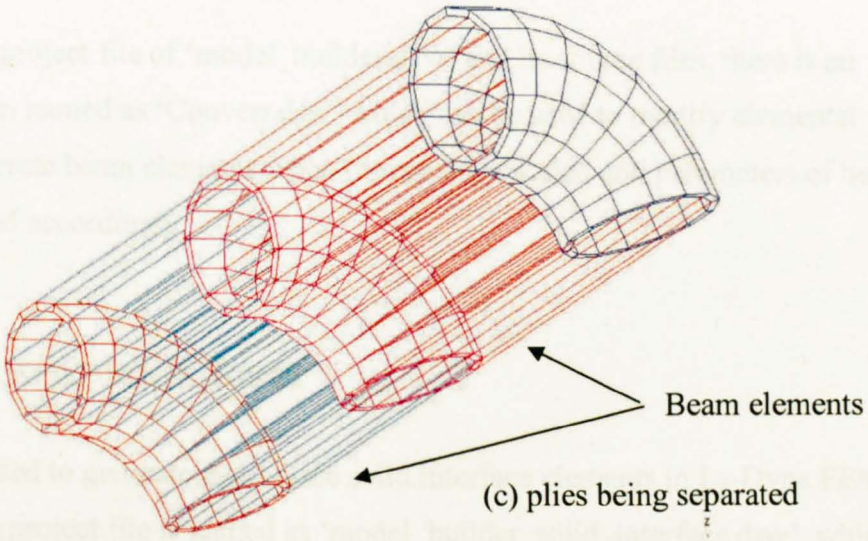

(c) plies being separated

Fig 3.3.1-6 Curved Pipe and the the effect of beam interface elements being generated in the original model

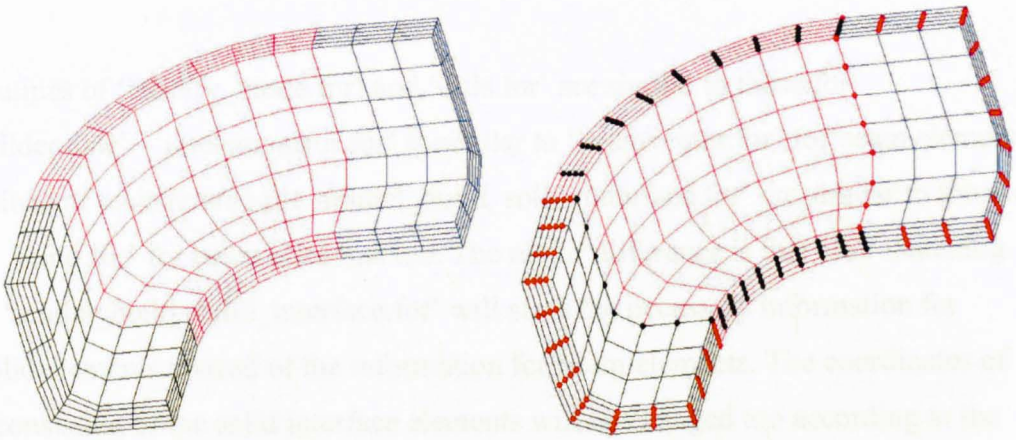

(a) original model (b) New model with beam interface elements

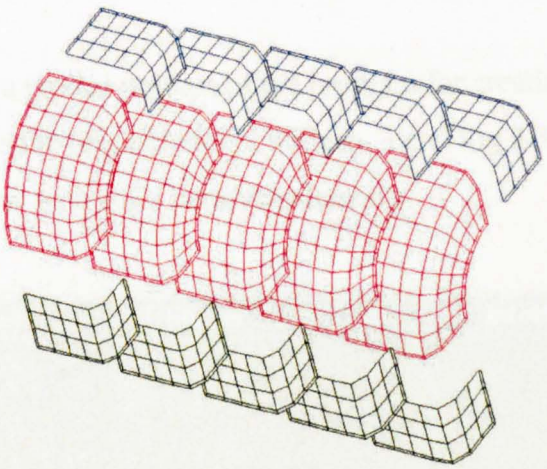

(c) 15 plies being separated (beams are blanked to clearly show the separated effect)

Fig 3.3.1-7 L-shape plate and the the effect of beam interface elements being generated in the original model

Besides the main project file of 'model_builder.dsw' and its source files, there is an additional program named as 'Convert.dsw' which can be used to modify elemental parameters of discrete beam elements when the model is scaled and parameters of beams need to be changed accordingly.

3.3.2 Program for solid interface element

This program is used to generate eight-node solid interface elements in Ls-Dyna FEM models. The main project file is named as 'model_builder_solid_interface.dsw', which includes 5 source files, respectively,
'intelemvector.for','model_build_solid_interface.for', 'modify_node.for', 'modules.for' and 'utils.for'.

The subroutines of 'modify_mode.for' and 'utils.for' are similar to those for 'model_builder.dsw'. 'intelemvector.for' is similar to 'beamvector.for' for beam elements. Most functions of main source file 'model_build_solid_interface.for' are similar to those of the 'model_build.for' for beam elements too. The major difference is that after matching interfaces, 'model_build_solid_interface.for' will store the necessary information for creating solid elements instead of the information for beam elements. The coordinates of the nodes consisting of the solid interface elements will be changed too according to the thickness of the interface.

Fig 3.3.2-1 demonstrates a typical process of the program for creating the solid interface elements. Fig 3.3.2-2(a) is the original model Fullcap_3 and Fig 3.3.2-2(b) is the resulted new model Fullcap_3_new with solid interface elements.

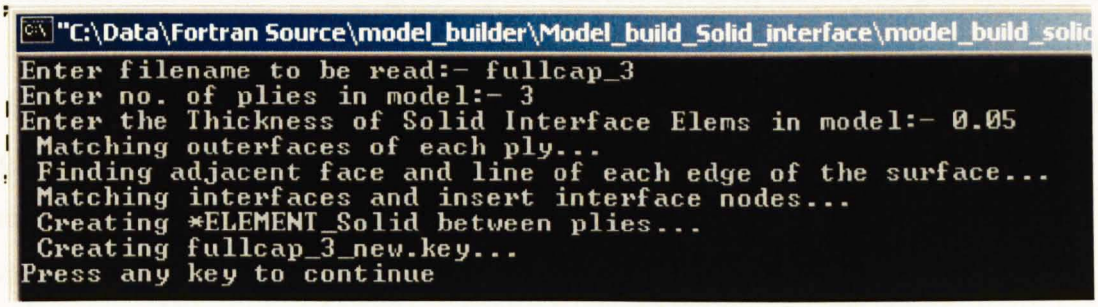

Fig 3.3.2-1 Running window of Solid interface elements pre-process program

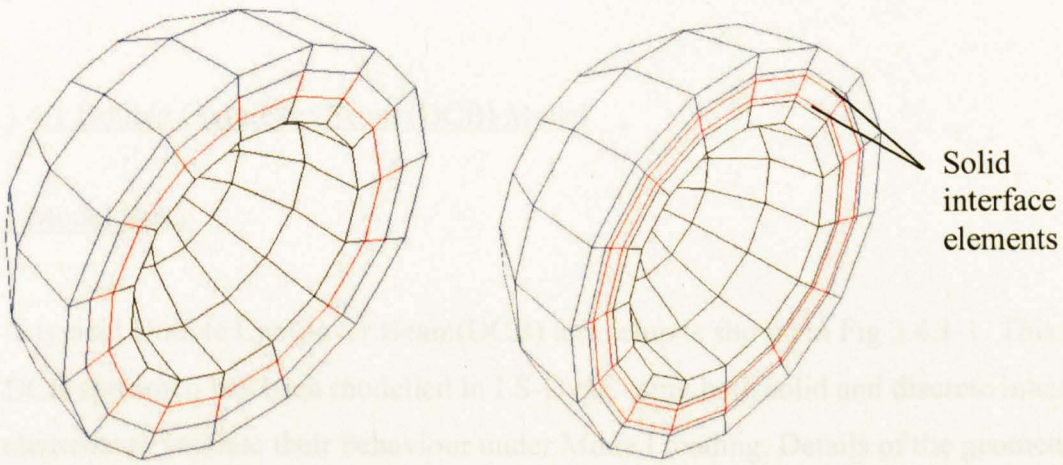

(a) original model (b) new model with solid interface elements

Fig 3.3.2-2 Fullcap_3 model and its resulted model with solid interface elements

3.4 Validation of the Interface Element Failure Models

Double Cantilever Beam (DCB)[96] and End Notch Flexure(ENF)[97,99] are two commonly used delamination toughness tests respectively for Mode I(opening mode) and Mode II(shear mode) behaviour. In this section these two specimens were modeled using the interface elements developed and compared with analytical results to validate interface failure formulations presented in Section 3.2. Even though the interface element has been implemented in LS-Dyna, essentially used for dynamic analyses, the benchmark tests presented in this section are quasi-static. Modelling quasi-static problems with an explicit FE code is bounded by some constraints. System damping has to be used to damp the dynamic vibrations, and the analysis requires a large number of time steps (during which numerical errors can potentially accumulate, and external work can be converted into energy forms other than internal, such as kinetic, hourglass control, and damping). The displacement-rate in the following examples was chosen such that, while guaranteeing that the kinetic and damping energy are negligible and the vibrations acceptable (thus ensuring the simulation of a quasi-static case), the CPU run time was kept under a few hours on a single Intel processor based PC. For considerably more complex problems, the analysis time can still be reasonably low, by using several CPUs in parallel. However, there are advantages of using explicit codes for quasi-static problems, since interface elements implemented in implicit codes usually have difficulties converging for large displacements, which does not happen for explicit codes.

3 4.1 Double Cantilever Beam (DCB) Model

1.Model Setup

A typical Double Cantilever Beam(DCB) test setup is shown in Fig 3.4.1-1. This type of DCB specimen has been modelled in LS-Dyna using both solid and discrete interface elements to validate their behaviour under Mode I loading. Details of the geometry and baseline mesh are shown in

Fig3.4.1-2, where:

L : DCB length = 150mm

a : starter crack length = 35mm (Interface Elements deleted from this section of the model)

w: width of the DCB specimen = 20mm (Half-model used to reduce program run-time)

h : thickness of the DCB specimen = 1.55mm

t : Interface element thickness

= 0 for discrete interface elements, and

= 0.1mm for solid interface elements.

B: width of solid interface elements used for DCB mesh = 1.25mm

l : length of solid interface elements = 0.5mm

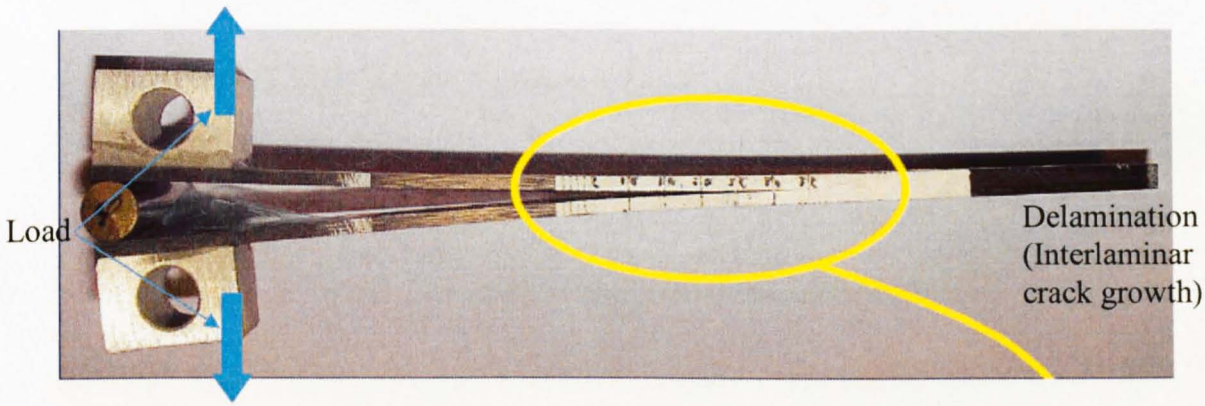

Fig 3.4.1-1 Typical Double Cantilever Beam(DCB) test setup[154]

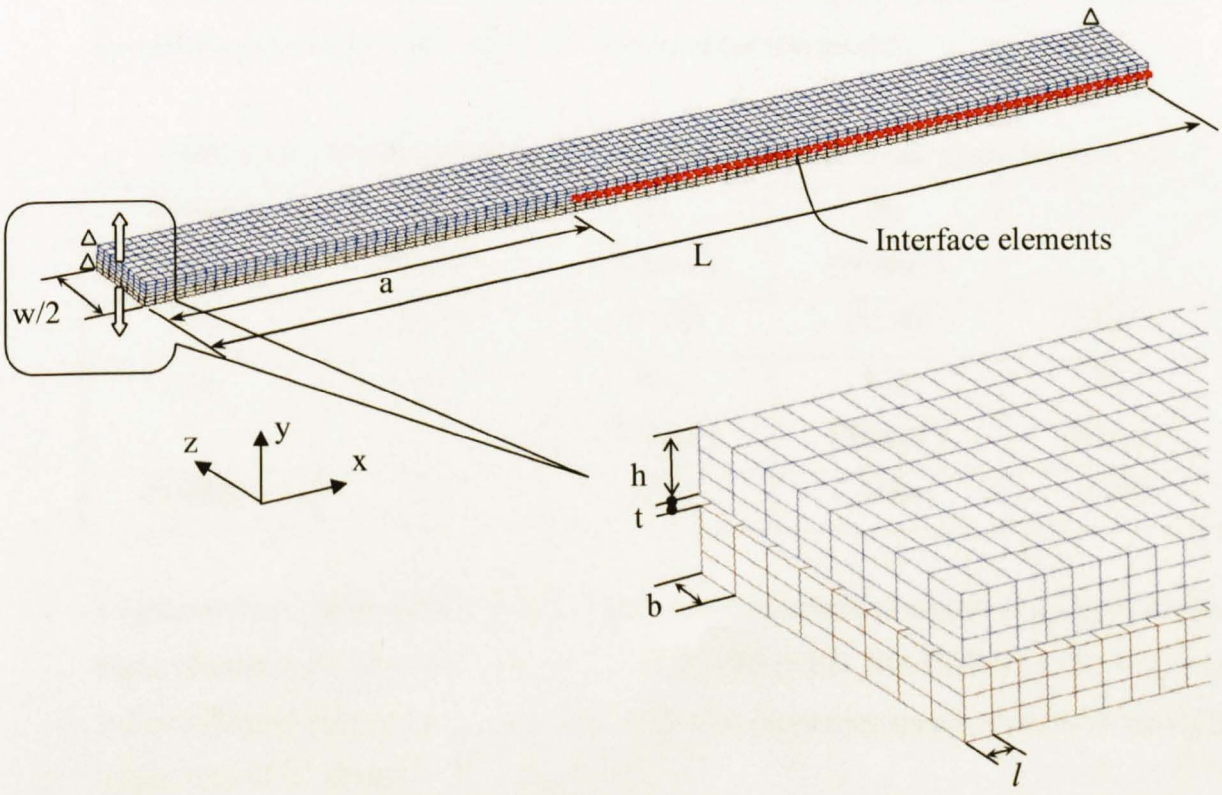

Fig3.4.1-2 DCB Model dimensions and details of the baseline mesh

Due to the symmetry of the DCB specimen a half model as shown in Fig 3.4.1-2 was used. All nodes along one side of the DCB were constrained with respect to z translation. Positive and negative linearly increasing y displacements, from 0-5mm over a period of 10sec, were applied to the tips of the top and bottom cantilever beams respectively, as shown in Fig 3.4.1-2.

Neglecting the initial separation of 0.1mm when using solid interface elements, this gave a linearly increasing separation of the DCB tips (Δ) from 0-10mm, as shown in Fig 3.4.1-3, applied as a prescribed displacement.

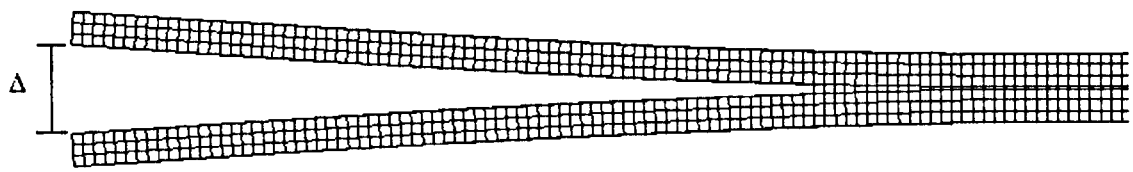

Fig 3.4.1-3 Linearly increasing separation applied to DCB tips

Constant stress solids (LS-Dyna solid element type 1) were used to model the DCB adherends and were implemented using the *MAT_ORTHOTROPIC_ELASTIC card (MAT_02) available within LS-DYNA. A carbon fibre/epoxy material with properties specified as shown in Table 3.4.1-1[62] was used for this model.

Table 3.4.1-1 Material properties used for adherends (Orthotropic Elastic Material Type)[62]

Density (g/mm^3)	E_1 (N/mm^2)	E_2 (N/mm^2)	E_3 (N/mm^2)	ν_{21}
1E-3	120,000	10,500	10,500	0.02625
ν_{31}	ν_{32}	G_{12} (N/mm^2)	G_{23} (N/mm^2)	G_{31} (N/mm^2)
0.02625	0.51	5250	3480	5250

Constant stress solids were also used for the solid interface elements, but properties for these elements are specified using the *USER_DEFINED_MATERIALS (Mat49) card (refer to Mat49 input card in Appendix A-2). The properties specified were as shown in Table 3.4.1-2[62], where:

σ_I^{max} = Tensile/Compressive (mode I) strength

σ_{II}^{max} = Shear (mode II) yield stress

E_I = Interface element tensile/compressive (mode I) stiffness per unit area, prior to yielding

E_{II} = Interface element shear stiffness per unit area, prior to yielding

G_{IC} = Mode I fracture toughness

G_{IIC} = mode II fracture toughness

t = Interface element thickness

Table 3.4.1-2 Solid Interface Element Properties[62]

Density (tonne/mm^3)	G_{IC} (N/mm)	G_{IIC} (N/mm)	σ_I^{max} (N/mm^2)	σ_{II}^{max} (N/mm^2)
1E-4	0.26	1.0	30	30
E_I (N/mm^3)	E_{II} (N/mm^3)	t (mm)		
1E+5	1E+5	0.1		

For the discrete interface elements, discrete beam elements (LS-Dyna beam element type 6) were used. The *USER_DEFINED_MATERIALS (Mat42) card (refer to Mat42 input card in Appendix A-1) was again used to enter the required interface element properties. Density for the discrete interface elements was specified as 1E-3 g/mm^3 and no thickness was defined, since beam interface nodes are coincident prior to loading. All other properties were as specified in Table 3.4.1-2.

2 Theoretical Analysis

Considering the DCB specimen as two single cantilever beams, of length equal to the initial pre-crack (a), and each subjected to a point load, P, at their free ends:

Prior to crack propagation, the vertical displacement of each free end is given by,

$$\frac{\Delta}{2} = \frac{Pa^3}{3EI} \qquad (3.4.1\text{-}1)$$

where,

Δ = Vertical separation of cantilever beam tips

E = Young's Modulus of each cantilever along its length

I = Second Moment of Area of each cantilever

For the crack to extend a small distance, δa,

Work Done = $P \times \delta a$

Rearranging equation 3.4.1-1 and differentiating Δ with respect to a,

$$\frac{d\Delta}{da} = \frac{2Pa^2}{EI} \qquad (3.4.1\text{-}2)$$

When the crack extends a small distance δa,

Work Done = P.δΔ (3.4.1-3)

Combining (3.4.1-2) and (3.4.1-3)

$$\text{Work Done} = P\left(\frac{2Pa^2}{EI}\right)\delta a = \left(\frac{2P^2a^2}{EI}\right)\delta a \qquad (3.4.1\text{-}4)$$

This energy is absorbed by the creation of the new surface with area 2Bδa, and if the critical strain energy release rate is G_{IC}, propagation occurs when:

$$\left(\frac{2P^2a^2}{EI}\right)\delta a = 2BG_{IC}\delta a \qquad (3.4.1\text{-}5)$$

Rearranging this expression, the force required to cause crack propagation, P_{crit}, is given by:

$$P_{crit} = \frac{\sqrt{G_{IC}BEI}}{a} \qquad (3.4.1\text{-}6)$$

Substituting in the relevant values for the DCB model:

$$P_{crit} = \frac{\sqrt{0.26*20*120000*6.21}}{35} = 56.24\ \text{N}$$

As displacement increases further, the force remains at P_{crit} for each increment of crack extension. Combining equations (3.4.1-1) and (3.4.1-6), the relationship between end displacement and force subsequent to initial crack propagation is as follows:

$$P = \frac{3EI\Delta}{2a^3} = \frac{3EI\Delta}{2}\left(\frac{P_{crit}}{\sqrt{G_{IC}BEI}}\right)^3$$

$$P^2 = \frac{2(G_{IC}BEI)^{3/2}}{3EI\Delta} = \frac{2\sqrt{EI}\,(G_{IC}B)^{3/2}}{3\Delta}$$

$$P = \sqrt{\frac{2}{3\Delta}}(EI)^{1/4}(G_{IC}B)^{3/4} \qquad (3.4.1\text{-}7)$$

Using equations 3.4.1-1, 3.4.1-6 and 3.4.1-7, the theoretical relationship between vertical separation of the cantilever beam tips and the applied load is as shown in Fig 3.4.1-4.

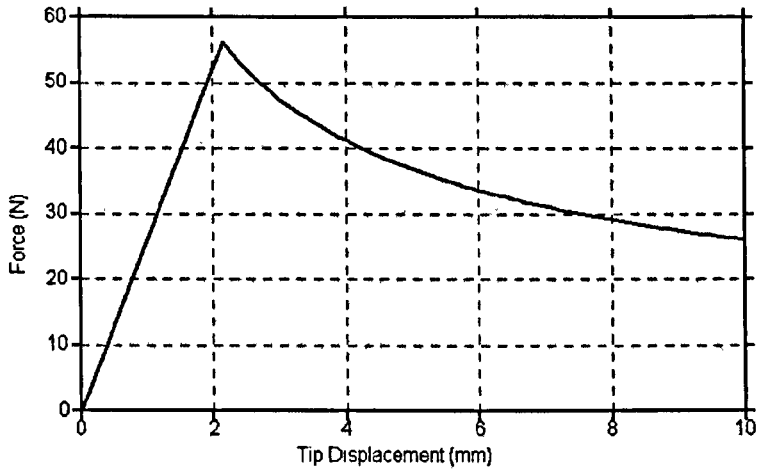

Fig3.4.1-4 Theoretical Force-Displacement Curve for DCB model

3. Model Results

In the model control setup, the default scaling factor of 0.9 was applied to the initial time-step calculated by LS-Dyna in order to calculate the minimum model time-step. For the baseline model, this resulted in a time-step of 1.20E-5s and a CPU time per zone cycle of 2840E-9s (total CPU time of 47976s). For the baseline model, type 5 hourglass control was used (Flanagan-Belytschko stiffness form with exact volume integration for solid elements[155]) with a co-efficient of 0.1 (default value). The default values of 1.5 and 0.06 were used for the quadratic and linear bulk viscosity co-efficients respectively. A Global Damping factor of 5 was applied to the baseline model.

Fig 3.4.1-5 gives the deformation and X direction stress distribution in the baseline model using discrete and solid interface elements at the end of the displacement application. Delamination is shown in Fig 3.4.1-6. Force-displacement curves gained from the baseline model using beam and solid interface elements are presented in Fig 3.4.1-7. A high level of consistency is evident between the two models. Although initial stiffness of the cantilever beams is less than the theoretical model and crack propagation occurs at a greater tip displacement, the models show close agreement with theory subsequent to initial crack propagation. The higher theoretical stiffness of the DCB is because the equation (3.4.1-1) for vertical displacement is only established for small deformation, while in the model the deformation developed to be very large and this caused an actual smaller stiffness than the predictions from equation (3.4.1-1). Also the effect of shear was not included in the theoretical solution. The oscillation of the curve in propagation comes from the numerical instability caused by the failure of beam elements.

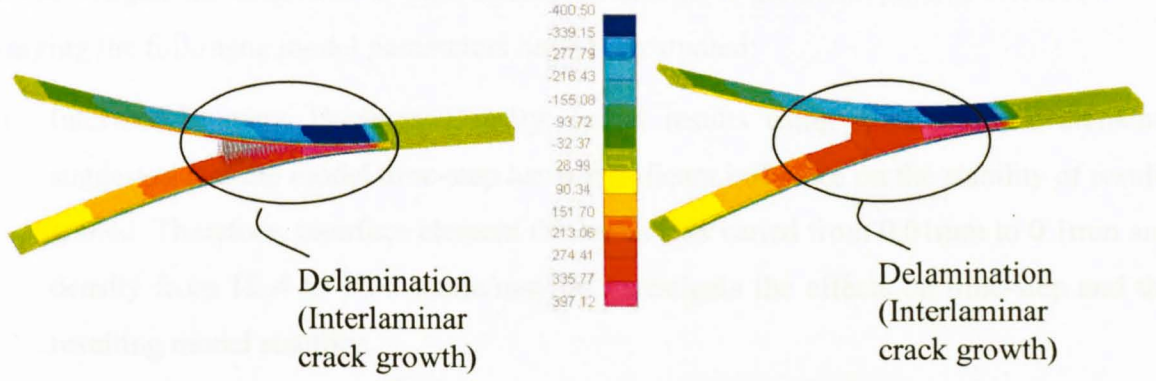

(a) using beam interface elements (b) using solid interface elements

Fig 3.4.1-5: Deformation and X direction stress distribution in the model at the end of the load.

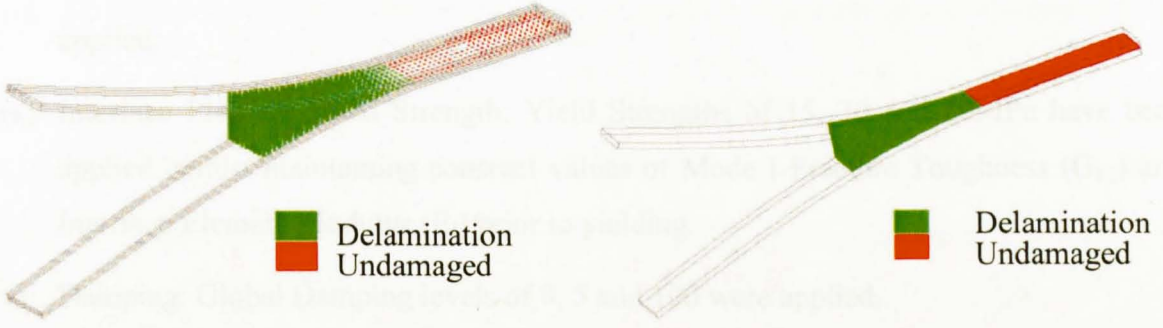

(a) using beam interface elements (b) using solid interface elements

Fig 3.4.1-6: Delaminations within the models at the end of the load.

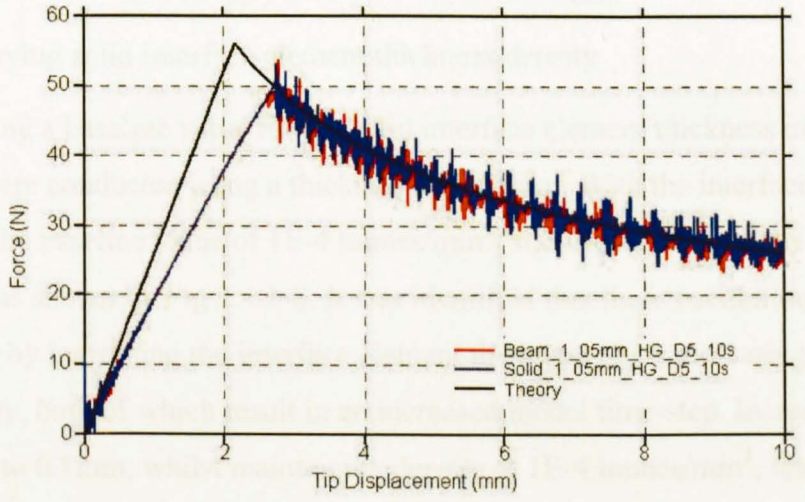

Fig 3.4.1-7 Force-displacement curves for the DCB baseline model using beam and solid Interface elements

4. Influence of various model parameters

To investigate the behaviour of solid interface elements in greater depth, the effects of varying the following model parameters have been studied:

i) Interface Element Thickness/Density: Initial results using solid interface elements suggested that the model time-step has a significant influence on the stability of results gained. Therefore, interface element thickness was varied from 0.01mm to 0.1mm and density from 1E-4 to 1E-3 tonne/mm^3 to investigate the effects on time-step and the resulting model stability.

ii) Mesh Density: Dimensions of 0.5mm and 0.25mm were used for elements along the length of the DCB to investigate the effects of increasing mesh refinement.

iii) Interface Element Modulus: Values of 5E4, 1E5, 5E5 and 1E6 N/mm^3 have been applied.

iv) Interface Element Yield Strength: Yield Strengths of 15, 30 and 60MPa have been applied, whilst maintaining constant values of Mode I Fracture Toughness (G_{IC}) and Interface Element Modulus (E_I) prior to yielding.

v) Damping: Global Damping levels of 0, 5 and 100 were applied.

When applying the variations detailed above, all other model parameters were maintained constant, using values specified in Table 3.4.1-1 and 3.4.1-2.

i) Effect of varying solid interface element thickness/density

Prior to adopting a baseline value for the solid interface element thickness of 0.1mm, initial model trials were conducted using a thickness of 0.01mm. With the interface element density set at the baseline value of 1E-4 tonnes/mm^3, significant oscillations were present in the results, as shown by Fig 3.4.1-8. It was identified that these oscillations could be reduced either by increasing the interface element thickness or by increasing the interface element density, both of which result in an increased model time-step. Increasing thickness from 0.01mm to 0.1mm, whilst maintaining density at 1E-4 tonnes/mm^3, results in a time-step increase from 1.75E-6 to 1.20E-5s. Increasing density from 1E-4 tonnes/mm^3 to 1E-3 tonnes/mm^3, whilst maintaining thickness at 0.01mm, results in a time-step increase from 1.75E-6 to 5.55E-6s. For each of these two cases, the resulting force-displacement curves are almost identical (see Fig 3.4.1-8), suggesting that a critical minimum time-step may exist, below which, significant oscillations occur.

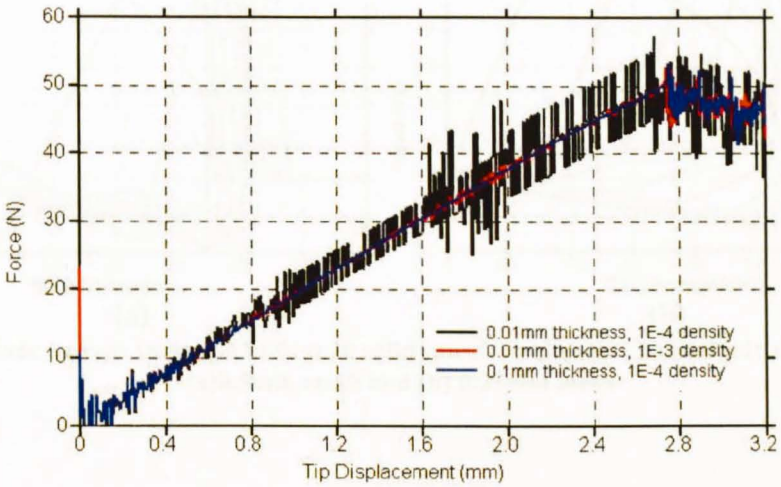

Fig 3.4.1-8 Force-displacement curves for various solid interface element thicknesses/densities (0.5mm mesh)

ii) Effect of mesh refinement along length of DCB for solid interface elements

Fig 3.4.1-9 shows the force-displacement curves for solid interface element lengths of 0.5mm and 0.25mm. It is evident that refining the mesh significantly reduces the magnitude of oscillations following crack propagation. The through-thickness stress of the first 10 interface elements behind the initial crack front are plotted in Fig 3.4.1-10 (a) for 0.5mm mesh and (b) for 0.25mm mesh. The comparison of the interface element stress variations shows that 4 elements in 0.25mm mesh and 2 elements in 0.5mm mesh have exceeded their mode I yield stress (are within the cohesive zone) prior to crack propagation. This indicates that 0.25mm mesh gives more accurate result than the 0.5mm mesh.

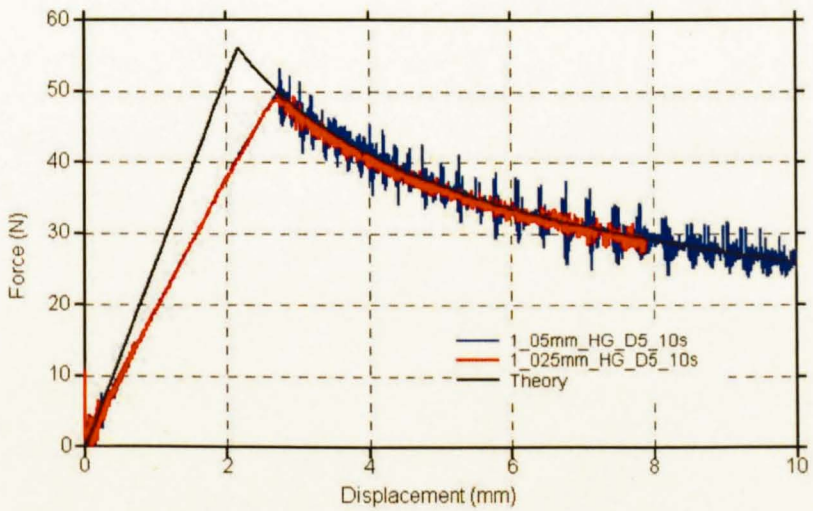

Fig 3.4.1-9 Force-Displacement Curves for 0.5mm and 0.25mm solid interface element lengths

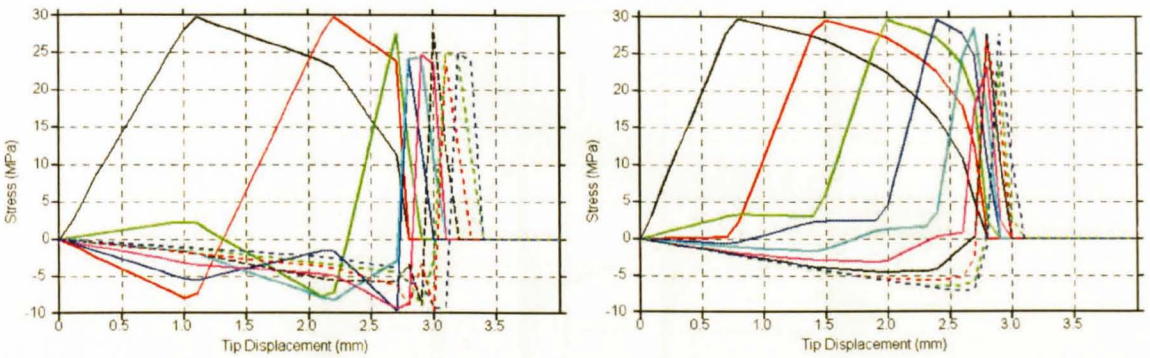

(a) (b)

Fig 3.4.1-10 Mode I stress variation in first 10 solid interface elements behind initial crack front for (a)0.5mm mesh and (b) 0.25mm mesh

iii) Effect of varying mode I stiffness (E_I), prior to yield, of solid interface elements

Fig 3.4.1-11 shows the force-displacement curves for solid interface elements, using E_I values of 5E4, 1E5, 5E5 and 1E6 N/mm^3. The results indicate that for a bi-linear traction-displacement curve, this parameter has a significant influence on correctly predicting crack propagation behaviour and ensuring model stability. For this particular DCB geometry and load case, E_I values of 5E4 and 1E5 N/mm^3 give very similar force-displacement curves. Increasing E_I to 5E5 N/mm^3 introduces significant oscillations in the force-displacement curve both prior and subsequent to crack propagation. A further increase in E_I to 1E6 N/mm^3 results in crack propagation at below the predicted load and subsequent unstable behaviour.

Whilst it is apparent that a value of 1E5 N/mm^3 is appropriate for the current DCB model, further work is required to establish whether this is true for other geometries and load cases.

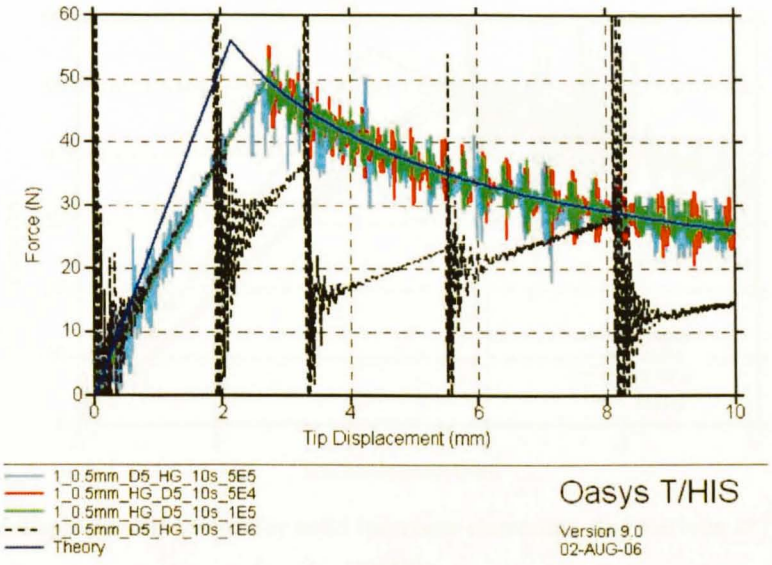

Fig 3.4.1-11 Force-displacement curves for solid interface elements using various E_I values (0.5mm mesh)

iv) Effect of varying Mode I Yield Strength (σ_I^{max}) of solid interface elements

Fig 3.4.1-12 shows the force-displacement curves obtained using solid interface elements with mode I yield strengths (σ_I^{max}) of 15, 30 and 60MPa. A 60MPa value for σ_I^{max} results in a reaction force at crack propagation (P_{crit}) of approximately 55N, which is the closest match to the theoretical P_{crit} of 56.24N. However, following crack propagation, there are significant oscillations present in the results. This is likely to be due to having an insufficient number of interface elements within the cohesive zone, resulting from the large value of σ_I^{max}. Reducing σ_I^{max} to the baseline value of 30MPa results in a P_{crit} value of 50N and although this is approximately 6N lower than the theoretical value, oscillations subsequent to crack propagation are significantly reduced. Reducing σ_I^{max} to 15MPa results in a further slight reduction in P_{crit} to approximately 49N, but again offers a significant reduction in oscillations subsequent to propagation.

In conclusion, it appears that reducing the value of σ_I^{max} offers the potential to reduce the mesh density required to gain reasonable crack propagation predictions. This result is consistent with the work of Turon et al[156]. Further work is required to determine acceptable reductions in σ_I^{max} for various model geometries, starter crack lengths and load cases. For situations where no initial crack is present, σ_I^{max} must remain fixed at a value which enables crack initiation to be accurately predicted.

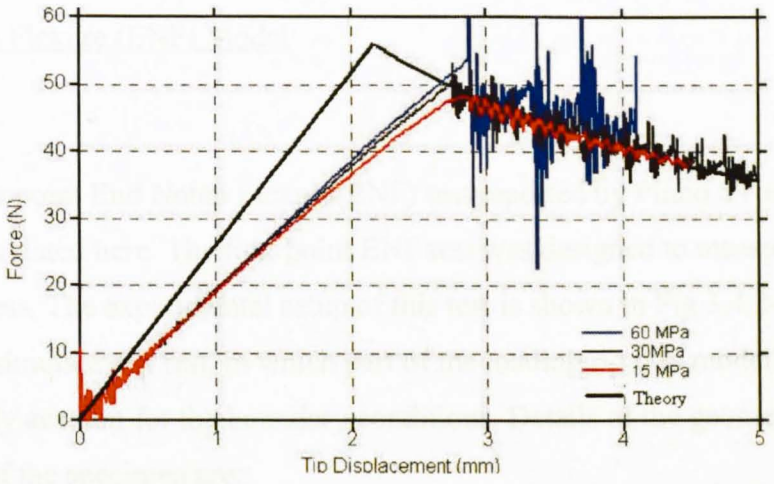

Fig 3.4.1-12 Force-displacement curves for solid interface elements using various σ_I^{max} values (0.5mm mesh)

v). Effect of damping on crack propagation behaviour using solid interface elements

Fig 3.4.1-13 shows the force-displacement curves obtained using solid interface elements, with global damping levels of 0, 5 and 100 applied. For a damping level of 100, oscillations following crack propagation are reduced, but the force-displacement curve is shifted significantly above the theoretical prediction. The curves for damping levels of 0 and 5 both show close agreement with the theoretical prediction and display similar levels of oscillation subsequent to crack propagation. However, relative to zero damping, a damping value of 5 significantly reduces oscillations present in the initial linear region of the force-displacement curve. On this basis, a damping value of 5 appears a reasonable baseline value to apply.

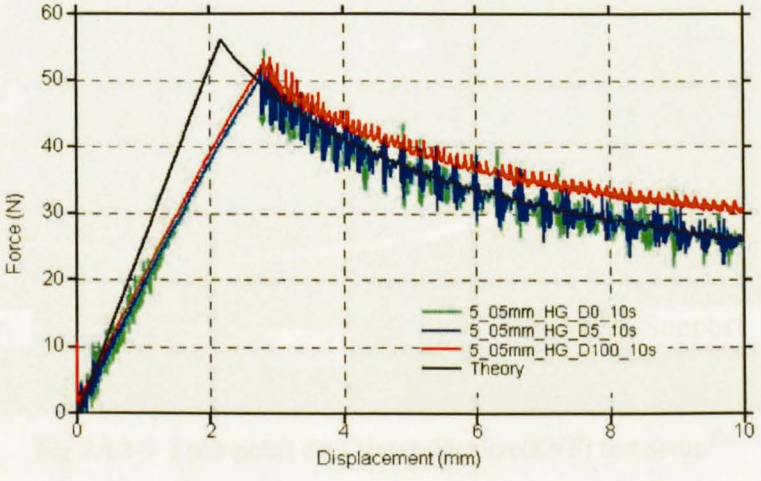

Fig 3.4.1-13 Load-displacement curves for various damping levels using solid interface elements

3 4.2 End Notch Flexure (ENF) Model

1 Model Setup

A particular four point End Notch Flexure(ENF) test reported by Pinho ST et al[62] was chosen to be simulated here. The four point ENF test was designed to measure Mode II fracture toughness. The experimental setup of this test is shown in Fig 3.4.2-1. Fig 3.4.2-2 is the model to simulate this test, in which part of the loading rig was modelled as well, in order to correctly account for the boundary conditions. Details of the geometry and the baseline mesh of the specimen are::

L : ENF length = 120mm

BL: loading rig length=80mm

a : starter crack length = 25mm (Interface Elements deleted from this section of the model)

w: width of the ENF specimen = 20mm (Half-model used to reduce program run-time)

h : thickness of the ENF specimen = 1.55mm

t : Interface element thickness

= 0 for discrete beam interface elements, and

= 0.1mm for solid interface elements.

B: width of solid interface elements used for ENF mesh = 2mm

l : length of solid interface elements = 0.5mm

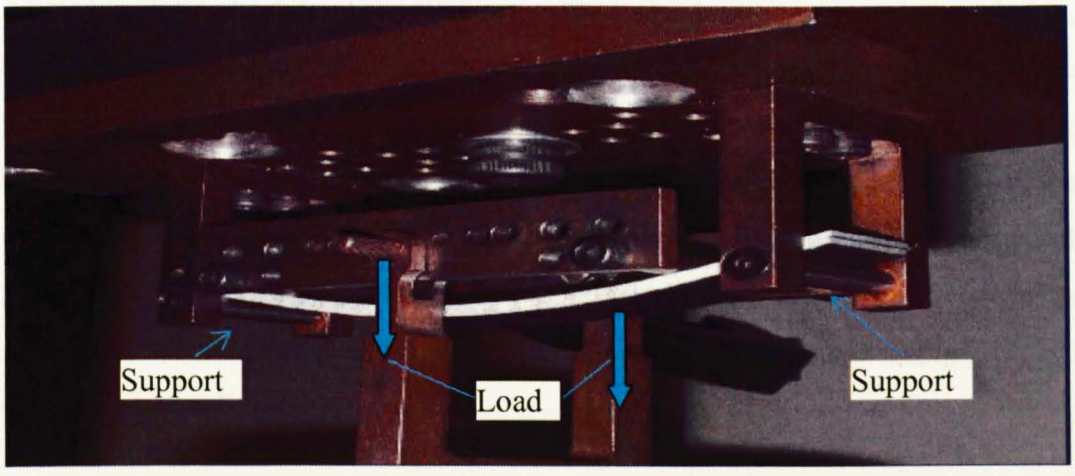

Fig 3.4.2-1 Four point End Notch Flexure(ENF) test setup[154]

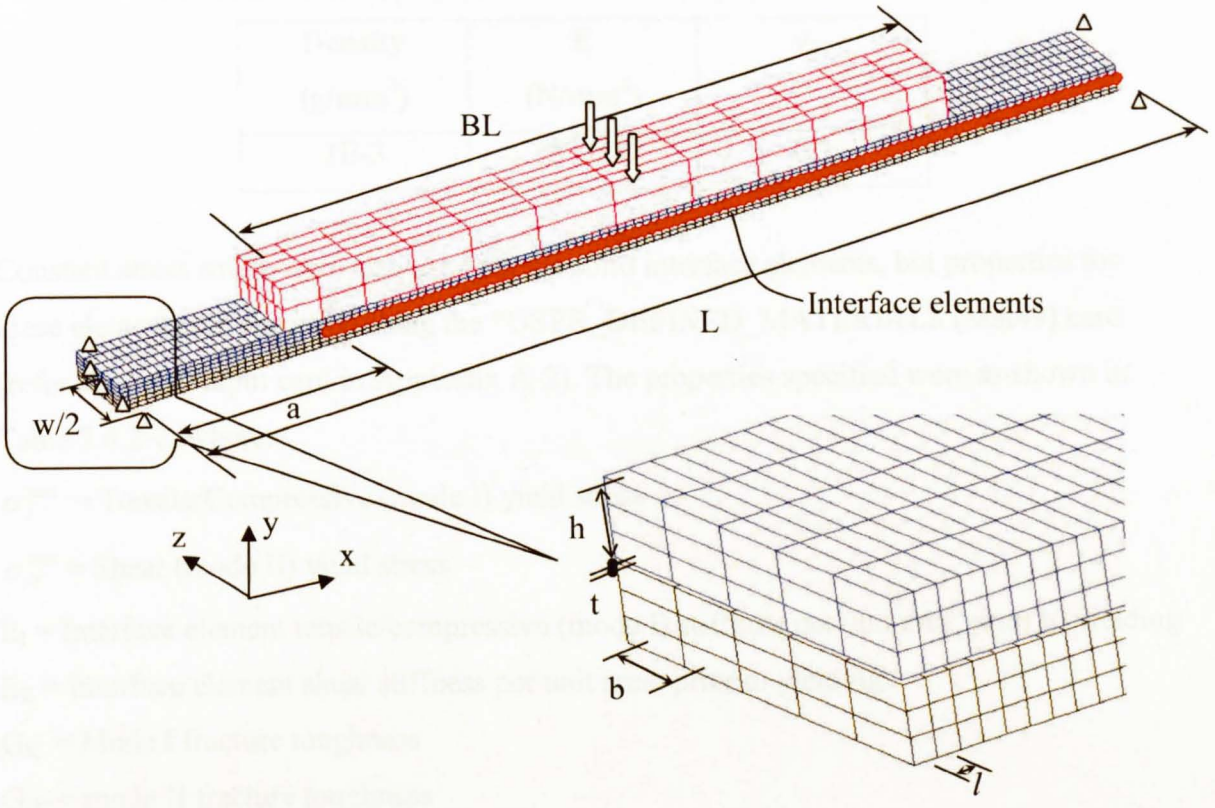

Fig 3.4.2-2 ENF Model dimensions and details of the baseline mesh

Due to the symmetry of the ENF specimen a half model as shown in Fig 3.4.2-2 was used. All nodes along one side of the ENF were constrained with respect to z translation, x rotation and y rotation. A displacement-rate of 240mm/s was applied to the appropriate points of the loading rig in the model. The ends of the specimen were simply supported in the y direction. Automatic surface to surface contact conditions were applied to the pre-crack region between the top and bottom parts of the specimen to prevent potential penetration of the two parts. The same contact conditions were applied between the loading rig and the specimen so as to transfer the applied load which is increasing linearly at the centre of the loading rig.

Constant stress solids (solid element type 1) were used to model the ENF adherends and were implemented using the *MAT_001_ELASTIC card available within LS-DYNA. The properties specified used isotropic values from Reference 62 and were shown in Table 3.4.2-1 below.

Table 3.4.2-1 Material properties used for adherends (Elastic Material Type)[62]

Density (g/mm^3)	E (N/mm^2)	ν_{21}
1E-3	137,000	0.3

Constant stress solids were also used for the solid interface elements, but properties for these elements are specified using the *USER_DEFINED_MATERIALS (Mat49) card (refer to Mat49 input card in Appendix A-2). The properties specified were as shown in Table 3.4.2-2, where:

σ_I^{max} = Tensile/Compressive (mode I) yield stress

σ_{II}^{max} = Shear (mode II) yield stress

E_I = Interface element tensile/compressive (mode I) stiffness per unit area, prior to yielding

E_{II} = Interface element shear stiffness per unit area, prior to yielding

G_{IC} = Mode I fracture toughness

G_{IIC} = mode II fracture toughness

t = Interface element thickness

Table 3.4.2-2 Solid Interface Element Properties[62]

Density (g/mm^3)	G_{IC} (N/mm)	G_{IIC} (N/mm)	σ_I^{max} (N/mm^2)	σ_{II}^{max} (N/mm^2)
1E-3	0.26	1.11	30	60
E_I (N/mm^3)	E_{II} (N/mm^3)	t (mm)		
1E+5	1E+5	0.05		

For the discrete interface elements, discrete beam elements (beam element type 6) were used. The *USER_DEFINED_MATERIALS (Mat42) card (refer to Mat42 input card in Appendix A-1) was again used to enter the required interface element properties. Density for the beam interface elements was specified as 1E-3 g/mm^3 and no thickness was defined, since beam interface nodes are coincident prior to loading. All other properties were as specified in Table 3.4.2-2.

2 Theoretical Analysis

Considering the DCB specimen as two single cantilever beams, of length equal to the initial pre-crack (a), and each subjected to a point load, P, at their free ends:

Prior to crack propagation, the vertical displacement of each free end is given by,

$$\Delta = [9a + 5\frac{L}{2} + \frac{BL}{2}] \frac{(\frac{L}{2} - \frac{BL}{2})^2 P}{96\left(E\frac{wh^3}{12}\right)} = [18a + 5L + BL] \frac{(L - BL)^2 P}{64Ewh^3} \qquad (3.4.2\text{-}1)$$

where,

Δ = Vertical displacement at the applied load point, mm

E = Young's Modulus of ENF specimen along its length

a, L, BL, w and h are the same as shown in Fig 3.4.2-2

For the crack to extend a small distance, δa,

Rearranging equation 3.4.1-1 and differentiating Δ with respect to a,

$$\frac{d\Delta}{da} = \frac{18(L - BL)^2 P}{64Ewh^3} = \frac{9(L - BL)^2 P}{32Ewh^3} \qquad (3.4.2\text{-}2)$$

When the crack extends a small distance δa,

Work Done = P.$\delta\Delta$ (3.4.2-3)

Combining (3.4.2-2) and (3.4.2-3)

$$\text{Work Done} = P\frac{9(L - BL)^2 P}{32Ewh^3}\delta a = \frac{9(L - BL)^2 P^2}{32Ewh^3}\delta a \qquad (3.4.2\text{-}4)$$

This energy is absorbed by the creation of the new surface with area $2w\delta$a, and if the critical strain energy release rate is G_{IIC}, propagation occurs when:

$$\frac{9(L - BL)^2 P^2}{32Ewh^3}\delta a = 2wG_{IIC}\delta a \qquad (3.4.2\text{-}5)$$

Rearranging this expression, the force required to cause crack propagation, P_{crit}, is given by:

$$P_{crit} = \sqrt{\frac{64G_{IIC}Ew^2h^3}{9(L - BL)^2}} = \frac{8wh}{3(L - BL)}\sqrt{G_{IIC}Eh} \qquad (3.4.2\text{-}6)$$

Substituting in the relevant values for the ENF model:

$$P_{crit} = \frac{8*20*1.55}{3*(120 - 80)}\sqrt{1.11*137000*1.55} = 1000.34 \text{ N}$$

As displacement increases further, the force remains at P_{crit} for each increment of crack extension. Combining equations (3.4.2-1) and (3.4.2-6), the relationship between end displacement and force subsequent to initial crack propagation is as follows:

$$\Delta = [18a + 5L + BL]\frac{(L-BL)^2 P}{64Ewh^3} = [18a + 5L + BL]\frac{(L-BL)^2}{64Ewh^3}\frac{8wh}{3(L-BL)}\sqrt{G_{IIC}Eh}$$

$$\Delta = [18a + 5L + BL]\frac{(L-BL)}{24h}\sqrt{\frac{G_{IIC}}{Eh}}$$

$$a = \frac{1}{18}\left(\Delta\frac{24h}{(L-BL)}\sqrt{\frac{Eh}{G_{IIC}}} - 5L - BL\right) \qquad (3.4.1\text{-}7)$$

From equations 3.4.2-6 and 3.4.2-7 we could conclude that the load applied to the ENF specimen would keep constant after the crack starts to propagate and the crack growth rate is only related with the loading rate itself. If the loading rate is constant the crack growth within the four point ENF specimen would be a stable rate as well. The theoretical relationship between the displacement at applied load points and the applied load is as shown in Fig 3.4.2-3.

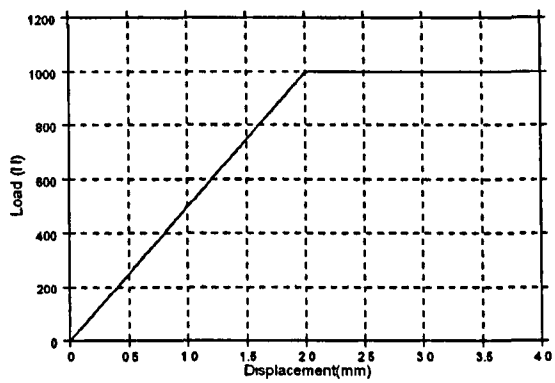

Fig3.4.2-3 Theoretical Force-Displacement Curve for ENF model

3. Model Results

In the model control setup, type 5 hourglass control was used (Flanagan-Belytschko stiffness form with exact volume integration for solid elements) with a co-efficient of 0.1 (default value). The default values of 1.5 and 0.06 were used for the quadratic and linear bulk viscosity co-efficients respectively. A Global Damping factor of 1.0 was applied to the baseline model.

Fig 3.4.2-4 gives the deformation and X direction stress distribution in the baseline model using discrete and solid (with thickness 0.05mm) interface elements at the end of the load. Delamination within the models at the end of the load are shown in Fig 3.4.2-5.

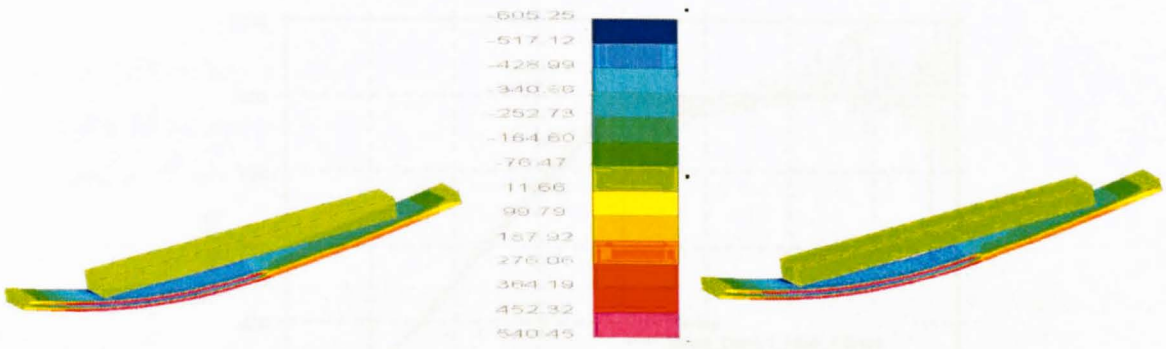

(a) using discrete interface elements (b) using solid interface elements

Fig 3.4.2-4: Deformation and X direction stress distribution within the models at the end of the load.

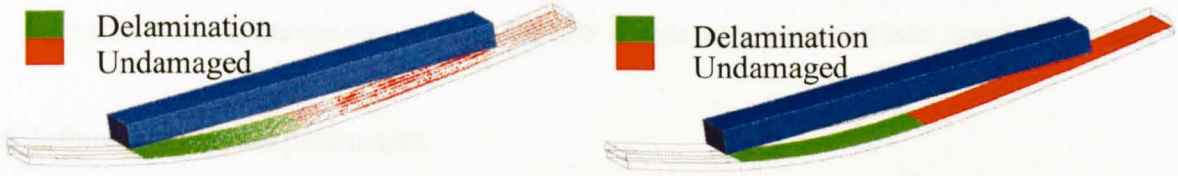

(a) using discrete interface elements (b) using solid interface elements

Fig 3.4.2-5: Delaminations within the models at the end of the load.

Besides adopting the baseline value for solid interface element thickness of 0.05mm, two more trials were conducted using thickness of 0.01mm and 0.1mm. Load-displacement curves gained from the ENF models using discrete and solid interface elements (using thickness of 0.01mm, 0.05mm and 0.1mm respectively) are presented in Fig 3.4.2-6. It can be seen that there are some oscillations in the simulated curves near and after the onset of delamination. Apart from this noise, a high level of consistency was obtained on the onset and propagation of delamination between model predictions and the analytical result. Thickness of solid interface elements mainly influenced the magnitude of oscillation and had very little effect on the predicted onset and propagation of delamination. Oscillations of the curves mainly came from the modelling of contact conditions. When delamination within the model started to propagate, there was an obvious slip between the loading rig and the specimen. This caused the major oscillations in the load-displacement curves.

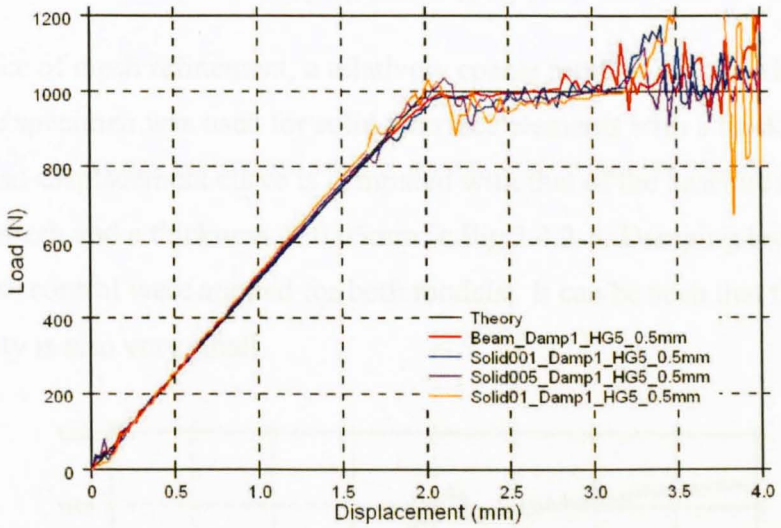

Fig 3.4.2-6 Force-displacement curves for the ENF models using beam and solid Interface elements

4. Influence of model parameters

Due to inevitable oscillations in the load-displacement curves from modelling contact conditions, the influence of model parameters was not thoroughly investigated for the ENF model as has been done for the DCB model. Only two major factors: damping and mesh refinement along the length direction were studied.

Global damping levels of 1.0 and 5.0 were respectively applied to the solid interface model with an interface thickness of 0.05mm. Load-displacement curves using these two levels of damping values are shown in Fig 3.4.2-7. It is evident that oscillation within the curve using a damping level of 5.0 was largely reduced compared with the curve using a damping level of 1.0.

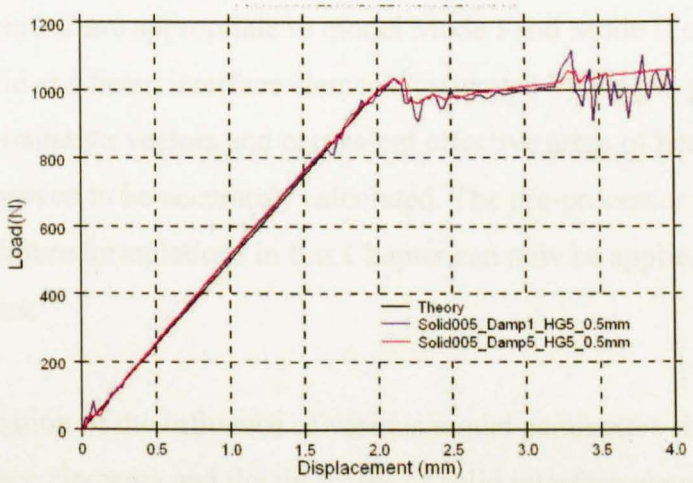

Fig 3.4.2-7 Load-displacement curves for various damping levels using solid interface elements with a thickness of 0.05mm

For the influence of mesh refinement, a relatively coarse mesh of 1.0mm along the length direction of the specimen was used for solid interface elements with a thickness of 0.05mm. Its load-displacement curve is compared with that of the baseline model using a 0.5mm length mesh and a thickness of 0.05mm in Fig 3.4.2-8. Damping level of 5.0 and type 5 hourglass control were applied for both models. It can be seen that the influence of the mesh density is also very small.

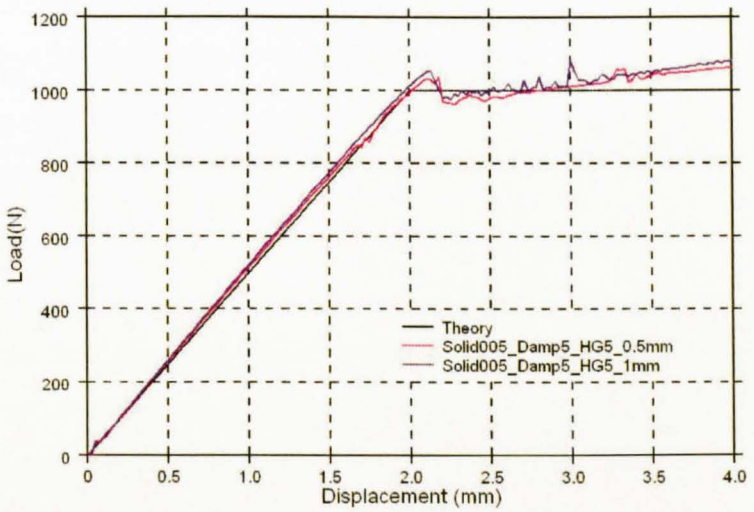

Fig 3.4.2-8 Load-displacement curves for 0.5mm and 0.25mm solid interface element lengths(thickness 0.05mm)

3.4.3 Conclusion

Modelling of a DCB specimen for Mode I delamination and ENF specimen for Mode II behaviour using interface elements shows that the interface element formulations introduced in section 3.2 are appropriate to model Mode I and Mode II crack propagation problems. Both solid and beam interface elements generated by the pre-processor program are reliable. The orientation vectors and equivalent effective areas of beam interface elements were all proven to be accurately calculated. The pre-processor program and interface element failure formulations in this Chapter can now be applied to a range of decohesion problems.

Parametric investigation of the influence of various model parameters showed that the mesh size of interface elements and the thickness of solid interface elements mainly influence the stability of models but not the initiation and propagation of delamination.

The stability of models can be improved by using an appropriate damping factor. The initial stiffness of interface elements is less important than the maximum interfacial strength and critical fracture energy but did have some influence on the delamination behaviour. When this initial stiffness is within a certain range of values, currently a level of 1.E5 N/mm^3 was recommended, its influence can be neglected.

3.5 Investigation of Effect of Through Thickness Compressive Stresses on Delamination

3.5.1 Introduction

Evidence has been presented in the literature that through-thickness compression can improve the interlaminar shear strength of laminates. Some researchers such as Deteresa et al [157,158] take this strengthening effect of compression on shear strength into account by modifying the stress interaction criterion as below:

$$\frac{\sigma_{33}}{Z_f}+\left(\frac{\sigma_{13}}{S_{13}}\right)^2+\left(\frac{\sigma_{23}}{S_{23}}\right)^2 \geq 1 \qquad (3.5.1\text{-}1)$$

Where Z_f is the maximum through-thickness stress and S_{shear} is the maximum interlaminar shear stress. Other investigations such as those by Hart-Smith[159, 160, 161], Sun[162] and Rotem[163] suggest it is the result of in-situ effects in laminates. Work by Cui et al[164] reveals that the through-thickness compression can suppress delamination in terms of improving the critical Mode II fracture energy (G_{IIC}) which is expressed as a linear function of average through-thickness normal stress.

To investigate the relation between through-thickness compressive stress and the increase of S_{shear} and G_{IIC}, two types of cut ply models and two types of dropped ply models, based on the work of Cui et al[164], are used here to generate different levels of through-thickness compressive stress. Three possible Mode II damage evolution laws under compression are proposed to represent the increase of S_{shear} and G_{IIC}. The interface failure criteria based on these assumptions have been implemented in LS-Dyna and are used to simulate the delamination in the cut ply and dropped ply experiments. By comparing the results of the three failure criteria in the cut ply and dropped ply models, it is found that the increases of S_{shear} and G_{IIC} are not independent. The increase of G_{IIC} can be predicted with a knowledge of the increase in S_{shear} and an appropriate assumption of the Mode II traction behaviour under compression. The increase of S_{shear} is determined by an analogous internal friction factor. Excellent correlation for the delamination stresses for all the four cut-ply and dropped-ply models was achieved.

3.5.2 New Delamination Criteria, Accounting for Compressive Effects

To study this effect, two types of cut ply models (cut ply with gap and cut ply with no gap) and two types of dropped ply models (dropped ply with shallow angle of 5.7° and dropped ply with sharp angle of 7.6°) reported in reference 160(refer to Fig 3.1-1) are simulated to compare the effectiveness of three different strengthening assumptions on the through-thickness failure stress and Mode II critical fracture energy. These tests were chosen since in each case they give a different level of compressive stress at the failure interface. Cui et al[160] also present a closed form analysis relating the delamination stress to apparent fracture energy. They assumed that the fracture energy is a linear function of the average through-thickness normal stress and obtained four different G_{IIC} values under the different compressive stress levels of the cut ply and dropped ply models. Using the revised G_{IIC} values, their models show excellent correlation with the experimental data.

1. Model Setup

The full experimental setup of the cut and dropped ply tests is described in reference 164. Two cases of cut ply specimens(Fig 3.1-1a and b) and two cases of dropped ply specimens with both a shallow ramp angle of 5.7° and a sharper angle of 7.6° (Figure 8c) are presented. The cut ply specimen is made of 8 continuous and 2 cut plies and the dropped ply specimen is made of 8 continuous and 2 dropped plies.

These tests have been analysed here using solid interface elements with thickness 0.01mm to predict the delamination failure and the geometries and meshes are shown in Fig 3.5.2-2. Due to symmetry, only a quarter of the specimen was modelled. The resin pockets in the dropped-ply specimens are neglected in the numerical models due to their much lower failure threshold. The shallow vs. sharp ramp angles of the dropped-ply specimen are modelled respectively with two half models. The effect of mesh refinement in the width direction on delamination prediction has been investigated. It was found that when the number of the elements is greater than three the predicted delamination stresses have no distinguishable difference. Three elements across the width were therefore used for all of the studies presented below. The left hand end of each of the models is constrained in the longitudinal direction and a prescribed displacement is applied at the right hand end to give a tensile loading. It should be noted that since LS-Dyna is an explicit code more commonly

used for dynamic analysis, the loading rate has to be increased over that which is applied in the quasi-static experiments in order to give reasonable run times. The loading rate applied here is still slow enough such that dynamic effects are not introduced into the model.

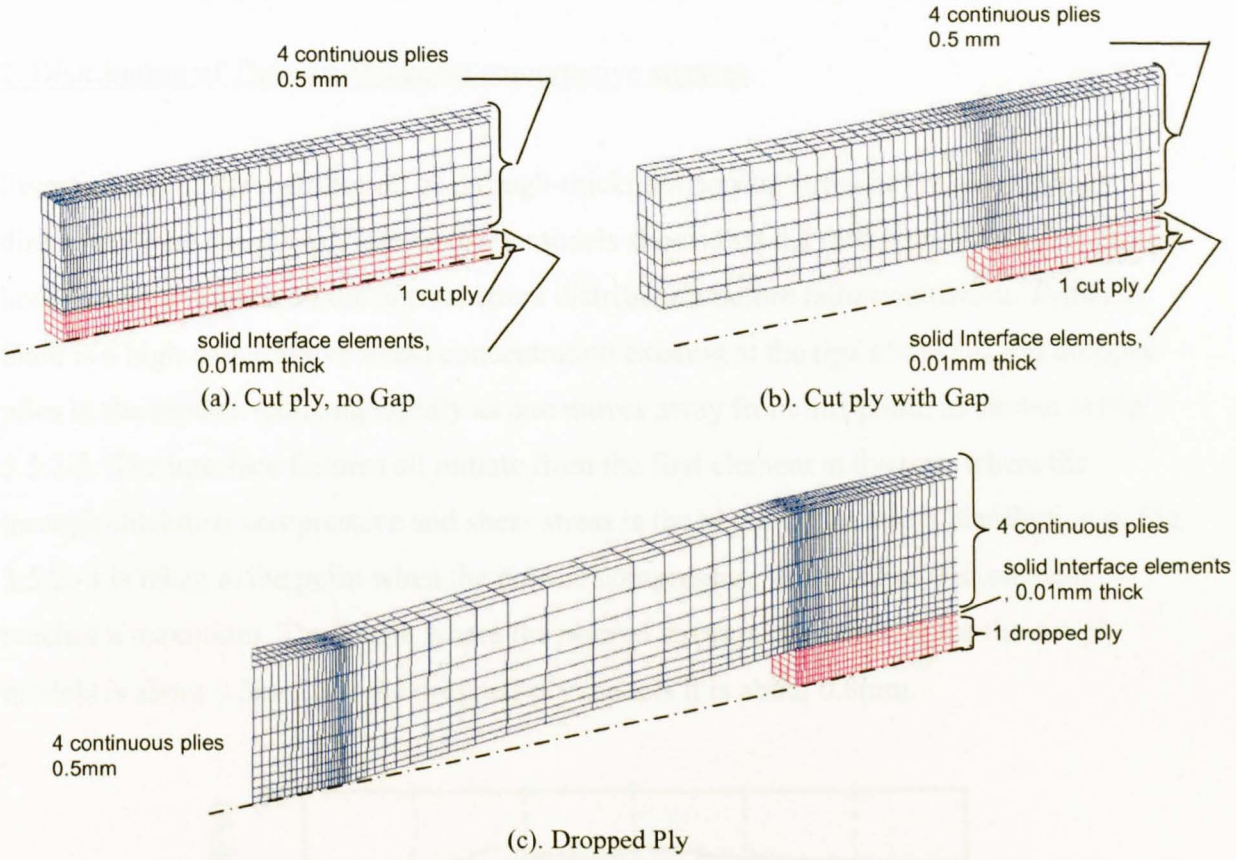

Fig 3.5.2-2 Finite element models of cut-ply and dropped-ply specimens

The material for both cut ply and dropped ply model is unidirectional glass fibre-epoxy pre-preg (E-glass/913). The material properties are obtained from Reference 167 and shown in Table 3.5.2-1. G_{IIC} for the epoxy (interface) is from Reference 165. Other properties of the epoxy are derived from references 166,167 and 168. These material properties are shown in table 3.5.2-2.

Table 3.5.2-1 Glass Fibre material properties (E-glass/913[166]

E_{11} (GPa)	E_{22} (GPa)	ν_{12}	G_{12} (GPa)
43.9	15.4	0.3	3.34

Table 3.5..2-2 Interface material properties (E-glass/913)[163-166]

G_{IIC} (N/mm)	Z_f (MPa)	$S_{12/13}$ (MPa)	E (GPa)	G (GPa)
0.87	94	75	3.2	1.5

2. Distribution of Through-thickness compressive stresses

Investigation of the distribution of through-thickness normal stress in the longitudinal direction of the cut-ply and dropped-ply models shows that the difference in applied failure laws has no influence on the normal stress distribution before failure initiation. Typically there is a high compressive stress concentration existing at the tips of the cut and dropped plies in the models reducing rapidly as one moves away from this point, as shown in Fig 3.5.2-3. The interface failures all initiate from the first element at the tips, where the through-thickness compressive and shear stress is the highest. The stress distribution in Fig 3.5.2.-3 is taken at the point when the normal compressive stress in the first element reaches a maximum. The length where the normal stress is compressive for the cut-ply models is about 0.5mm, for the dropped-ply models it is about 0.8mm.

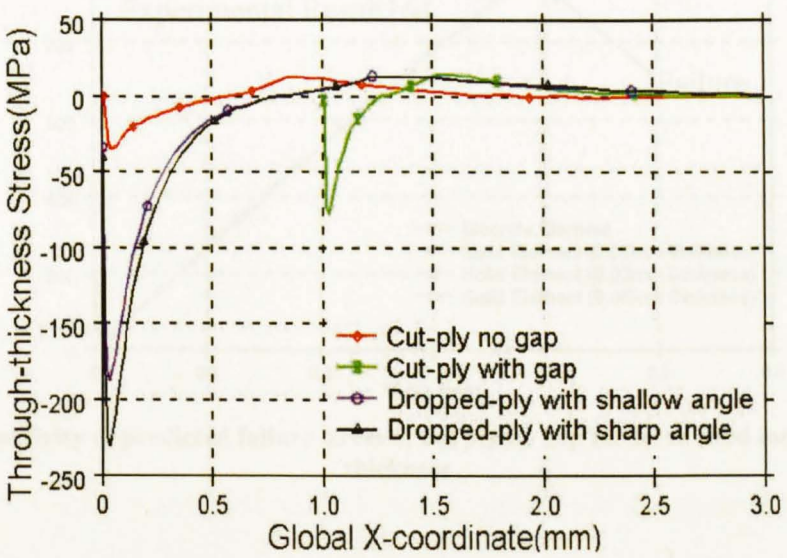

Fig 3.5.2-3 Through-thickness normal stress distribution along the interface between discontinuous and continuous plies stress

Due to the different normal compressive stress levels in the four models, Cui et al[162] gave four different values of modified G_{IIC}. These values have been used in the un-enhanced model and the results are presented in Table 3.5.2-3. This shows good agreement with the previous numerical and experimental results, but a variable G_{IIC} is required. Fig3.5.2-4

shows a typical predicted stress/time plot, here for the cut ply no gap model using the standard interface element formulation and Cui et al's enhanced G_{IIC}. The discrete interface element formulation as well as the solid interface element formulation with thicknesses of 0.01mm, 0.03mm and 0.05mm were used. The results with discrete interface elements and different thickness solid interface elements are nearly identical and compare well with experimental values.

Table 3.5.2-3 Comparison of measured and predicted delamination stress using variable G_{IIC}

	Measured Delam Stress (MPa)	Predicted Delam Stress				Diff., %
		Variable G_{IIC} (MPa) from eq^n 5				
		1.08	1.21	1.69	1.88	
Cut-ply No Gap	966	958				-0.83
Cut-ply with Gap	1021		1020			-0.01
Dropped-ply Shallow	1208			1197		-0.91
Dropped-ply Sharp	1274				1259	-1.18

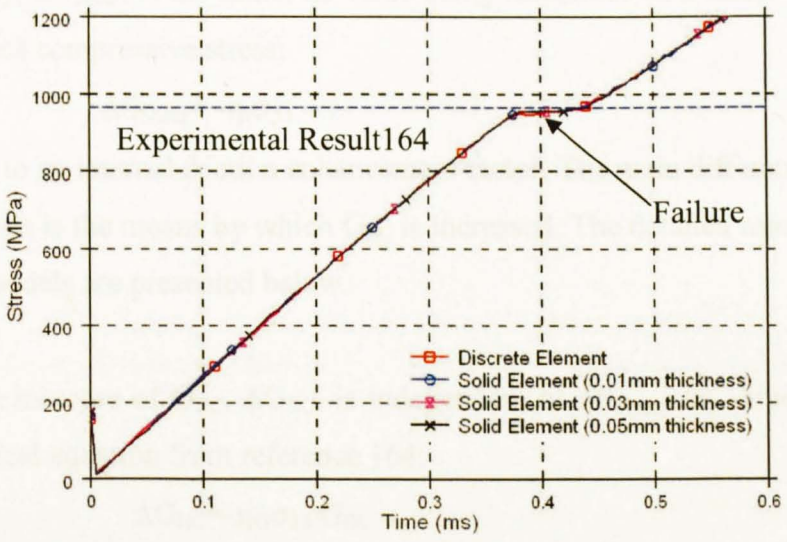

Fig 3.5.2-4 Sensitivity of predicted failure stress of cut ply no gap model to solid interface element thickness

With an appropriate assumption of the influence of through-thickness compressive stress on the Mode II failure evolution, we expect to raise a new set of failure criteria which can use the same input parameters to produce good failure predictions across all four models.

3 Mode II damage evolution laws under through-thickness compressive stress

The interface element failure is controlled by both the failure initiation and propagation criteria. It has been suggested in the literature[18-21] that compressive stress can have an enhancing effect on both the shear strength and mode II fracture toughness. Three different damage evolution assumptions under through-thickness compressive stress which take account of increases in strength and fracture energy are considered here and shown in Fig 3.5.2-5. δ_o, δ_{max}, S_{shear} and G_{IIC} are respectively the pure Mode II failure initiation displacement, final failure displacement, maximum shear stress and Mode II critical fracture energy. δ_{o_n}, δ_{max_n}, S_{shear_n} and G_{IIC_n} are the enhanced values under the influence of a compressive stress, σ_{33}. Figure 3.5.2-5a illustrates a model in which the improvements of S_{Shear} and G_{IIC} are independent of each other. Figure 3.5.2-5b illustrates a model in which the increase in G_{IIC} is determined by the increase of S_{Shear} only, keeping δ_{max} constant, and in Figure 10c the increase in G_{IIC} is determined by the increase in S_{Shear} and keeping the slope of the softening part of the curve constant. In all three models the increase in S_{Shear}, ΔS_{Shear}, is the same, its value being calculated as a linear function of the through thickness compressive stress:

$$\Delta S_{Shear} = -\eta_f \sigma_{33} \qquad (3.5.2\text{-}1)$$

η_f is analogous to an internal friction enhancement factor. The main difference between the three assumptions is the means by which G_{IIC} is increased. The detailed assumptions of the three damage models are presented below.

Model (a): The increase of G_{IIC}, ΔG_{IIC}, is independent of ΔS_{Shear}, its value is determined from the empirical equation from reference 164:

$$\Delta G_{IIC} = -\eta_G \sigma_{33} G_{IIC} \qquad (3.5.2\text{-}2)$$

η_G is an empirically derived enhancement factor and is dependent on the material used. In reference 164, σ_{33} is the average through-thickness stress over the distance where the stress is compressive, while here σ_{33} is the local through-thickness stress at an individual element. The elastic modulus before failure initiation is not influenced by the through-thickness compressive stress. The failure initiation displacement, δ_{o_n}, is determined by S_{Shear_n} and the final failure displacement δ_{max_n} by G_{IIC_n}. The unloading and re-loading curves after failure initiation and before final failure are assumed to be linear back to the origin. The failure criteria can be expressed as:

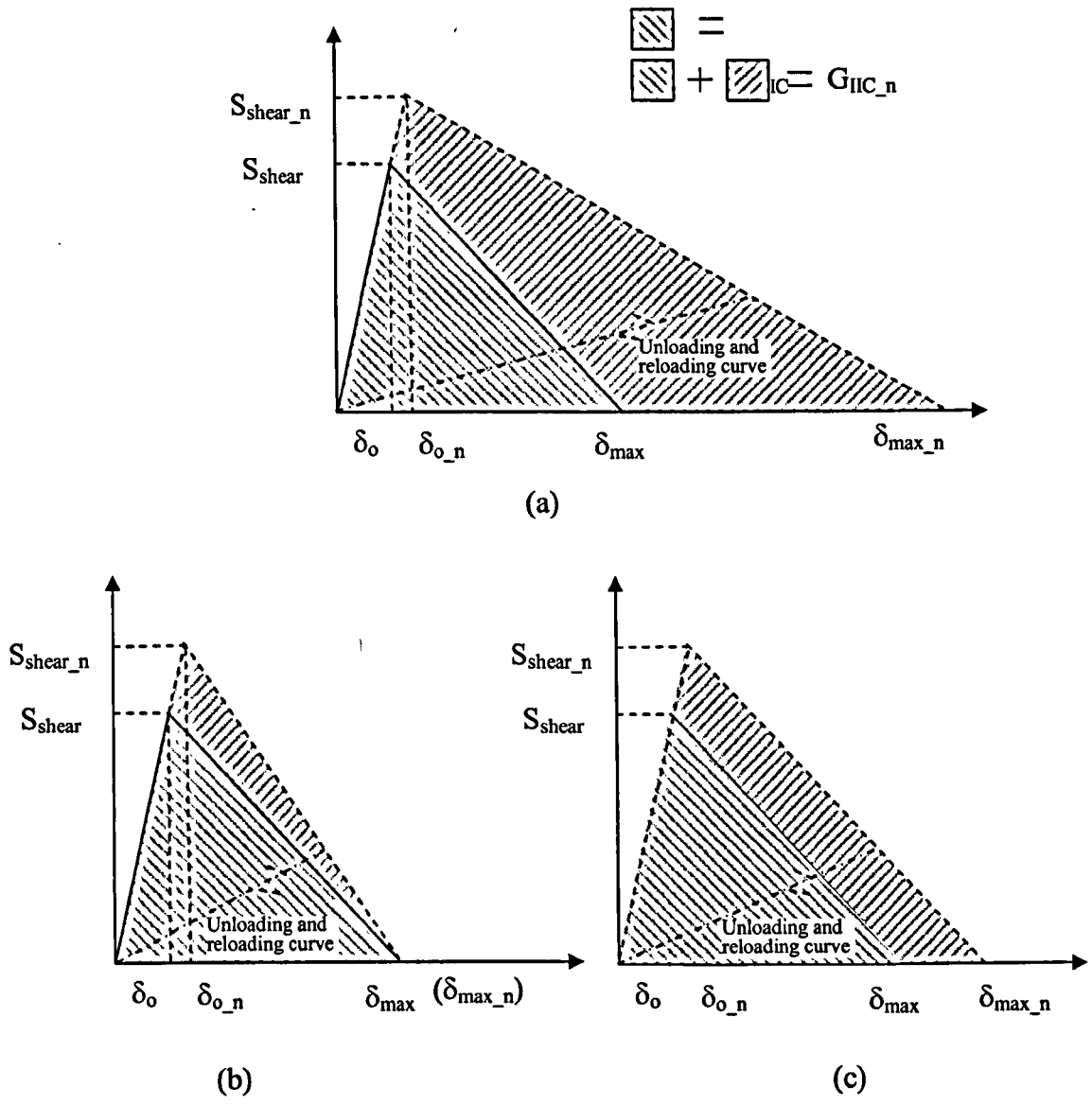

Fig 3.5.2-5 Mode II damage evolution laws under through-thickness compressive stress

Failure Initiation Criterion:

$$\left(\frac{\tau_{13}^2+\tau_{23}^2}{S_{shear\_n}^{\ 2}}\right)=1 \qquad (3.5.2\text{-}3)$$

Failure Propagation Criterion:

$$\left(\frac{G_{II}}{G_{IIC\_n}}\right)=1 \qquad (3.5.2\text{-}4)$$

Where

$$\begin{cases} S_{shear\_n}=S_{shear}-\eta_f\sigma_{33} \\ G_{IIC\_n}=G_{IIC}(1-\eta_G\sigma_{33}) \end{cases} \qquad (3.5.2\text{-}5)$$

It should be noted that the above equations are for shear loading in the presence of compressive through-thickness stress only. In the case of tensile through-thickness stress the mixed-mode failure criteria presented in Equation 3.2.2-3 and Equation 3.2.2-6 are required.

Model (b): The through-thickness compressive stress does not influence the elastic modulus and the final failure displacement, δ_{max}, but increases the shear strength causing an increase in the initial failure displacement, δ_o. The unloading and re-loading curves after failure initiation and before final failure are assumed to be linear. The increased shear strength, initial failure displacement and enhanced mode II fracture energy are:

$$\begin{cases} S_{Shear\_n} = S_{Shear} - \eta_f \sigma_{33} \\ \delta_{o\_n} = S_{Shear\_n} / G_{12} \\ G_{IIC\_n} = G_{IIC}[1 - \eta_f (\sigma_{33} / S_{Shear})] \end{cases} \quad (3.5.2\text{-}6)$$

Model (c): The through-thickness compressive stress does not influence the elastic modulus but increases the shear strength and the final failure displacement, δ_{max},. The initial failure displacement, δ_o, is increased by the increase in maximum shear stress. After initial failure, the slope of the softening part of the curve is the same as that of the un-enhanced model. The unloading and re-loading curves after failure initiation and before final failure are assumed to be linear. The increased shear strength, initial failure displacement, maximum failure displacement and enhanced mode II fracture energy are:

$$\begin{cases} S_{Shear\_n} = S_{Shear} - \eta_f \sigma_{33} \\ \delta_{o\_n} = S_{Shear\_n} / G_{12} \\ \delta_{max\_n} = (S_{Shear\_n} / S_{Shear}) \delta_{max} \\ G_{IIC\_n} = G_{IIC}[1 - (2\eta_f / S_{Shear}) \sigma_{33} + \eta_f (\sigma_{33} / S_{Shear})^2] \end{cases} \quad (3.5.2\text{-}7)$$

3.5.3 Numerical analysis

1.Predicted delamination Stress

The models of the cut and dropped ply experiments were re-analysed to determine if the revised failure model could predict the delamination failures using a single set of input parameters. The two constant parameters η_f and η_G in damage law(a) can be determined by applying the law to the two cut-ply and two dropped-ply models with $S_{12/13}$ and G_{IIC} as per table 5. A series of η_f values (0.45, 0.50, 0.55, 0.60, 0.65, 0.70, 0.75, 0.80, 0.85 and 0.90) are firstly assumed, then the corresponding η_G values in law(a) for the cut ply and dropped ply models are obtained by running the models to get failure predictions with a difference of less than ±2MPa from the experimental data. The obtained combinations of (η_f ,η_G) in law(a) are plotted in Fig 3.5.3-1 and a 2nd order curve fitted. The average values of (η_f ,η_G) for the four fitted curves at the overall closest point are taken to be the best combination for law(a), giving η_f=0.94 and η_G=0.0245MPa^{-1}. When these values, together with $S_{12/13}$ and G_{IIC} from table 5 are applied to the two cut-ply and two dropped-ply models the predicted delamination stresses are in very good agreement with those using the variable G_{IIC} from Cui et al[164] and experimental results (Table 3.5.3-1). Reference 161 gives a value of η_f=0.8 for the same material whilst the literature169 suggests that η_f should be below 0.5.

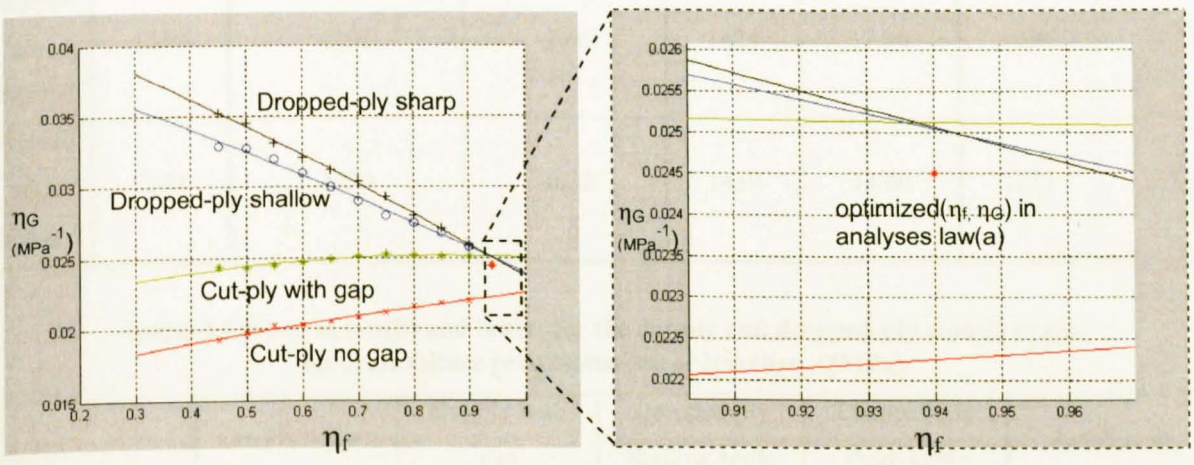

(a) (b) zoom in critical area

Fig 3.5.3-1 η_G vs. η_f in Law(a) for the cut ply and dropped ply models to get accurate failure predictions (each point on the graph represents an analysis with error less than ±2MPa from experiment)

In damage laws (b) and (c), the best values for parameter η_f for the cut ply and dropped ply models were obtained by running the models to get accurate failure predictions close to the experimental data with error less than ±2MPa. These η_f values are listed in Table 3.5.3-2 and their respective average value for the four models was taken as the optimized parameter for law(b) and law(c). The predicted delamination stresses by applying law(b) and law(c) with the optimized η_f and the interface element properties as per table 3.5.2-2 to the cut and dropped ply models in turn are listed in Table 3.5.3-1 and compared with the measured delamination stresses. It can be seen that there is some difference (>10%) between the predictions of law(b) and the experimental data, whilst the predictions of law(c) show an even closer agreement than the previous results using law (a).

Table 3.5.3-1 Comparison of measured and predicted delamination stress using law(a) ,law(b)and law(c) with optimized parameters

	Measured Delam Stress (MPa)	Predicted Delamination Stress (MPa)					
		law(a) (η_f=0.94 , η_G=0.0245MPa^{-1})	Difference from experiment(%)	law(b) (η_f=1.28)	Difference from experiment (%)	law(c) (η_f=0.74)	Difference from experiment (%)
Cut ply No Gap	966	979	1.24	943	-2.34	973	0.72
Cut ply Gap	1021	1018	-0.27	980	-3.98	1012	-0.88
Dropped ply Shallow	1208	1191	-1.45	1424	17.90	1204	-0.33
Dropped ply Sharp	1274	1270	-0.32	1459	14.60	1277	0.24

Table 3.5.3-2 η_f in law(b) and law(c) for the cut-ply and dropped-ply models to get accurate failure predictions (error less than ±2MPa)

	Cut-ply no gap	Cut-ply with gap	Dropped-ply shallow angle	Dropped-ply sharp angle	Average η_f
η_f in law(b)	1.53	1.55	1.04	1.00	1.28
η_f in law(c)	0.70	0.79	0.75	0.73	0.74

3.5.4 Summary and Discussion

Many publications on delamination with mixed-mode loading consider the interaction between tensile and shear stress. Some include studies on the strengthening effect of compressive stress on shear strength, but few consider the influence of compressive strength on the Mode II fracture energy, G_{IIC}. This study on the influence of through-thickness compressive stress on the Mode II damage evolution reveals that the increase of G_{IIC} is a necessary result of the increased shear strength. The normal compression can significantly suppress delamination by increasing both the shear strength and fracture energy.

From the assumptions in law(a) and law(c), it can be seen that the strengthening effect of the compressive stress on delamination is realised mainly through the improvement of G_{IIC}. Whilst law (a) can give good results, independent enhancement factors, η_f and η_G, are required to be established for both strength and fracture energy and the η_f is much higher than the values from other literature[165,168]. Using law(c), the four models need only one common input parameter, η_f, to produce the excellent results which previously, without the compressive stress interaction criteria, required different values of G_{IIC} for each model. Comparing with the value of $\eta_f = 0.8$ from reference 161, the value of $\eta_f = 0.74$ in model(c) seems quite reasonable. From the point of both number of parameters and the value of η_f, model (c) is a better assumption than model (a) for the delamination behaviour under compressive stress. Model (b) was shown to give unacceptably accurate results.

Fig 3.5.4-1 shows the sensitivities of the predicted failure stresses to the value of η_f in model (c) for the cut ply and dropped ply models. It can be seen that when the compressive stress increases between the cut ply and dropped ply models, the sensitivity of η_f is increased as well but overall sensitivity is relatively low for quite a wide range of input values. η_f is an enhancement factor on the material strength and therefore could be expected to vary with material type. Its dependence on layup and geometry is less obvious and has not been shown to be significant in this work. The enhanced interface element model has been applied here across a number of different material types and specimen geometries. An exact method for determining its value and the extent of its applicability should be the subject of further investigations.

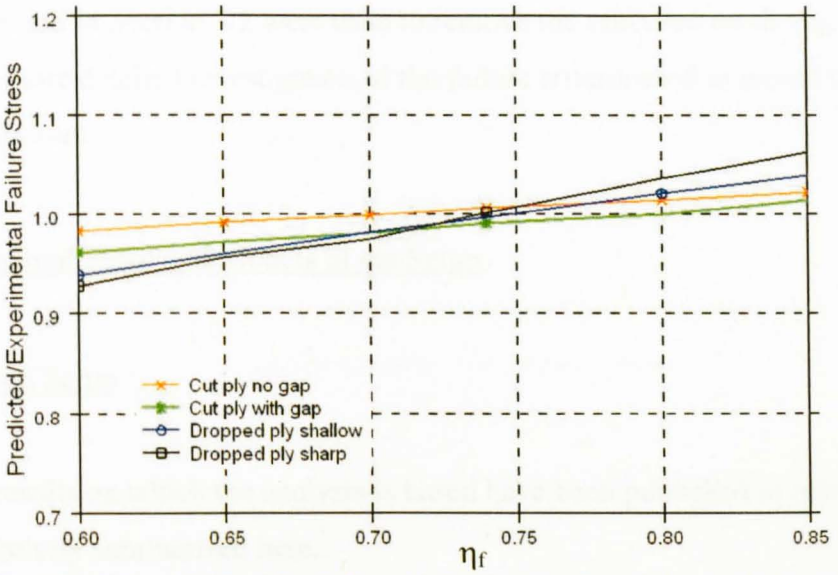

Fig 3.5.4-1 Sensitivities of η_f in Law(c) for the cut ply and dropped ply models

The new interface failure criterion based on the above understanding of the effect of compressive through-thickness stress on the delamination can be conveniently implemented in finite element codes and produces much improved predictions of delamination in the presence of compressive stresses.

3.6 Investigation of Dynamic Transverse Shear Failure in Single-lap Model

3.6.1 Introduction

As a validation of the newly developed interface element models a more complex case of a single-lap specimen, dynamically loaded has been investigated. Dong and Harding[170] developed a single-lap shear specimen for use at high strain rate to characterise the through-thickness shear strength of carbon/epoxy laminates. This strength was used as an input parameter into a finite element model to predict the delamination failure[171]. It was found that local stress concentrations existed in both shear and direct stress components and this caused significant differences between the test result and the finite element predictions. As a result of this highly localised stress concentration, results are further dependent on the mesh refinement in the area of high stress gradients.

To be able to investigate predictive models of delamination behaviour and failure criteria it is required to reduce or eliminate such mesh dependence. Hallett et al's work[171] has shown that analysis of a single-lap shear test resulted in the maximum stress localising in a single element. Further investigation of this phenomenon is carried out here and the interface

elements proposed in Section 3.2 were used to remove the observed mesh size effect. This then allows a more detailed investigation of the failure criteria used to model the delamination failure.

3.6.2 Experimental Setup and Models of the Setup

1. Experimental Setup

The full test results on which the analysis is based have been published in reference 170 and are only briefly summarised here.

A single-lap shear specimen design, optimised to achieve a uniform shear stress over the central failure plane and minimal normal stresses under dynamic loading was tested in a compressive split Hopkinson bar apparatus.

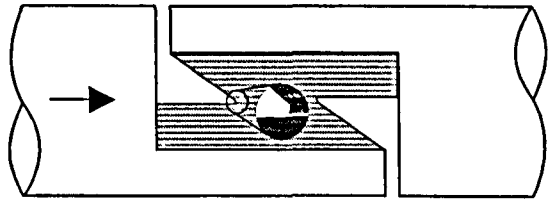

Fig 3.6.2-1 Schematic diagram showing loading mechanism and detail of failed specimen from testing in reference[171]

Fig 3.6.2-1 shows a schematic of the specimen design and loading. Inset is a photograph of the failure plane obtained with the two parts of the specimen separated after removal from the loading bars for clarity. The specimen was manufactured from carbon fibre/epoxy (T300/914) using unidirectional pre-preg tape in a cross-ply (0/90°) layup. Although a range of strain rates was tested, a single test at ~680/s has been chosen for comparison with the finite element analysis.

2. Model Setup

The single-lap test has been modelled in the explicit finite element code LS-Dyna. This takes account of the dynamic stress wave propagation and is therefore suitable for the high strain rates applied here.

Fig 3.6.2-2 and Fig 3.6.2-3 show the dimensions and boundary conditions of the model. Eight noded solid elements were used with a plane of symmetry on the centre-line. It was found to be necessary to include the input and output bars of the Hopkinson bar apparatus in order to correctly model the stress wave propagation and hence the dynamic stress state without spurious oscillations. A simplified rectangular cross sectional geometry for the bars was used instead of the circular cross section in the real case.

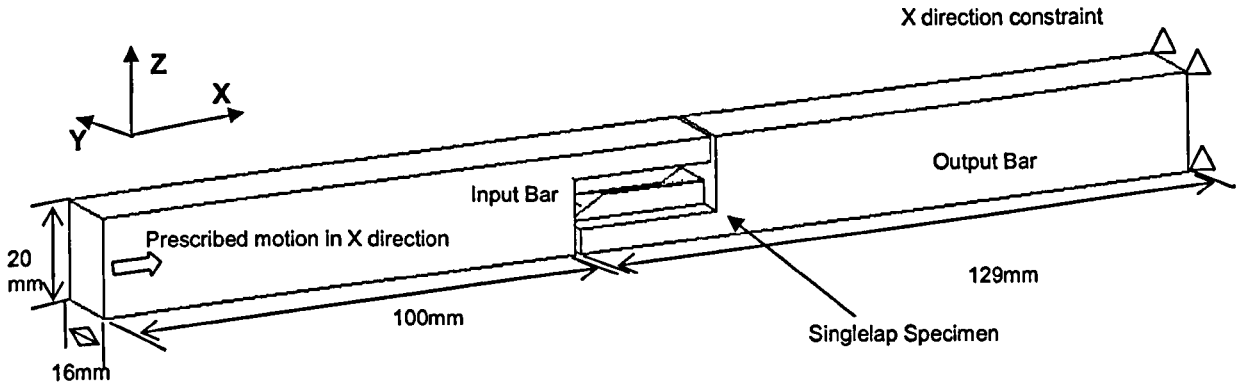

Fig 3.6.2-2 Finite element model dimensions and boundary conditions (mesh not shown)

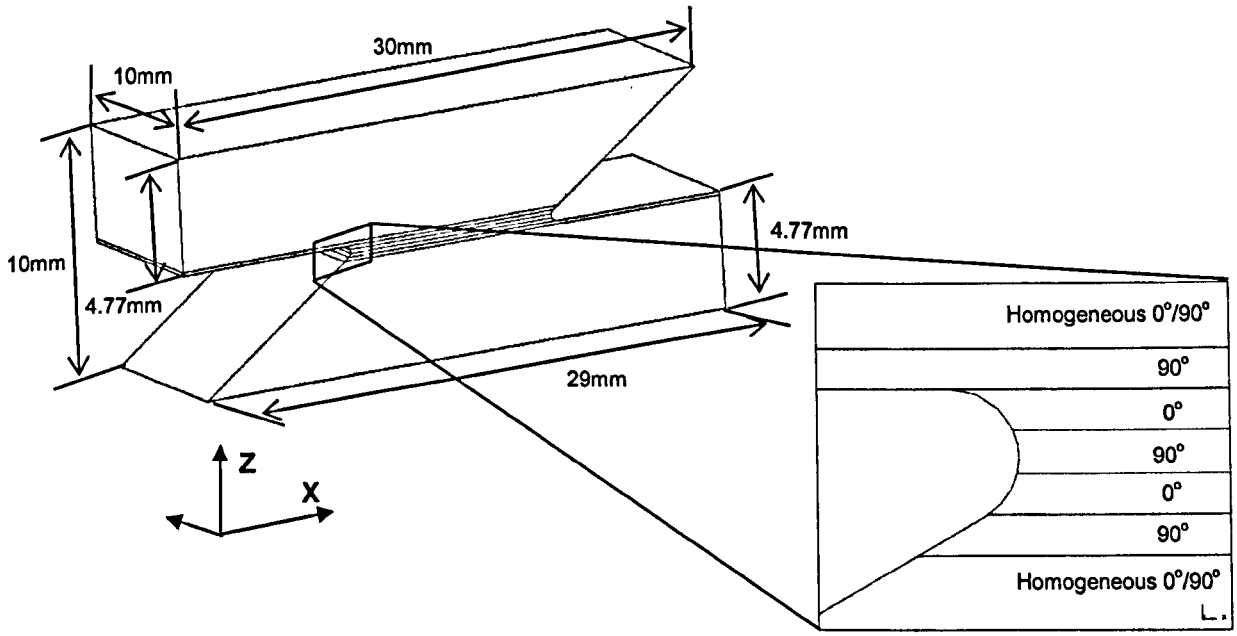

Fig 3.6.2-3 Detail of specimen dimensions and layup (see Fig 3.6.2-4 for mesh detail)

The single-lap specimen itself was modelled with homogenised properties for the plies located away from the failure plane and on a ply by ply basis in the region between the two

notch tips where failure occurred as shown in Fig 3.6.2-3 with the mesh details shown in Fig 3.6.2-4.

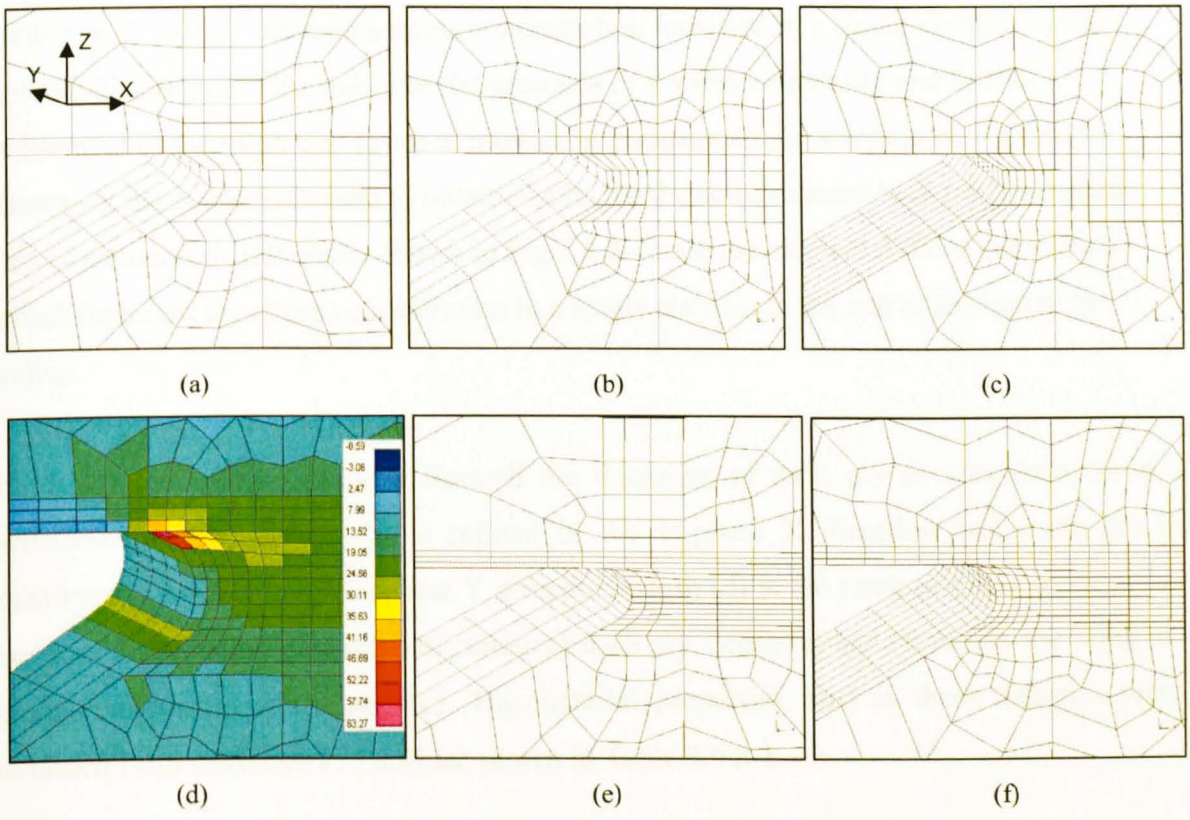

Fig 3.6.2-4 (a)-(f) Detail of specimen notch tip showing different mesh densities used with mesh (e) showing typical elemental XZ shear stresses

3. Baseline Original damage formulation – solid element based

The finite element model presented in reference 171 was revised to take advantage of advances in computing power with a refined mesh and the inclusion of the input and output bars as described above, necessary for correct modelling of the wave propagation. The delamination failure model in Equation 2 [equation no.] is based on that presented by Brewer and Lagace[172](embedded in LS-Dyna as material 22).

$$\left(\frac{\sigma_{33}}{Z_f}\right)^2+\left(\frac{\sigma_{13}}{S_{13}}\right)^2+\left(\frac{\sigma_{23}}{S_{23}}\right)^2 \geq 1 \qquad (3.6.2\text{-}1)$$

where Z_f is the direct through-thickness strength (only taken into account when tensile) and S_{13} and S_{23} are through-thickness shear strengths. When the stress state in a given element satisfies the equation 2 it is deemed to have failed and the moduli pertinent to the strengths in equation 3.6.2-2 are returned to zero. This is done over a short period of time rather than

instantaneously to overcome numerical instabilities. More details about material 22 formulation can be found in LS-Dyna user manual[173].

Hallett et al' work[171] showed a stress concentration localised in a single element in the notch radius region. This indicates the presence of a stress singularity and further refinement of the mesh will result in increasingly greater stress predictions. Fig 3.6.2-4 shows six mesh densities used to obtain results for the solid element based delamination failure criterion. Additionally shown in Fig 3.6.2-4e are the elemental XZ shear stresses which highlight the stress concentration in a single element at the end of the notch tip radius.

Mesh (a) uses only 1 element through the thickness of each ply as was done for the previous model[171]. Mesh (b) is refined in the in-plane X direction and mesh (c) is additionally refined in the in-plane Y direction. Mesh (d) is the same in-plane mesh as (a) but uses 3 elements through the thickness of each ply. Mesh (e) and (f) follow the same in-plane refinements as (b) and (c). The material properties used in these analyses were obtained from reference 171 and are shown in Table 3.6.2-1.

Table 3.6.2-1 Material data for T300/914[171]

E_{11}(MPa)	E_{22}(MPa)	E_{33}(MPa)	G_{12}(MPa)	G_{13}(MPa)	G_{23}(MPa)
139000	9400	9400	4500	4500	2850
ν_{21}	ν_{31}	ν_{23}	Z_f(MPa)	S_{13}(MPa)	S_{23}(MPa)
0.0209	0.0209	0.33	74	86	86

4. Interface element based damage formulation

Interface elements introduced in Section 3.3 have been put within the single-lap specimen using the pre-processor program at the interfaces between the plies. Locations of the interface elements are shown in Fig 3.6.2-5a for beam interface elements and Fig 3.6.2-5b for solid interface elements. Damage formulations of the interface elements are the same as those in Section 3.2

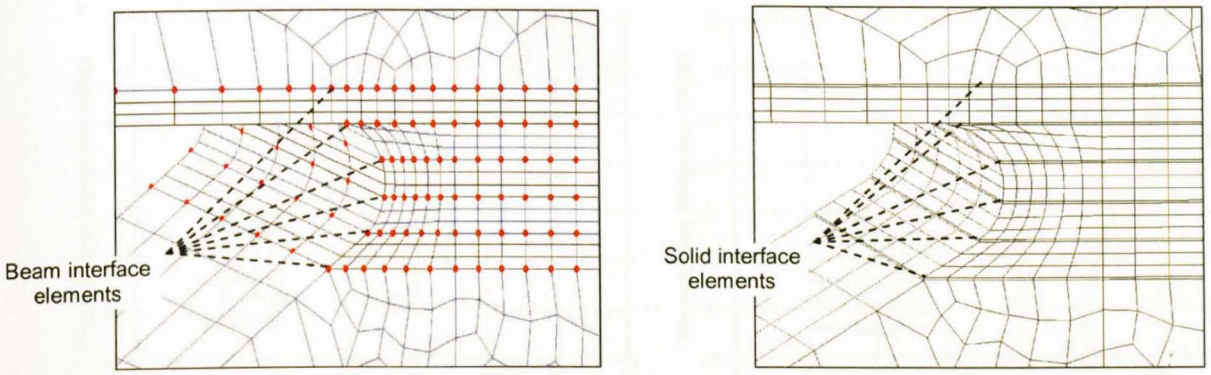

Fig 3.6.2-5 Interface element locations within the single-lap specimen model. (a) for beam interface elements and (b) for solid interface elements(thickness 0.01mm)

The interface material parameters of T300/914 are derived from references 174, 175, 176 and 177 and are shown in Table 3.6.2-2. E and G are the initial mode I and mode II elastic stiffnesses respectively.

Table 3.6.2-2 Material parameters of interface elements (T300/914)[178-181]

G_{IIC} (N/mm)	Z_f (MPa)	$S_{12/23}$ (MPa)	E (GPa)	G (GPa)
0.57	94	75	3.2	1.5

3.6.3 Results

1 Average Shear Stress

The average shear stress in the failure plane is derived by dividing the X direction output force (measured in the output bar) by the area of the failure plane. This is used to describe the model response under dynamic loading with delamination failure occurring at the maximum compressive stress in the output bar. The six mesh patterns shown in Fig 3.6.2-4 are respectively applied to the single-lap specimen model in Fig 3.6.2-3. When the baseline solid element based delamination model is adopted, the numerical shear response as a function of time of the six models is obtained and compared in Fig 3.6.3-1. The figure shows that the simulated results are severely influenced by the mesh density, especially the pattern along the X and Z directions.

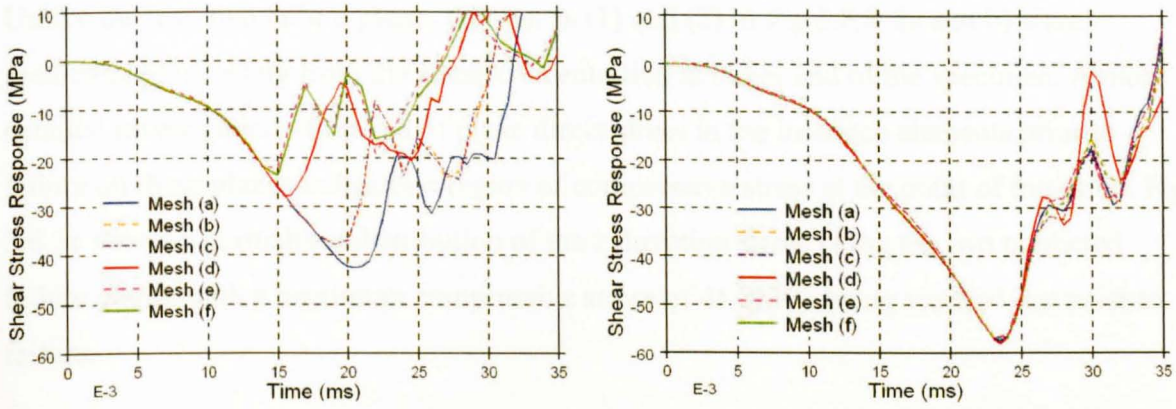

(a) solid element based failure (b) interface element based failure

Fig 3.6.3-1 Average shear stress vs. time for the six meshes shown in Fig 3.6.2-4

When the interface element based delamination model is adopted, results of the model using discrete interface elements and the model using solid interface elements are the same. The shear response of the six models with different mesh densities is again obtained and compared in Fig 3.6.3-1b. The results are nearly independent of the mesh patterns and can therefore be further used to investigate the failure criteria implemented.

2. Compressive stresses on the interfaces

The analyses shown in Fig 3.6.3-1a and Fig 3.6.3-1b are not compared with the experimental shear strength which was somewhat greater than all of the results presented, at 77 MPa, as discussed later.

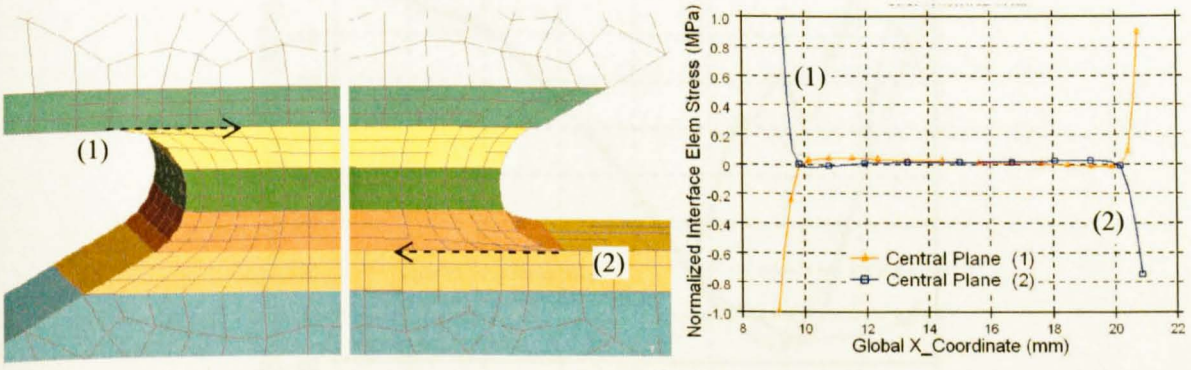

(a) (b) (c)

Fig 3.6.3-2 Typical Z_direction stress distribution in the model before failure

In the experimental results it was noted that the specimens failed slightly away from the centre-line, on a plane consistent with the local shear stress concentration. In the numerical analyses this was the predicted failure location for both the baseline and revised model.

Unlike the test, two failure planes (shown as (1) and (2) in Fig 3.6.3-2a and b) were predicted, progressing from the stress concentration at either end of the specimen. A more detailed investigation of the out of plane direct stress in the interface elements prior to failure on these planes indicates a region of compressive stress at the point of initiation. Fig 3.6.3c shows a normalised distribution of the z direction stress along the two predicted failure planes with a maximum compressive stress of 45.2MPa being reached just prior to failure.

3.Application of the compression enhanced interface element formulation

The single-lap model was re-run with the revised interface element formulation using law (c) . The same value for the enhancement factor as above, η_f=0.74, has been used although it is noted that it is now being applied to a different material. The predicted delamination stress for law (c) is compared with the experimental result in Fig 3.6.3-3, showing a very good agreement. Considering the possible dependence of η_f in law(c) on the material, the optimised value for the carbon/epoxy material used in the single-lap test might well be different from that for the glass-epoxy used in the cut-ply and dropped-ply specimens. When a new value of η_f=0.65 is applied in the single-lap model with law(c), it gives an even better post-failure prediction as well as a good prediction of the failure stress, as shown in Fig 3.6.3-3. The new failure criteria accounting for compressive effects greatly increases the predicted delamination stress compared with the standard mixed-mode failure criteria presented in Section 3.2 with much improved correlation.

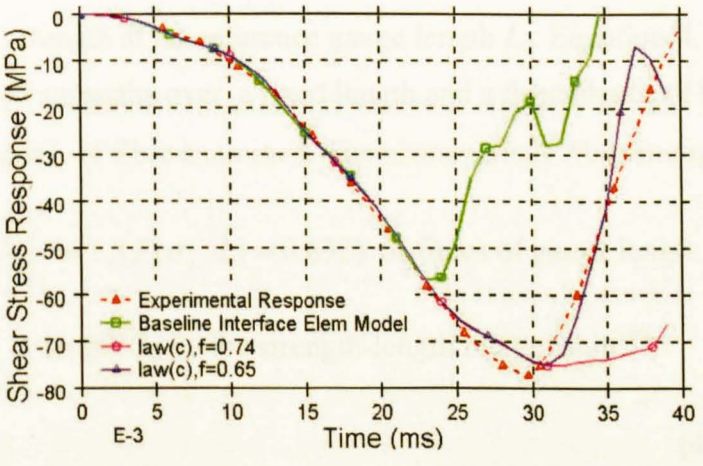

Fig 3.6.3-3 Predicted delamination stresses of single-lap models using damage law(c)

Chapter 4 Modelling Statistical Fibre Failure in Composite Laminates

4.1 Introduction

4.1.1 Probabilistic Analysis of Fibre dominated element failure in Composite Laminates

As reviewed in section 2.5, the influence of statistical defects on the fibre tensile strength is especially important for the size effect and was extensively investigated using probabilistic models for its quantitative analysis[135,178,179]. The most important point of the probabilistic analysis is how to assign the element strength along the fibre in those statistical simulations. Weibull strength distribution theory[180] has been widely accepted in analyzing this type of problem.

The traditional Weibull description of fibre strength assumes that the number of flaws in a fibre is linear along the fibre length, consistent with spatially random flaws, and is a power-law function of the stress. Specifically, the mean number of flaws N in a length L that will fail at or below stress σ and the associated cumulative probability of failure F are given by

$$N(\sigma,L)=\frac{L}{L_o}\left(\frac{\sigma}{\sigma_o}\right)^m \;;\; F(\sigma,L)=1-\exp\left(-\left(\frac{L}{L_o}\right)\left(\frac{\sigma}{\sigma_o}\right)^m\right) \qquad (4.1.1\text{-}1)$$

Here, m is the Weibull modulus describing the dispersion in fibre strengths and σ_o is the characteristic fibre strength at the reference gauge length L_o. Equation(4.1.1-1) implies both a distribution of strengths over a fixed length and a dependence of the characteristic strength on the length L of fibre examined. The characteristic fibre strength σ_L (at which, $N(\sigma_L,L)=\frac{L}{L_o}\left(\frac{\sigma_L}{\sigma_o}\right)^m=1, (F(\sigma_L,L)=0.632)$ of fibres of gauge length L is related to the reference value σ_o at length L_o by the strength-length relationship[188]

$$\sigma_L=\sigma_o\left(\frac{L_o}{L}\right)^{1/m} \qquad (4.1.1\text{-}2)$$

Based on Weibull distribution function, a Weibull weakest link model[181] was proposed to model the probabilistic fibre tensile failure in composites. The Weibull weakest link model assumes that a structure consists of a number of individual elements arranged in series. When one of these elements fails, the entire component fails. According to the simplest two-parameter Weibull function, the cumulative distribution function of reliability and failure of a unit volume subject to a uniform stress σ was determined as in the equations below:

$$F(\sigma) = 1 - \exp\left(-\left(\frac{\sigma}{\sigma_o}\right)^m\right)$$

$$S(\sigma) = 1 - F(\sigma) = \exp\left(-\left(\frac{\sigma}{\sigma_o}\right)^m\right) \qquad (4.1.1\text{-}3)$$

Here, m is the Weibull modulus(or Weibull shape parameter) and σ_o is the characteristic fibre strength at the reference volume.

Considering a volume of material to be composed of small elemental volumes under uniform tensile stress gives

$$F(\sigma) = 1 - \exp\left(-\int\left(\frac{\sigma}{\sigma_o}\right)^m dv\right) = 1 - \exp\left(-V\left(\frac{\sigma}{\sigma_o}\right)^m\right) \qquad (4.1.1\text{-}4)$$

For two laminated composites with volumes V_1 and V_2, assuming the same failure probability, the following expression may be derived:

$$\frac{\sigma_2}{\sigma_1} = \left(\frac{V_1}{V_2}\right)^{1/m} \qquad (4.1.1\text{-}5)$$

The Weibull weakest link model was generally successful in predicting failure of many brittle materials, but could not predict the strength of size effect with acceptable accuracy for composite materials[182]. Though much available literature[183],[184] suggests the constituent fibres of many composites do behave as brittle materials, the load of a broken fibre is locally transferred to surrounding fibres by matrix around the fibre and final failure generally occurs after some damage accumulation. Recently, parallel models have been developed which account for this load sharing ability, as opposed to series models, which user weakest link theory. Wisnom[185] hypothesized that a composite could be represented as being between the two extremes of a brittle solid and a loose fibre bundle, so that when one

bundle broke, the load was redistributed to the other fibres in the model. Phoenix[186] took this model a step further in a 'chain of bundles' model, by stating that when a fibre breaks, its load is shared by the fibres adjacent to it only. Gurvich and Pipes[187] developed a similar quantitative model employing a theory of progressive failure of aggregated sublaminates, which make up the laminate and use probabilistic failure. Curtin[188] proposed the 'Weibull of Weibull' model, which is based on the local load sharing , as opposed to global load sharing, ability of composites. Okabe and Takeda[189] have since backed this model up with experimental results, showing it to be more accurate than a traditional Weibull model. Tabei and Sun[190] developed a sequential multi-step failure model which assumed a structure as a parallel arrangement of elements. When an element fails, the load is redistributed among the remaining elements. Final failure occurs when all of the elements have failed. They showed that the sequential multi-step failure model presented more realistic results than the Weibull weakest link model.

Most of the earlier analytical strength models use idealized load sharing rules, such as nearest neighbour local load sharing, global load sharing or equal load sharing, and some parametric form of the Weibull distribution to describe fibre strength. To extrapolate to longer composite lengths and bundle sizes, asymptotic analyses and weak link scalings are used. Exact probability calculations for even the simplest of local load sharing rules are enormously difficult except for small numbers of fibers[191]. Moreover, the above theories are generally derived assuming simple tensile failure of unidirectional composites. It is questionable whether these theories could be applied where more complex failure modes of laminates occur. In some cases the theories have only been presented as mathematical exercises without any reference to experimental data. The complexity of some of the models becomes redundant when their parameters become difficult or impossible to estimate, and gross approximations are required. Also, the advantages of further refining the mathematical model must be balanced against the assumptions made in the derivation of the theory (especially concerning the uniformity of the microstructure). Regardless of the fact that the fibre statistical failure formulations proposed by the above authors have analytical forms, their practical realization is also connected with the inevitable realization of computer-aided time-consuming numerical procedures. And this, in turn, creates complexities for introduction into engineering practice and restricts the application of the results obtained in various theories.

Consequently, it is very important to develop a detailed method that uses simpler formulations but is adequate to account for the size effect of the most commonly used composites. The fewer parameters of such a method that need to be experimentally determined, the more generally and easily this method can be implemented in computer programs and be applied in practical analysis. Finite element analysis (FEA) is probably the best candidate for determining the complex stress and strain states in the composites and calculating stress redistribution without the use of ad hoc local sharing rules. The focus of this chapter is to analyze progressive fibre dominated element failure within a composite with arbitrary configurations of plies using the explicit finite element code, LS-Dyna, and determine the initiation and propagation of fibre dominated element failure as a result of the interplay between fibre stress concentrations and the statistical variation in fibre strength.

Factors influencing the size effect such as delamination and splitting from edge effects are modeled using interface elements. Thermal residual stress and statistical fibre strength are modeled using a user defined material introduced in this Chapter. The formulation of this material was implemented into the LS-Dyna code using a user defined material subroutine (Umat44). An overview of relevant points used within the LS-Dyna code is provided in the following section. For further details the LS-Dyna theoretical manual[192] is highly recommended and provides detailed examples of the methodology used within the code.

4.1.2 LS_Dyna solution overview

LS_Dyna is a non-linear material and geometrical explicit time integration Finite Element code. The code uses an updated Lagrangian formulation and a central difference time integration procedure[193]. The time-step is governed by the so-called Courant limit. Due to the explicit nature no stiffness matrix inversions are performed during an analysis. The time step is conditionally stable, i.e., the shortest distance between two nodes within the FE mesh controls the time step. This can result in time steps of the order of 10^{-8} s, e.g., when modelling each individual composite ply with one solid finite element. However, with the use of Rayleigh damping and modification to the density, in cases where the inertia effects are negligible, a solution to a non-linear static problem can be obtained in a realistic time.

Typically, the kinetic energy must be less than 0.001% of the total energy. This is sometimes referred to as dynamic relaxation (DR).

The general equation of motion to be solved in LS-Dyna is defined as

$$Ma^n=P^n-F^n+H^n \qquad (4.1.2\text{-}1)$$

where M is the diagonal mass matrix, a is the nodal acceleration, P^n is the external body loads, F^n is the stress divergence vector, H^n is the hourglass resistance, nth indicates the nth time step.

Rayleigh damping for non-linear static problem can be introduced by the addition of an appropriate damping matrix as shown below (4.1.2-2). The starting point is the dynamic equilibrium equations with the addition of a damping term.

$$Ma^n+Cv^n=P^n-F^n+H^n \qquad (4.1.2\text{-}2)$$

where C^n is the damping matrix and v is the nodal velocity.

Using the standard Rayleigh damping formulation, the mass and stiffness proportional damping can be introduced using the following equation:

$$C=\alpha M+\beta K \qquad (4.1.2\text{-}3)$$

where C, M and K are the damping, mass and stiffness matrices, respectively. The constants α and β are the mass and stiffness proportional damping constants, respectively. As recommended in the LS-Dyna manual, a value of 10% was used for the β in the high frequency domain. The α constant is set to critically damp the lowest frequency in the problem.

To advance to time t^{n+1} the LS-Dyna code uses a central difference time integration scheme, defined as

$$a^n=M^{-1}(P^n-F^n+H^n) \qquad (4.1.2\text{-}4)$$

$$v^{n+1/2}=v^{n-1/2}+a^n\Delta t \qquad (4.1.2\text{-}5)$$

$$x^{n+1/2}=x^n+v^{n+1/2}\Delta t^{n+1/2} \qquad (4.1.2\text{-}6)$$

$$\Delta t^{n+1/2}=\frac{(\Delta t^n+\Delta t^{n+1})}{2} \qquad (4.1.2\text{-}7)$$

where a, v and x are the global nodal accelerations, velocities and displacement vectors, respectively.

Stress update during the time integration is trivial, integrated incrementally, however, material rotation is consider using a Jaumann stress rate approach which ensures a co-rotational formulation and accounts for large movement of the local system with respect to the original position.

The treatment of sliding and impact is one of the major strengths of the LS-Dyna family of explicit codes. Two methods are available within the code, firstly, a kinematic constraint method, and secondly a penalty method.

The kinematic method is explained in detailed within the LS-DYNA3D theoretical manual[193]. Fundamentally, transformations are imposed on the nodal displacements of the slave nodes along the contact surface, thus eliminating the normal degree of freedom. The transformation imposes constraints on the global equations of the nodes along the contact surface. The second penalty method, which was used in the current study, places normal interface springs between all interpenetrating nodes and contact surfaces. Momentum is exactly conserved without the necessity of imposing impact and release specifications.

4.2 Formulation of Statistical Fibre dominated element failure in Composite Laminates

4.2.1 Material Formulation *of* a lamina before Fibre dominated element failure

The state of stress at a point in a lamina can be represented by nine stress components σ_{ij} (where i,j=1,2,3) acting on the sides of an elemental cube with sides parallel to the 1-, 2- and 3- axes of a reference coordinate system (Figure 4.2.1-1). Similarly, the state of deformation is represented by nine strain components, ε_{ij}.

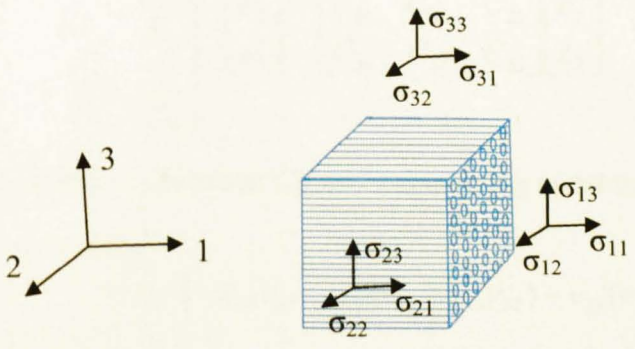

Fig 4.2.1-1 State of stress at a point of a lamina

The fibre direction(or longitudinal direction) in a lamina is usually defined as the 1- axis, in-plane transverse direction is the 2-axis and through thickness (or out-of plane) direction is the 3- axis of the reference coordinate system in a lamina.

Due to the symmetry of the stress and strain tensors, there are relations:

$\sigma_{ij} = \sigma_{ji}$, $\varepsilon_{ij} = \varepsilon_{ji}$. (where i,j=1,2,3) (4.2.1-1)

It is customary in mechanics of composites to use a contracted notation for the stress and strain as follows:

$\sigma_{11} = \sigma_1$, $\sigma_{22} = \sigma_2$, $\sigma_{33} = \sigma_3$, $\sigma_{12} = \sigma_{21} = \tau_{12}$, $\sigma_{23} = \sigma_{32} = \tau_{23}$, $\sigma_{31} = \sigma_{13} = \tau_{31}$ (4.2.1-2)

$\varepsilon_{11} = \varepsilon_1$, $\varepsilon_{22} = \varepsilon_2$, $\varepsilon_{33} = \varepsilon_3$ (4.2.1-3)

Before fibre failure, the mechanical behaviour of a lamina is considered to be elastic in the σ_1, σ_2 and σ_3 direction. The strain-stress relations can be expressed in terms of engineering constants as follows:

$$\begin{bmatrix} \varepsilon_1 \\ \varepsilon_2 \\ \varepsilon_3 \end{bmatrix} = \begin{bmatrix} \frac{1}{E_1} & -\frac{\nu_{21}}{E_2} & \frac{\nu_{31}}{E_3} \\ -\frac{\nu_{12}}{E_1} & \frac{1}{E_2} & \frac{\nu_{32}}{E_3} \\ -\frac{\nu_{13}}{E_1} & -\frac{\nu_{23}}{E_2} & \frac{1}{E_3} \end{bmatrix} \begin{bmatrix} \sigma_1 \\ \sigma_2 \\ \sigma_3 \end{bmatrix} \qquad (4.2.1\text{-}4)$$

Where E_1, E_2 and E_3 are Young's modulus in σ_1, σ_2 and σ_3 directions.

$\nu_{12}, \nu_{21}, \nu_{23}, \nu_{32}, \nu_{13}, \nu_{31}$ are Poisson's ratios. The stress-strain relations are:

$$\begin{bmatrix} \sigma_1 \\ \sigma_2 \\ \sigma_3 \end{bmatrix} = \begin{bmatrix} \frac{1}{E_1} & -\frac{\nu_{21}}{E_2} & \frac{\nu_{31}}{E_3} \\ -\frac{\nu_{12}}{E_1} & \frac{1}{E_2} & \frac{\nu_{32}}{E_3} \\ -\frac{\nu_{13}}{E_1} & -\frac{\nu_{23}}{E_2} & \frac{1}{E_3} \end{bmatrix}^{-1} \begin{bmatrix} \varepsilon_1 \\ \varepsilon_2 \\ \varepsilon_3 \end{bmatrix} = \begin{bmatrix} C_{11} & C_{12} & C_{13} \\ C_{21} & C_{22} & C_{23} \\ C_{31} & C_{32} & C_{33} \end{bmatrix} \begin{bmatrix} \varepsilon_1 \\ \varepsilon_2 \\ \varepsilon_3 \end{bmatrix} \qquad (4.2.1\text{-}5)$$

Substituting the relations between *Cij* and engineering constants in the above, we obtain:

$$\Delta = \begin{vmatrix} 1 & -\nu_{21} & -\nu_{31} \\ -\nu_{12} & 1 & -\nu_{32} \\ -\nu_{13} & -\nu_{23} & 1 \end{vmatrix} = 1 - \nu_{23}\nu_{32} - \nu_{21}(\nu_{12} + \nu_{13}\nu_{32}) - \nu_{31}(\nu_{12}\nu_{23} + \nu_{13})$$

$$C_{11} = \frac{(1-\nu_{23}\nu_{32})E_1}{\Delta}, \quad C_{22} = \frac{(1-\nu_{13}\nu_{31})E_2}{\Delta}, \quad C_{33} = \frac{(1-\nu_{12}\nu_{21})E_3}{\Delta}$$

$$C_{12} = \frac{(\nu_{21} + \nu_{31}\nu_{23})E_1}{\Delta},\ C_{23} = \frac{(\nu_{32} + \nu_{12}\nu_{31})E_2}{\Delta},\ C_{13} = \frac{(\nu_{13} + \nu_{12}\nu_{23})E_3}{\Delta}$$

$$C_{12} = C_{21}, C_{23} = C_{32}, C_{31} = C_{13}$$

When thermal load is applied in the lamina, the local thermal strains would be:

$$\varepsilon_{11}^T = \alpha_1 \Delta T \quad \varepsilon_{12}^T = \alpha_2 \Delta T,\ \varepsilon_{13}^T = \alpha_3 \Delta T \qquad (4.2.1\text{-}6)$$

Where $\varepsilon_1^T, \varepsilon_2^T$ and ε_3^T are thermal strains caused by change of temperature in the σ_1, σ_2 and σ_3 directions. α_1 α_2 and α_3 are thermal expansion coefficients in the three directions. ΔT is the change of temperature.

The strains at a point in the lamina are the combination of elastic strains and thermal strains:

$$\varepsilon_{1\text{-}total} = \varepsilon_1 + \varepsilon_{11}^T,\ \varepsilon_{2\text{-}total} = \varepsilon_2 + \varepsilon_{12}^T,\ \varepsilon_{3\text{-}total} = \varepsilon_3 + \varepsilon_{13}^T \qquad (4.2.1\text{-}7)$$

Shear stress-strain relations in the τ_{12}, τ_{23} and τ_{31} directions are treated as nonlinear and expressed in the form of a piecewise 2nd order polynomial interpolation:

$$\tau_{12} = a_2\varepsilon_{12}^2 + a_1\varepsilon_{12} + a_0$$

$$\tau_{23} = b_2\varepsilon_{23}^2 + b_1\varepsilon_{23} + b_0 \qquad (4.2.1\text{-}8)$$

$$\tau_{31} = c_2\varepsilon_{31}^2 + c_1\varepsilon_{31} + c_0$$

Where a_i b_i c_i (i=1,2,3) are the 2nd order polynomial interpolation coefficients that need to be experimentally determined.

In the absence of experimental data about the non-linear shear behaviour of a lamina, the behaviour of this lamina can be taken as orthotropic elastic and the shear stress-strain relations as linear. This elastic shear stress-strain behaviour can be considered as a special situation represented by equation (4.2.1-8), where:

$$a_2 = a_0 = 0,\ a_1 = G_{12}$$

$$b_2 = b_0 = 0, b_1 = G_{23} \qquad (4.2.1\text{-}9)$$

$$c_2 = c_0 = 0, c_1 = G_{31}$$

G_{12}, G_{23}, G_{31} are the shear moduli.

4.2.2 Statistical Fibre dominated element failure Formulation in Composite Laminates

Modelling statistical fibre dominated element failure in a composite laminate is based on the following assumptions:

1. A multi-directional composite laminate consists of a number of laminae with different orientations connected by matrix which can be modeled using interface elements. The influence of one lamina on another in a laminate model is realized by the interface elements between them.

2. The role of interface elements is only to transfer the load from one lamina to another, but does not influence the material properties of a lamina on its own.

With assumption(1) and (2), the material properties of a laminate can be determined by the orientation and properties of laminar that are involved, thus the effect of layups on the composite properties can be reflected..

3. Fibres in a laminate are brittle. The tensile failure probability of fibres in a laminate is mainly influenced by the flaw distribution and longitudinal tensile stress. Though stresses including transverse in-plane stress, out-of-plane stress and shear stresses might have influence on the fibre tensile failure probability as well, for the absence of relevant study from experiments and the literature, also for the fact that fibre statistic failure theories are generally derived assuming simple tensile failure of unidirectional composites [177-186], the influence of non-tensile stresses on fibre tensile failure probability is neglected.

4. In a finite zone where one constant stress solid element is applied in the laminate specimen, the tensile stress is considered as being uniformly distributed through the material volume. The tensile survival (or reliable) probability of this zone follows the simplest two-parameter Weibull model[128]:

$$S_i(\sigma) = \exp\left(-V_i\left(\frac{\sigma_i}{\sigma_o}\right)^m\right) \qquad (4.2.2\text{-}1)$$

Where σ_o is the characteristic strength (or scale parameter) and m is the Weibull modulus (or shape parameter). σ_i and V_i are elemental longitudinal tensile stress and volume respectively.

$$S_{laminate}(\sigma) = \prod_{i=1}^{TotalNoofSolidElements} S_i(\sigma) = \prod_{i=1}^{TotalNoofSolidElements} \left(\exp\left(-V_i \left(\frac{\sigma_i}{\sigma_o} \right)^m \right) \right)$$
$$= \exp\left(\sum_{i=1}^{TotalNoofSolidElements} -V_i \left(\frac{\sigma_i}{\sigma_o} \right)^m \right) \qquad (4.2.2\text{-}2)$$

Using the assumption of the equal probability of survival at the failure load for the fibres in a laminate and in a unit volume material, we have:

$$S_{laminate}(\sigma) = S_{unit}(\sigma) \Rightarrow$$
$$\exp\left(\sum_{i=1}^{TotalNoofSolidElements} -V_i \left(\frac{\sigma_i}{\sigma_o} \right)^m \right) = \exp\left(-\left(\frac{\sigma_{unit}}{\sigma_o} \right)^m \right) \Rightarrow$$
$$\sum_{i=1}^{TotalNoofSolidElements} V_i \left(\frac{\sigma_i}{\sigma_{unit}} \right)^m = 1 \qquad (4.2.2\text{-}3)$$

where σ_{unit} is the unidirectional failure stress of a unit volume of material.

When the probability of survival of the fibres in a laminate satisfies the following equation (4.2.2-4), tensile failure of fibres occurs within the laminate.

$$S_{laminate}(\sigma) \le S_{unit}(\sigma) \Rightarrow$$
$$\exp\left(\sum_{i=1}^{TotalNoofSolidElements} -V_i \left(\frac{\sigma_i}{\sigma_o} \right)^m \right) \le \exp\left(-\left(\frac{\sigma_{unit}}{\sigma_o} \right)^m \right) \Rightarrow$$
$$\sum_{i=1}^{TotalNoofSolidElements} V_i \left(\frac{\sigma_i}{\sigma_{unit}} \right)^m \ge 1 \qquad (4.2.2\text{-}4)$$

The criterion in Equation 4.2.2-4 has been successfully applied in a post-processing approach by the Scaling Effects in Notched Composites (SINCS) project in University of Bristol to predict fibre tensile failure in open hole tension tests[194]. The post-processing approach only extracts elemental tensile stresses and volumes in 0 plies of a laminate from the derived model results and performs Weibull integrations. In this thesis, this criterion was also used to predict the initiation of fibre tensile failure within a laminate, but the Weibull integration was performed on all plies of the laminate and in every time step of the simulation to give more accurate predictions.

5. Unlike the weakest-link theory or other parallel and sequential multi-step failure models which usually assume that the whole specimen or lamina fails after the critical failure probability is satisfied, it is assumed in this Chapter that only the element with the maximum longitudinal tensile stress fails when the equation (4.2.2-4) was satisfied. The

failed element is removed from the laminate model and the load is automatically redistributed to other remaining elements by the FEA program. With the load continuing, stresses keep accumulating in the fibres till the equation (4.2.2-4) is satisfied again, then further elements with the maximum longitudinal tensile stresses are removed.

In this way, the fibre dominated element failure in a laminate is progressive and arbitrary configurations of fibre tensile failure are analyzed without use of idealized load sharing rules.

4.2.3 Implementation of Statistical Fibre dominated element failure Formulation in Composite Laminates

The implementation of the statistical fibre tensile failure formulation in composite laminates involves four major steps:

1. Stress update in a laminate before fibre failure.
2. Weibull integration as shown in equation (4.2.2-4) through the whole specimen.
3. Finding the maximum elemental tensile stress in the fibre direction.
4. Stress update after failed elements are removed from the model

Stress update before fibre failure and after failed elements are removed from the model follows equations (4.2.1-5), (4.2.1-7) and (4.2.1-8). This is implemented in user defined material (Umat44) subroutines. The explanation of the material input card for Umat44 is covered in Appendix A-3. Within the user material, the nodal displacements and the strains are known, the stress tensors are updated as below:

$$\begin{bmatrix}\sigma_1\\ \sigma_2\\ \sigma_3\end{bmatrix} == \begin{bmatrix}C_{11} & C_{12} & C_{13}\\ C_{21} & C_{22} & C_{23}\\ C_{31} & C_{32} & C_{33}\end{bmatrix}\begin{bmatrix}\varepsilon_{1-total}-\alpha_1\Delta T\\ \varepsilon_{2-total}-\alpha_2\Delta T\\ \varepsilon_{3-total}-\alpha_3\Delta T\end{bmatrix} \qquad (4.2.3\text{-}1)$$

$$\tau_{12} = a_2\varepsilon_{12}^2+a_1\varepsilon_{12}+a_0$$

$$\tau_{23} = b_2\varepsilon_{23}^2+b_1\varepsilon_{23}+b_0 \qquad (4.2.3\text{-}2)$$

$$\tau_{31} = c_2\varepsilon_{31}^2+c_1\varepsilon_{31}+c_0$$

The Weibull integration and finding the maximum elemental stress have to be conducted in the major subroutine 'urmathn' of LS-Dyna for solid elements. The subroutine 'urmathn'

is mainly used to convert elemental deformation and strains from global coordinates system to local material coordinate system and transform the updated stresses by user defined material subroutines from local material coordinate systems back to the global system. This subroutine itself does not include any loop to go through all elements in a specimen so that the Weibull integration of all elements could be fulfilled conveniently. There is however a parameter for 'time' in 'urmathn'. In each time step when stresses of all elements in a model are updated, the value of this 'time' parameter is updated to the new current time. Thus, codes summing up all elemental Weibull terms $V_i\left(\frac{\sigma_i}{\sigma_{unit}}\right)^m$ and finding the maximum elemental stress are put in 'urmathn'. By tracking the change of this 'time' parameter, the Weibull integration and finding the maximum elemental stress within the whole model for each timestep could be realized.

To get the value of elemental volume, a small subroutine 'elemvolume' was put in the code as well. The algorithm of 'elemvolume' is described below:
For an arbitrary octahedron ABCDA^{1}B^{1}C^{1}D^1 as shown in Fig 4.2.3-1, its volume is a sum of three tetrahedrons: ABCDA^1, BCC^{1}B^{1}A^1 and DCC^{1}D^{1}A^1.

Volumes of the three tetrahedrons are:

$$V_{ABCDA^1}=\left(\frac{1}{2}\overrightarrow{AC}\times\overrightarrow{BD}\right)\bullet\frac{1}{3}\overrightarrow{AA^1}$$

$$V_{BCC^1B^1A^1}=\left(\frac{1}{2}\overrightarrow{BC^1}\times\overrightarrow{CB^1}\right)\bullet\frac{1}{3}\overrightarrow{B^1A^1}$$

$$V_{DCC^1D^1A^1}=\left(\frac{1}{2}\overrightarrow{DC^1}\times\overrightarrow{CD^1}\right)\bullet\frac{1}{3}\overrightarrow{D^1A^1}$$

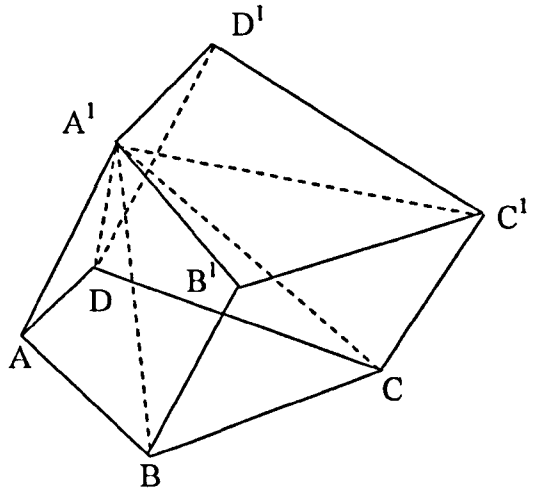

Fig 4.2.3-1 Elemental geometry

Nodal coordinates of ABCDA^{1}B^{1}C^{1}D^{1}ABCDABCD are given in the user material, then $\overrightarrow{AC},\overrightarrow{BD},\overrightarrow{AA^1},\overrightarrow{BC^1},\overrightarrow{CB^1},\overrightarrow{B^1A^1},\overrightarrow{DC^1},\overrightarrow{CD^1},\overrightarrow{D^1A^1}$ can be obtained. The elemental volume $V_{ABCDA^1B^1C^1D^1}$ is calculated using the following equations(4.2.3-3), (4.2.3-4),(4.2.3-5) and (4.2.3-6):

$$V_{ABCDA^1} = \frac{1}{6}\begin{bmatrix} x_{AC} \\ y_{AC} \\ z_{AC} \end{bmatrix} \times \begin{bmatrix} x_{BD} \\ y_{BD} \\ z_{BD} \end{bmatrix} \bullet \begin{bmatrix} x_{AA^1} \\ y_{AA^1} \\ z_{AA^1} \end{bmatrix} = \frac{1}{6}\begin{bmatrix} y_{AC}z_{BD} - y_{BD}z_{AC} \\ x_{BD}z_{AC} - x_{AC}z_{BD} \\ x_{AC}y_{BD} - x_{BD}y_{AC} \end{bmatrix} \bullet \begin{bmatrix} x_{AA^1} \\ y_{AA^1} \\ z_{AA^1} \end{bmatrix} \quad (4.2.3\text{-}3)$$

$$= \frac{1}{6}\left[x_{AA^1}(y_{AC}z_{BD} - y_{BD}z_{AC}) + y_{AA^1}(x_{BD}z_{AC} - x_{AC}z_{BD}) + z_{AA^1}(x_{AC}y_{BD} - x_{BD}y_{AC})\right]$$

$$V_{BCC^1B^1A^1} \quad (4.2.3\text{-}4)$$

$$= \frac{1}{6}\left[x_{B^1A^1}(y_{BC^1}z_{CB^1} - y_{CB^1}z_{BC^1}) + y_{B^1A^1}(x_{CB^1}z_{BC^1} - x_{BC^1}z_{CB^1}) + z_{B^1A^1}(x_{BC^1}y_{CB^1} - x_{CB^1}y_{BC^1})\right]$$

$$V_{BCC^1D^1A^1} \quad (4.2.3\text{-}5)$$

$$= \frac{1}{6}\left[x_{D^1A^1}(y_{DC^1}z_{CD^1} - y_{CD^1}z_{DC^1}) + y_{D^1A^1}(x_{CD^1}z_{DC^1} - x_{DC^1}z_{CD^1}) + z_{D^1A^1}(x_{DC^1}y_{CD^1} - x_{CD^1}y_{DC^1})\right]$$

$$V_{ABCDA^1B^1C^1D^1} = V_{ABCDA^1} + V_{BCC^1B^1A^1} + V_{DCC^1D^1A^1} \quad (4.2.3\text{-}6)$$

The flowchart of implementing the statistical fibre dominated element failure formulations in a laminate is illustrated in Fig 4.2.3-2.

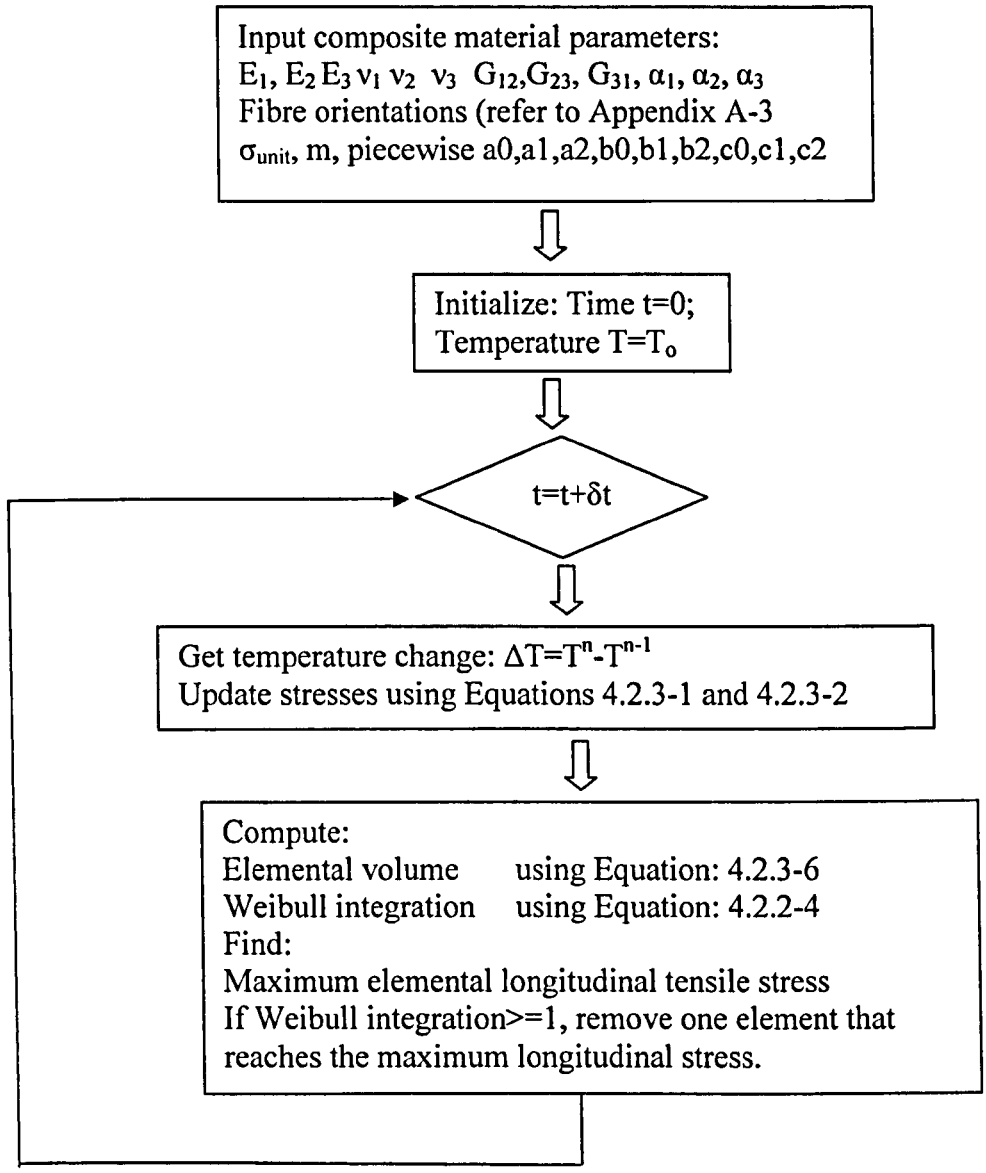

Fig 4.2.3-2 Flowchart for implementing statistical fibre dominated element failure formulations in LS-Dyna

4.3 Validation of the Statistical Fibre dominated element failure Formulation

The validation of the statistic fibre dominated element failure formulation includes the thermal elastic behavior before fibre failure, nonlinear shear behaviour, Weibull integration and finding the maximum elemental stress in the laminate.

4.3.1 Thermal Elastic Behaviour before Fibre Failure

The thermal elastic behaviour of user material (Umat44) is compared with that of *MAT_ORTHOTROPIC_THERMAL (MAT_21) available within LS-DYNA. Two unit cells with one using MAT_21 and another using Umat44 are modeled for the comparison, refer to Fig 4.3`.1-1.

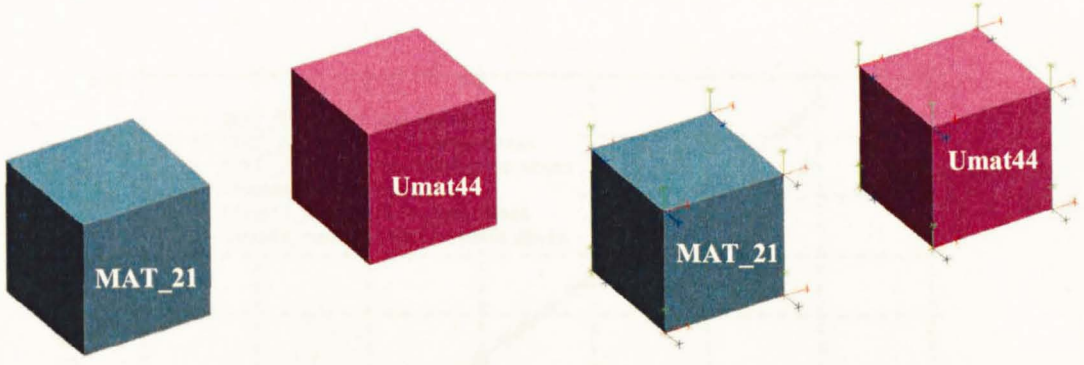

(a) no boundary constraint (b) boundary constrained in x, y, z directions.

Fig 4.3.1-1 Unit Cells for comparison of MAT_21 and Umat44

In Fig 4.3.1-1(a), there is no boundary constraint being applied on the two unit cells. In Fig 4.3.1-1(b), the eight nodes of the unit cells are constrained in the x, y and z directions. When a thermal load with temperature decreasing at a rate of -50°C/ms was applied, unit cells in Fig 4.3.1-1(a) are expected to shrink freely, while in Fig 4.3.1-1(b) thermal stresses would arise.

Fig 4.3.1-2 gives the responses of two unit cells under boundary conditions (a) and (b) when the temperature decreased by 80°C. Fig 4.3.1-3 shows the progressive thermal stresses within unit cells when boundary constraint was applied and temperature decreased.

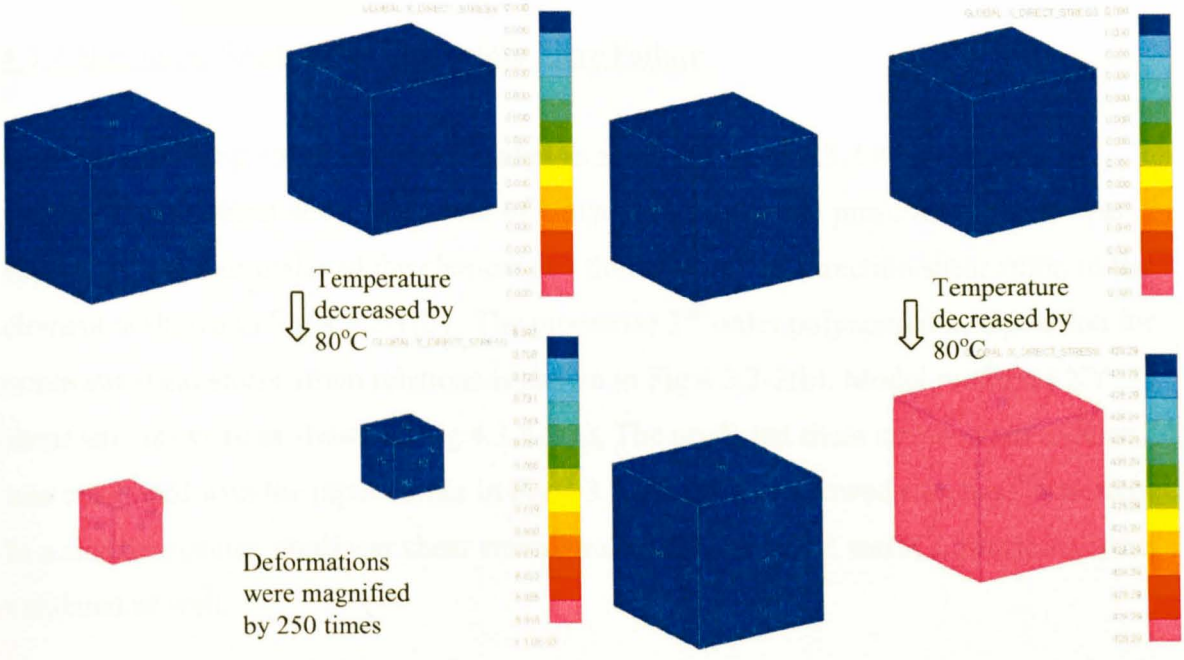

(a) no boundary constraint (b) boundary constrained in x, y, z directions.

Fig 4.3.1-2 Thermal responses of Unit Cells under different boundary conditions

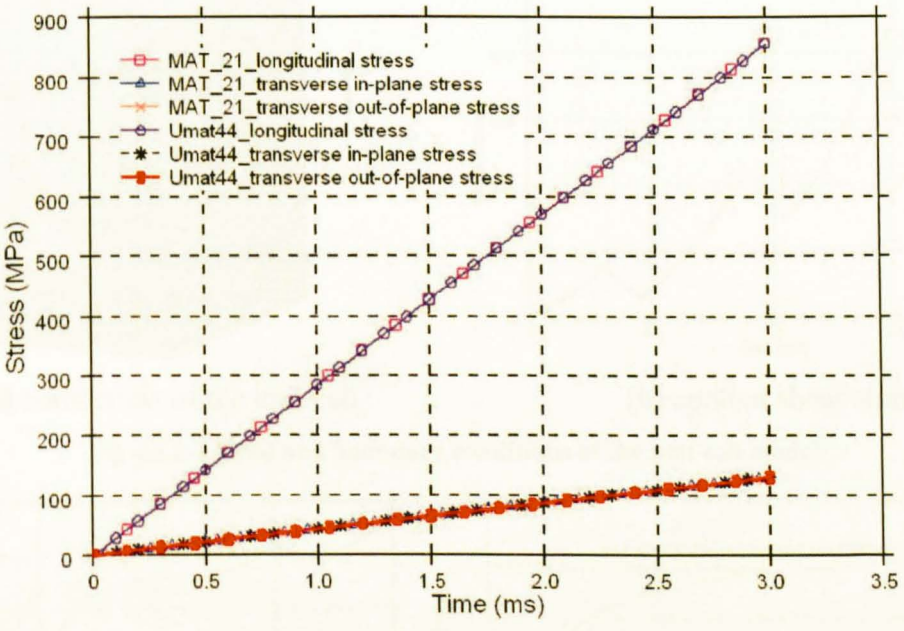

Fig 4.3.1-3 Stress-time curves for unit cells with boundary condition (b)

It can be seen that thermal responses of MAT_21 and Umat44 are the same in the unit cells. The thermal elastic behaviour implemented in Umat44 proved to be effective.

4.3.2 Non-linear Shear Behaviour before Fibre Failure

One unit cell being constrained and loaded as show in Figure 4.3.2-1(a) was used to validate the nonlinear shear behaviour of Umat44. A multi-path prescribed motion was applied on the four nodes of the element and the induced XY direction shear strain in the element is shown in Fig 4.3.2-1(b). The piecewise 2nd order polynomial interpolation for nonlinear shear stress-strain relations is shown in Fig 4.3.2-2(b). Model predicted XY shear stresses were as shown in Fig 4.3.2-2(a). The predicted shear stress-strain relation was compared with the input values in Fig 4.3.2-2(b), which showed excellent consistency. In a similar manner, nonlinear shear stress-strain relations in YZ and XZ directions were validated as well.

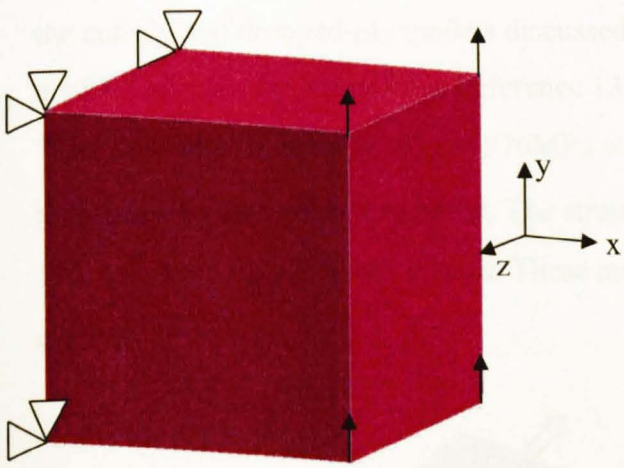

(a) load and constraints of the unit cell

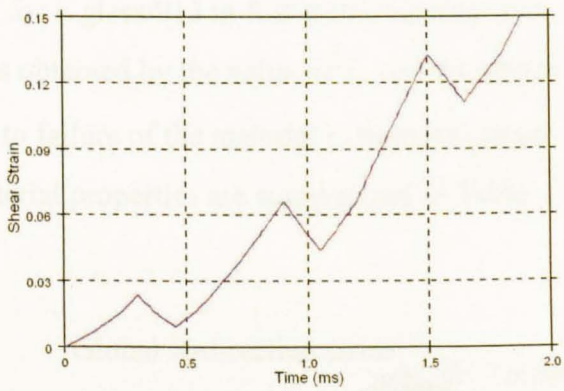

(b) applied shear strain

Fig 4.3.2-1 Load and boundary conditions of the unit cell model

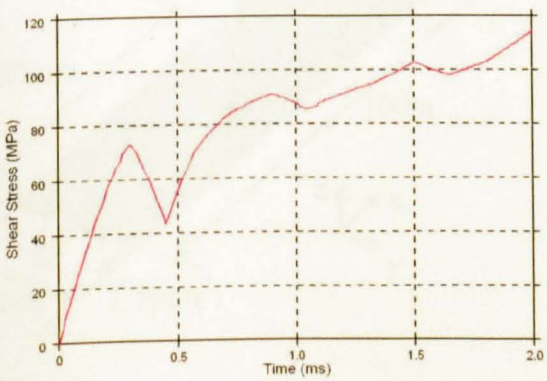

(a) Shear Stress

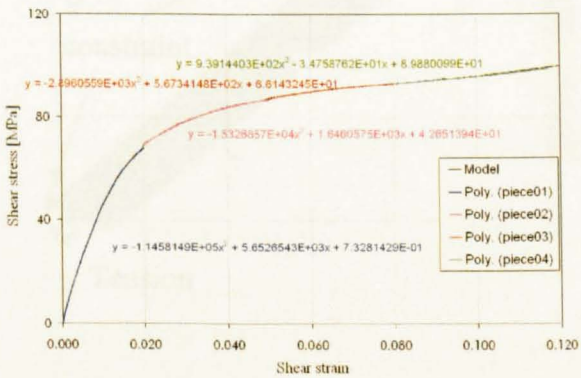

(b) piecewise stress-strain relation and model result

Fig 4.3.2-2 Elemental shear stress and the relation with shear strain

4.3.3 Weibull Integration and Finding the Maximum Elemental Stress

A tensile test on a unidirectional Ciba E glass/913 double edge-notched specimen with dimensions shown in Fig 4.3.3-1(a) was modeled to verify the algorithm of Weibull integration and finding the maximum elemental longitudinal stress in specimens. Due to symmetry of the specimen, a half model with boundary and load conditions as shown in Fig 4.3.3-1(b) was used. The mesh has 3 elements in the thickness (z) direction and 4788 eight-node solid elements in total for the half specimen. Although this is not a particularly realistic case since severe splitting (which is not modeled) would blunt the notch, it represents a suitable numerical example for verification of the numerical model.

Material elastic properties of E glass/913 are the same values as those for E glass/913 in the cut-ply and dropped-ply models discussed in Section 4.6. The Weibull modulus m=29.3 adopted the value from Reference 135 for E glass/913 in four point bending tests. The characteristic strength σ_{unit}=1976MPa was obtained by the value of E_1 and the strain to failure of a unit volume material. The strain to failure of the material is from reference 135 too, here $\varepsilon_{unit} = 0.045$ is used. These material properties are summarized in Table 4.3.3-1.

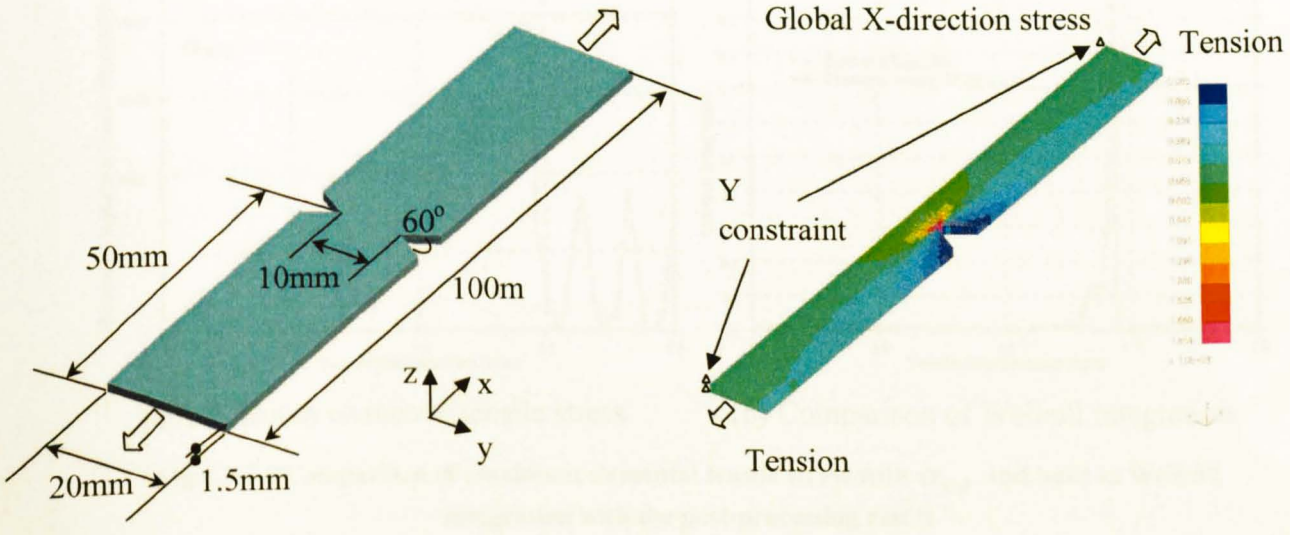

(a)geometry of double edge notched specimen (b) half model of the specimen

Fig 4.3.3-1 Geometry of the double edge notched specimen and the half model for this specimen

Table 4.3.3-1 Material Properties of E glass/913

E_{11} (GPa)	E_{22} (GPa)	ν_{21}	ν_{32}	G_{12} (GPa)	G_{23} (GPa)	m	σ_{unit} (MPa)
43.9	15.4	0.1052	0.3	4.34	2.75	29.3	1976

There was no damping and hourglass control in the model and a tension rate of 1000mm/s was applied. The longitudinal stress distribution in the model right before fibre failure is shown in Fig 4.3.3-1(b). Fig 4.3.3-2 gives views of how fibre breakage progresses from the notch tip: (a) right before fibre breakage (b)fibres started to break, and (c) fibre breakage developed through the middle section of the specimen.

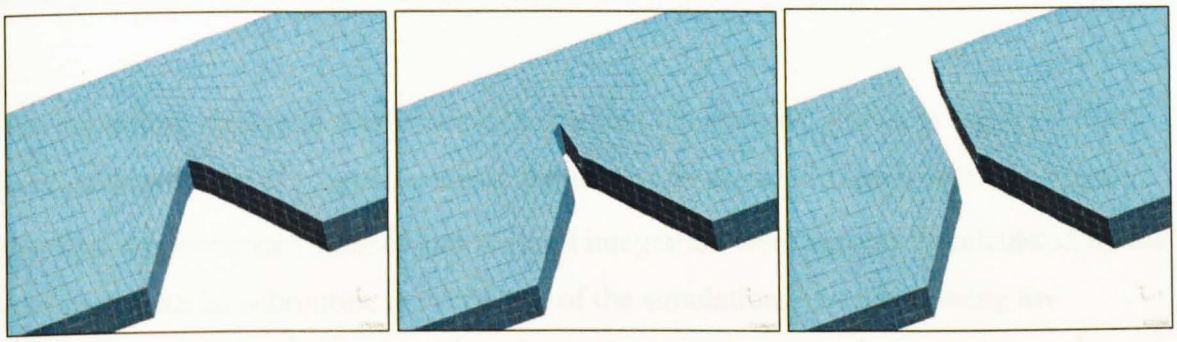

(a) (b) (c)

Fig 4.3.3-2 Progressive fibre breakage at the notch

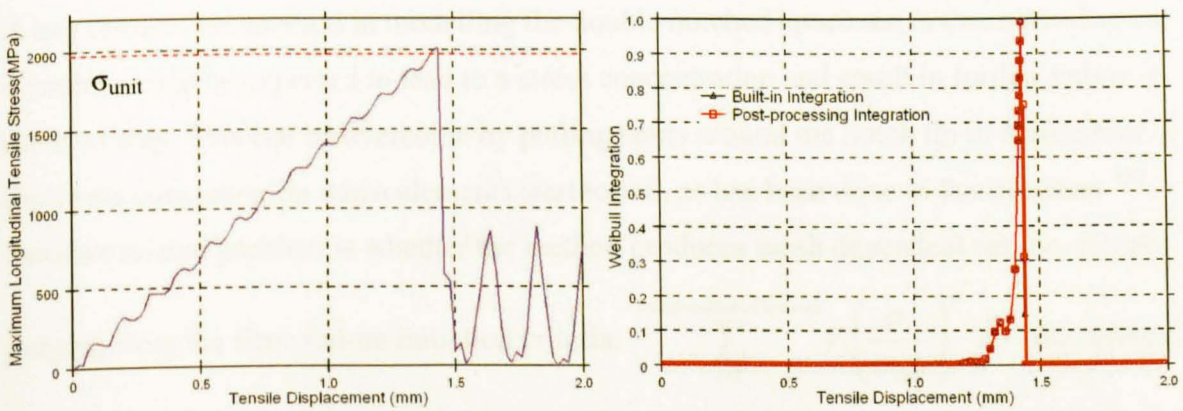

(a) maximum elemental tensile stress (b) Comparison of Weibull integration

Fig 4.3.3-3 Comparison of maximum elemental tensile stress with σ_{unit} and built-in Weibull integration with the post-processing result

The Weibull integration in equation 4.2.2-4 and maximum elemental longitudinal tensile stress in each time step were stored in historic variables. After finishing the simulation, a post-processing program was used to extract elemental tensile stresses and volumes from

the derived results and perform Weibull integrations again as has been done in the published work[195]. This post-processing Weibull integration was considered to be accurate and was compared with the stored Weibull integration history variable (comparatively called built-in Weibull integration here) in Fig 4.3.3-3(b). It is noticed that the Weibull integration in Fig 4.3.3-3(b) reached around 0.9914<1.0 when elements started to be removed, this is because the output data intervals are much larger than the actual time step in the simulation and could not catch the exact time when the Weibull integration reached 1.0. The maximum Weibull integration value 0.9914 for equation 4.2.2-4 here was an average result of those at several time steps around the fibre failure.

The maximum elemental tensile stress throughout the analysis, shown in Fig 4.3.3-3(a), was compared with σ_{unit} and the stress distribution in the whole specimen. This shows that both the maximum stresses and Weibull integration were accurately calculated by the new user material subroutine in every step of the simulation, hence validating the algorithm in Section 4.2.3.

A key issue of the method in modelling the double notched specimen is that removing an element would be expected to lead to a stress concentration and result in further failure in the next step. This can be overcome by putting splits around the notch tip to redistribute the stress concentration when elements start to fail, as has been done in the literature [196]. Another related problem is whether the method produces mesh dependent results. Simply judging from the fibre failure initiation criteria: $\sum_{i=1}^{TotalNoofSolidElements} V_i\left(\frac{\sigma_i}{\sigma_{unit}}\right)^m \geq 1$, the refined mesh would increase the stress concentration but decrease the elemental volume of the maximum stress, thus the result from this statistic approach is expected to be less mesh-dependant than that from the stress-based failure model. The extent of mesh dependency using this method is also largely related with the specific loading conditions. In this section the double edge notched specimen was modeled mainly for testing the algorithms in Umat44 and not compared with experimental results. The following two sections provide the comparison of model prediction with experimental results on open-hole tests and four

point bending tests respectively. The technique to use interface elements to reduce the stress concentration from removed elements were applied in these two sections and the mesh dependency of this approach was discussed in modelling the four point bending tests.

4.4 Modelling Open Hole Tension Tests

To understand the effect of scaling on the tensile behaviour of notched composites, a series of open-hole experiments have been done in ACCIS at the University of Bristol on carbon fibre/epoxy laminates with a quasi-isotropic lay-up, varying both the hole diameter and ply and laminate thickness (while keeping constant hole diameter to specimen width and length ratios)[197]. It was observed that both strength and failure mechanisms of the open-hole laminates varied with lay-up configurations. The modelling of these open hole tests has been done in Jiang et al's work [194,195], but used embedded material formulation (Mat 21 in LS-Dyna) and fully integrated solid elements(Solid Type 2 in LS-Dyna) for the laminates and post-processing Weibull integration to catch the fibre failure stresses. The major limitation of Jiangs et al's post-processing method to obtain the fibre failure stress is that the interaction between splitting, delamination and fibre failure cannot be predicted. Especially when fibre failure is progressive instead of being catastrophic, Jiang et al's post-processing method is not able to predict the propagation of fibre breakage and its interaction with splitting and delamination. As a further validation of the material formulation and the built-in Weibull integration in section 4.2.3, six of the tests on different lay-ups were selected to be modeled again in this section using interface elements and sold elements implementing Umat44. With the embedded progressive fibre failure formulation, all the models not only predicted similar failure stresses as Jiang et al's work[195] but also gave the final failure modes of the specimens, which are compatible with experimental results from Reference 209.

4.4.1 Experimental Setup

The experimental details are presented fully by Green et al in reference 209. Key details are recounted here for comparison to the numerical results generated. The material used was IM7/8552, a unidirectional (UD) carbon fibre-epoxy pre-preg system, supplied by Hexcel. The nominal ply thickness is 0.125mm, while the properties of IM7/8552 as required are given on the Hexcel website[198] and are presented in Table 4.4.1-1.

The specimen design is shown in plan form in Fig 4.4.1-1. It consists of a parallel sided gauge section of constant cross-sectional area, with width w, thickness t and length l, and a centrally located hole of diameter D. At either end of the gauge section is a gripping

region. The specimen gauge length has constant ratios of w/D=5 and l/D=20 for all specimen sizes.

Table 4.4.1-1 IM7/8552 properties

0° Tensile Modulus (GPa)	90° Tensile Modulus (GPa)	Tensile Strength (MPa)	OHT Strength (MPa)
161	11.4	2780	419

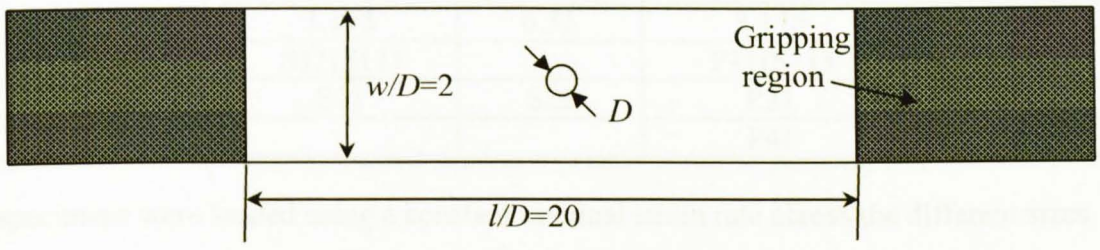

Fig 4.4.1-1 Specimen dimensions

For a balanced, symmetric, quasi-isotropic lay-up to be achieved from UD plies oriented at 0°, $\pm 45^{\circ}$ and 90°, the minimum number of plies required is eight and the chosen stacking sequence is $[45/90/-45/0]_s$. Therefore the minimum thickness being tested was 1mm, with other thickness being scaled accordingly. The minimum hole diameter used is 3.175mm.

Two different methods were used to increase the thickness of the specimens: sublaminate and ply-level scaling. For the sublaminate level scaling, laminate thickness was increased by increasing the number of repeated ply stacks [45/90/-45/0], refer to Fig 4.4.1-2(a). The ply-level scaling was to increase laminate thickness by blocking multiple plies with the same orientation as shown in Fig 4.4.1-2(b).

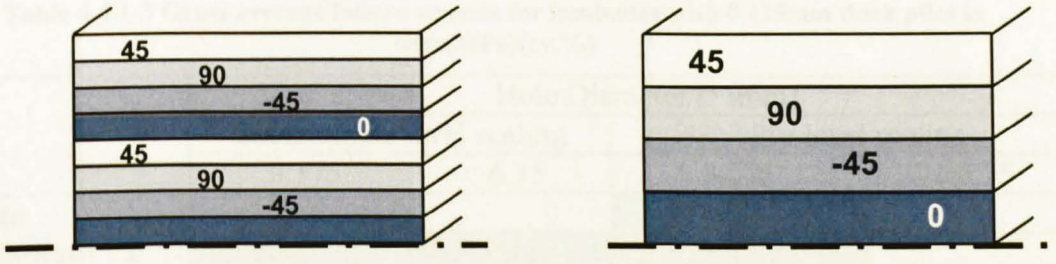

Fig 4.4.1-2 Schematic (a)sublaminate level scaled and (b) ply-level scaled laminates

The thickness scaling factor n=1,2 and 4 is the number of repeated [45/90/-45/0] blocks for sublaminate level scaled laminates and the number of blocked plies with the same

orientation for ply level scaled specimen. This scaling factor also corresponds to the laminate thickness of 1mm, 2mm and 4mm. The testing matrix and nomenclature convention used for the modelling work in this Section are shown in Table 4.4.1-2.

Table 4.4.1-2 Sublaminate-level and ply-level scaling testing matrix, and nomenclature convention of sample size

		Hole Diameter D (mm)			
		Sublaminate level scaling		Ply-level scaling	
		3.175	6.35	3.175	6.35
Laminate thickness(mm)	1	S11(P11)		P11(S11)	
	2	S21	S22	P21	
	4			P41	P42

The specimens were loaded using a constant nominal strain rate across the different sizes. The displacement rate for the baseline gauge length of 64mm(with the hole diameter 3.175mm) was 0.5mm/min. This rate was scaled accordingly for other length of the specimen, i.e., 1.0mm/min for a gauge length of 128mm and 2.0mm/min for 256mm.

The failure load F_x was taken as being the first significant (greater than 5%) load drop on the load-displacement curve, which corresponded to either fibre failure or extensive delamination throughout the gauge section. The failure strength σ_x was obtained by dividing the failure load with the gross cross-sectional area of the specimen:

$$\sigma_x = \frac{F_x}{wt} \qquad (4.4.1\text{-}1)$$

Table 4.4.1-3 shows the experimental strength results and dominant failure modes from Reference 210 for the laminates listed in Table 4.4.1-2.

Table 4.4.1-3 Gross average failure stresses for laminates with 0.125mm thick plies in tests(MPa)(cv,%)

		Hole Diameter D (mm)			
		Sublaminate level scaling		Ply-level scaling	
		3.175	6.35	3.175	6.35
Laminate thickness(mm)	1	570(7.7)		570(7.7)	
	2	500(4.0)	438(2.4)	396(5.2)	
	4			275(5.6)	285(5.2)

Fibre breakage Delamination

4.4.2 Model Setup and Simulation Results

For the convenience of comparison, meshes developed by Jiang in Reference 194 were adopted to model the failure of the above laminates. To reduce the model size, only the gauge length was modeled. For the symmetry of the lay-ups, half the thickness of the laminates was modeled and plane symmetric boundary conditions on the mid-plane of the laminates were applied. Small areas at the hole boundary were removed (refer to Fig 4.4.2-1) to avoid degenerated elements which led to very small time steps in explicit analyses. This did not significantly affect the results as the splits which formed early on in the loading caused notch blunting and reduced the local stress concentration.

Discrete beam interface elements were generated between all adjacent plies where delamination was expected. Interface elements were also used to model the splitting between fibres within a ply and located at the sites where splits were found to occur in the tested samples, see Fig 4.4.2-1. In-plane meshes as shown in Fig 4.4.2-2 were used for all models in this Section. In the thickness direction, one solid element was used for each ply, i.e., in sublaminate level scaled models, the element thickness is uniformly 0.125mm and in ply-level scaled samples, element thickness is 0.25mm for P21 and 0.5mm for P41 and P42 models. Meshes in the thickness direction for different models are shown in Fig 4.4.2-3.

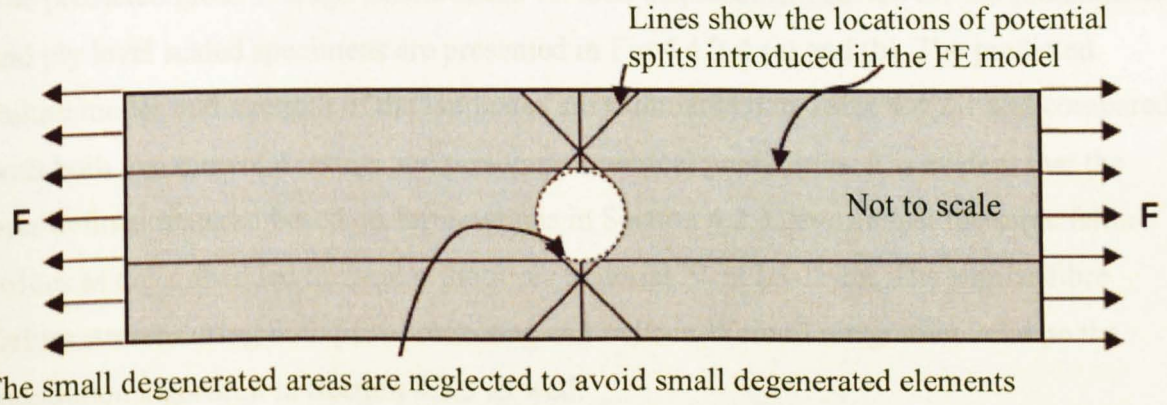

The small degenerated areas are neglected to avoid small degenerated elements

Fig 4.4.2-1 The typical failure mode of tested sample and simplified geometry of sample modelled

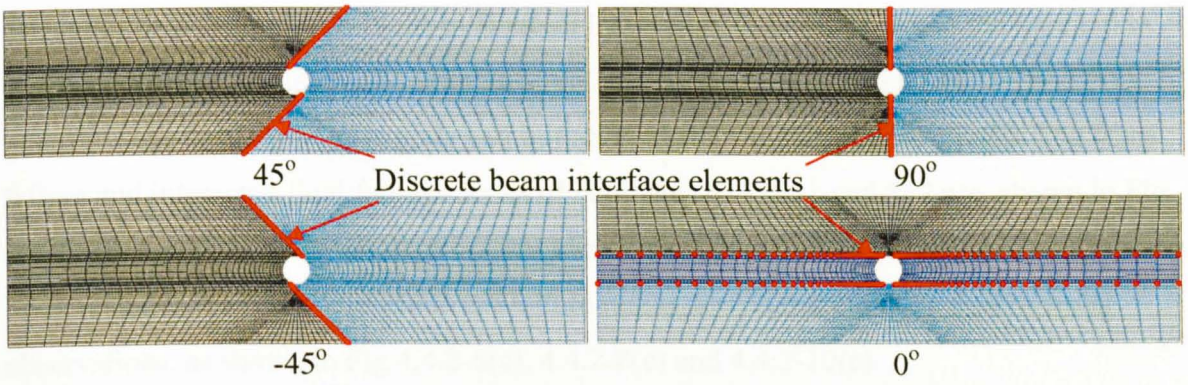

Fig 4.4.2-2 In-plane meshes applied in all models

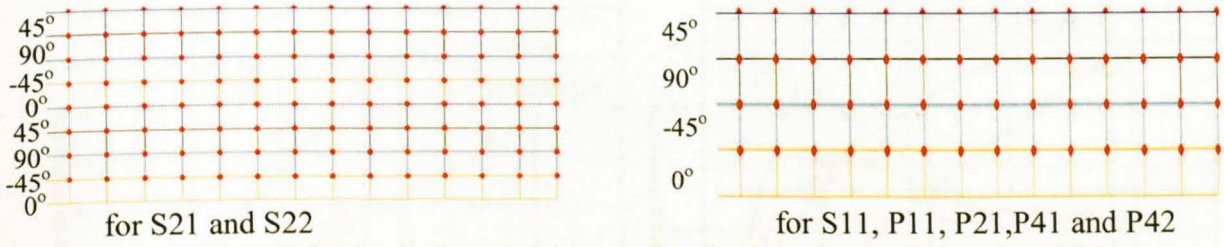

Fig 4.4.2-3 Meshes in through thickness direction in various models (not to scale)

In all models, a thermal load with temperature decreasing from 180°C to 20°C was applied first, then a pair of prescribed motions with constant rate of 317.5mm/s was applied on the two ends of the S11, S21, P21 and P41 specimens. For S22 and P42 specimens, this rate was 635mm/s.

A global damping factor of 1.0 was applied in all the models. Type 5 hourglass control was used (Flanagan-Belytschko stiffness form with exact volume integration for solid elements) with a co-efficient of 0.1 (default value). The default values of 1.5 and 0.06 were used for the quadratic and linear bulk viscosity co-efficients respectively. Values of these parameters are the same as those from previous analyses [194,195,200].

The predicted gross average tensile stress vs. load displacement curves for the sublaminate and ply level scaled specimens are presented in Fig 4.4.2-4 (a) and (b). The predicted failure modes and strength of the laminates are summarized in Table 4.4.2-1 and compared with both experimental results and previous numerical predictions. It is evident that the user defined material based on formulations in Section 4.2.3 gave almost the same failure values as the embedded thermal orthotropic material 21 in LS-Dyna. The similar fibre failure stresses using both post-processing and built-in Weibull integration validate the integration algorithm in Section 4.2.3 as well.

The additional advantage of built-in Weibull integration in Umat44 is that the interaction of fibre failure and delamination can be simulated, while in references 194,195 and 200 only the delamination failure mode and initiation of fibre failure can be caught. The fibre failure and interacted final failure modes of laminates S11, S21 and S22 are shown in Fig 4.4.2-5 to 4.4.2-10, in which fibre breakage in 0° plies dominated the failure in sublaminate level scaled laminates.These predicted failure modes are consistent with experimental observations, as shown in Fig 4.4.2-6(c), 4.4.2-8(c) and 4.4.2-10(c).

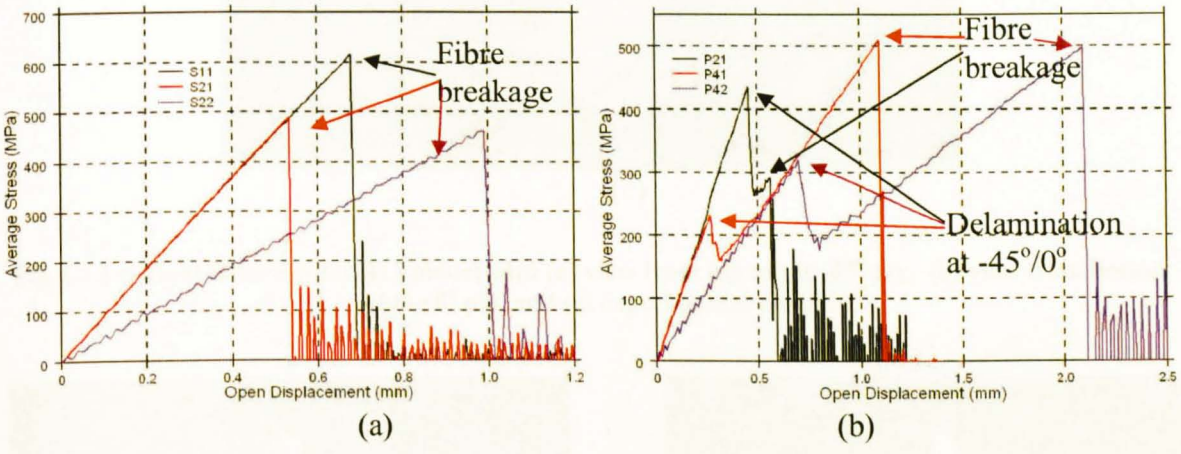

Fig 4.4.2-4 Predicted average tensile stress-load displacement curves for sublaminate and ply level scaled specimens

Table 4.4.2-1 Gross average failure stresses for laminates with 0.125mm thick plies in models and comparison with results from tests and previous analysis (in bold, from reference 194)(MPa)(diff,%)

		Hole Diameter D (mm)			
		Sublaminate level scaling		Ply-level scaling	
		3.175	6.35	3.175	6.35
Laminate thickness (mm)	1	605(6.1) **610(-0.8)**		605(6.1) **610(-0.8)**	
	2	486(2.8) **498(-2.4)**	460(5.0) **460(0.0)**	435(9.8) **434(0.2)**	
	4			239(13.1) **239(0.0)**	301(5.6) **301(0.0)**

Values in bold are predictions from Reference 200

Fig 4.4.2-5 Fibre breakage initiation (a) and final failure (b) in 0° ply of S11 laminate, interface elements were put beteen parts with diffierent colors

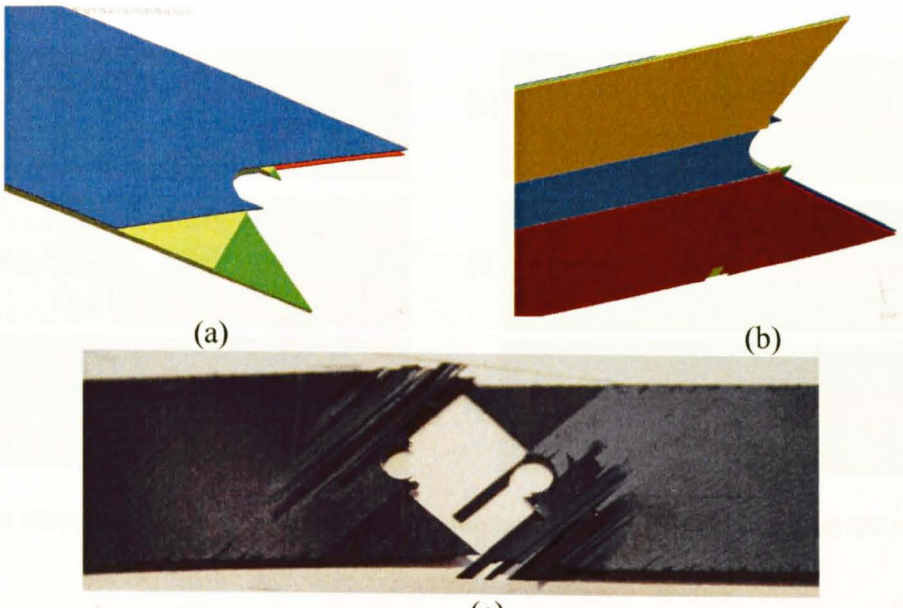

Fig 4.4.2-6 Final failure of the S11 model with (a) view from top of the 45° ply, (b) view from bottom of the 0° ply, and (c) experimental result

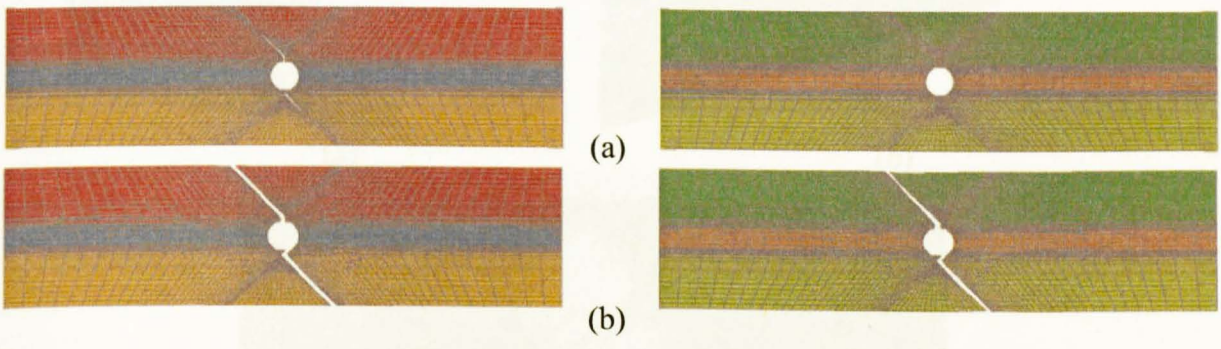

Fig 4.4.2-7 Fibre breakage initiation (a) and final failure (b) in 0° plies of S21 laminate

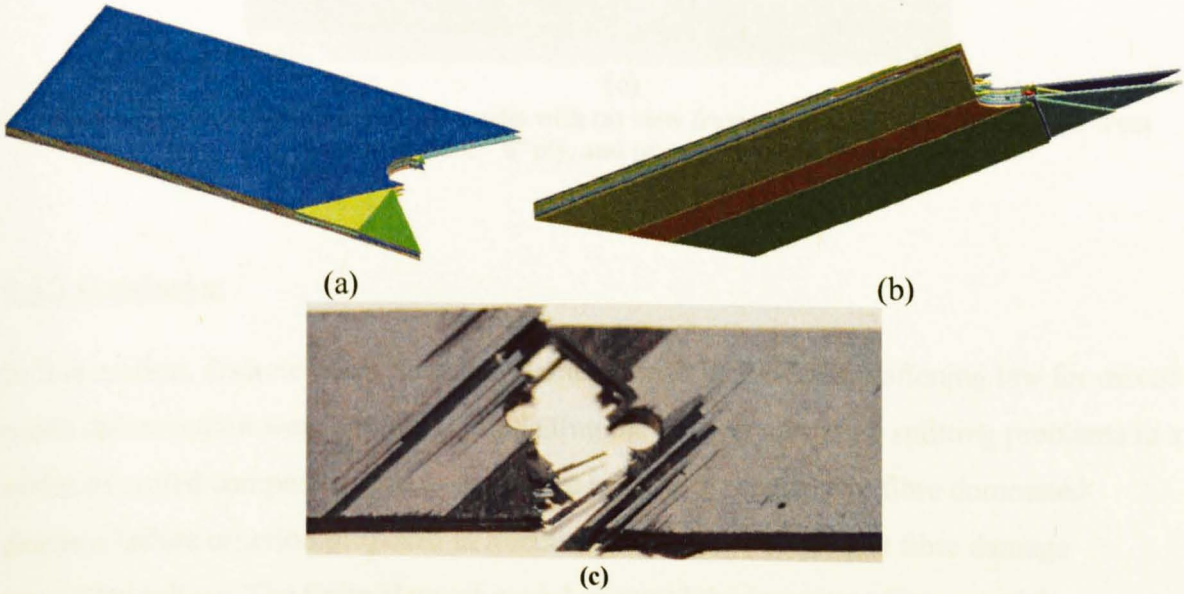

Fig 4.4.2-8 Final failure of the S21 model with (a) view from top of the 1st 45° ply, (b) view from bottom of the 2nd 0° ply, and (c) experimental result

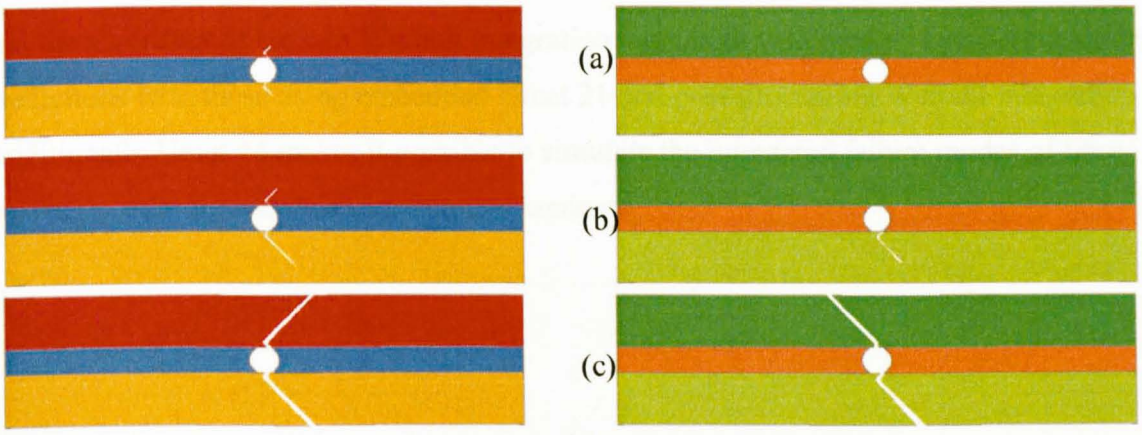

Fig 4.4.2-9 Fibre breakage initiation (a),progressing into the 2nd 0° ply (b) and final failure (c) in 0° plies of S22 laminate

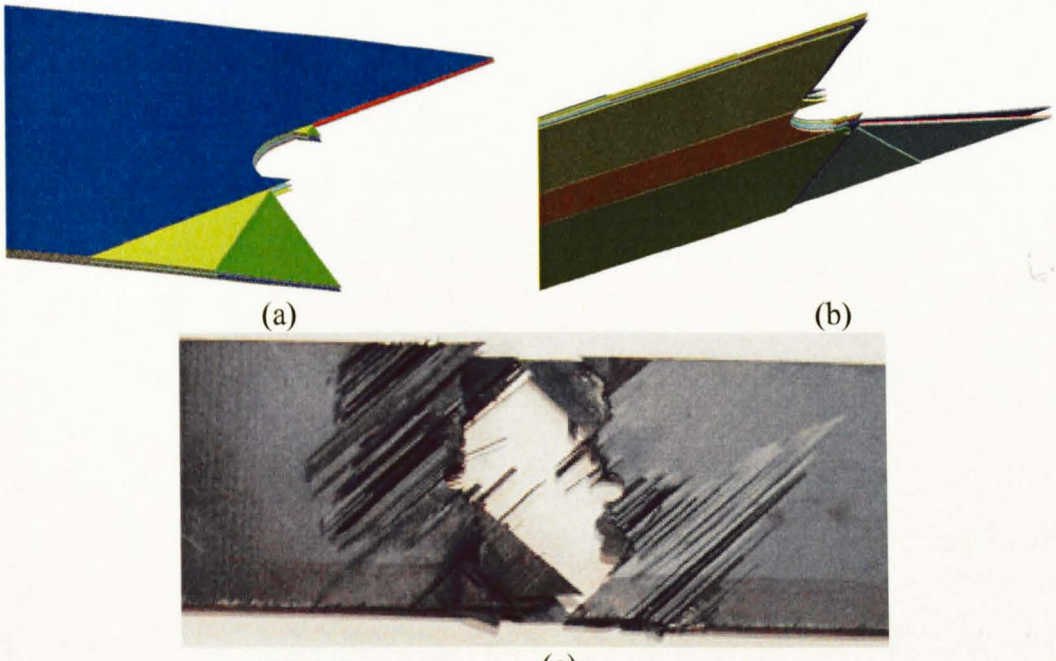

Fig 4.4.2-10 Final failure of the S22 model with (a) view from top of the 1st 45° ply, (b) view from bottom of the 2nd 0° ply, and (c) experimental result

4.4.3 Conclusion

In this section, discrete beam interface elements with the bi-linear softening law for mixed mode delamination were applied in modelling the delamination and splitting problems in a series of scaled composite open hole tension tests. The progressive fibre dominated element failure criterion proposed in Section 4.2 was used to predict fibre damage controlled failure. The finite element model captured the important features of the progressive delamination and splitting processes involved and good agreement was

obtained for delamination stress predictions. Fibre breakage in the sublaminate level scaled specimens could be well-predicted as well. The formulation of user defined material 44 and the algorithm of built-in Weibull integration were both validated by comparing model predictions with those using embedded Umat 21 and post-processing Weibull integration. Additionally Umat 44 makes it possible to simulate the interacted failure modes of fibre breakage, splitting and delamination in a laminate.

4.5 Modelling Four-point Bending Tests

4.5.1 Four-point Bending Test Setup

The modelling of four-point bending tests in this section was based on the experimental work published in reference 199. Three sets of tests were carried out on 16ply, 32ply and 64ply unidirectional glass/epoxy specimens. The testing configuration for the smallest 16ply specimen is shown in Fig 4.5.1- 1.

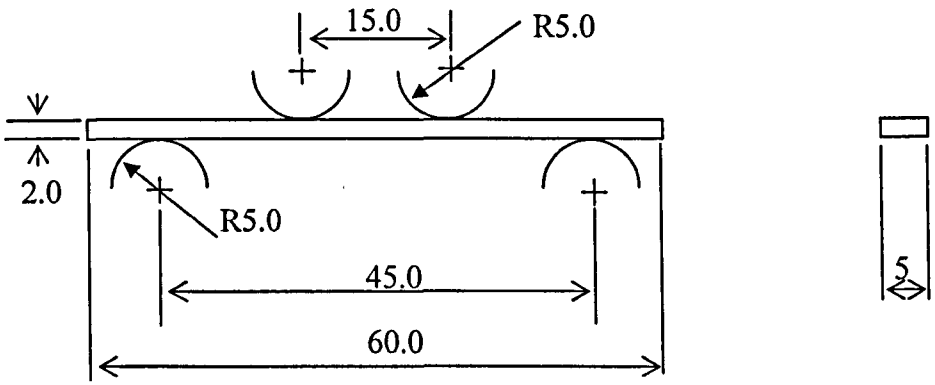

Dimensions in mm

Fig 4.5.1-1 Bending test configuration for the smallest 16ply specimen

The geometry and test setups for 32ply and 64ply specimens were increased in all dimensions by factors of 2 and 4 respectively compared with the 16ply specimens.

The material for all tests was unidirectional Ciba E glass/913 epoxy prepreg. The volume fraction of the composites is about 56%[135]. Material properties are the same as those for E glass/913 in the cut-ply and dropped-ply models in Section 3.6 and those for double edge notched specimen in Section 4.3.3, as shown in Table 4.5.1-1 and Table 4.5.1-2. σ_{unit} was obtained by the value of E_{11} and the strain to failure of a unit volume material, ε_{unit}, from reference 135.

Table 4.5.1-1 Glass Fibre composite material properties (E-glass/913)

E_{11} (GPa)	E_{22} (GPa)	ν_{21}	ν_{32}	G_{12} (GPa)	G_{23} (GPa)	m	σ_{unit} (MPa)
43.9	15.4	0.1052	0.3	4.34	2.75	29.3	1976

Table 4.5.1-2 Interface material properties (E-glass/913)

G_{IIC} (N/mm)	Z_f (MPa)	$S_{12/13}$ (MPa)	E (GPa)	G (GPa)
0.87	94	75	4.2	1.5

4.5.2 Modelling of 4-point bending test

The model of the 16 ply 4-point bending test is shown in Fig 4.5.2-1(a). In order to account correctly for the boundary conditions, both loading and support rollers were modelled as well. Support rollers were constrained in x and y directions. The loading rollers were constrained in the x direction and a prescribed motion in the y direction with a constant rate of 1mm/ms for the 16 ply model, 2mm/ms for the 32 ply model and originally 4mm/ms for the 64 ply model was applied to load the specimen to produce failure in similar times as in the experiments. To achieve computing efficiency, these loading rates are much faster than in the tests. Due to the largest span and mass of the 64 ply specimen, the original loading rate of 4mm/ms caused a large dynamic oscillation in the model. Then a reduced rate of 0.4mm/ms was applied in the 64ply model and produced much more smooth results. The results of the 64ply model in this section use values from the rate of 0.4mm/ms. To prevent the specimen sliding on the support bar in the x direction the center plane of the specimen was constrained in the x direction as well. Automatic surface to surface contact conditions were applied between the rollers and the specimen.

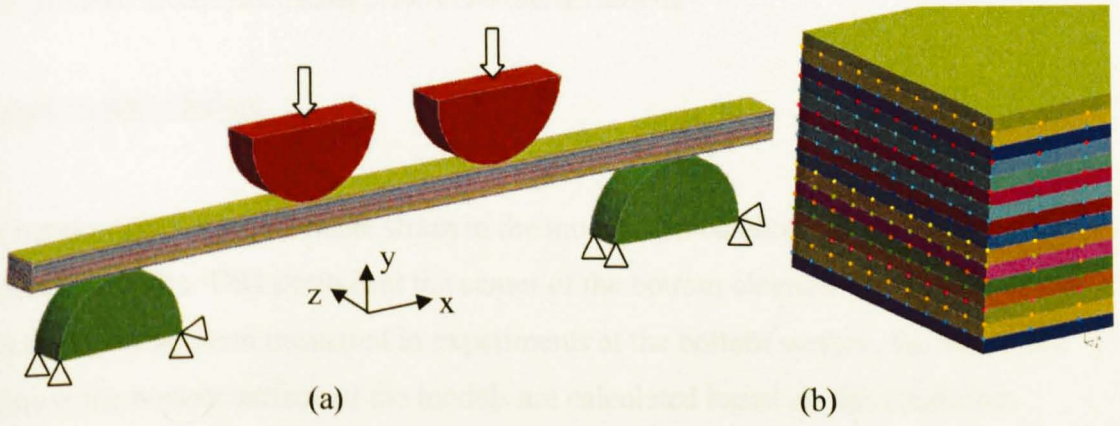

Fig 4.5.2-1 Model of the 4-point bending test (a) and interface elements put in the specimen(b)

Constant stress solids (solid element type 1 in LS-Dyna) with user defined material Umat44 were used to model the plies and Umat42 was used for the interface elements in LS-Dyna.

In the 16 ply model, one solid element for each ply was used in the thickness direction, i.e., the thickness of solid elements was 0.125mm. The width of solid elements was uniformly 0.25mm. The length of solid elements was 0.5mm at the ends of the specimen and linearly decreased to 0.125mm at the center of the specimen. The meshes for the 32 ply model and 64 ply model simply scaled the mesh of the 16 ply model in all dimensions by factors of 2 and 4 respectively.

Discrete interface elements were put in the specimen between each layer of elements in the model. This resulted in delamination interfaces between every ply in the 16 ply model, every 2 plies in the 32 ply model and every 4 plies in the 64 ply model, as shown in Fig 4.5.2-1(b). Interface elements in the 32 ply and 64 ply models were re-generated with the pre-processing programs to update the effective areas.

In the model control setup, type 5 hourglass control was used (Flanagan-Belytschko stiffness form with exact volume integration for solid elements) with a coefficient of 0.1 (default value). The default values of 1.5 and 0.06 were used for the quadratic and linear bulk viscosity coefficients respectively. A global damping factor of 1.0 was applied to the whole model.

4.5.3 Simulation Results of the 4-point Bending Models

1. Load-strain to failure

The maximum elemental tensile strain in the models can be obtained directly from the simulation results. This strain is at the center of the bottom element. To be comparable with the bending strain measured in experiments at the bottom surface, the maximum strains at the bottom surface of the models are calculated based on this maximum

elemental tensile strain. Assuming a linear distribution of bending tensile stress through the thickness, the maximum tensile strain at the bottom surface can be derived as:

$$\varepsilon_{\max-surface} = \varepsilon_{\max-element} * \frac{t_{specimen}}{t_{specimen} - t_{element}} \qquad (4.5.3\text{-}1)$$

Where $\varepsilon_{\max-surface}$ is the maximum tensile strain at the bottom surface of the model. $\varepsilon_{\max-element}$ is the maximum elemental tensile strain. $t_{specimen}$ is the thickness of the bending specimen and $t_{element}$ the thickness of bottom element.

The predicted values of loads were extracted from the nodes at which the prescribed motion was applied to the loading roller. The Load vs. (Load displacement/specimen span) curves for the 16ply, 32ply and 64ply models are shown in Fig 4.5.3-1(a). It can be seen that the fibre failure development is very rapid (taking around 0.12ms from failure initiation to the complete failure of the specimen) so that load curves dropped down very sharply after fibre failure being initiated. Using equation 4.5.3-1, the load-strain to failure curves of the 16 ply, 32 ply and 64 ply models are given in Fig 4.5.3-1(b).

The maximum tensile strains and loads in the models are compared with experimental results from Reference 135 in Table 4.5.3-1 and show good agreement. The main reason for the higher predicted values compared with test is the single point integration and limited no. of elements through the thickness.

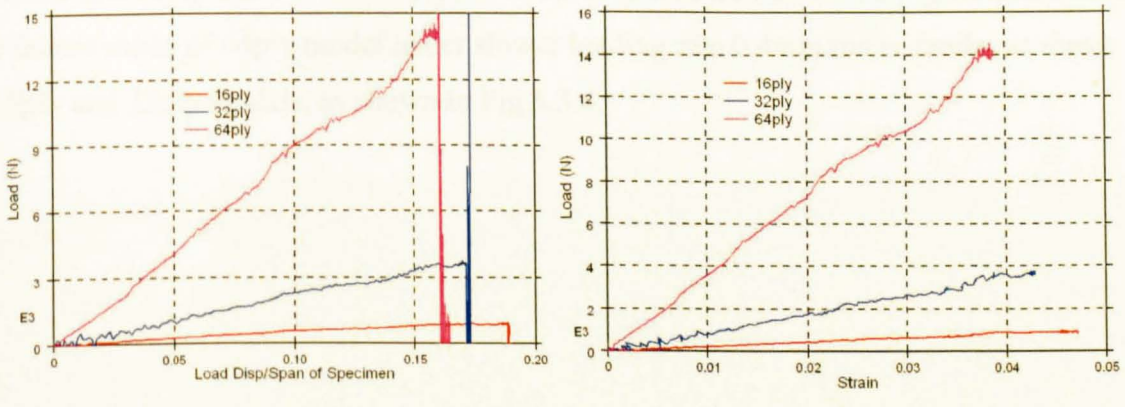

(a) (b)

Fig 4.5.3-1 Historic load and Load-strain to failure curves for 16ply, 32ply and 64ply models

Table 4.5.3-1 Comparison of measured and predicted maximum tensile strain and load

No. of plies	Maximum tensile strain(microstrain)			Maximum load(kN)		
	Experiment (c.v. %)	Model	Diff,%	Experiment	Model	Diff, %
16	43950 (2.3)	47028	7.0	1.08	0.94	13
32	42210 (5.9)	42901	1.6	N/A	3.8	
64	37110 (5.7)	38899*	4.8*	N/A	14.1*	

* The values with superscript '*' for 64ply model is from loading rate 0.4mm/ms

2.Model failure modes

The failure modes of the 16 ply, 32 ply and 64 ply models using Umat44 and discrete interface elements are shown in Fig 4.5..3-2, 4.5.3-3 and 4.5.3-4 respectively. The failure modes of 16 ply and 32 ply models are similar, both started with fibre breakage from the bottom center of the specimen. After fibre breakage developed into seven layers of elements, the failure propagated in the form of delamination between the 7^{th} and the 8^{th} layer of elements. In Fig 5.5.3-2, a typical failure mode of a unidirectional carbon fibre laminate in four point bending test, which is similar as that of the glass fibre laminate, is provided as a comparison with the predicted failure mode and shows very good correlation. The failure mode of 64ply model under slower loading rate 0.4mm/ms is similar as those of 16ply and 32ply models, as shown in Fig 5.3.4.

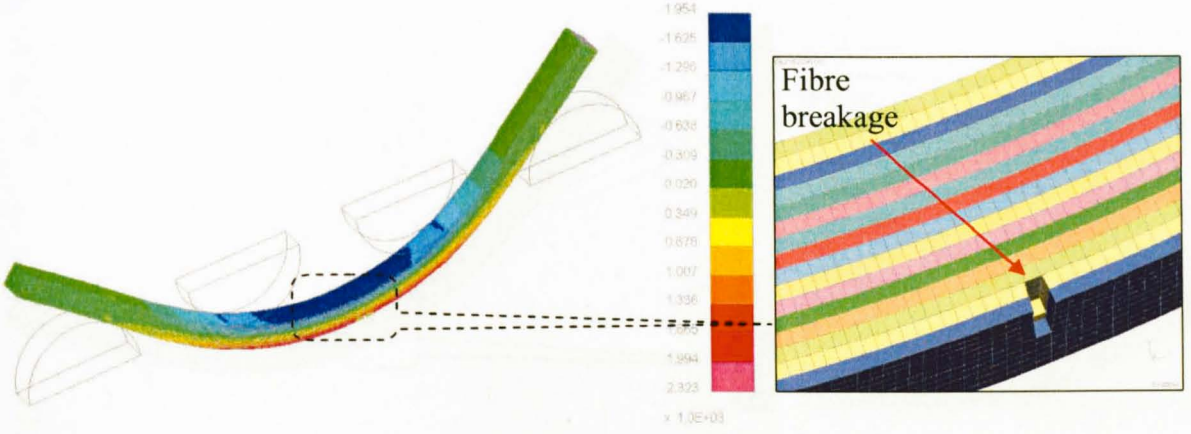

Fibre failure initiated

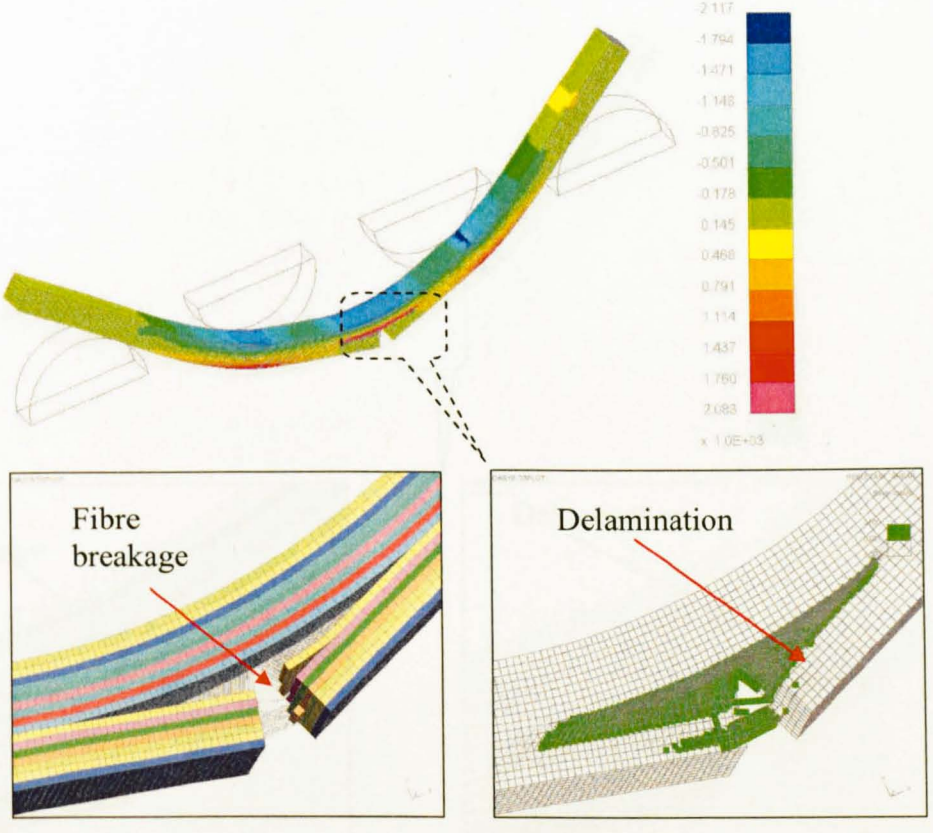

Final failure mode

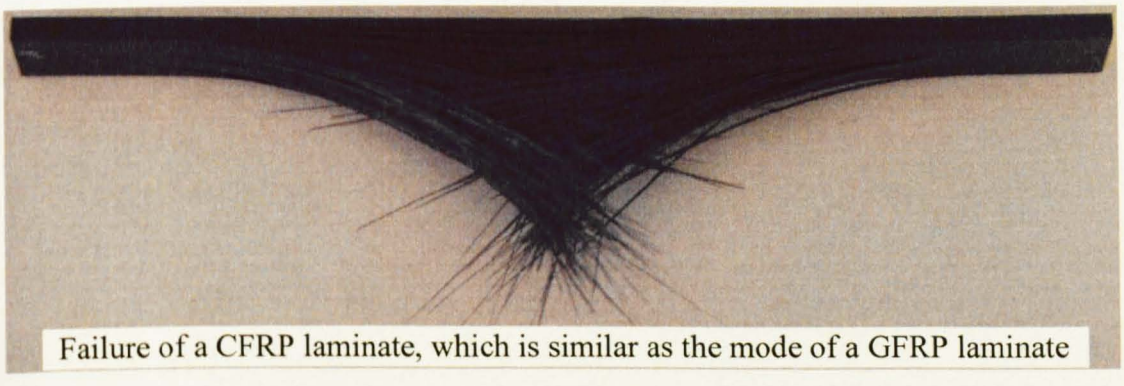

Failure of a CFRP laminate, which is similar as the mode of a GFRP laminate

Fig 4.5..3-2 Failure development of 16ply model with one maximum stress element being removed when Weibull Criteria was satisfied and the comparison with experimental result of a CFRP

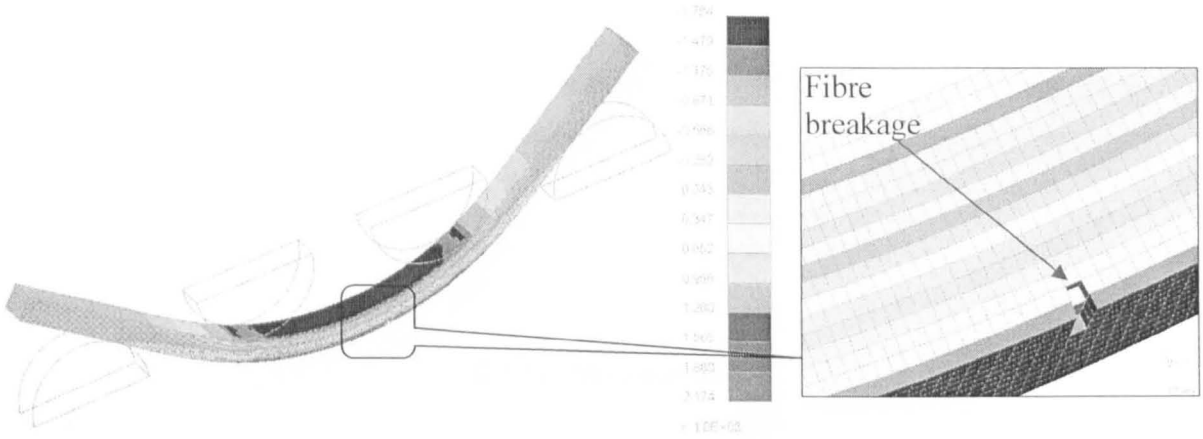

Fibre failure initiated

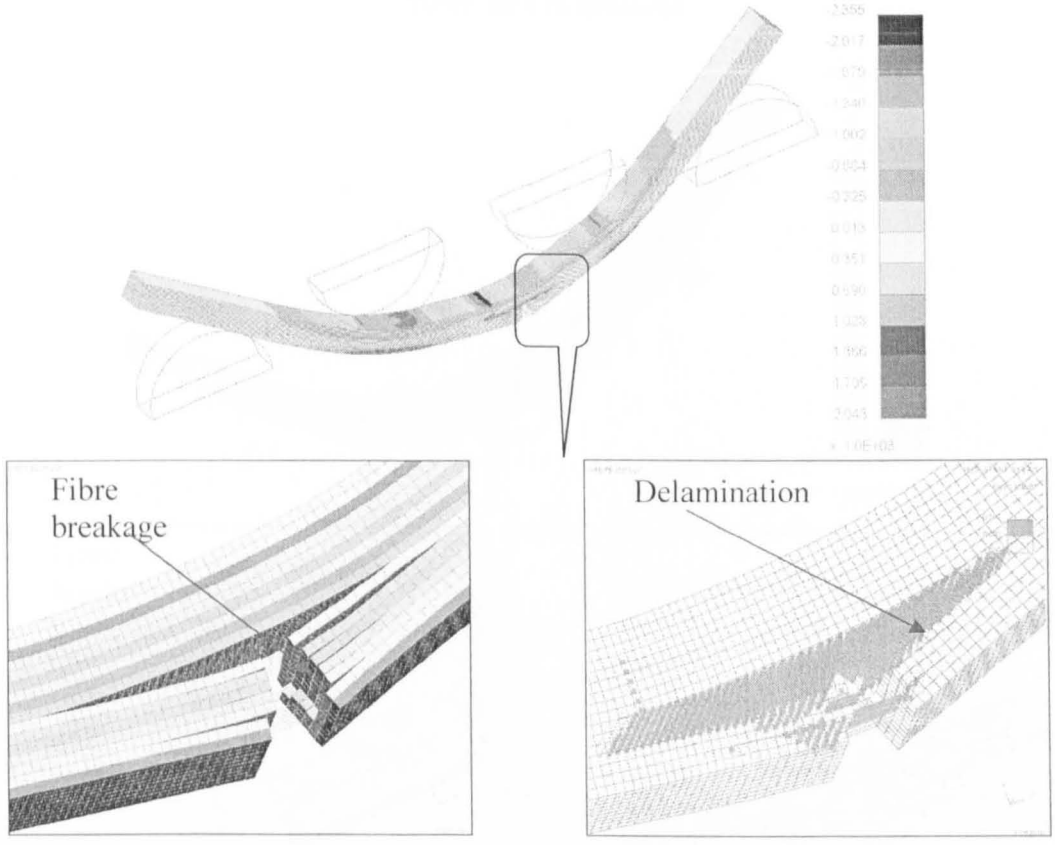

Final failure mode

Fig 4.5..3-3 Failure development of 32ply model with one maximum stress element being removed when Weibull Criteria was satisfied

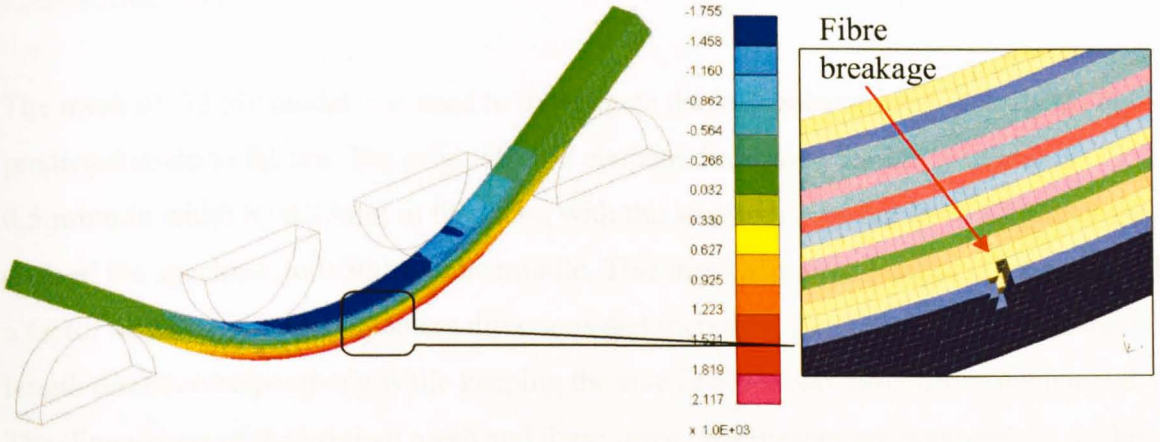

Fibre failure initiated

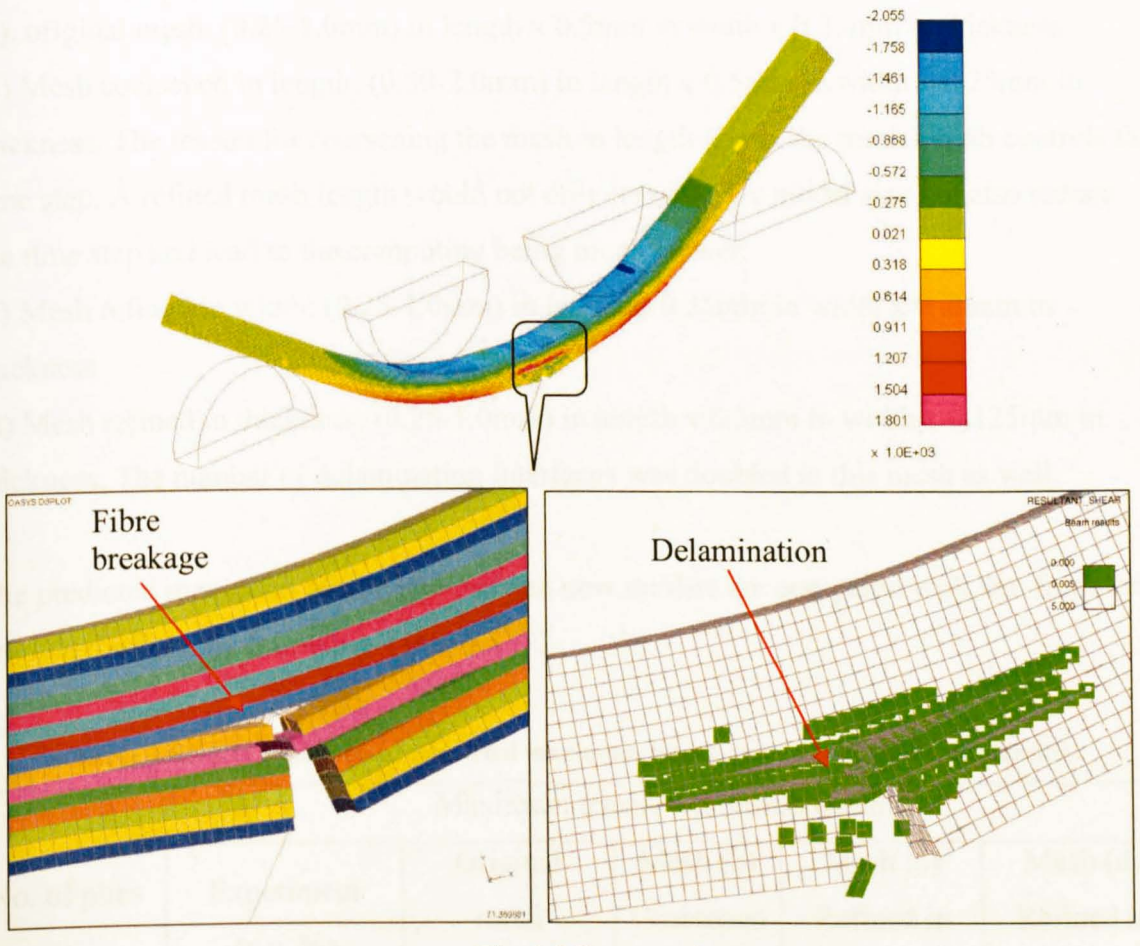

Final failure mode

Fig 4.5..3-4 Failure development of 64ply model with maximum stress elements being removed when Weibull Criteria was satisfied

3.Mesh size effect

The mesh of 32 ply model was used to investigate the influence of mesh density on the predicted strain to failure. The original solid element dimension for 32ply model is 0.5mmm in width by 0.25mm in thickness with the length decreasing from 1.0mm at the ends of the specimen to 0.5mm in the middle. This mesh size was decreased (or refined) by a factor of 2 in width and thickness directions and increased (or coarsened) by 2 in the length direction respectively while keeping the size in other two dimensions unchanged. The dimensions of the original mesh and these three new meshes are summarized as the below:

(a). original mesh: (0.25-1.0mm) in length x 0.5mm in width x 0.25mm in thickness

(b) Mesh coarsened in length: (0.50-2.0mm) in length x 0.5mm in width x 0.25mm in thickness. The reason for coarsening the mesh in length is that the mesh length controls the time step. A refined mesh length would not only increase the model size but also reduce the time step and lead to the computing being much slower.

(c) Mesh refined in width: (0.25-1.0mm) in length x 0.25mm in width x 0.25mm in thickness

(d) Mesh refined in thickness: (0.25-1.0mm) in length x 0.5mm in width x 0.125mm in thickness. The number of delamination interfaces was doubled in this mesh as well.

The predicted maximum tensile strains from new meshes are compared with that from the original mesh in the following Table 4.5.3-2.

Table 4.5.3-2.Comparison of predicted maximum tensile strains using different meshes

No. of plies	Maximum tensile strain(microstrain)				
	Experiment (c.v. %)	Original mesh (a)	Mesh (b) Coarsened in length	Mesh (c) Refined in width	Mesh (d) Refined in thickness
32	42210 (5.9)	42901	44673	42827	43023
Diff,%		1.6	5.8	1.5	1.9

It can be seen that the influence of mesh size in length direction is the largest and negligible in the width and thickness direction. The small influence of mesh size in width

direction comes from the fact that stress variations in the width direction of the four point bending specimen are negligible. Comparatively, stress distribution along length direction varies largely and in turn the influence of mesh size in length direction is also larger than in the width direction. It is expected that the smaller element thickness in mesh (d) brings them closer to the surface and have a higher average stress, hence an earlier failure than the mesh (a). The models here gave a counteracting prediction, in which the strain to failure of mesh (d) is even slightly larger than that of mesh (a). The reason for this contradiction might be explained as below:

Mesh (a) and Mesh (d) have the same thickness t and elemental cross section area s. Mesh (a) has 16 elements through the thickness and the thickness of each element is t_a. The maximum elemental tensile stress in mesh(a) is $\sigma_{a\_elem\_max}$ and the corresponding bending stress on the bottom surface is σ_{a_max}. Mesh (d) has 32plies and the thickness of each ply is t_d. The maximum elemental tensile stress and bending stress for mesh (d) are $\sigma_{d\_elem\_max}$ and σ_{d_max}. From the stress contour in Fig 4.5.3-3, it can be seen that the tensile stresses concentrate in the areas between two loading rollers where the bending moment is constant and the stress distribution through the thickness is linear. The Weibull integration for mesh(a) and mesh(d) would be roughly:

$$\sum_{i=0}^{7}\left[\frac{\sigma_{a\_max}(t_a+2it_a)}{t}\right]^m t_a s=\left[\frac{\sigma_{a\_max}t_a}{t}\right]^m t_a s\sum_{i=0}^{7}(1+2i)^m \quad (4.5.3\text{-}2)$$

and

$$\sum_{i=0}^{15}\left[\frac{\sigma_{d\_max}(t_d+2it_d)}{t}\right]^m t_b s=\left[\frac{\sigma_{d\_max}t_d}{t}\right]^m t_d s\sum_{i=0}^{15}(1+2i)^m \quad (4.5.3\text{-}3)$$

Where $t_a=2t_d$ and m=29.3. For equal failure probabilities of mesh (a) and mesh (d), the ratio of σ_{a_max} and σ_{d_max} is given by:

$$\frac{\sigma_{a\_max}}{\sigma_{d\_max}}=\left(\frac{t_d}{t_a}\right)\left(\frac{t_d\sum_{i=0}^{15}(1+2i)^m}{t_a\sum_{i=0}^{7}(1+2i)^m}\right)^{1/m}=\left(\frac{1}{2}\right)\left(\frac{\sum_{i=0}^{15}(1+2i)^{29.3}}{2\sum_{i=0}^{7}(1+2i)^{29.3}}\right)^{\frac{1}{29.3}}=1.0138 \quad (4.5.3\text{-}4)$$

The relations of maximum elemental stress and bending stress are:

$$\sigma_{a\_max}=\sigma_{a\_elem\_max}\frac{t}{t-t_a} \quad \text{and} \quad \sigma_{d\_max}=\sigma_{d\_elem\_max}\frac{t}{t-t_d} \quad (4.5.3\text{-}5)$$

If the two meshes used maximum stress failure criteria, then $\sigma_{a\_elem\_max} = \sigma_{d\_elem\_max}$ and the ratio of σ_{a_max} and σ_{d_max} would be:

$$\frac{\sigma_{a\_max}}{\sigma_{d\_max}} = \frac{\sigma_{a\_elem\_max}\dfrac{t}{t-t_a}}{\sigma_{d\_elem\_max}\dfrac{t}{t-t_d}} = \frac{t-t_d}{t-t_a} = \frac{4-0.125}{4-0.25} = 1.0333 \qquad (4.5.3\text{-}6)$$

It can be seen here that the Weibull integration criteria reduced the mesh dependency by 2% compared with the stress based failure criteria. Because the bending stress of mesh (a) σ_{a_max} and mesh (d) σ_{d_max} are very close, the influence of additional numerical oscillation of mesh (d) induced by its doubled number of elements might exceed the influence of mesh density and cause the result that σ_{d_max} was even slightly larger than σ_{a_max}. Using whichever mesh, the difference in predicted maximum tensile strain from the experimental result is less than the coefficient variation of the experiment itself.

4.5.4 Conclusion

The four point bending models with Weibull failure criteria being implemented predicted good strain to failure values for all the 16ply, 32ply and 64ply models.. The size effect observed in experiments where the failure strain decreased with increasing specimen size can be well predicted by the models.

The similar failure modes of the models as those in experiments demonstrated that the assumption of only failing and removing the maximum stress element when the Weibull criteria was satisfied was a simple but effective approach to model the progressive fibre failure in four point bending laminates. The interface elements between plies can effectively eliminate the stress concentration caused by removed elements. This method of determining the failed elements is worth further application and verification in future work.

Chapter 5 Experimental and Numerical Investigation of Damage propagation in Overheight Compact Tension(OCT) Tests

The statistical progressive fibre-dominated element failure model in Chapter 4 gave good predictions of fibre failure stresses for both four point bending and open hole tension tests. However, in all the cases that failed by fibre failure the ultimate damage was sudden and catastrophic. This gives little opportunity to study the influence of the sub-critical damage on the progression of fibre failure. To examine progressive fibre failure in laminates and the influence of layups on the damage initiation and propagation modes, Overheight Compact Tension (OCT) tests on eight different layups of IM7/8552 laminates were carried out and models on the tests using interface elements and progressive fibre failure material were also built in this chapter. The advantage of the OCT test is that it allows the stable formation of a process zone ahead of the crack tip and subsequent crack growth, thus making it possible to investigate the development of sub-critical fibre damage and its influence on the final failure modes of the laminates. Ultrasonic C-scan and X-ray were used to examine the splitting, delamination and fibre breakage damages within OCT specimens. The obtained damage information was compared with model predictions and show good correlation.

5.1 Overheight Compact Tension (OCT) Tests

5.1.1 Background

Composites failure is usually dominated by local effects and involves complex interaction of various damage modes [200]. Sub-critical damage such as splitting and delamination can occur at load levels well below ultimate failure. This sub-critical damage causes stress redistribution and the different mechanisms interact with each other to determine the ultimate failure mode and strength. Kortschot and Beaumont's investigation on damage development in 914C/T300 double-edge-notched cross-ply specimens[201] and work by Hallett and Wisnom on E-glass/913 double-edge-notched cross-ply and quasi-isotropic specimens[202] both indicated that splits and delaminations prior to ultimate failure could modify the notch-tip stress field and result in a significant improvement in notched strength. In Reference 202 it was found that when the central 0° load carrying ply was doubled in thickness, much greater splitting ensued and significant delamination preceded

fibre failure. There have been a number of other studies which have shown the effect of thicker ply blocks promoting intra-ply splitting and hence increase in notched strength [203,204].

Much of the work which has been done investigating in detail the progressive development of damage at notches has used centre or edge notched specimens[205,206,207]. Previous work at the University of Bristol on open hole tensile tests identified the sequence of splits and delaminations which precede ultimate failure and significantly affect measured strength[208,209]. In all the cases that failed by fibre failure this was sudden and catastrophic. This gives little opportunity to study the influence of the sub-critical damage on the progression of fibre failure. To examine progressive failure a compact tension test provides a suitable solution[210,211,212]. In most cases this specimen has been used for determining intra-laminar fracture toughness values, and details of the sub-critical damage developing during loading and its subsequent interaction with fibre fracture have not been considered. The Overheight Compact Tension (OCT) test that has been devised at the University of British Columbia[213] is specifically aimed at capturing the behaviour of laminates typical of large structures, representative for example of a disk burst in a composite wing skin. The advantage of the OCT test is that it allows the stable formation of a process zone ahead of the crack tip and subsequent crack growth, thus making it possible to investigate the development of sub-critical fibre damage and its influence on the final failure modes of the laminates.

Compact tension type tests are usually devised such that extraneous damage modes are minimized and that a brittle type crack progresses from the pre machined notch in order that a laminate or fibre direction fracture toughness can be measured[210]. The objective of this work however has been to design laminates such that sub-critical damage in the form of splitting and delamination is promoted and thus to experimentally investigate their interaction with progressive fibre failure. Altogether 8 different lay-ups were tested with the OCT geometry using dispersed and blocked plies in the thickness direction. As shown in Fig 5.1.1-1, the dispersed ply method increases the thickness of specimen by repeating sublaminates as required whereas the blocked ply method involves increasing the thickness of ply blocks of the same orientation. In each case a number of interrupted tests were performed to capture the damage process as it occurred before the onset of fibre fracture. Non-destructive C-scan testing was used to determine the extent of delamination.

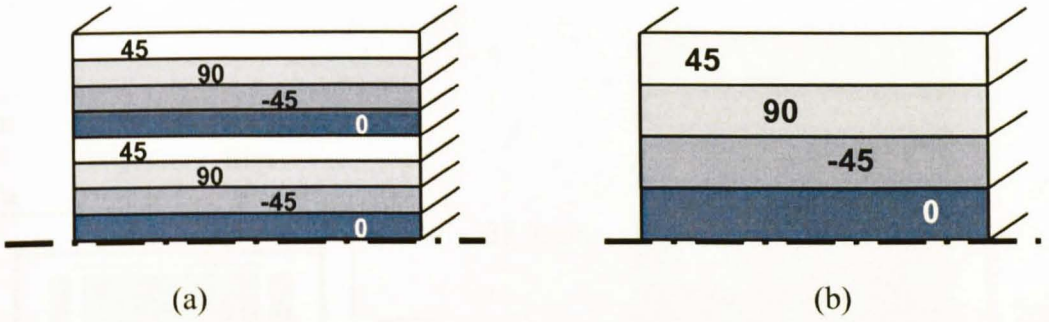

(a) (b)

Fig 5.1.1-1 Schematic (a) dispersed plies and (b) blocked plies in thickness direction of the specimen

5.1.2 OCT Test Setup and Procedure

1. Material

The material used in this testing program was the IM7/8552 carbon-epoxy pre-preg system with a nominal ply thickness of 0.125mm. There were altogether 8 different lay-ups tested, see Table 5.1.2-1. All laying-up was performed using the University of Bristol's in-house facilities. To help achieve a low void percentage, the laminate was consolidated in a vacuum bag every 4 plies, or 0.5mm thickness, during the process. For each lay-up, a large panel was laid up and cured (refer to Fig 5.1.2-1a) according to the manufacturer's recommendations and then cut into 6 specimens with the same OCT geometry as shown in Fig 5.1.2-1b. Holes for the pin loading were drilled using tungsten carbide drill bits and the notch was cut with a diamond sintered cutting wheel with a 1mm thick blade. The single result for the $[45/90/45/0]_{4s}$ layup came from a pilot study carried out by UBC which investigated a number of other testing parameters such as notch tip radius and was not repeated for this testing programme .

Table 5.1.2-1 Lay-ups tested in the OCT experimental program

Dispersed plies in thickness direction			**Blocked plies in thickness direction**		
Layup	**Thickness (mm)**	**Number of specimens**	**Layup**	**Thickness (mm)**	**Number of specimens**
$[0/90]_{4s}$	2	6	$[0_2/90_2]_{2s}$	2	6
$[0/90]_{8s}$	4	6	$[0_4/90_4]_{2s}$	4	6
$[45/90/45/0]_{2s}$	2	6	$[45_2/90_2/-45_2/0_2]_s$	2	6
$[45/90/45/0]_{4s}$	4	1	$[45_4/90_4/45_4/0_4]_s$	4	6

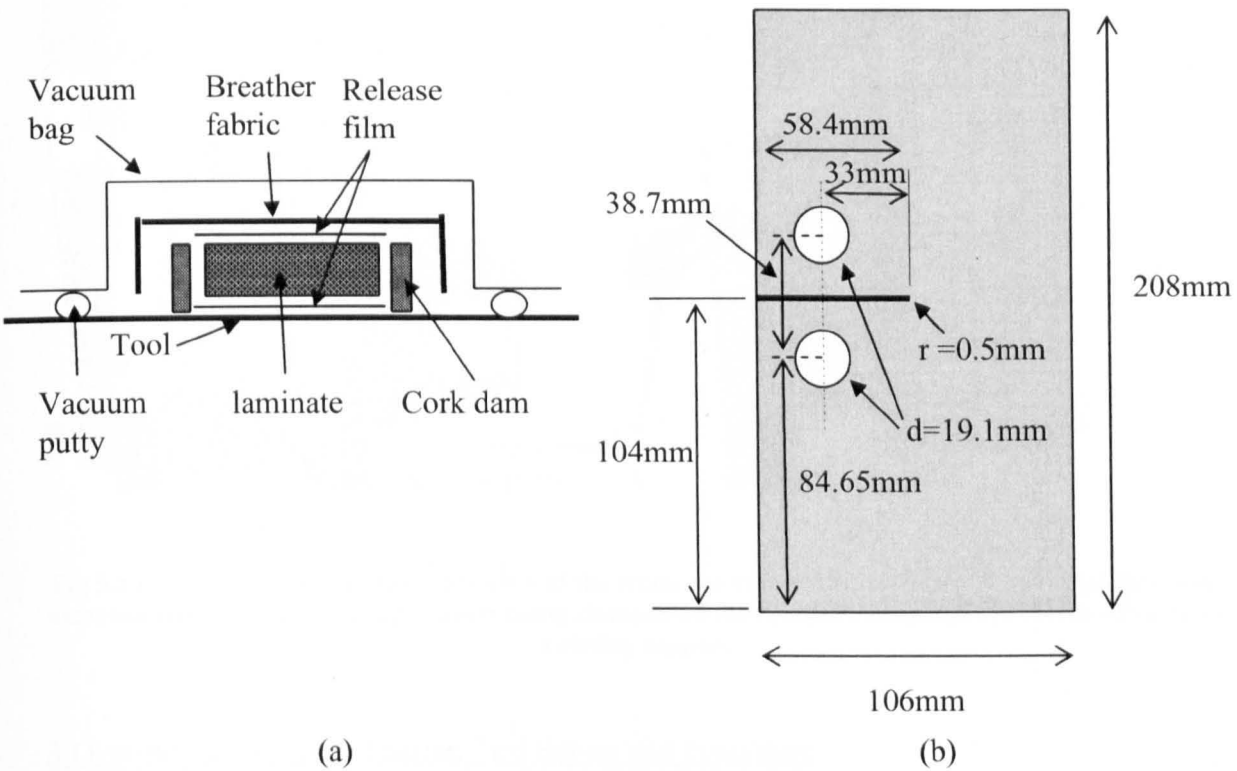

Fig 5.1.2-1 Curing set-up of laminates (a) and OCT specimen geometry (thickness B ranged from 2.0 mm to 4.0mm) (b)

2 Test Equipment

The OCT test set-up is shown in Fig 5.1.2-2a. A screw-driven universal testing machine was used to load the OCT specimens at rates between 0.5 and 1mm/min. Tensile loading was applied through 19 mm diameter pins inserted through the holes shown in Fig 5.1.2-1. An extensometer, as shown in Fig 5.1.2-2b, was fixed to the specimens to measure the pin opening displacement (POD). The load cell signal and the extensometer signal were output and recorded with a dedicated PC using Davis StrainMaster software [214].

One LaVision Imager QE camera with a micro Nikkor 60mm lens mounted on a stationary tripod in front of the test set-up were used to take photographs during each test. The photography was controlled and recorded with the Davis StrainMaster software which can also be used to do full-field strain analysis of the specimen with these photos but is not reported here.

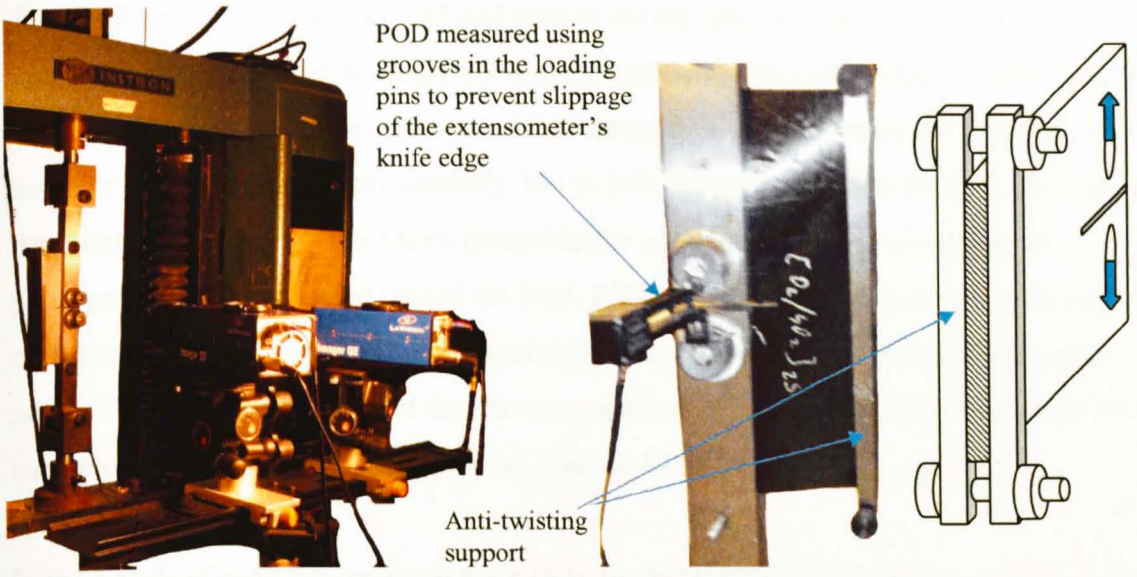

Fig 5.1.2-2 OCT test set-up: (a) front view of the whole set-up and (b) Back view of the specimen with extensometer and anti-twisting support being clamped on the specimen (c)schematic details of the anti-twisting support

3 Over-height Compact Tension Test Set-up and Procedure

The Over-height Compact Tension (OCT) specimen geometry developed at the University of British Columbia [14] was chosen to produce stable crack growth in a specimen so that the composite damage zone could be investigated. Kongshavn and Poursartip [14] demonstrated that the OCT specimen geometry with a sharp notch tip is stable under displacement control and is large enough so that the boundaries do not greatly affect the damage zone size or shape. For this study, the tip radius of the sharp notch in the OCT specimen is 0.5mm. Other dimensions of the specimen are shown in Fig 5.1.2-1.

The specimen in the OCT test, as shown in Fig 5.1.2-2(a), was loaded in tension through pins located above and below the notch. To prevent buckling, a stiffening support with a width of 10mm was attached to the back edge of the specimen, refer to Fig 5.1.2-2(b) and Fig 5.1.2-2(c). It has little effect on the response of the specimen and where possible loading was stopped before the crack grew into the region covered by the stiffener.

The displacement rate during load and unload for the tests was set between 0.5 and 1mm/min. The data from the load cell and the extensometer were output at a frequency of 1000 s^{-1}. Photographs of the specimen were taken at regular intervals of 2s during each test. For each specimen approximately 300 to 500 photographs were taken depending on the duration of loading. The Davis StrainMaster software was used to control the photographing intervals and record the load, POD and the specimen photos in all tests. For each image, 2000 data points of the load and POD values were recorded. During post-processing, the software output the average values of load and POD for each image so that each photograph could be placed on the load vs. POD curve.

In the 6 tests of each lay-up, three were fully loaded till the specimen was damaged and the load dropped to below half the value of the peak load and another three tests were interrupted at different load levels before the peak load was reached. All the tests were unloaded by reversing the displacement to the point of zero load.

5.1.3 OCT Test Result

Fig 5.1.3-1 gives the load vs. POD curves of all the tested specimens. Detailed comments on each load curve are given in Appendix C together with the C-scan results and surface failure images of the specimens. Typical load vs. POD curves from each of the dispersed and blocked ply laminates are extracted and compared side-by-side in Fig 5.1.3-2. For dispersed ply specimens, it can be seen that, apart from some initial bedding in at the pin contact points, the load-POD curves are in most cases essentially linear up to the point of the first load drop. After the first load drop the crack progresses across the width of the specimen in a series of small "jumps" which result in further load drops. The overall trend is for the crack growth to progress at approximately constant load.

In contrast the blocked ply specimens showed a large degree of non-linearity in the load-POD curves. This is caused by the substantial amount of splitting and delamination that occurs in the specimen prior to fibre failure This type of specimens usually failed in the form of global delamination and fibre failure were not initiated.

Following marked load levels in Fig 5.1.3-2a, fibre breakage was clearly observed near the notches in the cross-ply dispersed ply laminates and a 45° splitting in the surface plies extended from the notch in the quasi-isotropic laminates. In Fig 5.1.3-2b, it can be seen that the $[45_4/90_4/45_4/0_4]_s$ and $[0_4/90_4]_{2s}$ laminates failed sharply. A clear surface split in the $[45_2/90_2/45_2/0_2]_s$ laminates in the 45° direction and in the $[0_2/90_2]_{2s}$ laminates in the 0° ply direction developed from the notches after the marked load levels. In all cases after these 'o' marked load levels the curves have the first significant drops. Table 5.1.3-1 gives the average load at the first significant load drop of all the tests. It can be seen that the strength of the cross-ply dispersed ply laminates scales with thickness. For the quasi-isotropic layup the scaling is not so good but this is compared to only a single specimen at 4mm thickness. Blocked ply specimens in all cases showed considerably higher load than the equivalent dispersed ply specimens with the same thickness.

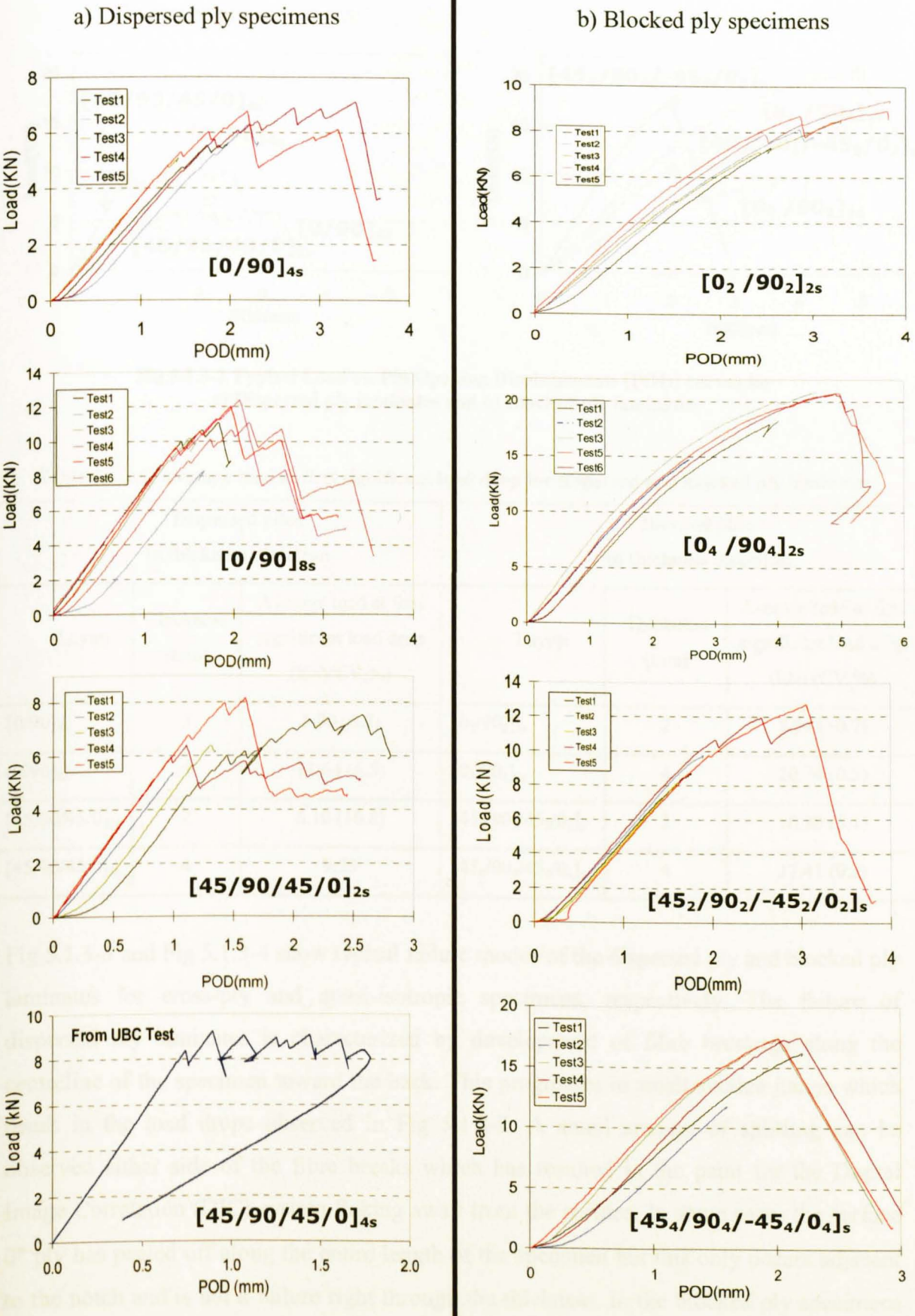

Fig 5.1.3-1 Load vs. Pin Opening Displacements (POD) curves for a) Dispersed ply specimens and b) Blocked ply specimens

a). Dispersed ply specimens

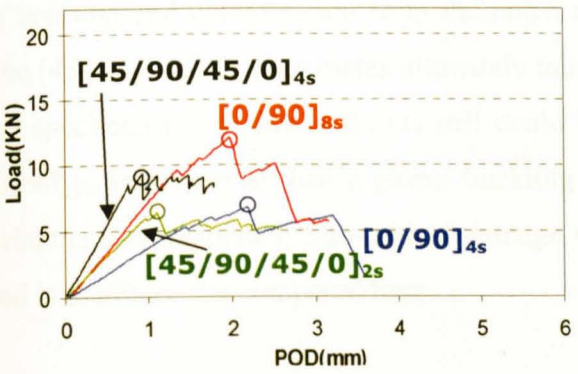

b) Blocked ply specimens

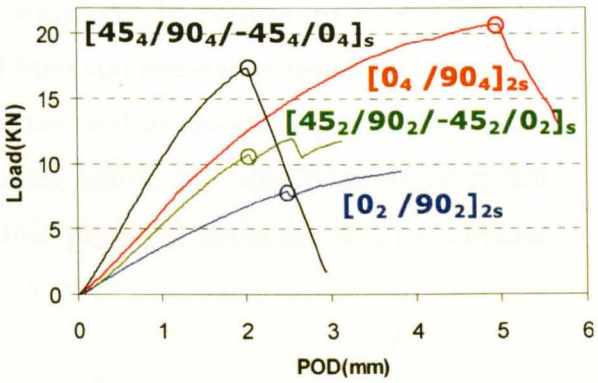

Fig 5.1.3-2 Typical Load vs. Pin Opening Displacements (POD) curves for a) Dispersed ply laminates and b) Blocked ply laminates

Table 5.1.3-1. Average load at first significant load drop for dispersed and blocked ply laminates

Dispersed plies in thickness direction			**Blocked plies in thickness direction**		
Layup	Thickness (mm)	Average load at first significant load drop (kN)(CV,%)	Layup	Thickness (mm)	Average load at first significant load drop (kN) (CV,%)
$[0/90]_{4s}$	2	5.90 (6.9)	$[0_2/90_2]_{2s}$	2	7.94 (10.7)
$[0/90]_{8s}$	4	11.64 (6.5)	$[0_4/90_4]_{2s}$	4	20.74 (0.5)
$[45/90/45/0]_{2s}$	2	6.10 (10.8)	$[45_2/90_2/45_2/0_2]_s$	2	10.30 (5.1)
$[45/90/45/0]_{4s}$	4	9.23	$[45_4/90_4/45_4/0_4]_s$	4	17.41 (0.2)

Fig 5.1.3-3 and Fig 5.1.3-4 show typical failure modes of the dispersed ply and blocked ply laminates for cross-ply and quasi-isotropic specimens, respectively. The failure of dispersed ply laminates is characterized by development of fibre breakage along the centreline of the specimen toward the back. This progresses in small sudden jumps which result in the load drops observed in Fig 5.1.3-2. A small amount of splitting can be observed either side of the fibre breaks which has resulted in the paint for the Digital Image Correlation (DIC) system flaking away from the surface. In some cases the surface 0° ply has peeled off along the entire length of the specimen but this only occurs adjacent to the notch and is not a failure right through the thickness. In the blocked ply specimens by contrast the 0° ply blocks adjacent to the notch tip pulled out from the specimen completely without any fibre failure. This can be observed on the images of the failed specimen ends (top and bottom) in Fig 5.1.3-3b and Fig 5.1.3-4b. This causes the sharp

load drop as shown in Fig 5.1.3-2b and the prior non-linearity is a result of the progression of splitting and delamination from the notch tip which can be seen in the C-scan results. The $[45_2/90_2/-45_2/0_2]_s$ laminates ultimately failed from compressive crushing at the back of the specimen but 0^o ply pull-outs still could be observed as shown in Fig 5.1.3-4b. The $[0_2/90_2]_{2s}$ laminates all had a global buckling failure before any fibre breakage or global delamination happened. Sub-critical damage within $[0_2/90_2]_{2s}$ laminates was not obvious and is therefore not compared here.

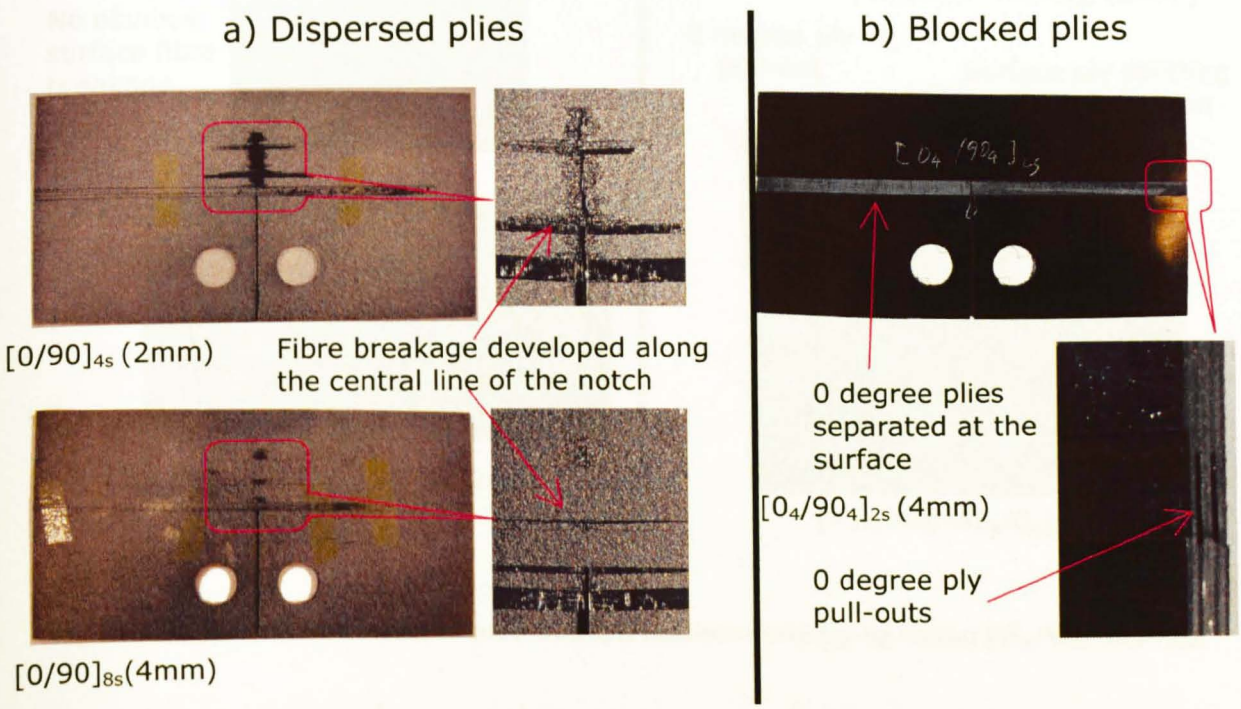

Fig 5.1.3-3 Typical failure modes of cross-ply laminates with lay-up format $[0_m/90_m]_{ns}$

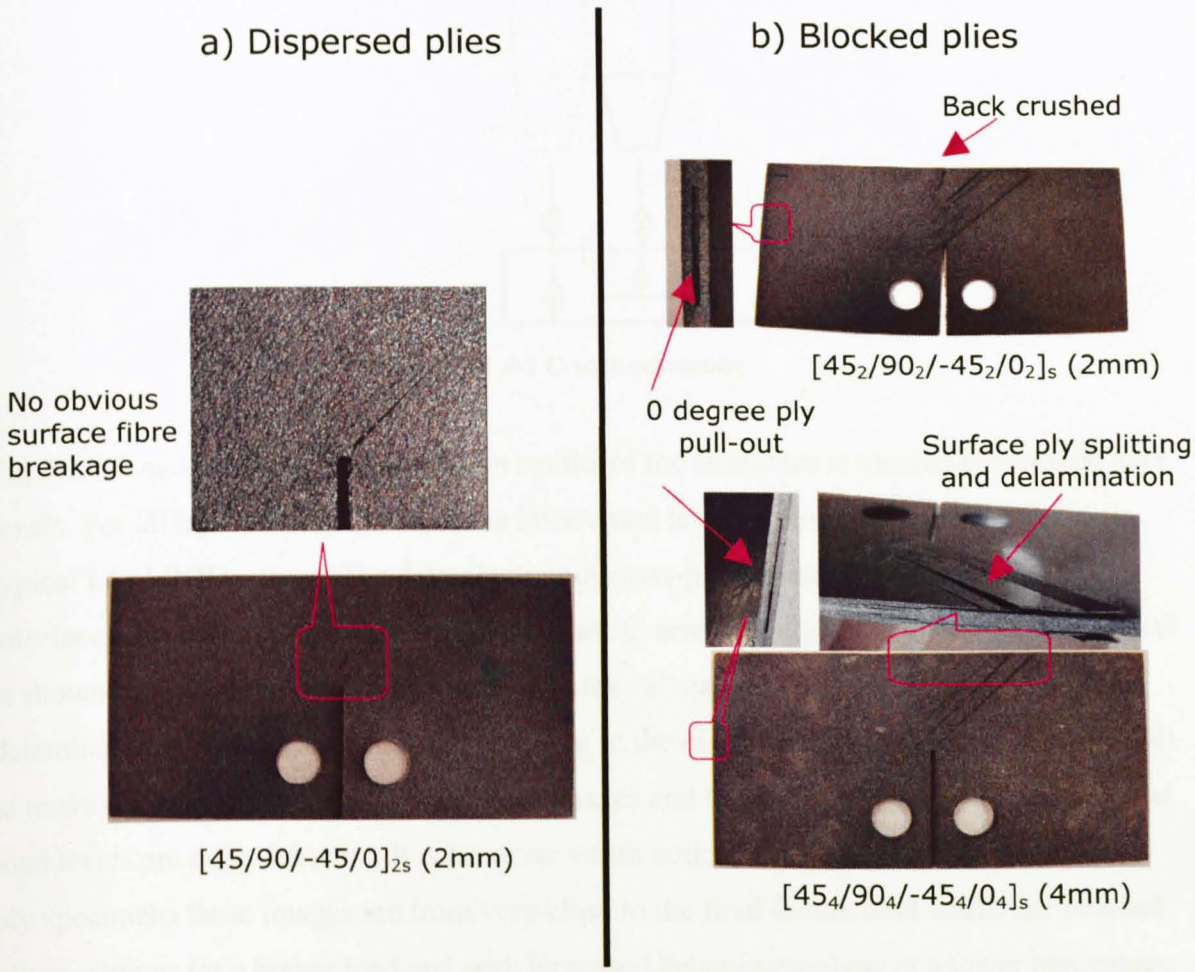

Fig 5.1.3-4 Typical failure modes of quasi-isotropic laminates with lay-up format $[45_m/90_m/-45_m/0_m]_{ns}$

5.1.4 C-scan Results

All specimens were C-scanned after testing to obtain the internal delamination information. The schematic C-scan mechanism is shown in Fig 5.1.4-1. In the undamaged zone of the specimen, the ultrasonic wave was reflected at the front surface and the back surface. When there is a delamination, the ultrasonic wave would be reflected at the delamination zone before reaching the back surface. By analyzing the delay time and amplitude of the reflected signal, the position and the size of the delamination zone at different interfaces can be obtained.

Detailed C-scan results for all specimens are given in Appendix C together with load-POD curves.

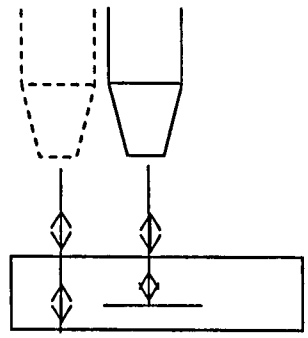

Fig 5.1.4-1 C-scan schematic

Fig 5.1.4-2 and 5.1.4-3 show the C-scan results of the laminates at various interrupted load levels. For all lay-ups, load levels of the interrupted tests are marked with a,b,c and d on typical Load-POD curves. The delamination in cross-ply laminates is similar at all interfaces through the thickness and so only one C-scan result at each interrupted load level is shown in Fig 5.1.4-1. It can be seen that in the "a" images there is negligible delamination and associated intra-ply splitting in the dispersed ply specimens. It is difficult to make direct comparisons between these images and the blocked ply specimens since the load levels are quite different. It is however worth noting that in the case of the dispersed ply specimens these images are from very close to the final failure load whilst the blocked ply specimens (at a higher load and with increased delamination) are at a lower percentage of ultimate failure at point a. In the "b" images the delamination has now grown more significantly in the dispersed ply specimens. This is after the first minor drop on the load curve. The "c" images are from a point after a more major drop in load for the dispersed ply specimens. At this point the delamination can be seen to be advancing away from the notch tip, perpendicular to the loading direction. This is indicative of fibre failure having taken place and a through-thickness crack progressing away from the notch.

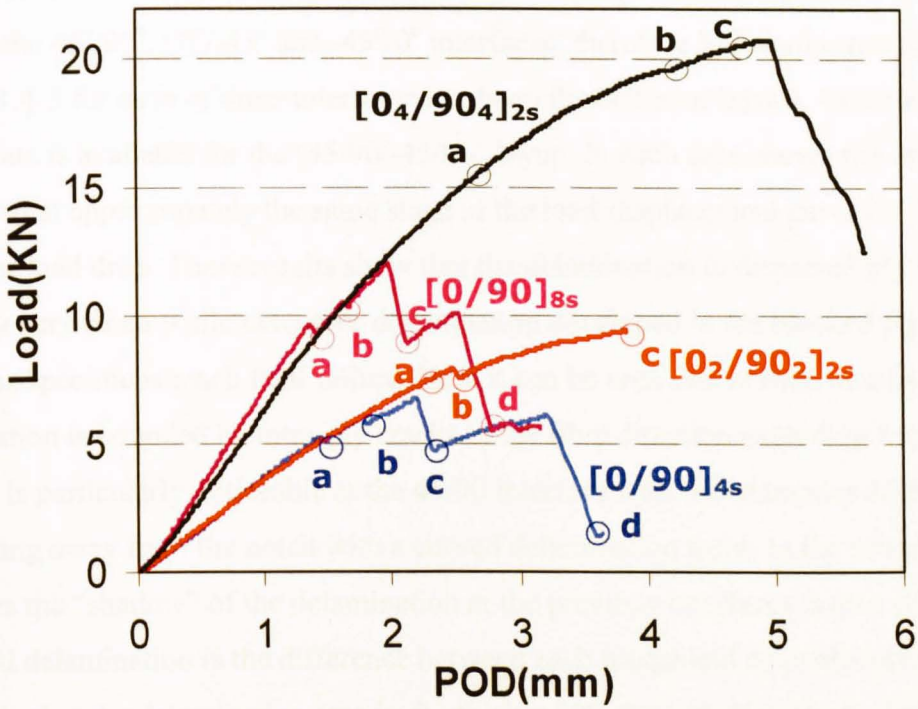

	[0/90]4s	[0/90]8s	[0₂/90₂]2s	[0₄/90₄]2s
a	20mm	20mm	20mm	20mm
b				
c				
d			Tapes used to fix the separated surface 0° plies	

Note: specimens were scanned in full length in the 0° ply direction. In the 90° ply direction only the area from the edge of the pin holes to the back of the specimen was scanned.

Fig 5.1.4-2 C-scan results of cross-ply laminates at various interrupted load levels

In contrast the growth of the delamination in the blocked ply specimens is much more continuous, advancing in a self-similar manner with a triangular region being formed between the 90° matrix cracks ahead of the notch and the 0° splits either side of the notch as has been reported in other investigations [194, 195]. Eventually this delamination reaches the ends of the specimens and causes the final failure via pullout of the 0° ply block which can be seen in Fig 5.1.3-3.

The delamination in quasi-isotropic laminates with lay-up format $[45_m/90_m/-45_m/0_m]_{ns}$ varies at the 45°/90°, 90°/-45° and -45°/0° interfaces, therefore 3 C-scan results are shown in Fig 5.1.4-3 for each of three interrupted tests on the different layups. Unfortunately no C-scan data is available for the $[45/90/-45/0]_{4s}$ layup. In each case shown the test has been interrupted at approximately the same stage in the load-displacement curve i.e. just before any major load drop. These results show that the delamination in dispersed ply laminates is generally very small while extensive delamination developed in the blocked ply laminates before the specimens reach final failure. Here it can be seen that at each interface the delamination is bounded by intra-ply cracks in the fibre direction extending from the notch tip. This is particularly noticeable at the 45/90 interface with the triangular delamination progressing away from the notch with a curved delamination front. In the subsequent interfaces the "shadow" of the delamination at the previous interfaces is also still visible so the actual delamination is the difference between each image and its predecessors. It is also noticeable that the delamination area in the thicker $[45_4/90_4/-45_4/0_4]_s$ blocked ply specimen is larger than in the $[45_2/90_2/-45_2/0_2]_s$ specimen, which is half the thickness, even though the load is not yet doubled. This is due to the thicker ply blocks in the first case having a greater propensity to delaminate due to the increase in energy available as can be determined from fracture mechanics. It is indeed this same mechanism which results in the greatly reduced delamination area of the dispersed ply specimen. At the -45/0 interface in the blocked ply specimens it can be seen that there is a much longer delamination which at its extremities becomes bounded by two 0° ply cracks. It is this delamination which causes the ultimate failure of the specimens as it reaches the free edge. The block of 0° plies which has completely delaminated from the adjacent plies can then be seen at the ends of the specimen as in Fig 5.1.3-4.

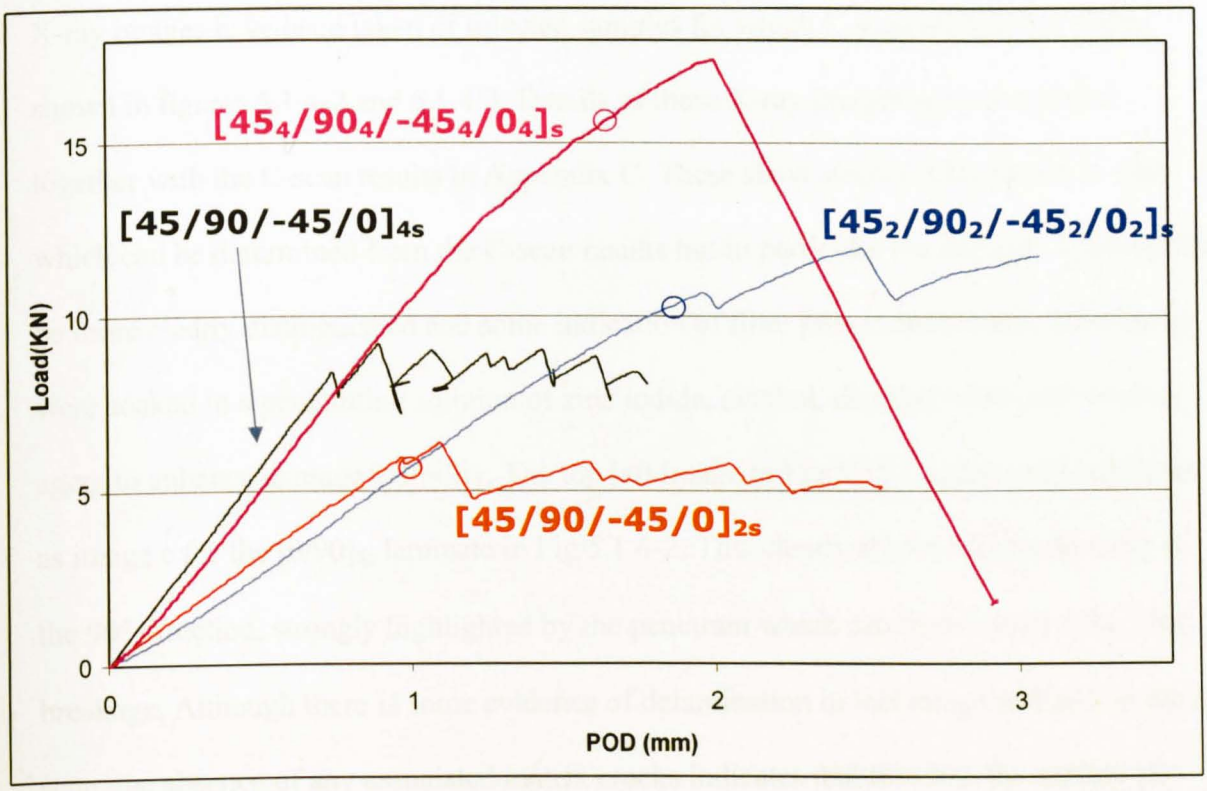

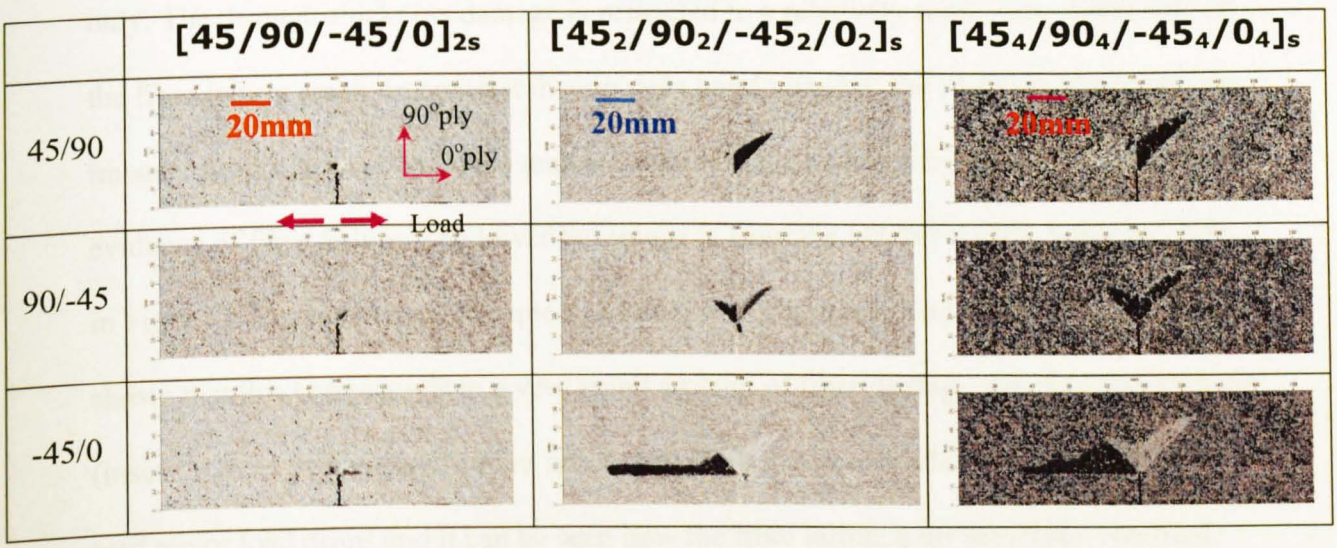

Fig 5.1.4-3 C-scan results of quasi-isotropic laminates at different interfaces

5.1.5 X-ray images

X-ray images have been taken of selected samples for which C-scan images have been shown in figures 5.1.4-2 and 5.1.4-3. Details of these X-ray images are summarized together with the C-scan results in Appendix C. These show similar information to that which can be determined from the C-scan results but in particular the intra-ply splitting can be more clearly distinguished and some indication of fibre failure determined. Specimens were soaked in a penetrating solution of zinc iodide, alcohol, distilled water and wetting agent to enhance damage visibility. The top left image in Fig 5.15-1 is the same specimen as image c for the $[0/90]_{8s}$ laminate in Fig 5.1.4-2. This clearly shows a line extending in the 90° direction, strongly highlighted by the penetrant which can be assumed to be fibre breakage. Although there is some evidence of delamination in this image and also in the c-scan, the absence of any associated matrix cracks indicates that this is in the surface ply only. The through-thickness damage is restricted to a relatively small zone either side of the fibre failure crack. In contrast the top right hand image of the $[0_4/90_4]_{2s}$ laminate (also image c from Fig 5.1.4-1) shows major delaminations, bounded by matrix cracks and no evidence of fibre failure. The lower left image is from the $[45/90/-45/0]_{2s}$ laminate shown in Fig 5.1.5-1, which was interrupted just after the first minor load drop. The x-ray image shows that this corresponds to a very small amount of fibre damage ahead of the crack tip (inset 1). Inset 2 shows a different specimen which has been loaded substantially further, past major load drops and it can be seen how the fibre failure path develops. The final, bottom right image shows the same $[45_2/90_2/-45_2/0_2]_s$ laminate as the c-scan in Fig 5.1.4-3. This again highlights the extensive delamination, bounded by matrix cracks and indicates the absence of any fibre failure. It can also be seen that there are a number of discrete cracks within the delaminated area at almost regular intervals.

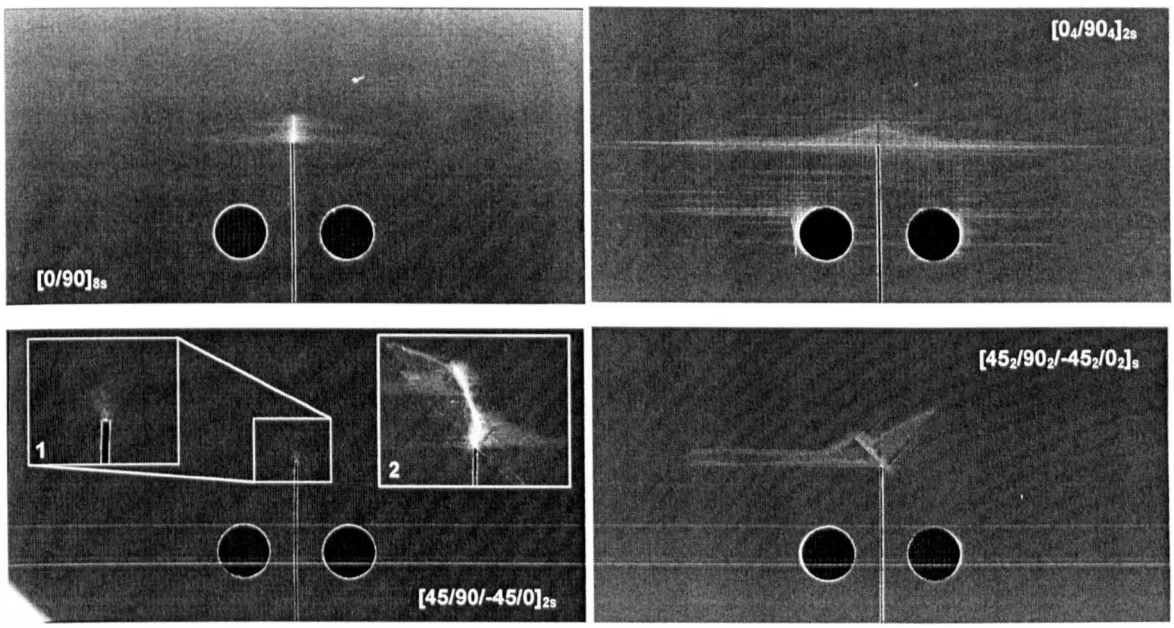

Fig 5.1.5-1 X-ray images of 4mm cross-ply and 2mm quasi-isotropic specimens, both dispersed and blocked plies

5.1.6 Summary and Conclusions

In this work the Over-height Compact Tension (OCT) test has been used to investigate the damage interaction and propagation in notched laminates. 8 different lay-ups of IM7/8552 carbon-epoxy laminates with OCT geometry were tested. The results show that the layup and ply block thickness (stacking sequence of laminates) has a significant influence on the failure mode and propagation of damage. When ply blocks are thin as in the dispersed ply laminates, damage growth is restricted. This promotes fibre failure and crack growth through the whole thickness since the local stress at the notch tip is higher due to the reduced notch "blunting" by the damage. Load curves of dispersed ply specimens are approximately linear before the first load drop. The through-thickness crack progresses across the width of the specimen in a series of small "jumps" which result in further load drops. The overall trend is for the crack growth to progress at approximately constant load. The size of these jumps varied widely from test to test for each lay-up and was not obviously related to the tow size. But in general load jumps in the quasi-isotropic laminates were much smaller than those in cross-ply laminates, which might suggest that 45° and -45° plies could help reduce the stress accumulation in the 0° plies and foster smoother or more stable fibre breakage progressing.

In contrast, thicker ply blocks in the ply blocked specimens promote a larger amount of splitting and delamination and cause a larger process zone. Due to this splitting and delamination, the load curves of specimens with blocked plies show a large degree of nonlinearity. These specimens generally failed suddenly due to blocks of plies pulling out via delamination. Damage initiation or "first ply failure" of blocked ply specimens is lower than that of dispersed ply specimens with the same thickness. This however results in a significant reduction of the stress concentration at the notch tip that ultimately results in a tougher laminate. The main focus of this work has been to look at the effect of sub-critical damage and damage mode interaction. Variations in the size of the process zone have been controlled by changing the ply block thickness and hence the propensity for the different layups to split and delaminate. It could be argued that in the case of the blocked ply specimens the process zone has become so large that the specimen size is no longer sufficient. If the delamination were to be allowed to continue to grow in a larger specimen, eventually the fibre failure stress at the notch would be exceeded and a through thickness crack would start to propagate. This would be an interesting study for future work.

5.2 Modelling Overheight Compact Tension (OCT) Tests

The OCT specimen tests described in section 5.1 were analysed using the modelling tools developed in chapters 3 and 4. This is described in detail in the sections below.

5.2.1 Model Setup

Splitting and delamination were modeled using discrete interface elements with mixed mode failure criteria being implemented. Fibre dominated element failure used the global Weibull statistical failure theory implemented in Umat44. Material properties for interface elements and fibre dominated element failure models used the same values as for IM7/8552 in the Open Hole Tension tests in Section4.4.

1. Mesh in thickness direction

Each individual ply was modeled with one solid element in the thickness direction. Eight different layups were considered, four cross-ply and four quasi-isotropic. For each of the cross-ply and quasi-isotropic layups there were 2 and 4mm thick laminates. Each thickness for each layup included a blocked ply and dispersed ply variant. The total number of elements in the thickness direction for different lay-ups are shown in Table 5.2.1-1. Cohesive elements were put between plies to simulate the delamination within a laminate.

Table 5.2.1-1 Number of elements in thickness direction for different lay-ups

Layup	Number of elements in thickness direction	Layup	Number of elements in thickness direction
$[0/90]_{4s}$	8	$[0_2/90_2]_{2s}$	4
$[0/90]_{8s}$	16	$[0_4/90_4]_{2s}$	4
$[45/90/-45/0]_{2s}$	8	$[45_2/90_2/-45_2/0_2]_s$	4
$[45/90/-45/0]_{4s}$	16	$[45_4/90_4/-45_4/0_4]_s$	4

2. In-plane mesh

In the 45° and -45° plies, there are 6 potential splits modeled from the edge of the notch with 0.5mm offset. These are included through lines of coincident nodes joined by the cohesive interface elements. In the 90° plies, there are 3 splits. In the 0° plies, there is 1 split before the notch tip, 1 split right through the notch tip and 24 splits after the notch tip. Details of the potential splits in different plies are summarized below and shown in Fig

5.2.1-1. This particular arrangement of splits in various plies refers to X-ray images of specimens in Appendix C, in which intra-ply splitting can be clearly distinguished.

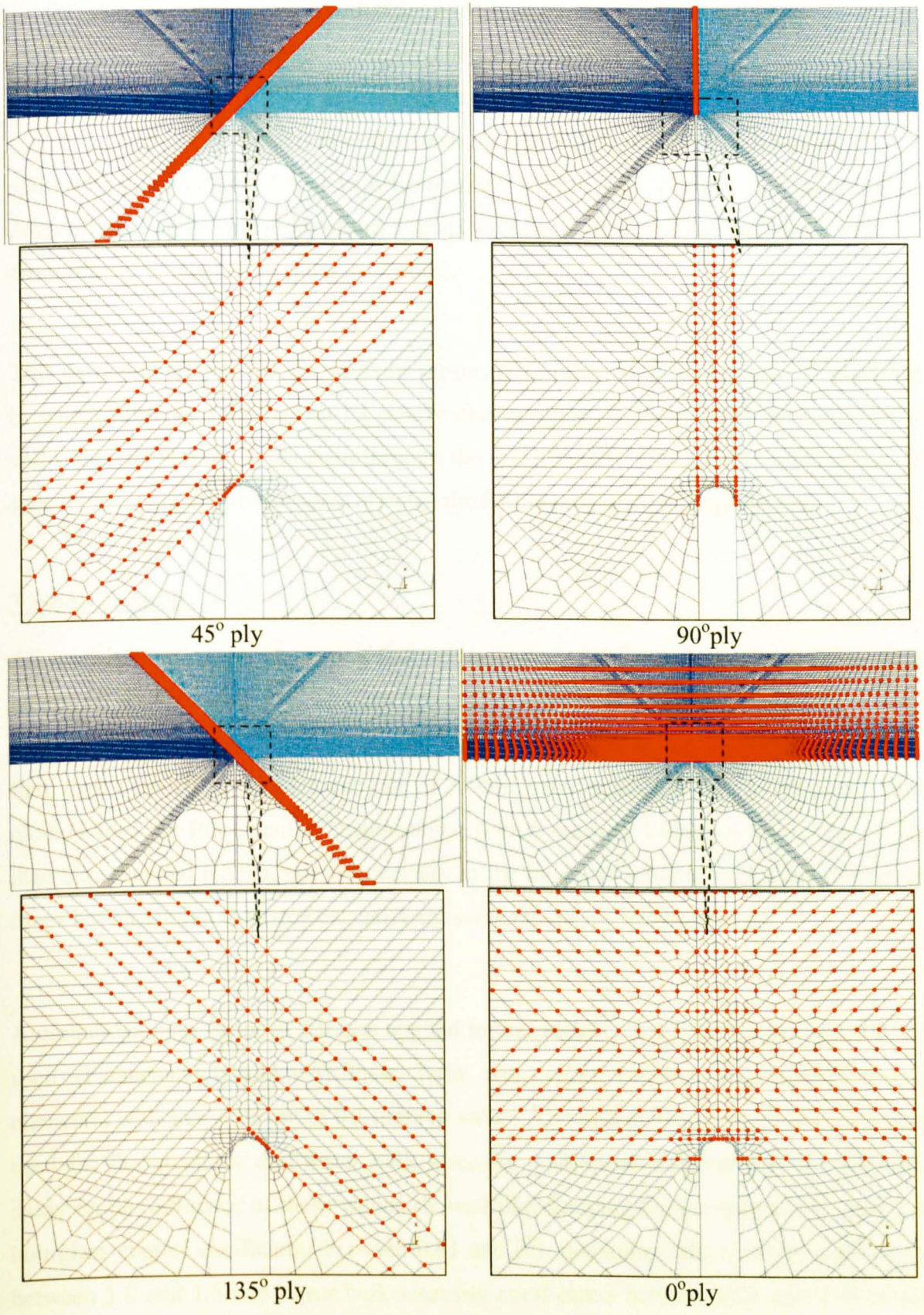

Fig 5.2.1-1. Details of splits put within plies

Details of the splits are:

45° and -45° plies: 6 splits from the tip of the notch with 0.5mm offset

90° plies: 3 splits with 0.5mm offset at the center of the specimen

0° plies: 1 splits before the notch tip with 0.5mm offset

1 splits right through the notch tip

1 splits after the notch tip with 0.213mm offset, followed by 13 splits with 0.5mm offset, 2splits with 1mm offset, 1 splits with 2mm offset, 3 splits with 3mm offset, 1 splits with 4mm offset, 1 splits with 5mm offset and finally 2 splits with 6mm offset.(altogether 26 splits in 0° plies).

This particular arrangement of splits in various plies refers to X-ray images of specimens, in which intra-ply splitting can be clearly distinguished. A study about the influence of splits showed that the splits right through the notch largely affected the initial failure of specimens and splits off the notch affected the failure propagation in specimens.

3 Model Controls

All models were run in the explicit finite element code LS-Dyna. Due to symmetry of the layup, all models used half models through the thickness as shown in Fig 5.2.1-2. A thermal load with temperature decreasing from 180° C to 20° C was applied to each model first, then a prescribed motion with rate of 200mm/s was applied at each of the holes of the models until the Pin Opening Displacement (POD) reached 3.8mm or more. The higher than experimental loading rate is necessary in the model to achieve reasonable simulation times but monitored to ensure excessive dynamic effects are not introduced.

A global damping factor of 1.0 was applied in the models. Type 5 hourglass control was used (Flanagan-Belytschko stiffness form with exact volume integration for solid elements) with a co-efficient of 0.1 (default value). The default values of 1.5 and 0.06 were used for the quadratic and linear bulk viscosity coefficients respectively. A parametric study on the influence of these values showed that damping factors between 0.1 and 3.0, hourglass control coefficients between 0.01 and 0.1, quadratic bulk viscosity coefficients between 1.0 and 1.5 and linear bulk viscosity coefficients between 0.01 and 0.06 would have very small influences on the simulation results.

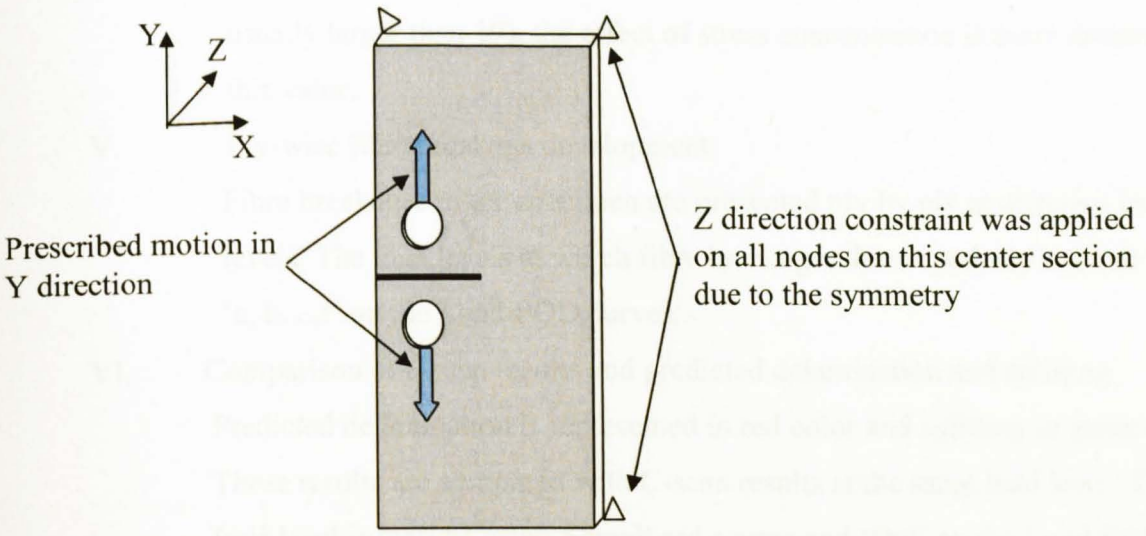

Fig 5.2.1-2 Load and boundary conditions of the specimen

5.2.2 Simulation Results

Model results are summarized in

I. Load-POD curves

II. Maximum elemental fibre direction stress curves

In each step, the maximum elemental fibre direction stress in the whole specimen was found and stored in the historic variable. Its value vs. POD is presented here. This curve shows how different the Weibull integration criterion is from the maximum stress failure criterion.

III. Global Weibull integrations $\sum_{i=1}^{TotalNoofSolidElements} \left(\frac{\sigma_i}{\sigma_{unit}}\right)^m V_i$, this indicates the overall failure probability of the whole specimen and more accurately captures the fibre failure behavior in loading.

:

IV. Maximum elemental contributions to Weibull integration:

$$\underset{i=x}{\overset{TotalNoofSolidElements}{Max}} \left(\left(\frac{\sigma_i}{\sigma_{unit}}\right)^m V_i\right)$$

This indicates the maximum failure probability of a single element in loading and reflects the stress concentration level. The closer to 1.0 this

value is the higher stress concentration exists in the specimen. Though this value is also affected by element size, due to the large value of m(m is usually larger than 19), the effect of stress concentration is more dominant in this value.

V. Ply-wise fibre breakage development

Fibre breakages in the specimen are presented ply by ply at different load levels. The load levels at which fibre breakages developed, are marked with 'a, b, ..,f' on the Load-POD curves..

VI. Comparison of c-scan results and predicted delamination and splitting

Predicted delamination is represented in red color and splitting in green color. These results are compared with C-scan results at the same load level. This load level is marked using a small red square and 'Del' on the Load-POD curves.

VII. Comparison of experimental surface failure and model predictions. For some layups, this also includes a comparison of internal fibre failure from X-ray scan results and model predictions.

1.Results of blocked ply $[45_4/90_4135_4/0_4]_s$(4mm) laminates

Load-POD curves(I), maximum elemental fibre direction stresses(II), global Weibull integration(III), maximum elemental contribution to Weibull integration(IV), ply-wise fibre breakage development(V) and comparison of delamination, splitting(VI) and surface failure(VII) of this lay-up are presented in from Fig 5.2.2-1 to Fig 5.2.2-4 respectively.

It can be seen that apart from a removed single element at POD=0.72mm (point a in Fig 5.2.2-1) in the 45° ply (this element was removed for its large deformation to avert numerical collapse), there was no further fibre breakage development in the model until the catastrophic failure of the specimen. The non-linearity in the curve derives from the large scale delamination occurring. The final failure of the model was characterized by the pull-out of a block of 0° plies just ahead of the notch and surface 45° ply delamination. This failure mode is very similar to the experimental observation as shown in Fig 5.2.2-4. The predicted 0° ply pullout width is 8.7mm, which is slightly smaller than the experimental range of 11-17mm. Since the load-POD curves of this lay-up are very similar (refer to Fig

5.1.3-1), only a typical experimental result as that in Fig 5.1.4-3 was compared with the model result in Fig 5.2.2-1.

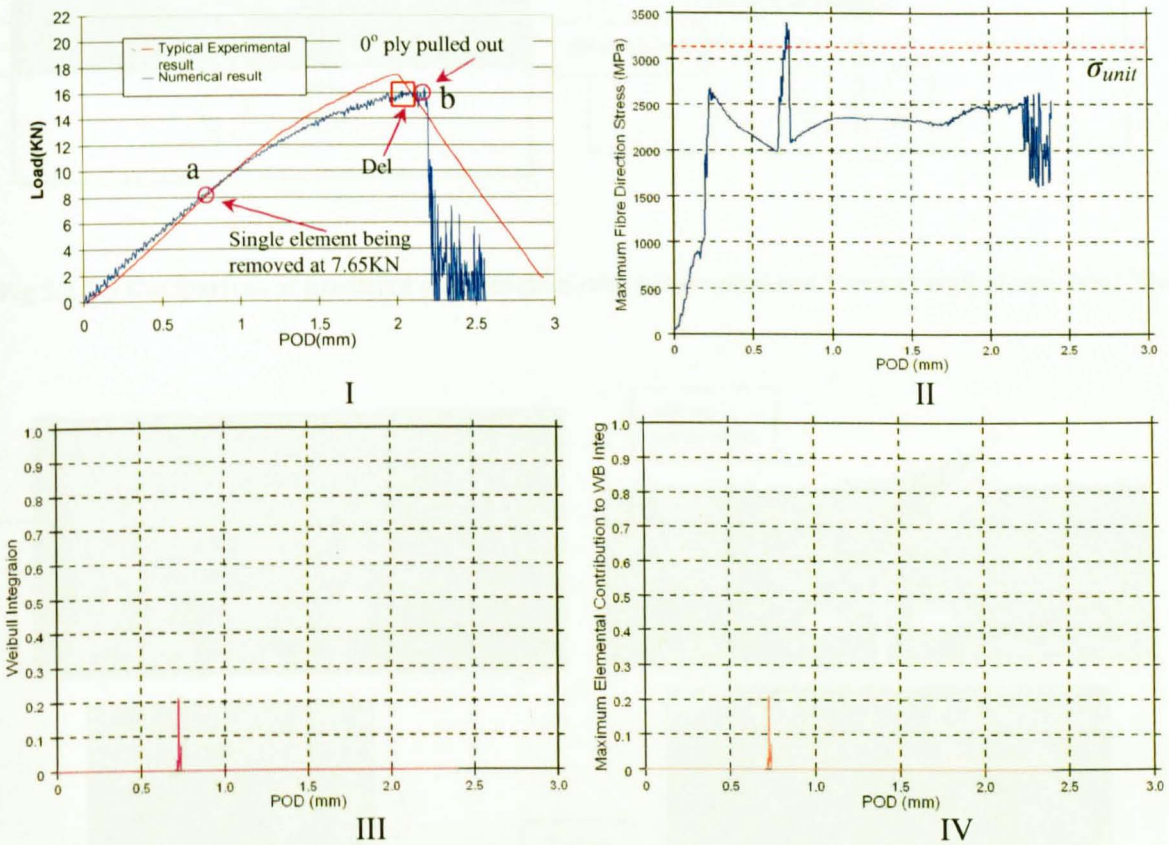

Fig 5.2.2-1 Load-POD, maximum elemental fibre direction stress, global Weibull integration and maximum elemental contribution to weibull integration curves

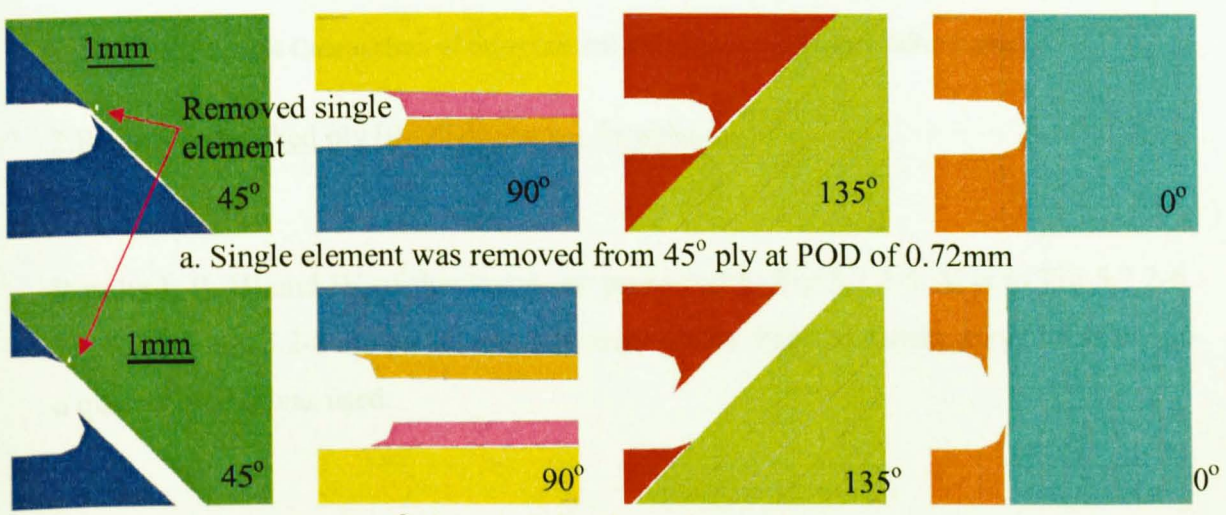

Fig 5.2.2-2 Fibre breakage development in plies and splitting

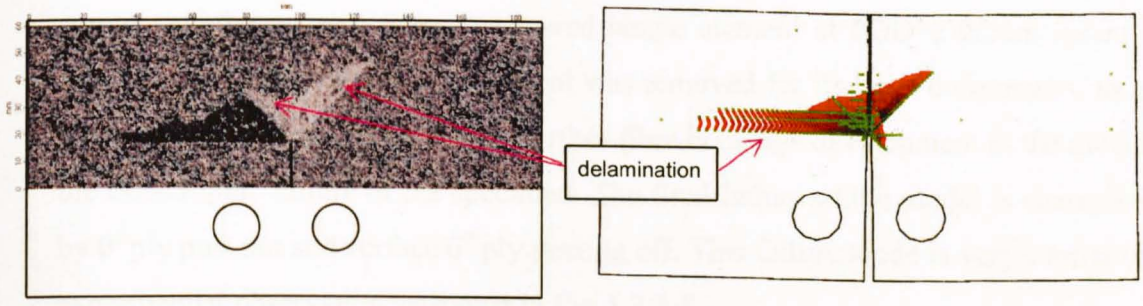

Fig 5.2.2-3 Comparison of predicted delamination with interrupted test C-scan result at load level 'Del'

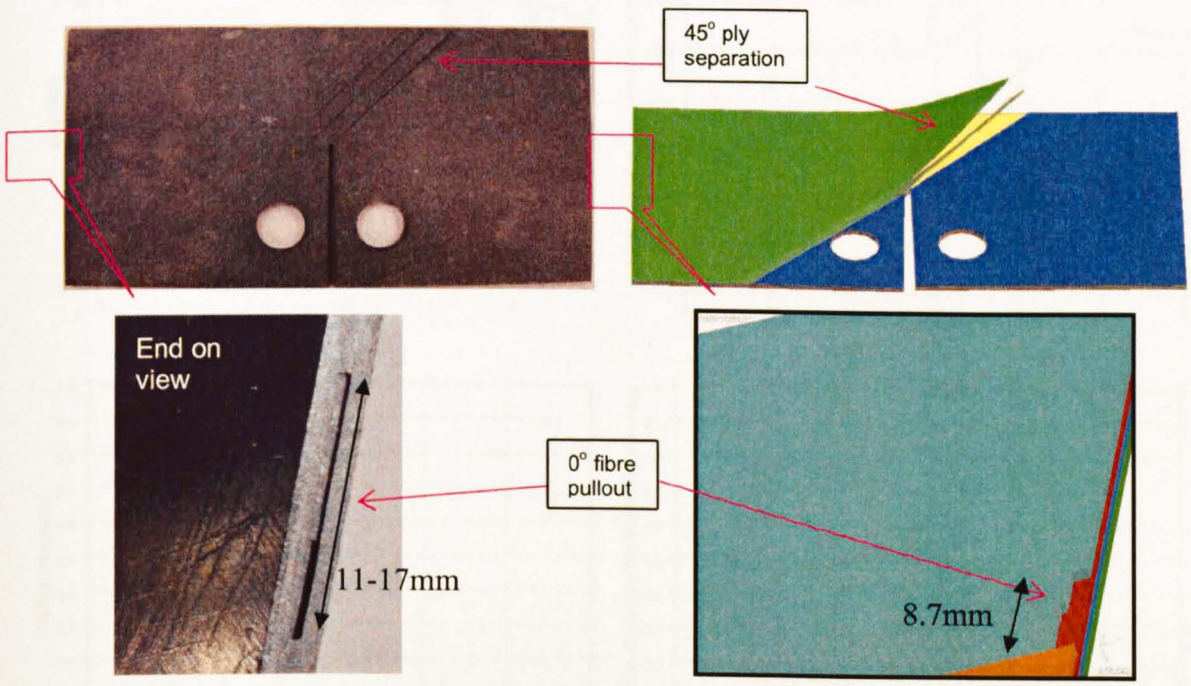

Fig 5.2.2-4 Comparison of experimental and predicted surface failure mode

2.Results of blocked ply $[0_4/90_4]_{2S}$(4mm) laminates

Results I, II, III and IV of this layup are presented in Fig 5.2.2-5. V is in Fig 5.2.2-6. Fig 5.2.2-7 and 3.2-8 are for VI and VII respectively. From the symmetry of this lay-up a quarter model was used.

The delamination images taken at points marked "Del" in figure 6 were from very slightly different load levels due to the model not quite achieving the load level at

which the test was interrupted. In this case the model image is taken from just prior to complete failure. Apart from a removed single element at POD=2.92mm (point a in Figure 6) in the 2nd 0° ply (this element was removed for its large deformation to avert numerical collapse too), there is no further fibre breakage development in the model till the catastrophic failure of the specimen. The final failure of the model is characterized by 0° ply pull-out and surface 0° ply peeling off. This failure mode is very similar to the experimental observation as shown in Fig 5.2.2-8.

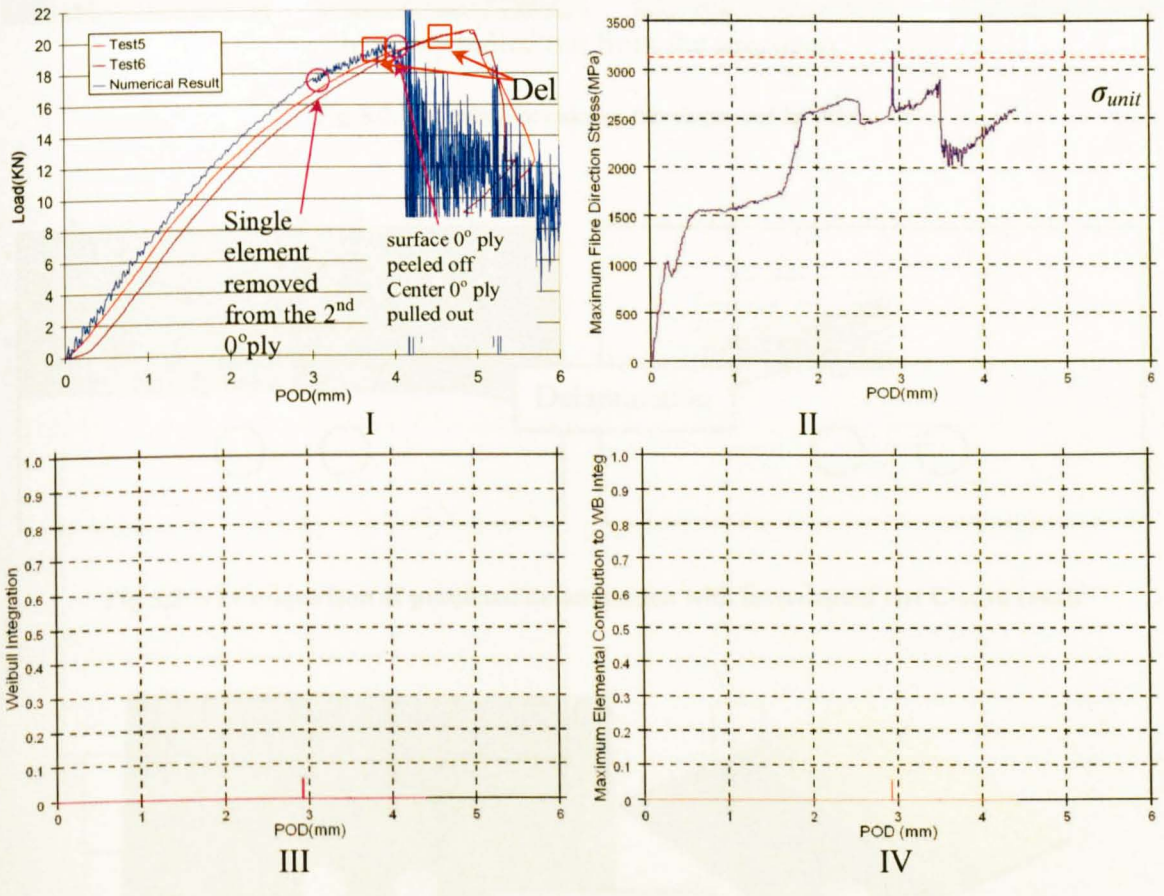

Fig 5.2.2-5 Load-POD, maximum elemental fibre direction stress, global Weibull integration and maximum elemental contribution to Weibull integration curves

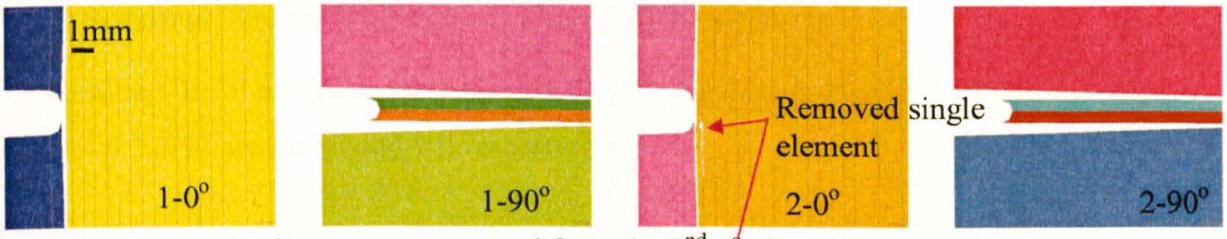

a. Single element was removed from the 2nd 0° ply at POD of 2.92mm

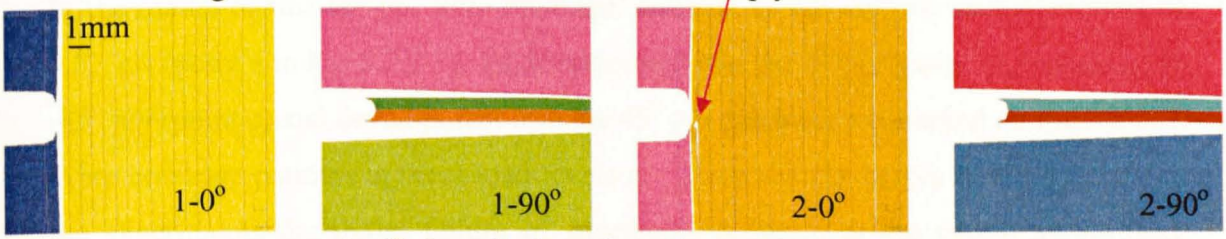

b. 0° ply pulled out from the specimen

Fig 5.2.2-6 Fibre breakage development in plies

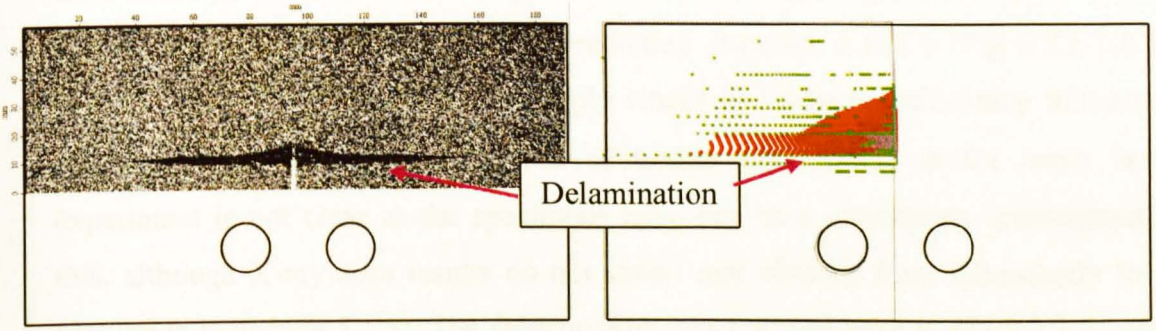

Fig 5.2.2-7 Comparison of predicted delamination with interrupted test C-scan result

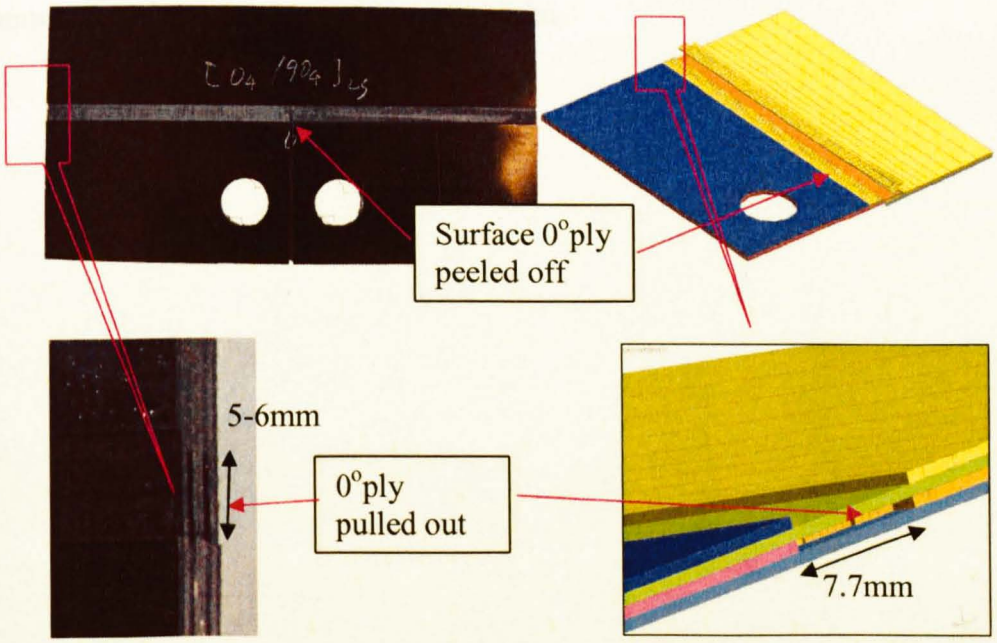

Fig 5.2.2-8 Comparison of experimental and predicted surface failure mode

3. Results of blocked ply $[45_2/90_2/135_2/0_2]_s$(2mm) laminates

Results I, II, III and IV are presented in Fig 5.2.2-9. V is in Fig 5.2.2-10. Fig 5.2.2-11 and 5.2.2-12 are for VI and VII respectively.

In the model of this lay-up, fibre breakage initiated in the -45° ply at a load level of 9.57 kN (point a in Fig 5.2.2-9). Its development into the 0° ply (point b), expansion in -45° ply (point c) and development into the 45° ply (point d) are marked on Fig 5.2.2-9. Fibre breakage patterns at these load levels are presented ply by ply in Fig 5.2.2-10 In the experiments the initial failure of specimens occurred at the notch but no fibre failure was observed on the surface till the specimens finally failed by crushing at the back end, a mode which is not included in the model. The model failed by extensive fibre breakage in the 45° and -45° plies which eventually progressed to the 0° plies. It can be seen that the -45° ply failure prediction at points d and e (Fig 5.2.2-10) has extended beyond the zone of inserted ply cracks and now unrealistically follows the adjacent 0° ply crack. The presence of tensile fibre failure at the notch in the experiment is not clear as the specimens have not been extensively interrogated for this, although X-ray scan results do not show any obvious fibre failure(refer to the discussion in section 5.1.5). The delamination patterns compared in Fig 5.2.2-11 are in reasonable agreement but the numerical prediction is not as extensive as the experimental C-scan result. The visual appearance of the two failure modes is compared in Fig 5.2.2-12, and is very similar.

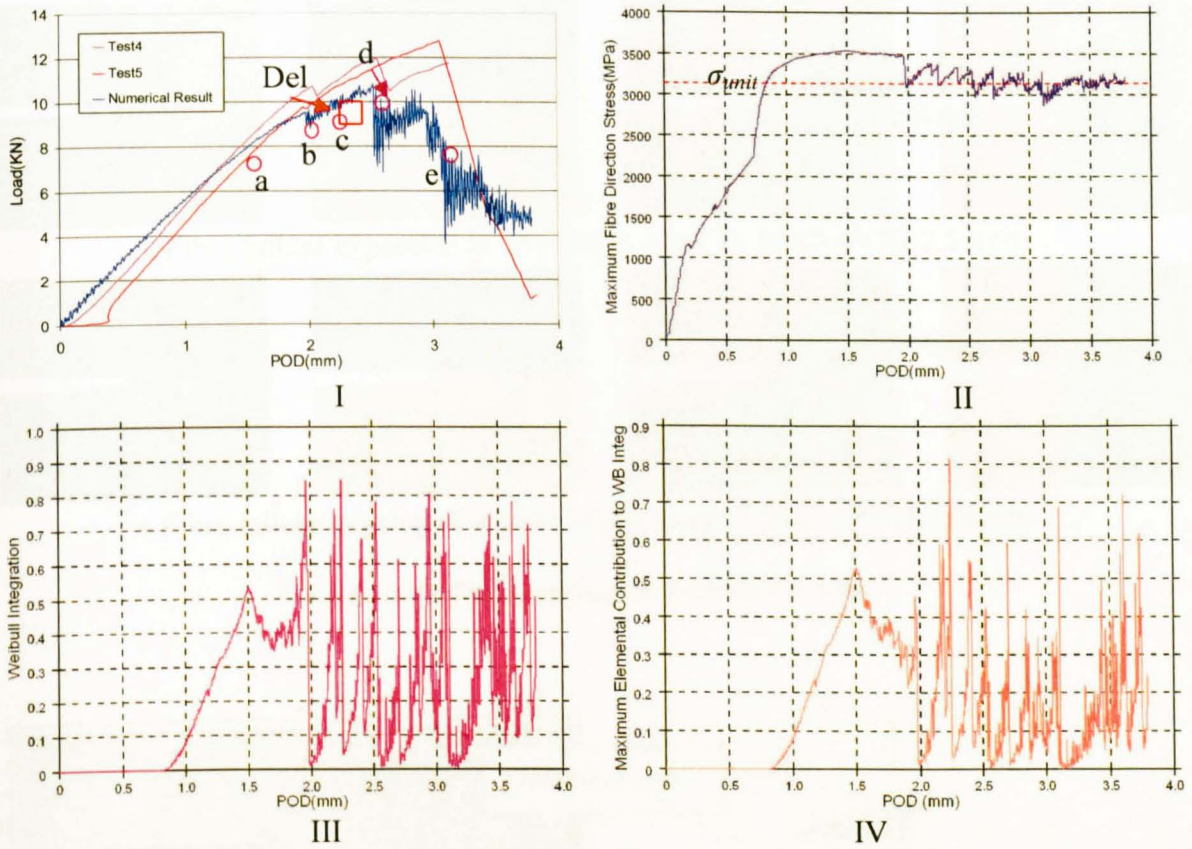

Fig 5.2.2-9 Load-POD, maximum elemental fibre direction stress, global Weibull integration and maximum elemental contribution to weibull integration curves(due to the numerical precision, the output Weibull integration didnot go to 1)

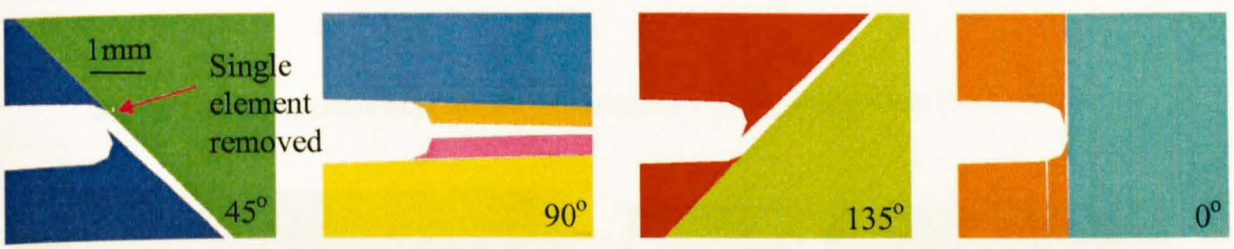

a. Single element was removed from 45° ply at Load:7.95KN-POD:1.51mm

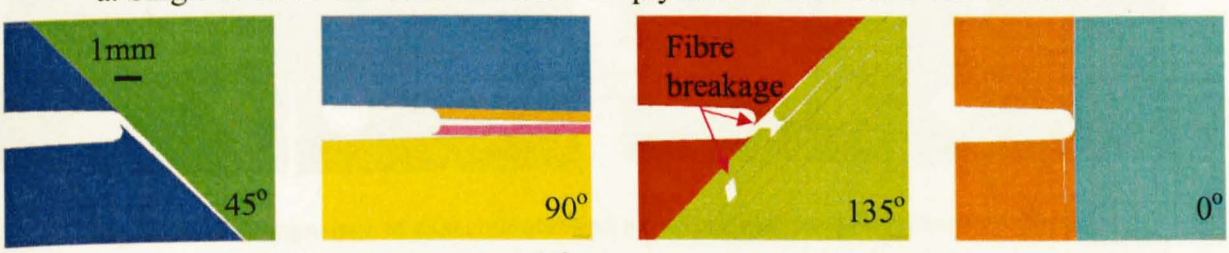

b. Fibre failure initiated at 135°ply at Load:9.57KN-POD:1.98mm

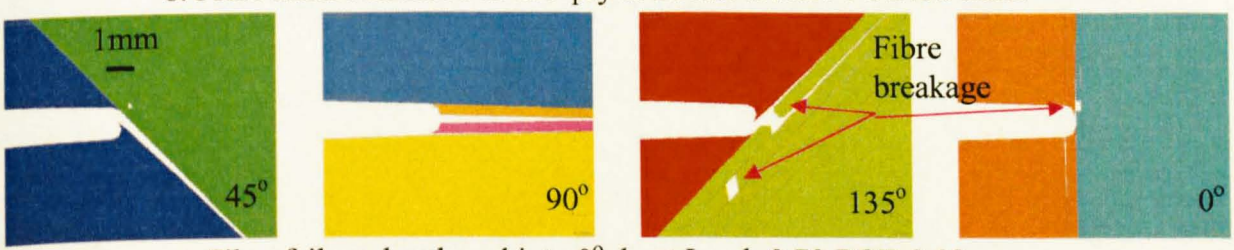

c. Fibre failure developed into 0°ply at Load: 9.78-POD.2.22mm

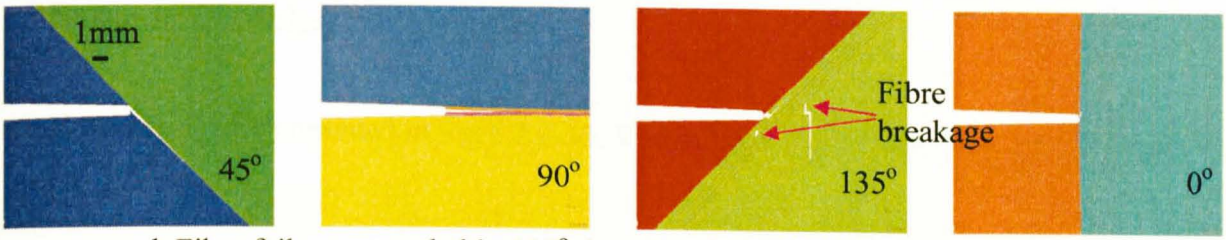

d. Fibre failure expanded in 135°ply at Load 10.80KN-POD:2.53mm

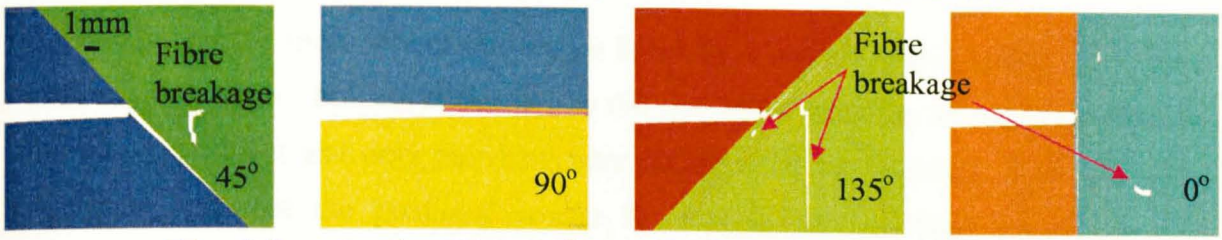

e Fibre failure developed into 45°ply at Load: 8.24KN-POD:3.08mm

Fig 5.2.2-10 Fibre breakage development in plies

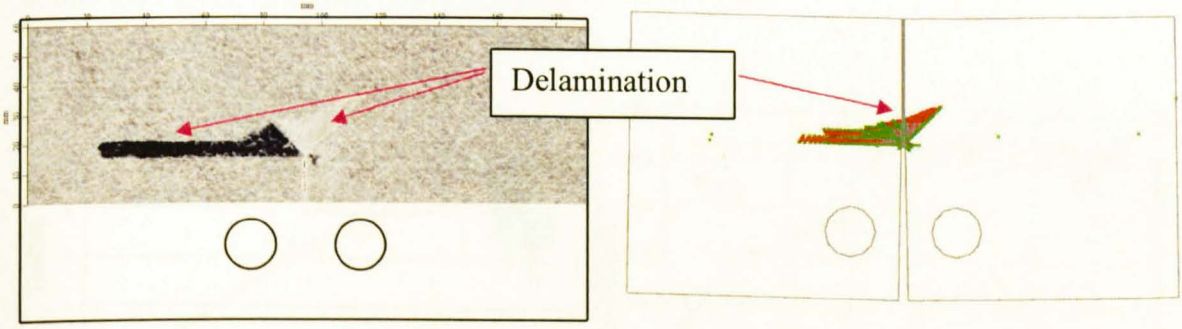

Fig 5.2.2-11 Comparison of predicted delamination with interrupted test C-scan result

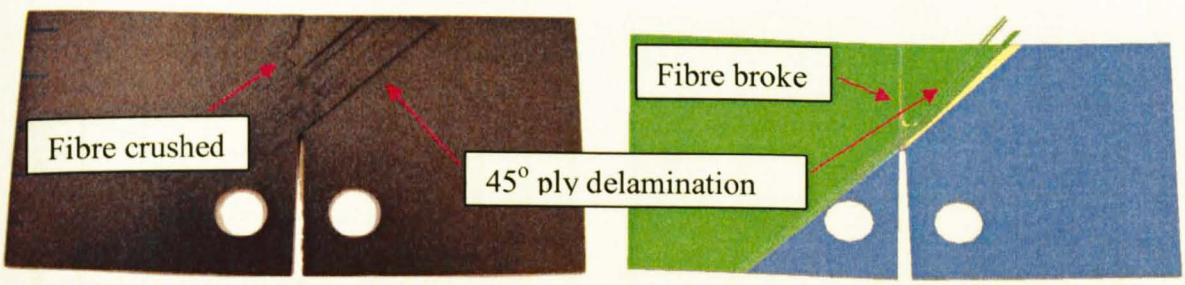

Fig 5.2.2-12 Comparison of experimental and predicted surface failure mode (8.72mm)

4.Results of $[0_2/90_2]_{2s}$(2mm) laminates

I, II, III and IV are presented in Fig 5.2.2-13. V is in Fig 5.2.2-14 and Fig 5.2.2-15 is for VI.

In the experiments, specimens of this lay-up failed by a form of global buckling at a load level of around 8kN. Models of this lay-up did not allow buckling due to the mid-plane symmetry constraint and only failed by fibre failure after the buckling load had been exceeded. Therefore the predicted results for this lay-up for final failure are not comparable with experimental results and only presented here as a reference in Fig 5.2.2-13. C-scan results showed that a large extent of delamination developed in the 0^o ply direction before the buckling failure of the specimens. The model gave similar predictions at this load level, as shown in Fig 5.2.2-15.

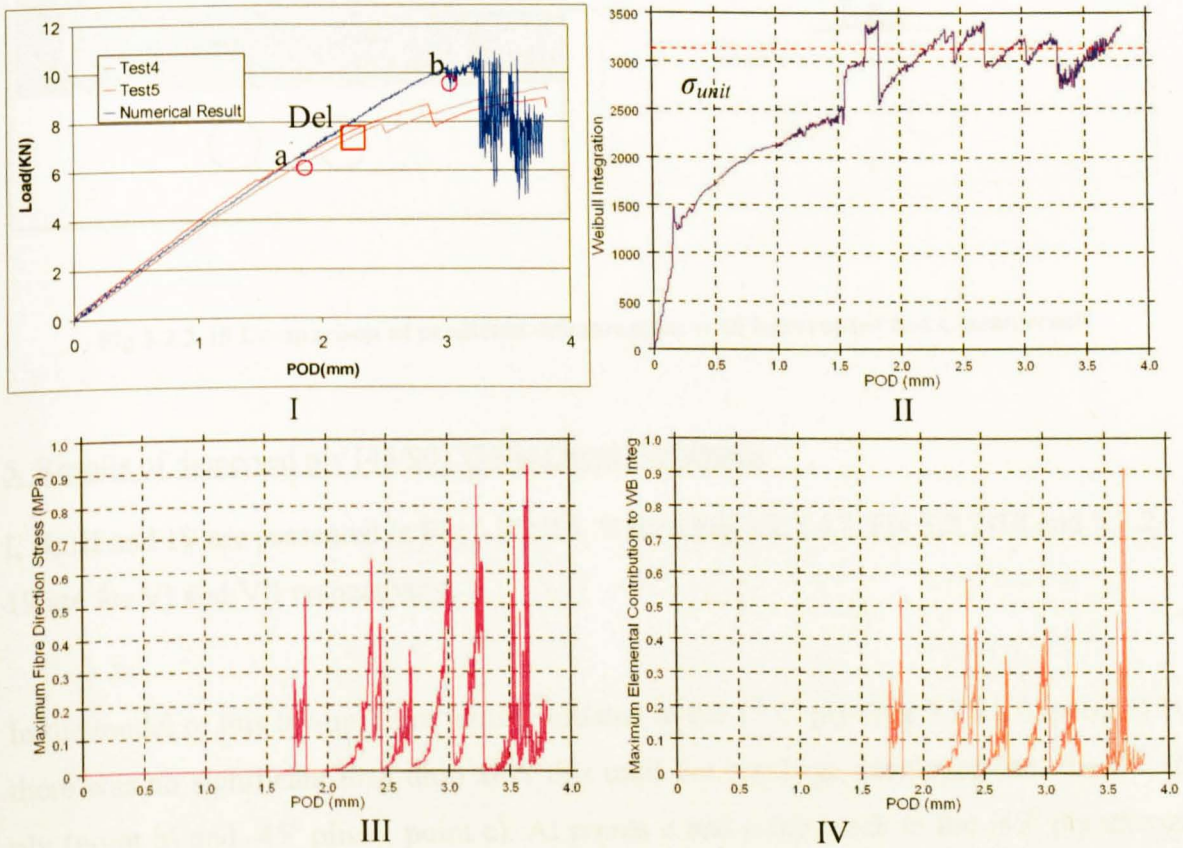

Fig 5.2.2-13 Load-POD, maximum elemental fibre direction stress, global Weibull integration and maximum elemental contribution to weibull integration curves

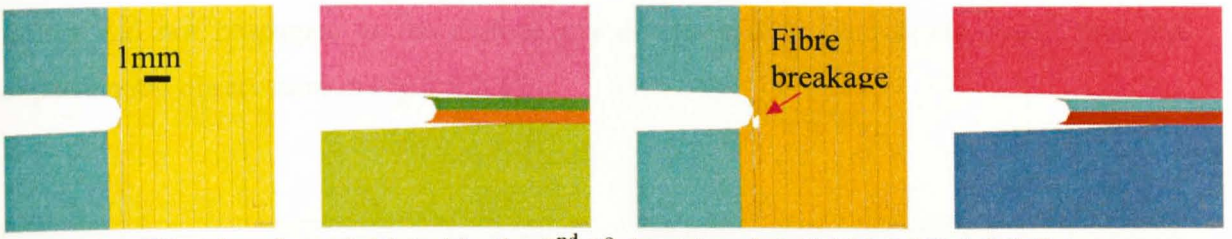

a. Fibre breakage initiated in the 2nd 0°ply at Load:6.61KN-POD:1.83MM

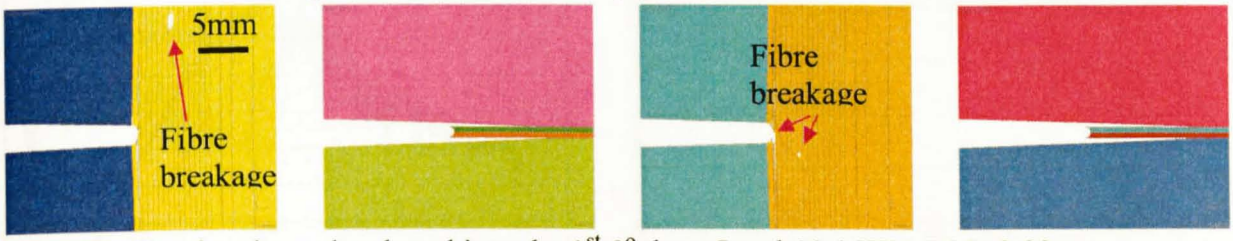

b. Fibre breakage developed into the 1st 0°ply at Load:10.15KN-POD:3.02mm

Fig 5.2.2-14 Fibre breakage development in plies

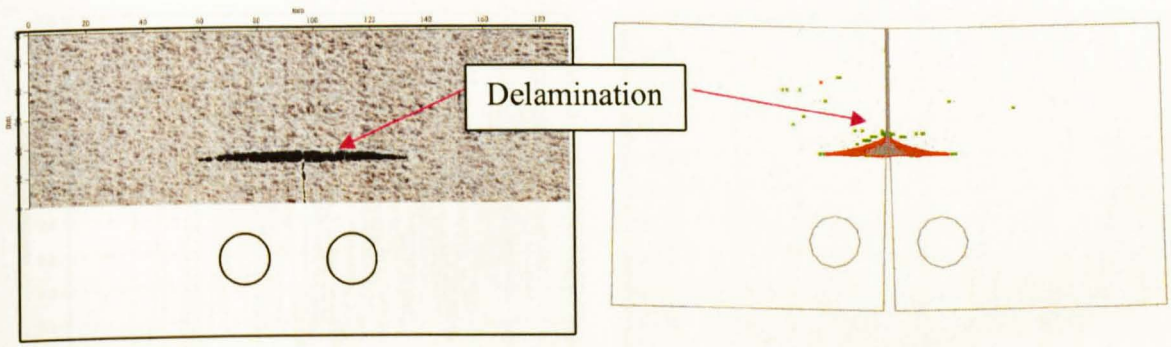

Fig 5.2.2-15 Comparison of predicted delamination with interrupted test C-scan result

5. Results of dispersed ply $[45/90135/0]_{2s}$(2mm) laminates

I, II, III and IV are presented in Fig 5.2.2-16. V is in Fig 5.2.2-17. Fig 5.2.2-18 and 5.2.2-19 are for VI and VII respectively.

In the model of this lay-up, fibre failure initiated in the 1st 0° ply (Fig 5.2.2-16, point a) but there was no significant load drop after this until the breakage developed into the 2nd 45° ply (point b) and -45° plies (point c). At points d and e the crack in the -45° ply extends beyond the region of the inserted intra ply cracks and unrealistically turns to follow the adjacent 0° ply splits. This load-POD curve is very similar to that of test no. 5. Both C-scan and model simulation showed that very limited delamination developed in this lay-up, as shown in Fig 5.2.2-18. There was extensive fibre failure inside the model but this

failure did not propagate to the surface ply of the model. This is consistent with the experimental observation in Fig 5.2.2-19.

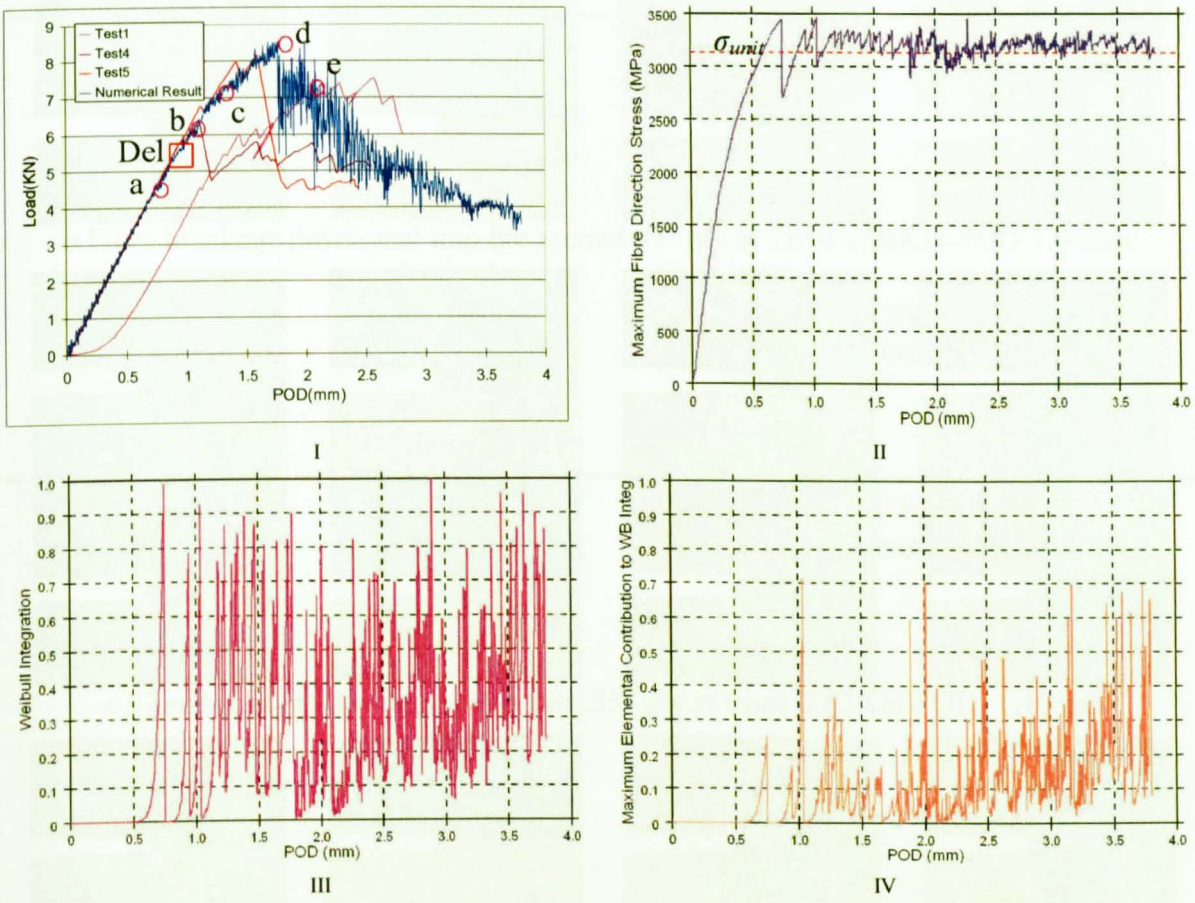

Fig 5.2.2-16 Load-POD, maximum elemental fibre direction stress, global Weibull integration and maximum elemental contribution to weibull integration curves

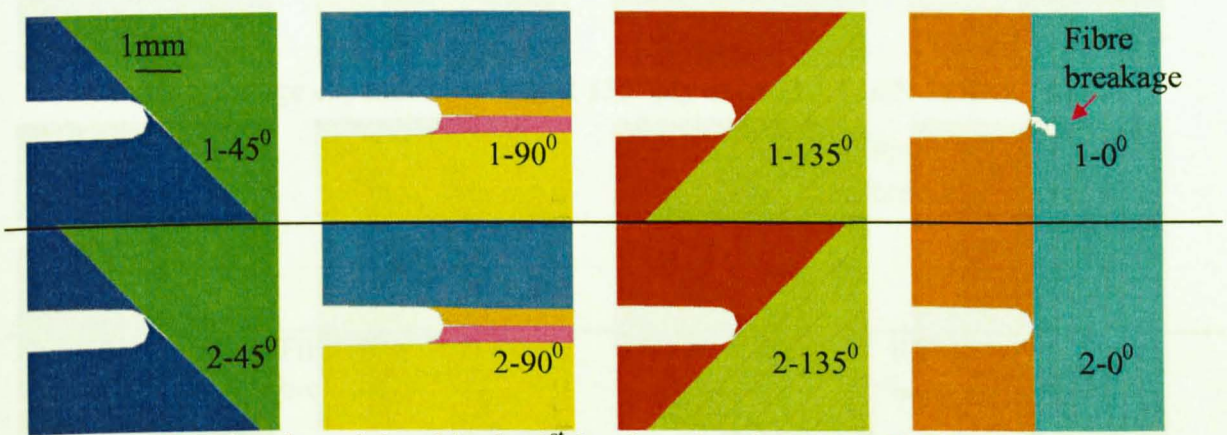

a. Fibre breakage iniated in the 1st 0o ply at Load 4.53KN-POD:0.75mm

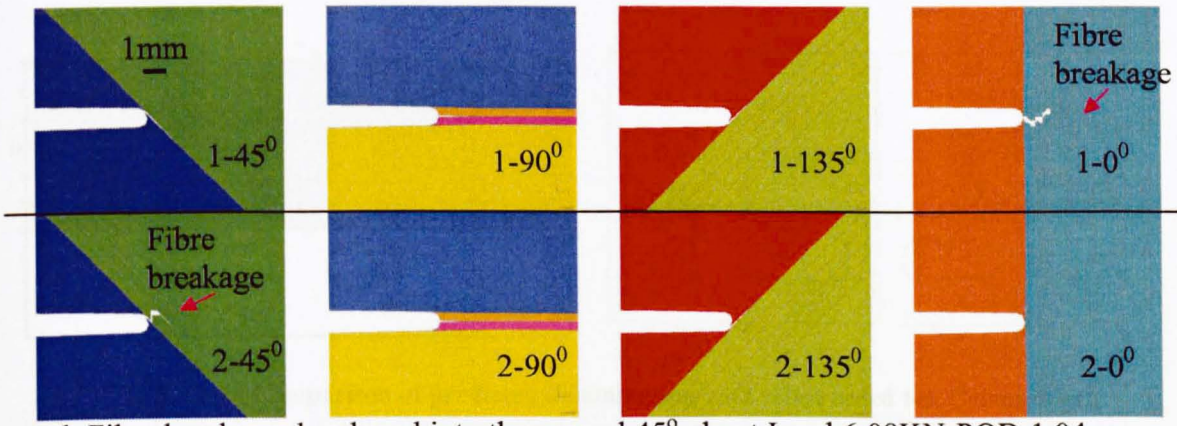

b Fibre breakage developed into the second 45° ply at Load 6.08KN-POD:1.04mm

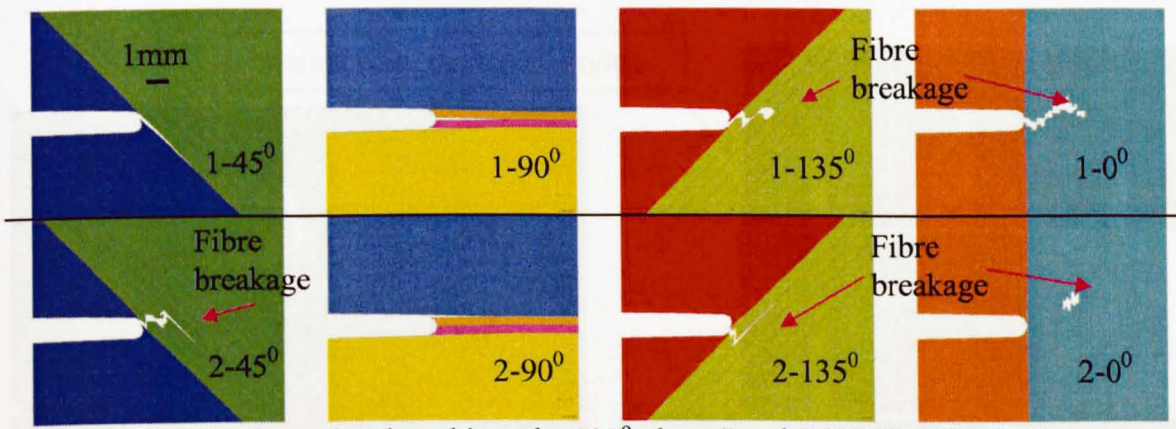

c Fibre breakage developed into the 135° ply at Load 7.03KN-POD: 1.40mm

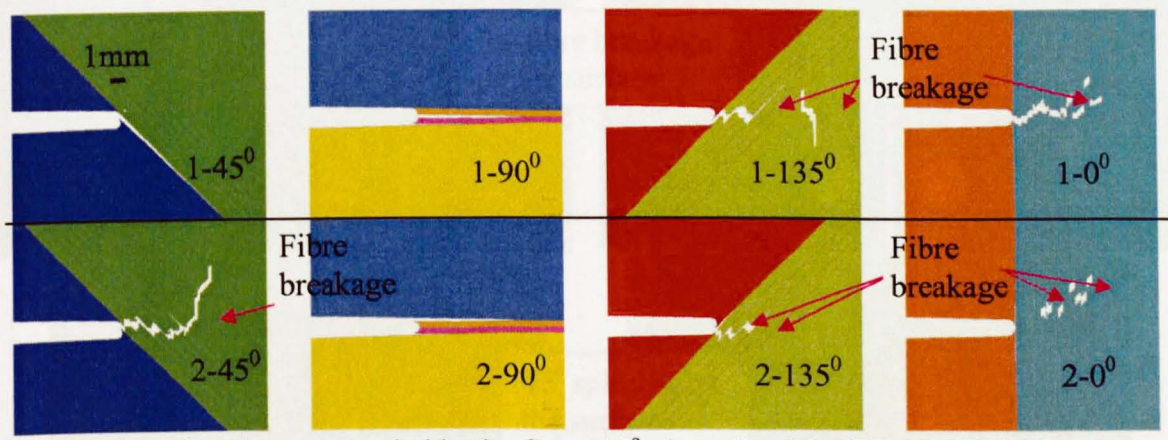

d. Fibre breakage expanded in the first 135° ply at Load 8.38KN-POD:1.78mm

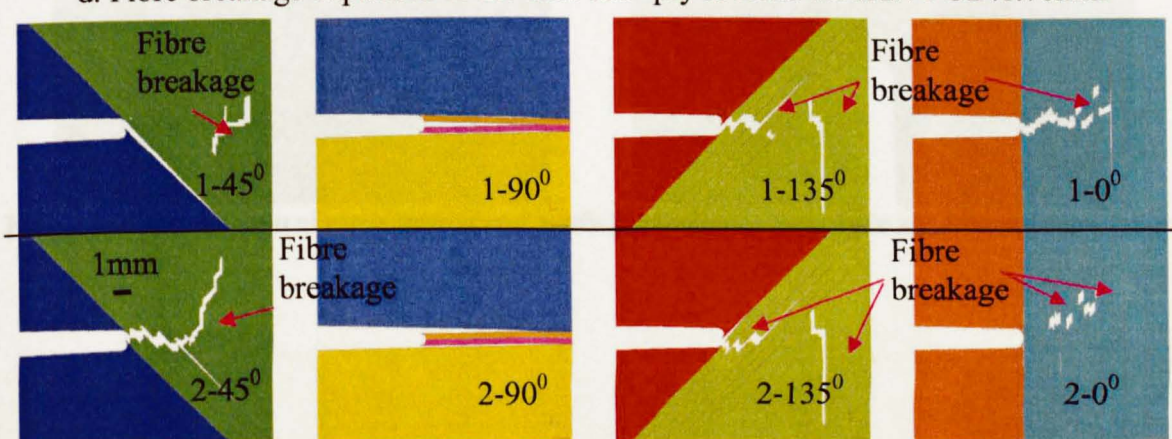

e. Fibre breakage developed to into the surface 45° ply at Load 7.22KN-POD:2.00mm

Fig 5.2.2-17 Fibre breakage development in plies

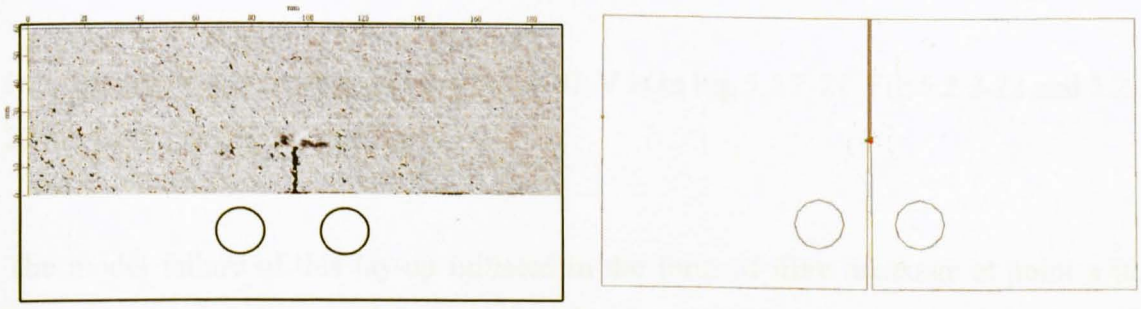

Fig 5.2.2-18 Comparison of predicted delamination with interrupted test C-scan result

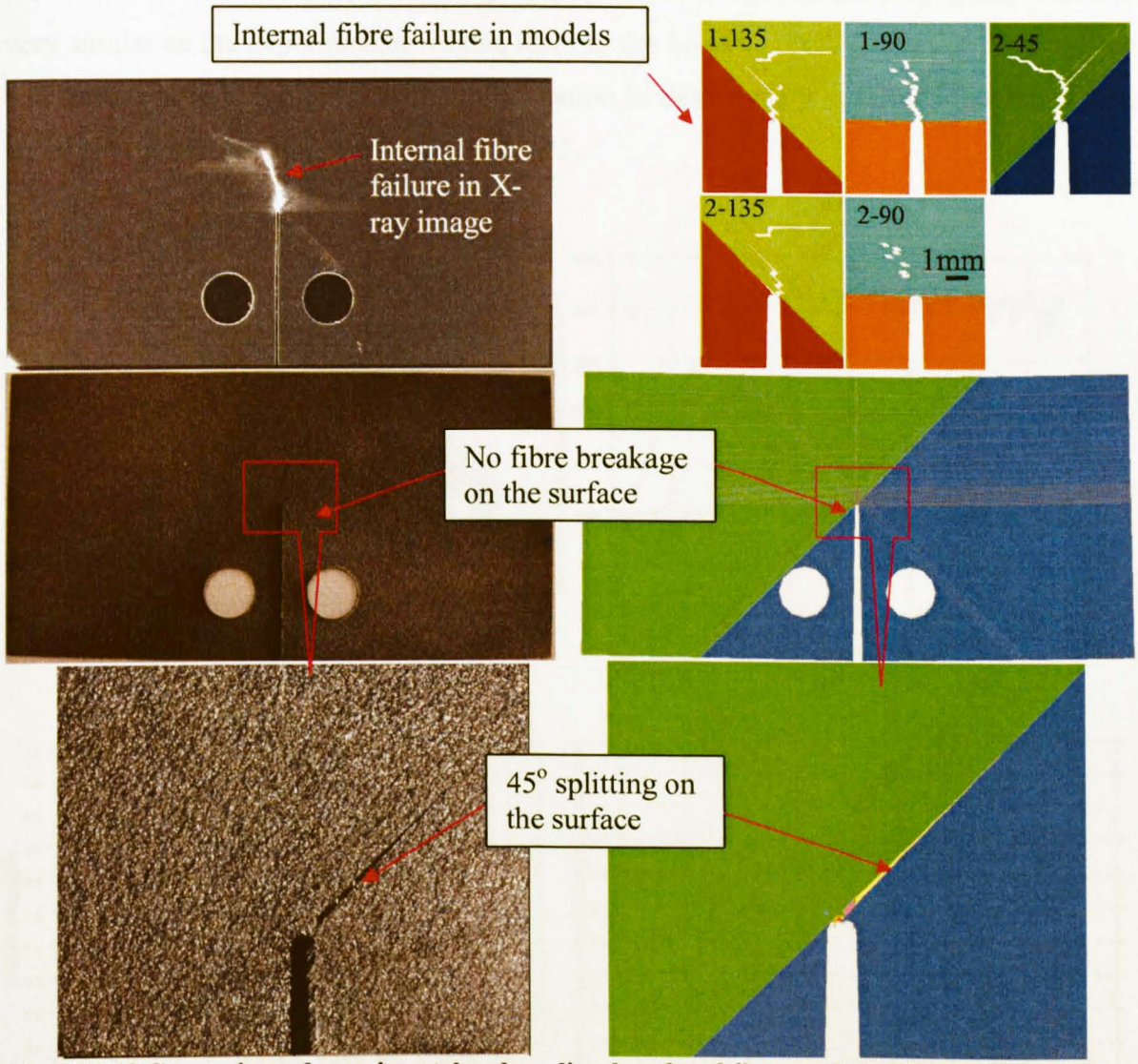

Fig 5.2.2-19 Comparison of experimental and predicted surface failure mode and internal fibre failure

6. Results of $[0/90]_{4s}$(2mm) laminates

I, II, III and IV are presented in Fig 5.2.2-20. V is in Fig 5.2.2-21. Fig 5.2.2-22 and 5.2.2-23 are for VI and VII respectively.

The model failure of this lay-up initiated in the form of fibre breakage at point a in Fig 5.2.2-20. After point a, fibre breakage developed stably along the centerline of the specimen toward the back. The load in this process experienced a series of small jumps till the crack was close to the back edge (points b, c and d). This failure propagation mode is very similar as the experimental results, refer to the Load vs. POD curves in Fig 5.2.2-20 and surface failure in Fig 5.2.2-23. Delamination in this lay-up was limited to a small area around the notch tip, as shown in Fig 5.2.2-22.

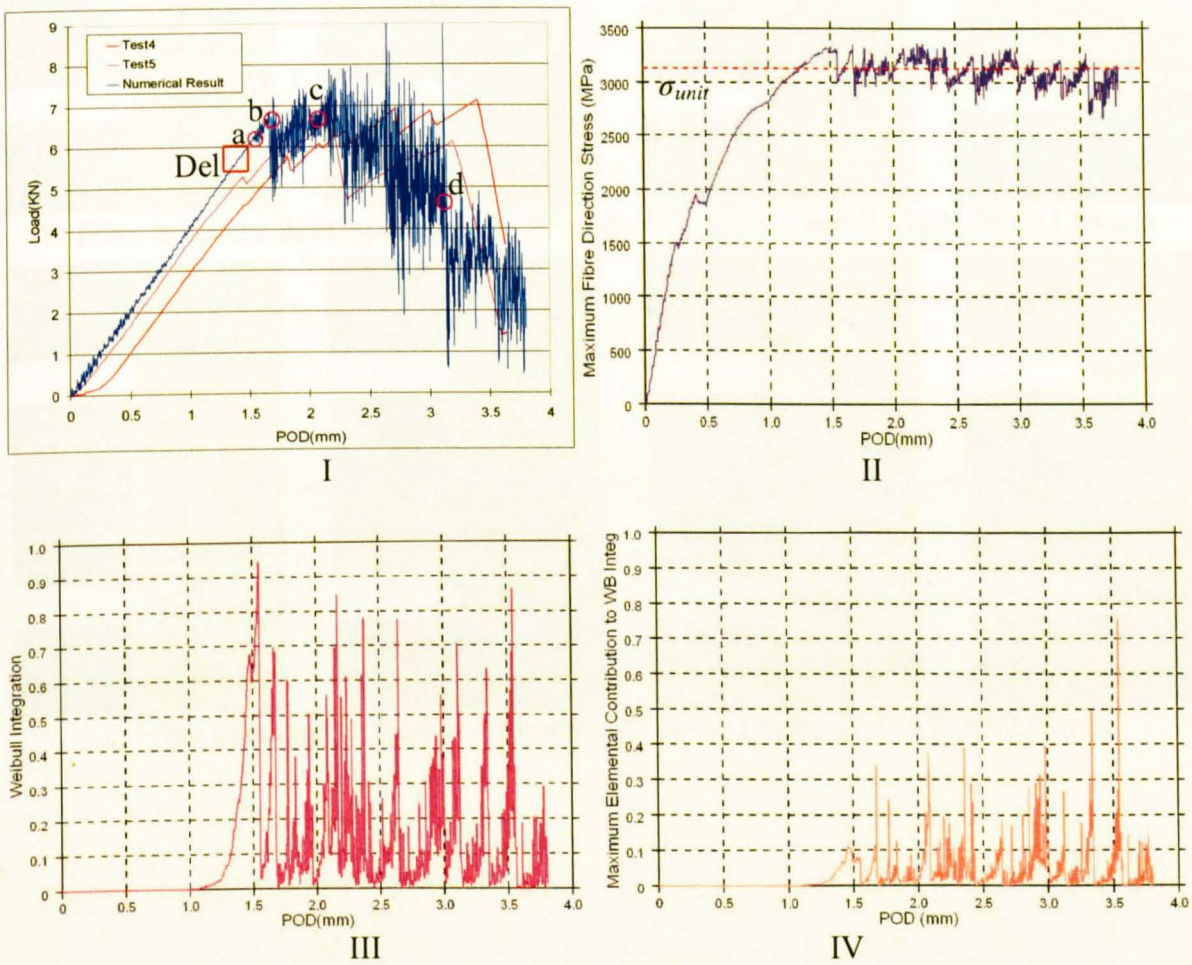

Fig 5.2.2-20 Load-POD, maximum elemental fibre direction stress, global Weibull integration and maximum elemental contribution to weibull integration curves

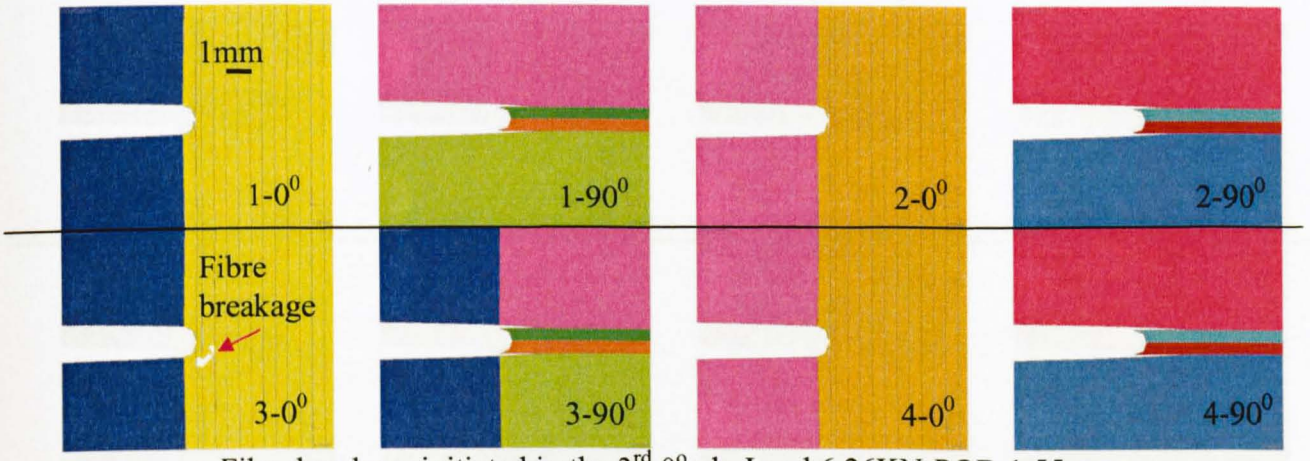

a. Fibre breakage initiated in the 3rd 0° ply Load 6.26KN-POD:1.55mm

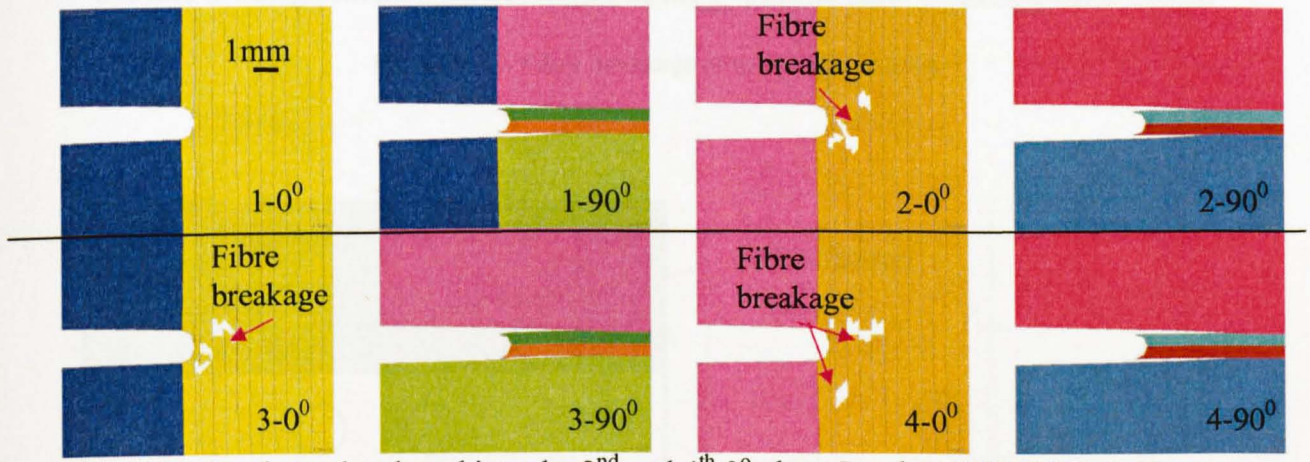

b. Fibre breakage developed into the 2nd and 4th 0° ply at Load 6.73KN-POD:1.68mm

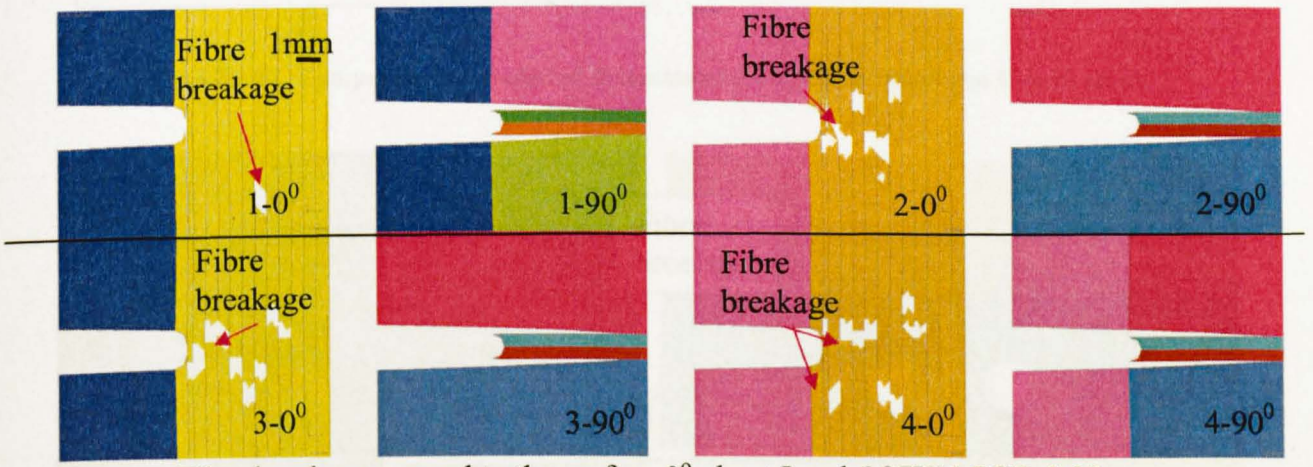

c. Fibre breakage expand to the surface 0° ply at Load 6.27KN-POD:2.09mm

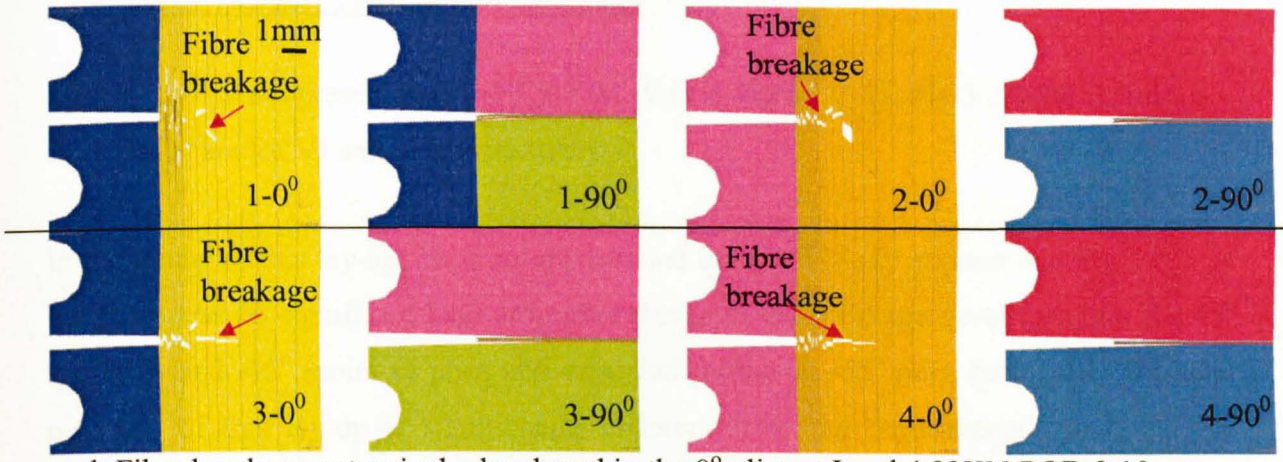

d. Fibre breakage extensively developed in the 0° plies at Load 4.93KN-POD:3.10mm

Fig 5.2.2-21 Fibre breakage development in plies

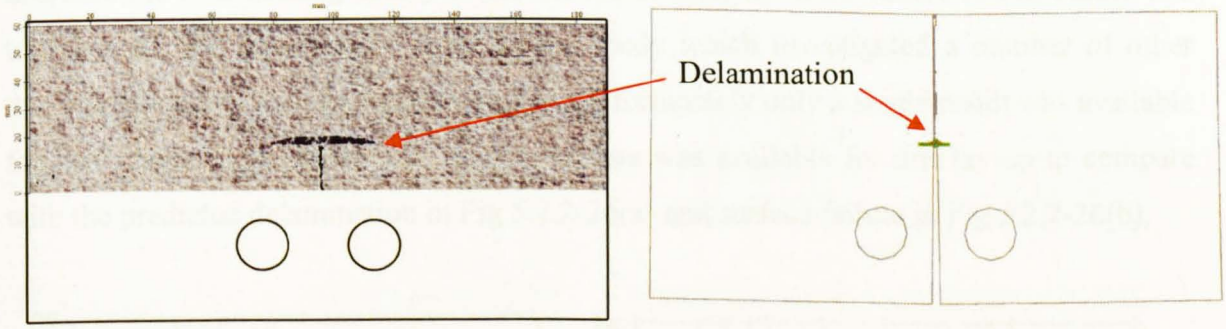

Fig 5.2.2-22 Comparison of predicted delamination with interrupted test C-scan result

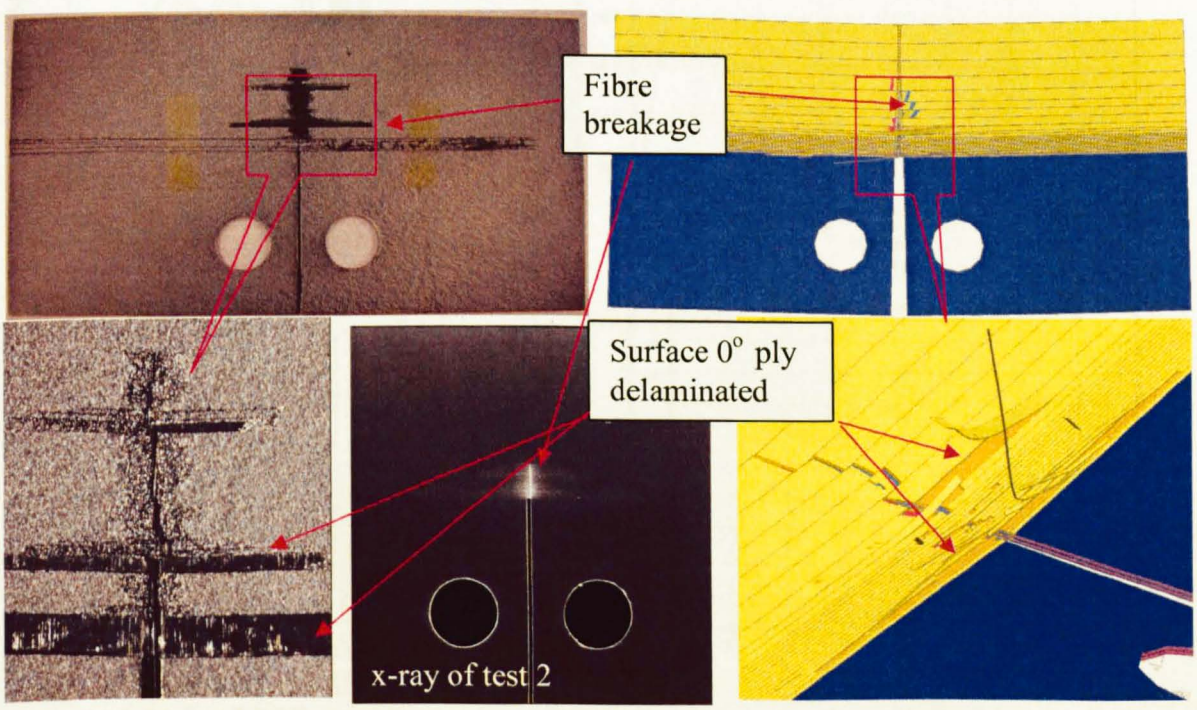

Fig 5.2.2-23 Comparison of experimental and predicted surface failure mode

I, II, III and IV are presented in Fig 5.2.2-24. V is in Fig 5.2.2-25. Fig 5.2.2-26(a) and fig 5.2.2-26(b) are for VI and VII respectively.

In the model of this lay-up, fibre failure initiated in the 1st 0° ply at point a in Fig 5.2.2-24 but there was no significant load drop after this until the breakage developed into the 45° (point b) and -45° (point c) plies and extended further in -45° plies (point d) . The load response of this lay-up is significantly different from the experimental result but the predicted fibre breakage initiation load level is very close to the experimental value, which suggests that a more significant number of failed elements rather than the single maximum stressed element should be removed after the Weibull criterion is satisfied. This would decrease the load bearing ability of the laminates after the fibre failure has initiated. The test data of this lay-up came from a pilot study which investigated a number of other testing parameters such as notch tip radius. Unfortunately only a single result was available for the 0.5mm radius notch and no C-scan data was available for this lay-up to compare with the predicted delamination in Fig 5.2.2-26(a) and surface failure in Fig 5.2.2-26(b).

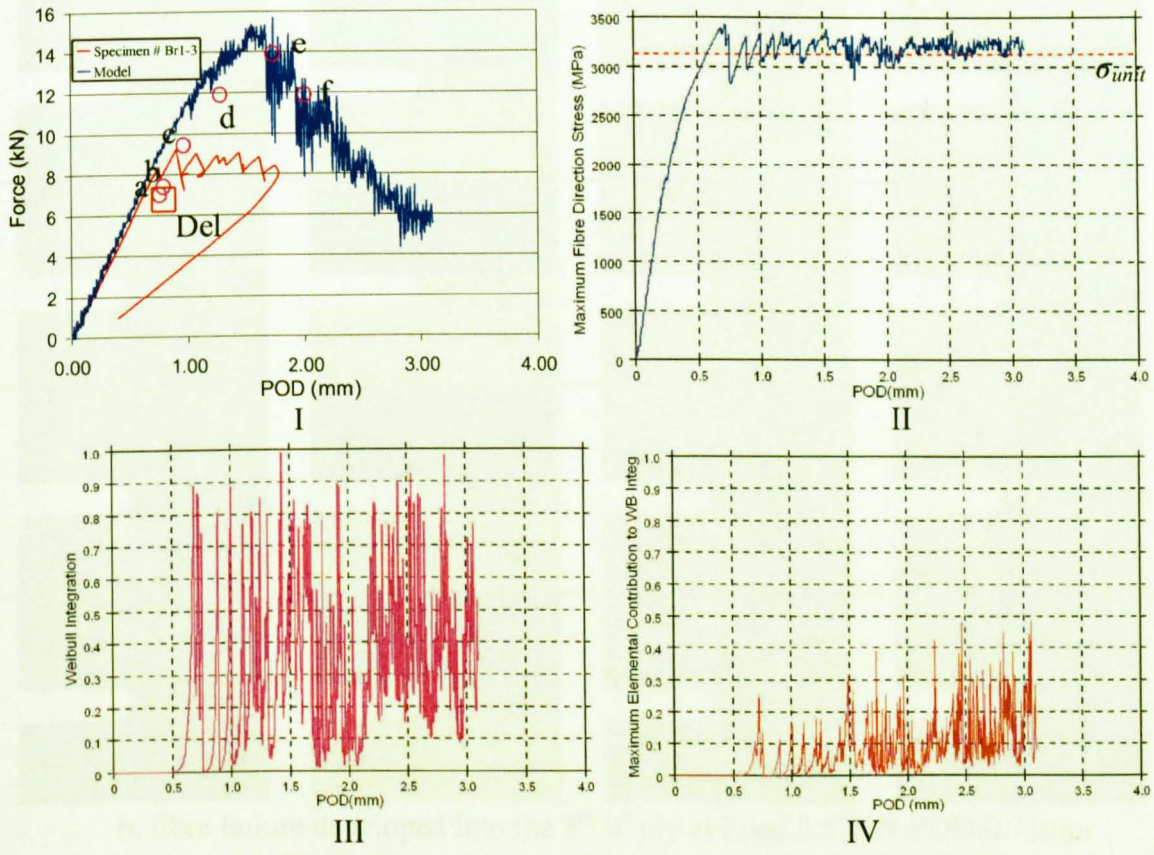

Fig 5.2.2-24 Load-POD, maximum elemental fibre direction stress, global Weibull integration and maximum elemental contribution to weibull integration curves

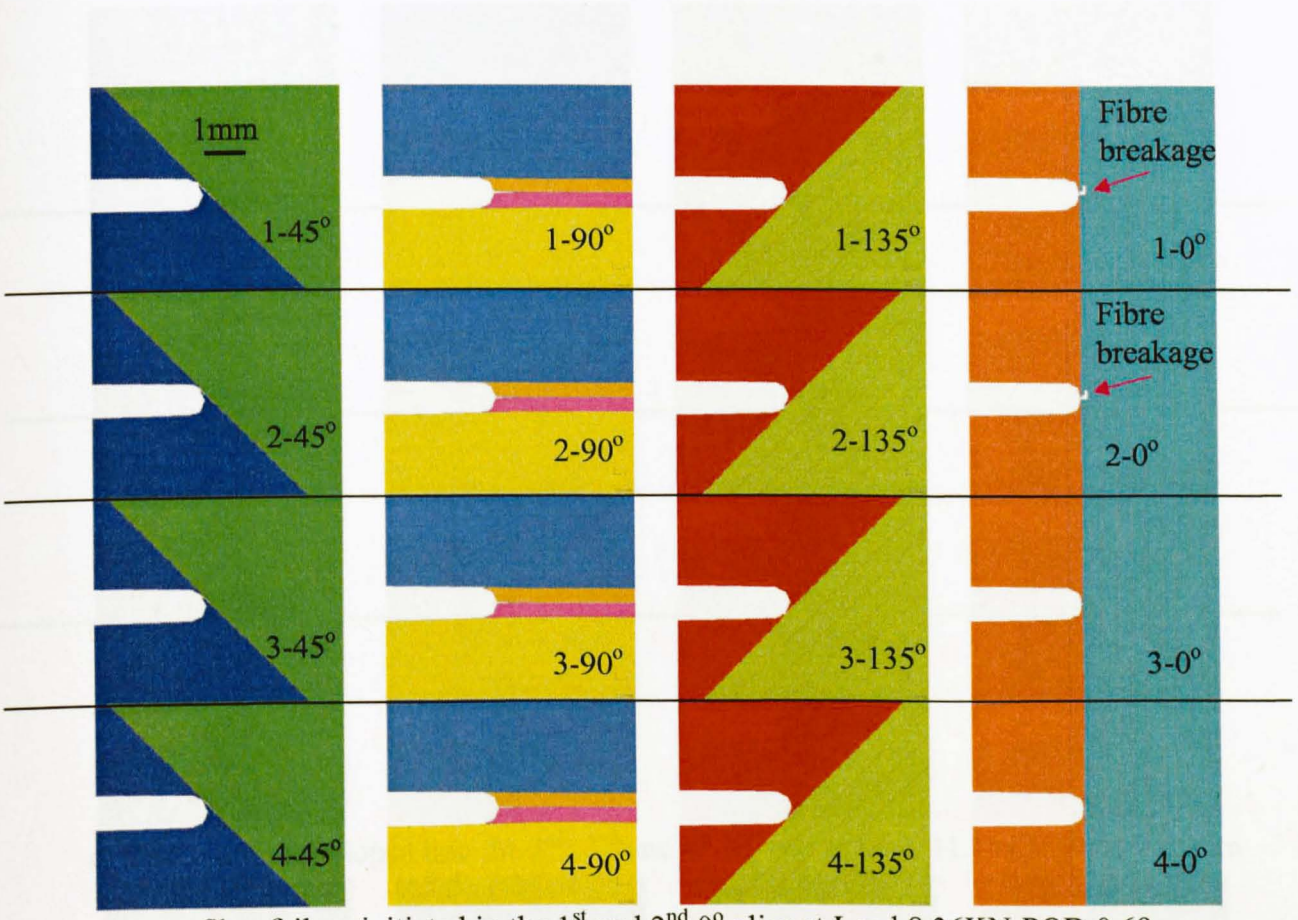

a. fibre failure initiated in the 1st and 2nd 0° plies at Load 8.36KN-POD:0.69mm

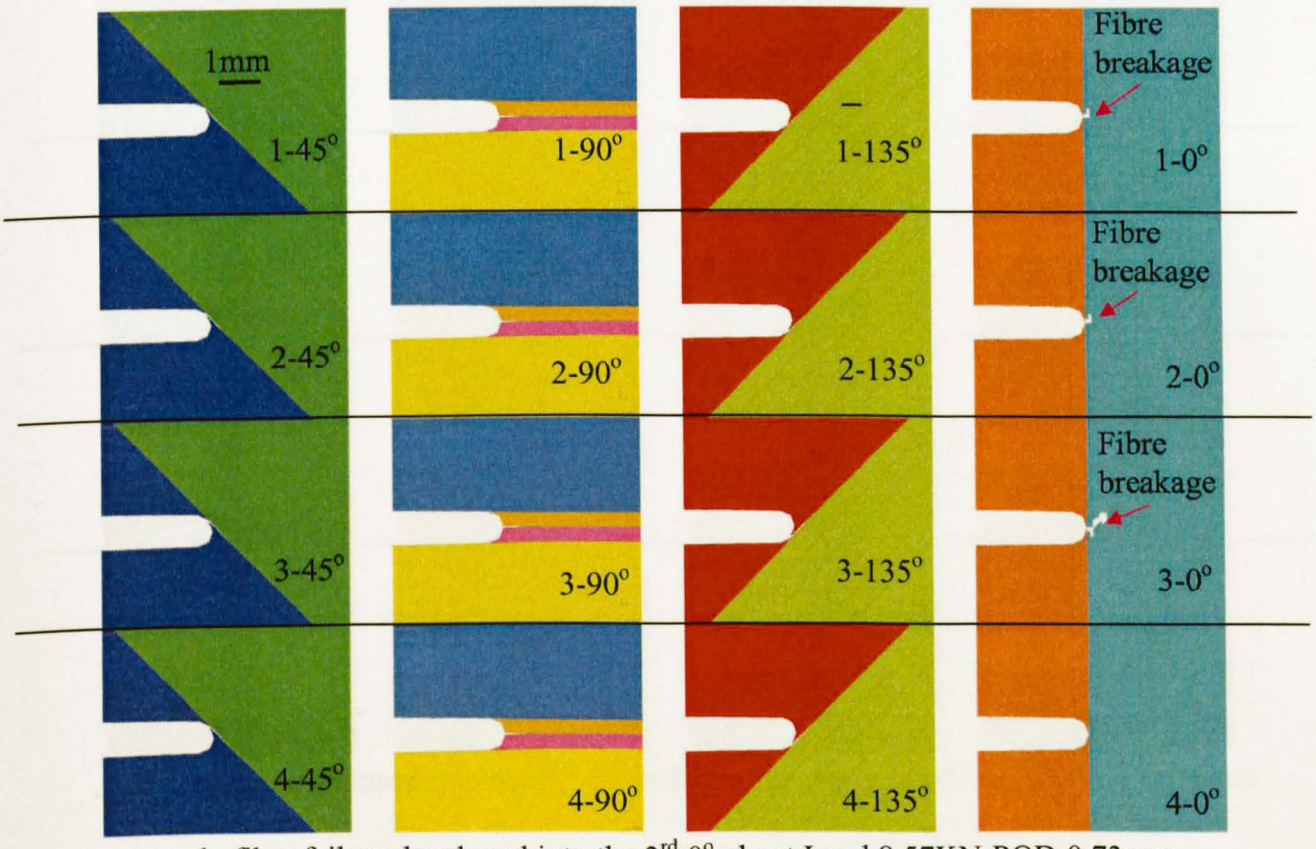

b. fibre failure developed into the 3rd 0° ply at Load 8.57KN-POD:0.73mm

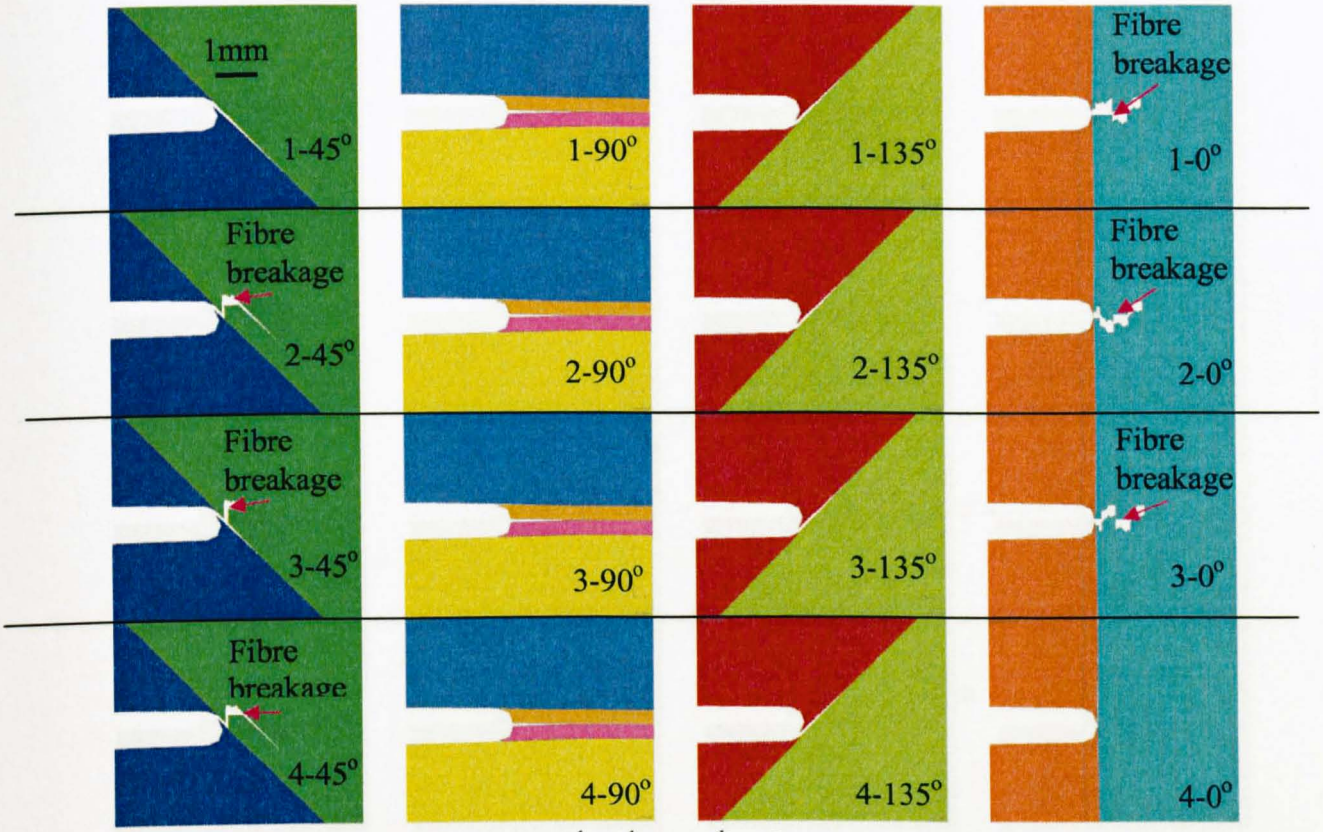

c. fibre failure developed into the 2nd, 3rd and 4th 45° ply at Load 11.79KN-POD:1.01mm

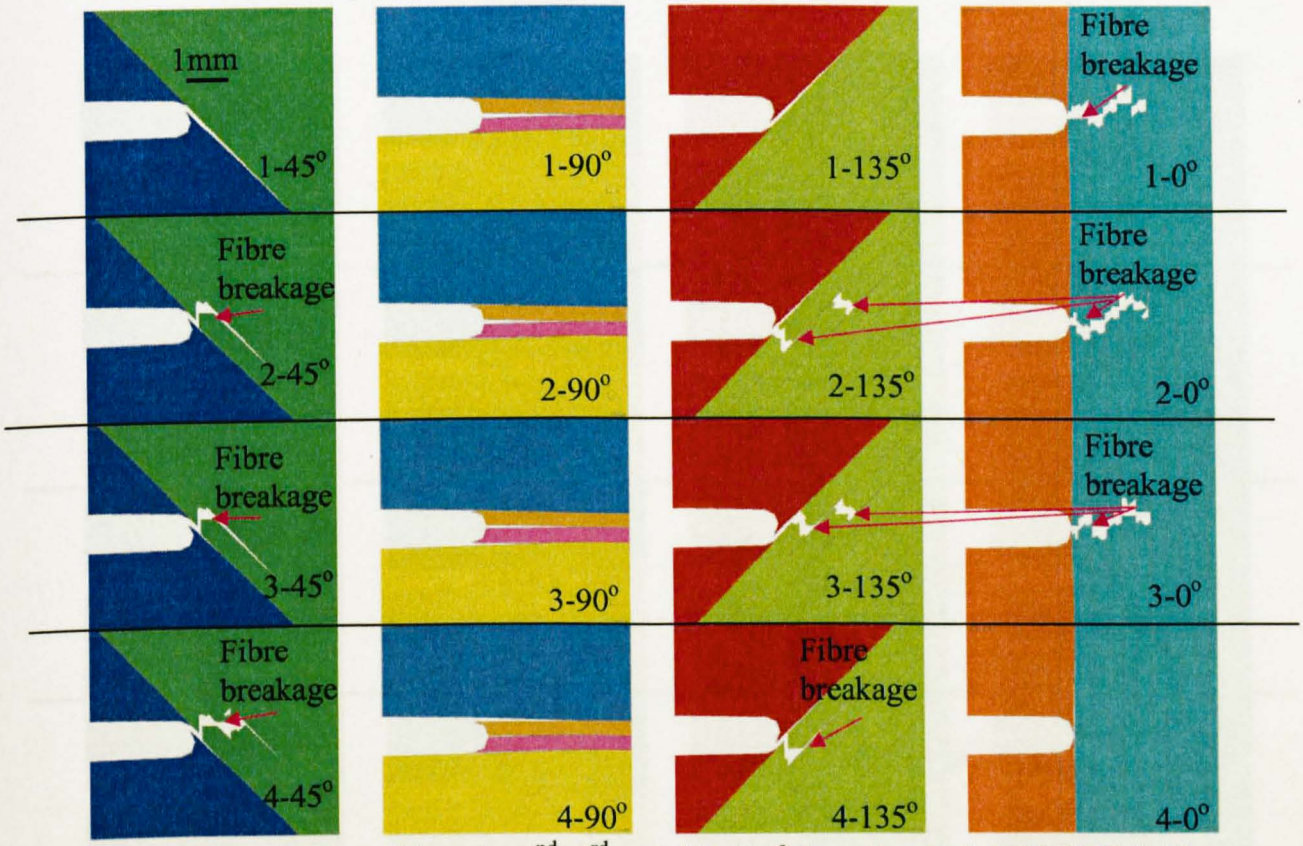

d. fibre failure developed into the 2nd ,3rd and 45h 135°ply at Load 13.2KN-POD:1.18mm

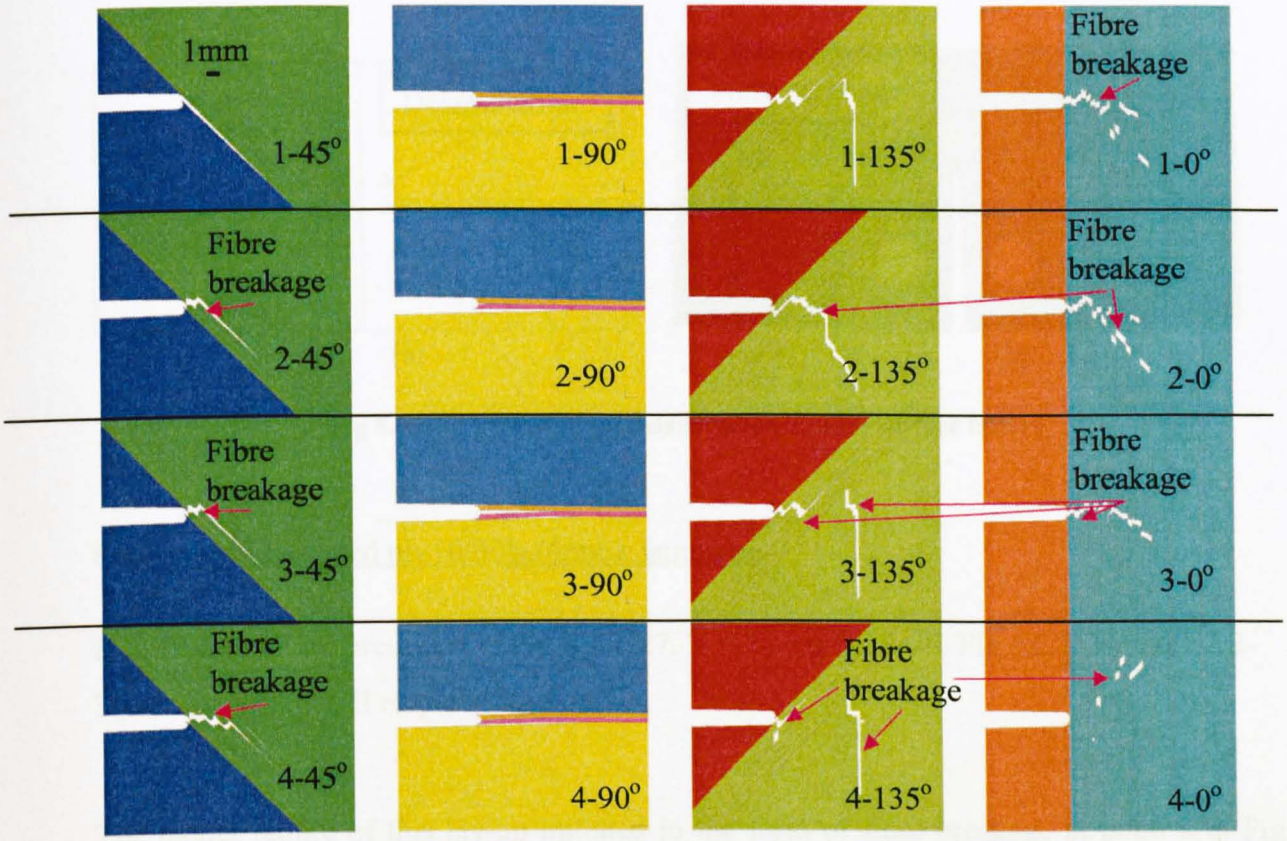

e. fibre failure in 135° plies expanded at Load 15.3KN-POD:1.68mm

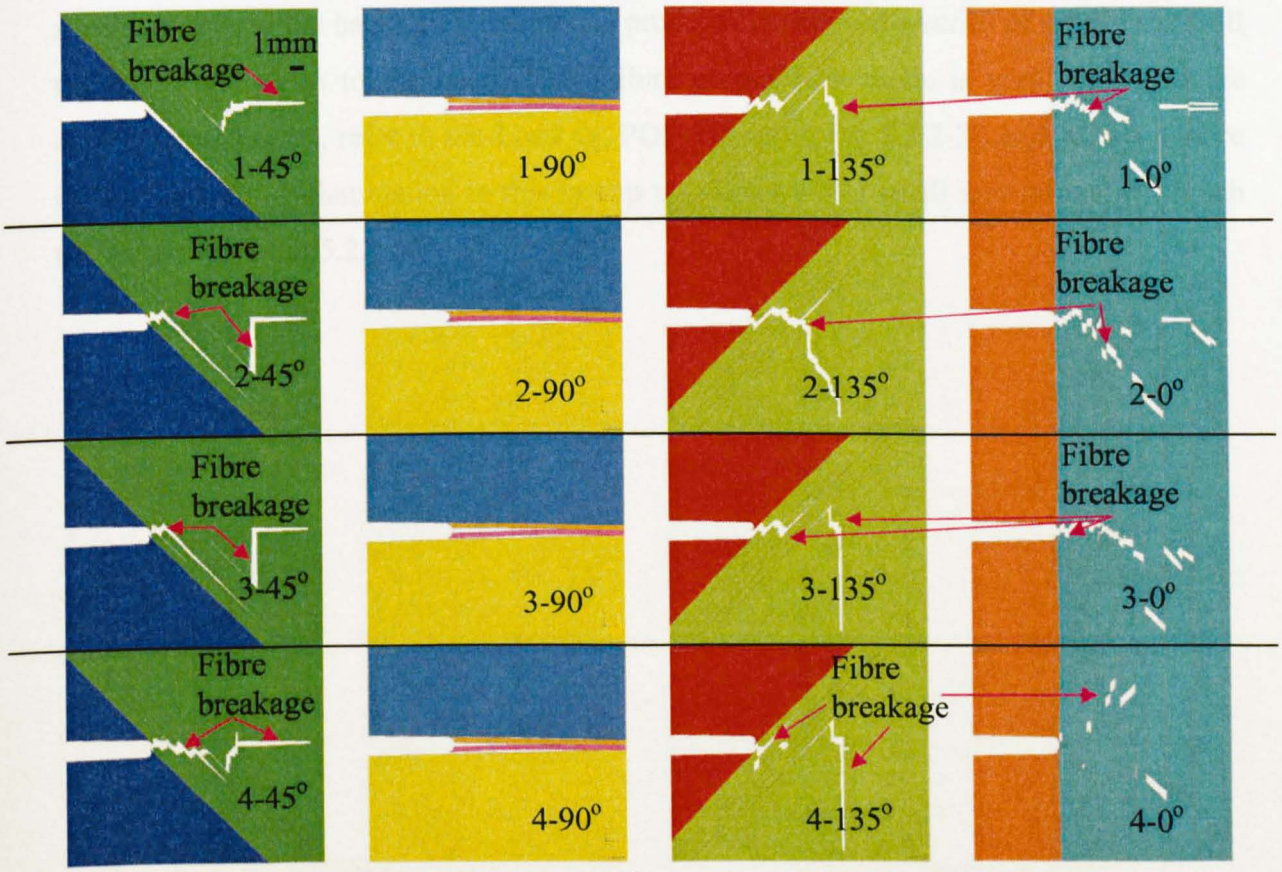

f. fibre failure developed into the surface 45° ply at Load 13.17KN-POD:1.94mm

Fig 5.2.2-25 Fibre breakage development in plies

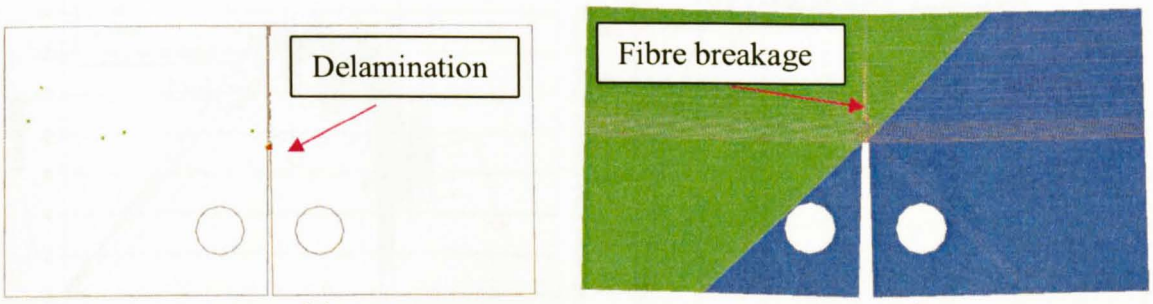

Fig 5.2.2-26 Predicted (a) delamination and (b) surface failure

8.Results of dispersed ply $[0/90]_{8s}$(4mm) laminates

I, II, III and IV are presented in Fig 5.2.2-27. V is in Fig 5.2.2-28. Fig 5.2.2-29 and 5.2.2-30 are for VI and VII respectively.

The model failure of this lay-up initiated in the form of fibre breakage at point a in Fig 5.2.2-27. After the initiation, fibre breakage developed stably along the centerline of the specimen toward the back. The load in this process experienced a series of small jumps till the crack was close to the back. This failure propagation mode is very similar to the experimental results, refer to the Load vs. POD curves in Fig 5.2.2-27 and surface failure in Fig 5.2.2-30.. Delamination in this lay-up was limited to a small area around the notch tip, as shown in Fig 5.2.2-29.

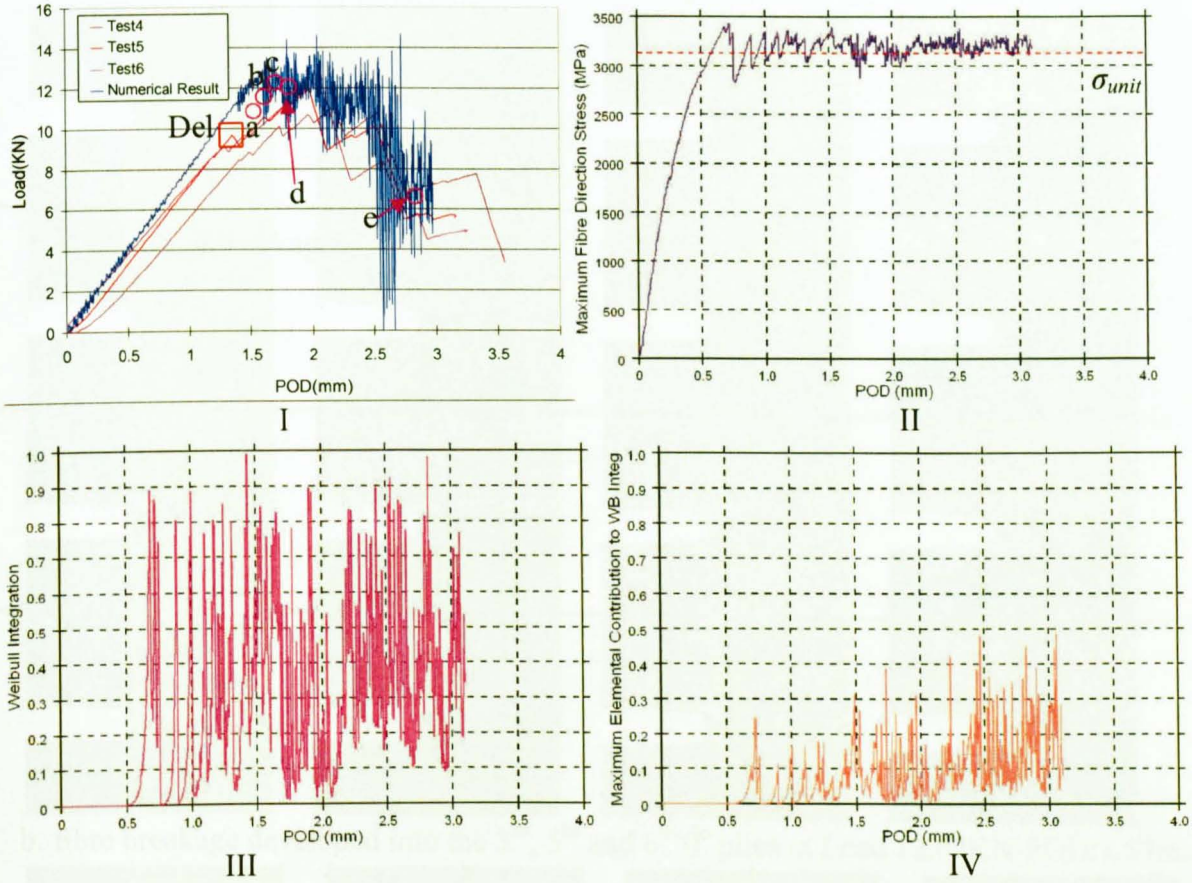

Fig 5.2.2-27 Load-POD, maximum elemental fibre direction stress, global Weibull integration and maximum elemental contribution to weibull integration curves

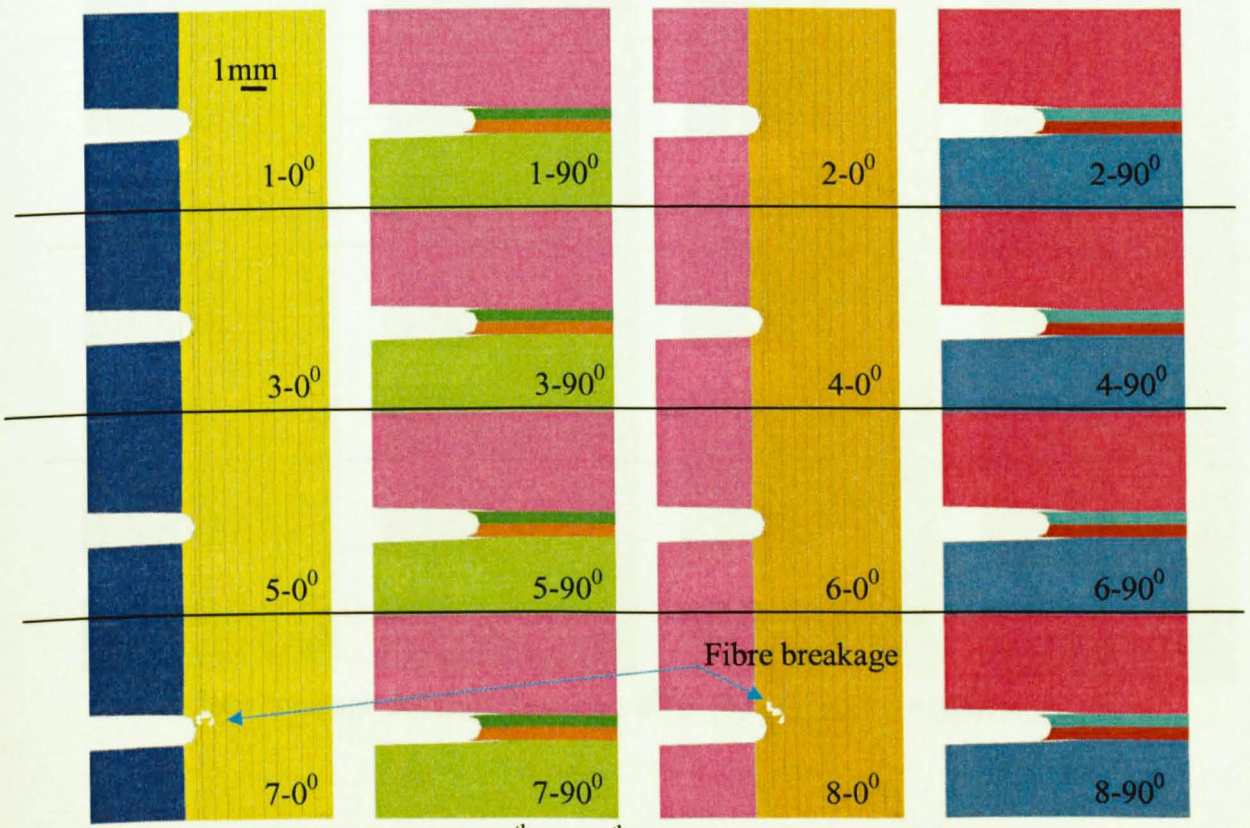

a. fibre breakage initiated in the 7th and 8th 0° plies at Load 10.85KN-POD:1.40mm

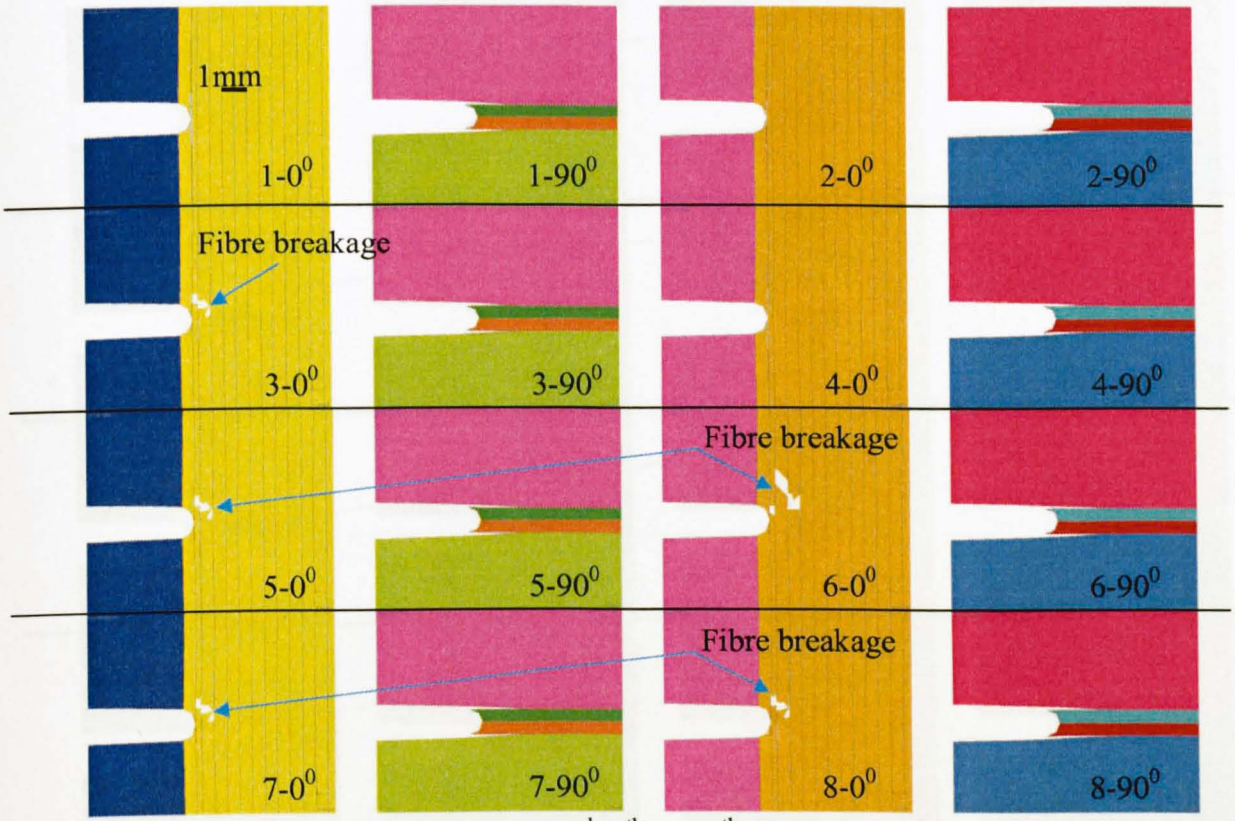

b. fibre breakage developed into the 3rd, 5th and 6th 0° plies at Load 12.07KN-POD:1.53mm

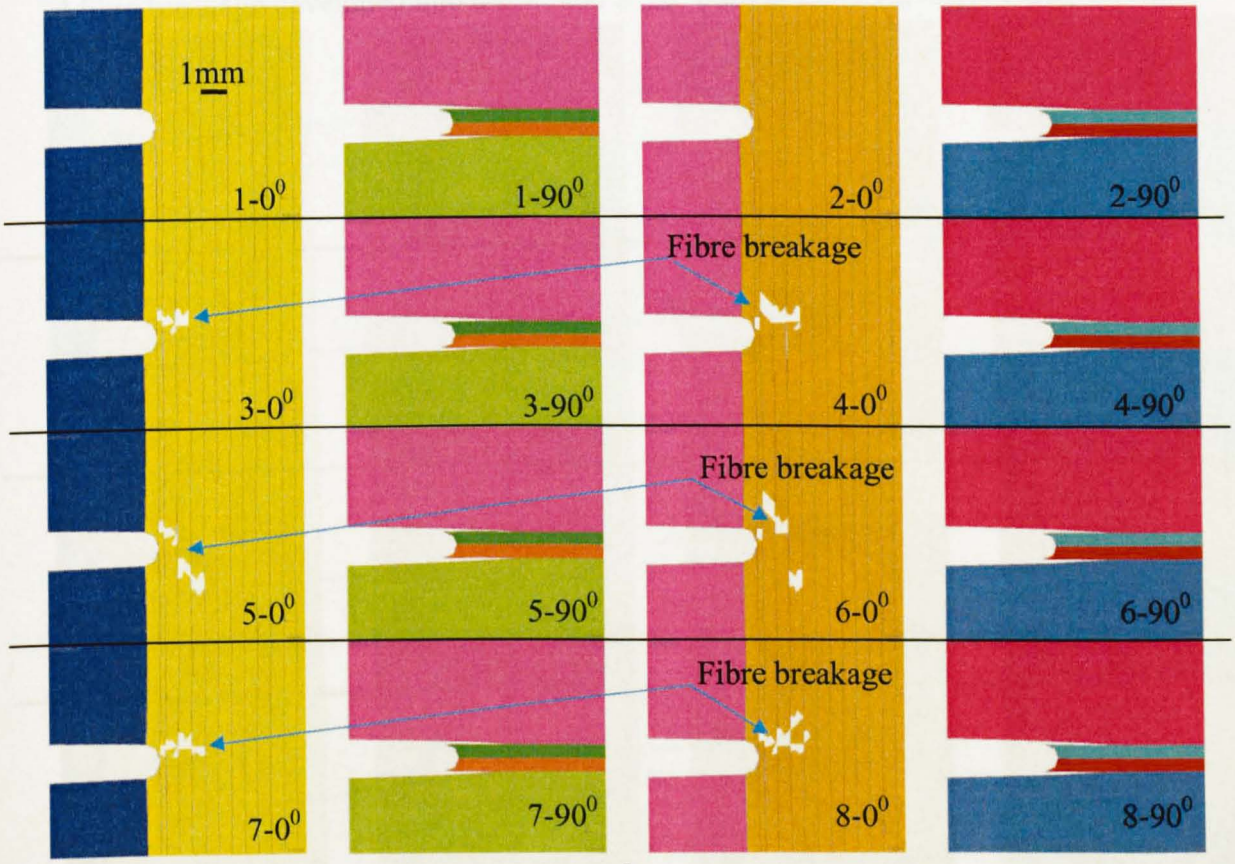

c. fibre breakage developed into the 4th 0° ply at Load 12.91KN-POD:1.61mm

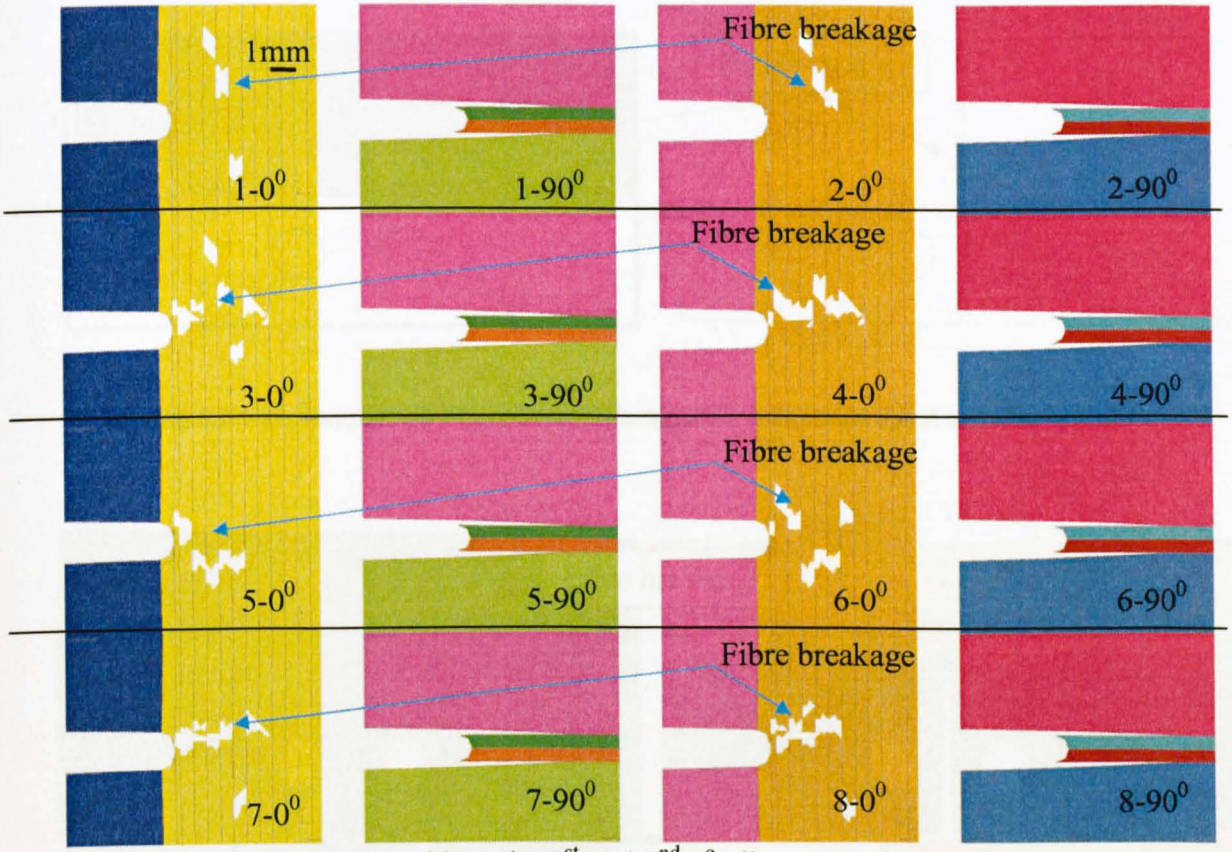

d fibre breakage developed into the 1st and 2nd 0° plies at Load 12.75KN-POD: 1.78mm

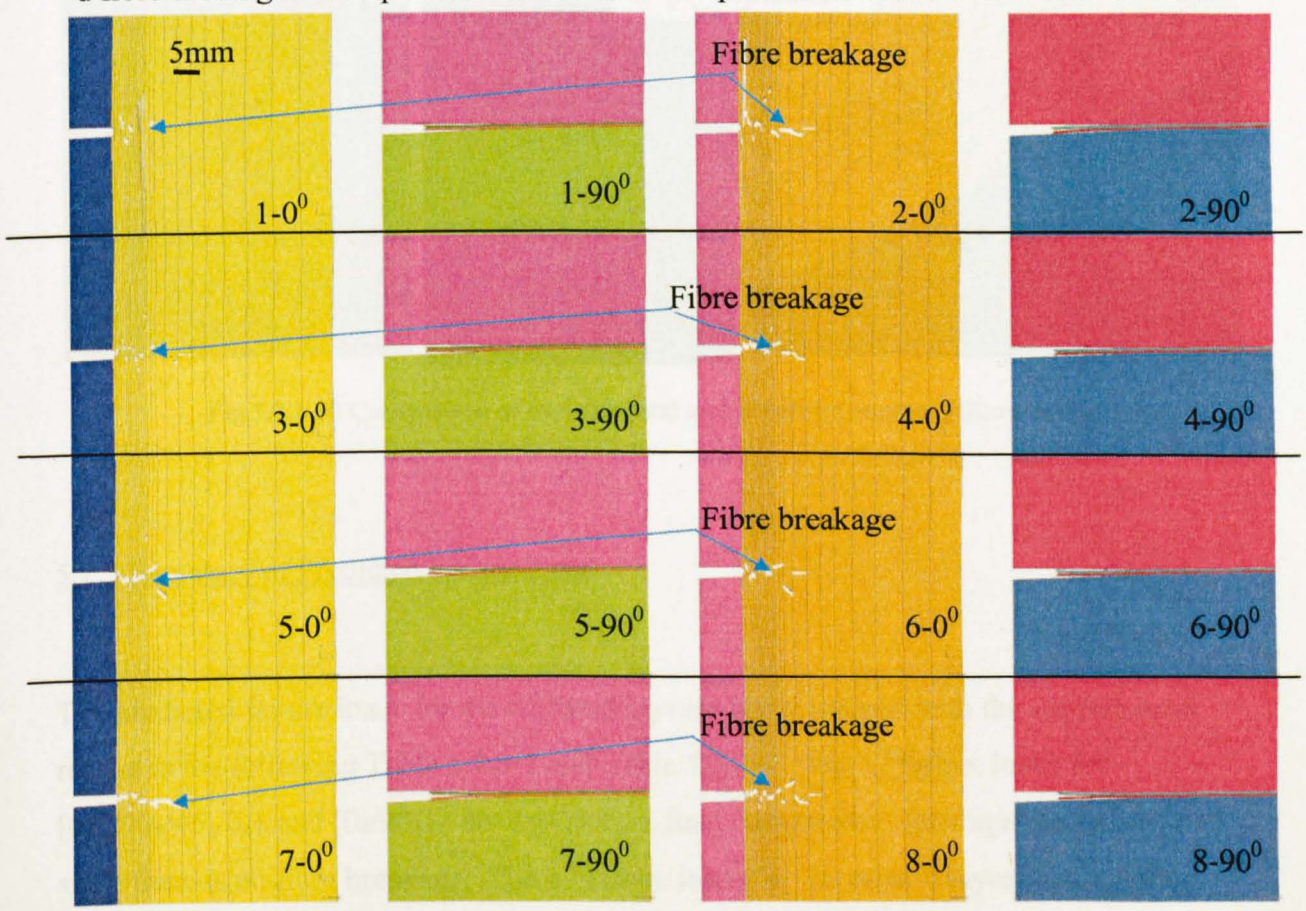

e. fibre breakage extensively developed at Load 7.60KN-POD: 2.76mm

Fig 5.2.2-28 Fibre breakage development in plies

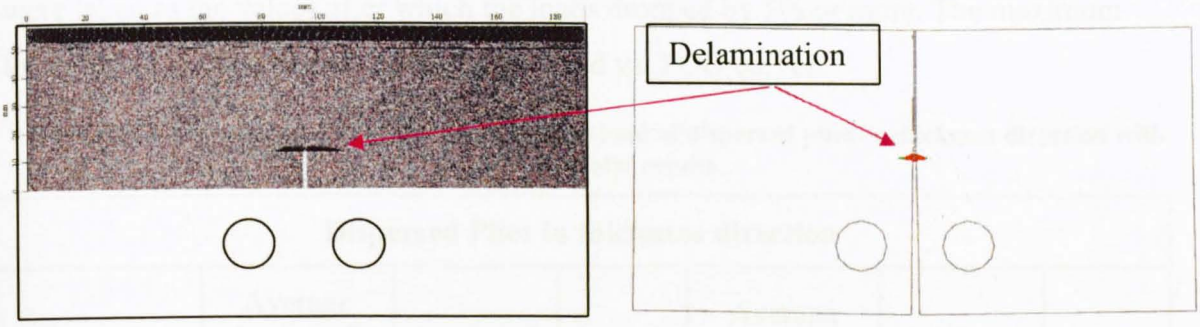

Fig 5.2.2-29 Comparison of predicted delamination with interrupted test C-scan result

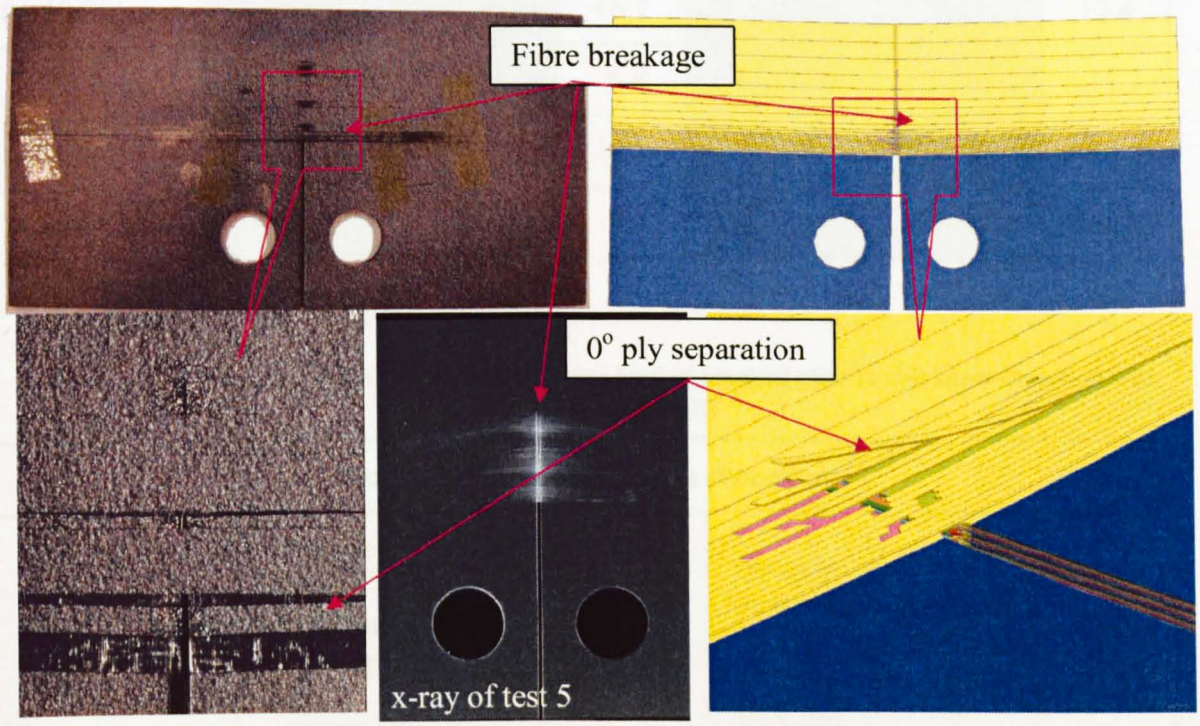

Fig 5.2.2-30 Comparison of experimental and predicted surface failure mode

5.2.3 Summary of Predicted Failure Load

The predicted failure loads for the different lay-ups are compared with the experimental results in the following Table 5.2.3-1 and Table 5.2.3-2. The 1st failure loads for $[45_4/90_4/45_4/0_4]_s$ and $[0_4/90_4]_{2s}$ lay-ups use the final catastrophic delamination failure load since there is no fibre breakage. The 1st failure loads for the other 6 lay-ups adopted the load levels when the first fibre breakage initiated. In the experiments the 1st failure loads

were taken as the values after which the loads dropped by 5% or more. The maximum loads for all lay-ups were taken from the Load vs. POD curves.

Table 5.2.3-1 Comparison of predicted 1st failure load of dispersed plies in thickness direction with experimental results

Dispersed Plies in thickness direction						
Layup	Average load at 1st significant load drop (kN)(CV,%)	Predicted 1st Failure Load(kN)	Diff (%)	Average Maximum Load (kN)(CV,%)	Predicted Maximum Load(kN)	Diff (%)
$[0/90]_{4s}$	5.90(6.9)	6.26	+6.1	6.94(2.6)	7.11	+2.4
$[0/90]_{8s}$	11.64(6.5)	10.85	-6.8	11.64(6.5)	12.95	+11.2
$[45/90/45/0]_{2s}$	6.10(10.8)	6.08	-0.3	6.99(24.3)	8.38	+19.9
$[45/90/45/0]_{4s}$	9.23	8.36	-9.4	9.23	15.34	+66.2

Fibre breakage

Table 5.2.3-2 Comparison of predicted 1st failure load of blocked plies in thickness direction with experimental results

Blocked Plies in thickness direction						
Layup	Average load at 1st significant load drop (kN) (CV,%)	Predicted 1st Failure Load(KN)	Diff (%)	Average Maximum Load (kN) (CV,%)	Predicted Maximum Load(KN)	Diff (%)
$[0_2/90_2]_{2s}$	7.94(10.7)	6.61	-16.8	9.12(3.0)	10.49	+15.0
$[0_4/90_4]_{2s}$	20.74(0.5)	19.69	-5.1	20.74(0.5)	19.69	-5.1
$[45_2/90_2/45_2/0_2]_s$	10.30(5.1)	9.57	-7.1	12.24(4.0)	10.80	-11.8
$[45_4/90_4/45_4/0_4]_s$	17.41(0.2)	16.00	-8.1	17.41(0.2)	16.00	-8.1

Fibre breakage pull-out failure Buckling failure

5.2.4 Splits and Mesh effects

It is important to know how the number and location of pre-defined splits, especially the split directly passing through the notch tip influence the model results. To investigate the effect of pre-defined splits, four new meshes with splits in either 0 plies or 45 plies being changed from the baseline meshes in Fig 5.2.1-1. were applied to four selected lay-ups. The changes of splits in new meshes and corresponding applied lay-ups are:

1. new mesh with only the number of splits in 0 plies being halved from the original mesh, as shown in Fig 5.2.4-1(b), for $[0/90]_{4s}$ and $[0_4/90_4]_{2s}$ lay-ups
2. new mesh with only the split right passing through the notch tip in 0 plies being removed from the original mesh, as shown in Fig 5.2.4-1(c), for $[0/90]_{4s}$ and $[0_4/90_4]_{2s}$ lay-ups.
3. new mesh with only the split directly passing through the notch tip being kept in 45/-45 plies from the original mesh, as shown in Fig 5.2.4-2(b) for $[45_4/90_4/45_4/0_4]_s$ lay-up.
4. new mesh with only the split right passing through the notch tip being kept and halved the length in 45/-45 plies from the original mesh, as shown in Fig 5.2.4-2(c), for $[45_4/90_4/45_4/0_4]_s$ lay-up.

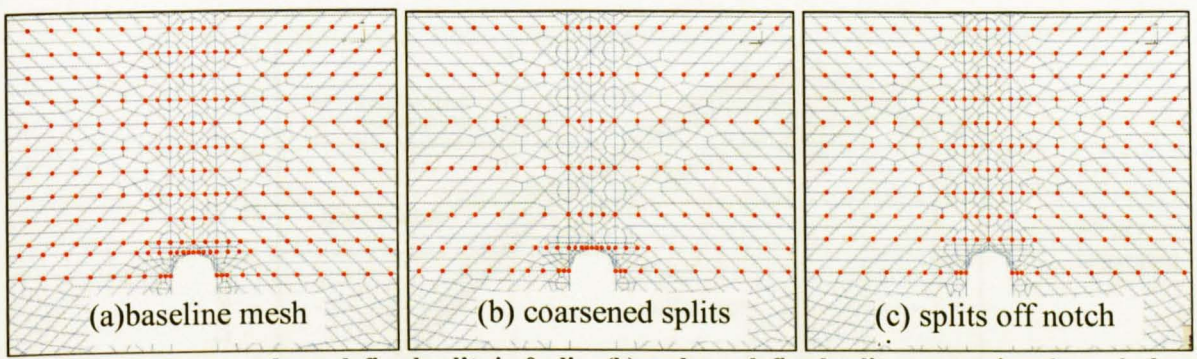

Fig 5.2.4-1 Coarsened pre-defined splits in 0 plies (b) and pre-defined splits not passing through the notch tip in 0 plies (c) for $[0/90]_{4s}$ and $[0_4/90_4]_s$ layups

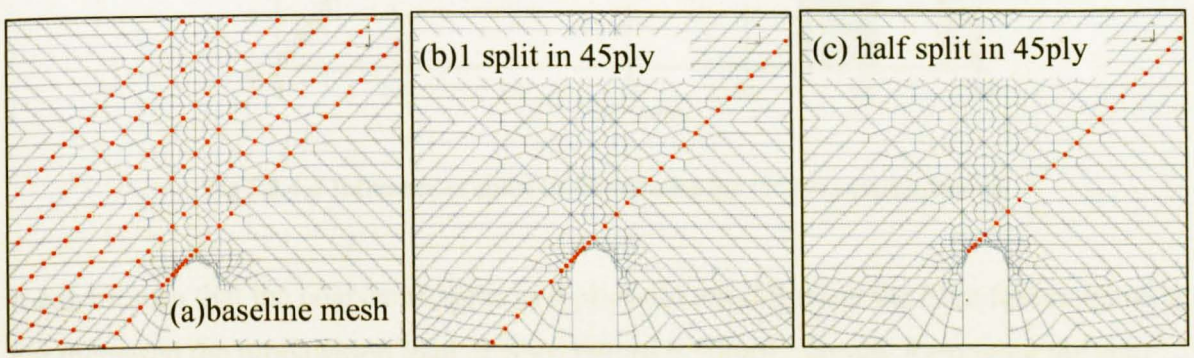

Fig 5.2.4-2 Splits in 45/-45 plies are reduced to 1 (b) and further halved (c)

In above 4 new meshes, location and number of splits in other plies kept unchanged from the baseline meshes. $[45_4/90_4/45_4/0_4]_s$ and $[0_4/90_4]_{2s}$ lay-ups are used to check the influence of splits on the global delamination failure mode. $[0/90]_{4s}$ lay-up is selected to check the split effect on the local fibre failure mode. Model control, loading condition and boundary condition of the new models are the same as those for the baseline models. The load vs. POD curves using the new meshes for the four lay-ups are compared with those using the original baseline mesh in Fig 5.2.4-3 and Fig 5.2.4-4.

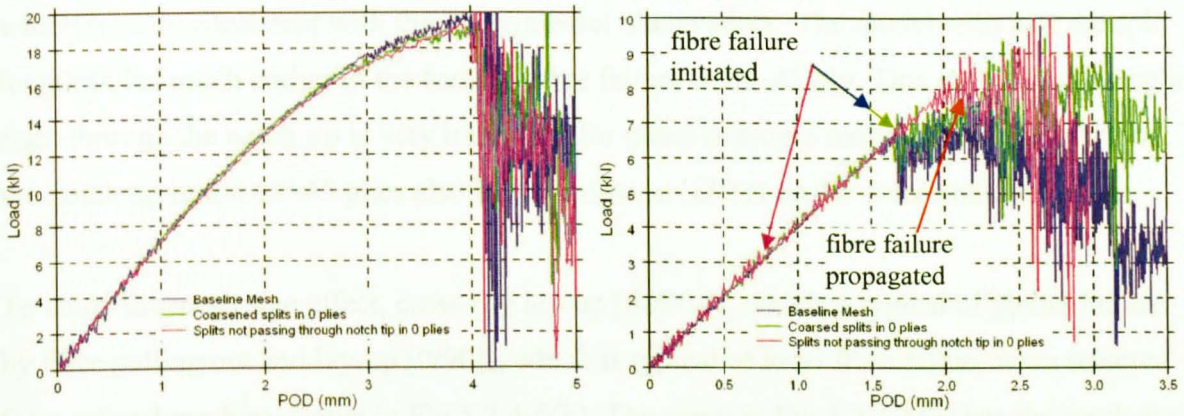

(a) $[0_4/90_4]_s$ (b)$[0/90]_{4s}$

Fig 5.2.4-3 Influence of coarsened splits and splits not passing through the notch tip in 0plies for $[0/90]_{4s}$ and $[0_4/90_4]_s$ layups

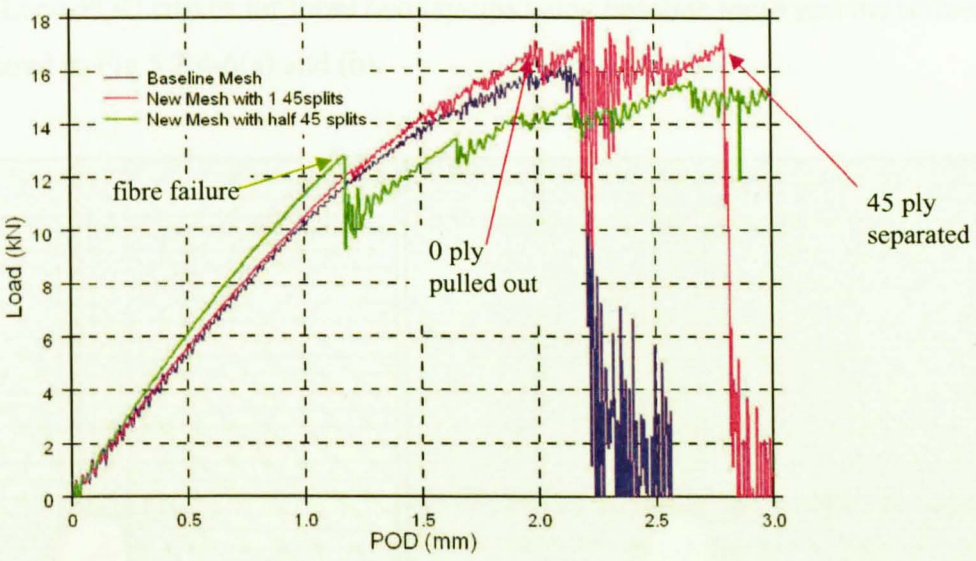

Fig 5.2.4-4 Influence of splits in 45/-45 plies for $[45_4/90_4/45_4/0_4]_s$ lay-up

It can be seen that the coarsened splits in 0 plies did not influence the fibre failure ignition but increased the propagation load of fibre failure in $[0/90]_{4s}$ lay-up. Removing the split

right acrossing the notch tip initiated much earlier fibre failure at the tip, but the global load curve was not obviously influenced until the fibre failure started to propagate. Overall the ultimate failure load of $[0/90]_{4s}$ was improved by removing the split directly acrossing the notch tip.

The model with only 1 split in the 45/-45 plies had the 0 ply pulling out first which led to the 1st load drop in the load curve and the surface 45 ply separating later which caused the catastrophic failure of the model. Comparatively, 0 ply pulling out and surface 45 ply separating happened nearly simultaneously in the model with more splits in 45/-45 plies, which is more consistent with the experimental observation. The model with half the split length failed much earlier in the form of fibre failure in the 45 ply. This shows that the split right through the notch tip is very important for quasi-isotropic models. Splits away from the notch tip in the 45/-45 plies also have an obvious effect on the delamination failure.

To study the mesh size effect, cross-ply lay-up $[0_4/90_4]_{2s}$ which is typical of global failure by fibre pulling out and lay-up $[0/90]_{4s}$ which is typical of local fibre failure were selected for a refined mesh as shown in Fig 5.2.4-5(b). The mesh in Fig 5.2.4-5(b) has the mesh size around and behind the notch tip refined by two times from the baseline mesh, but the location and number of pre-defined splits in 0 plies and 90plies are the same as those in the baseline mesh. Load-POD curves for these two lay-ups using baseline mesh and the refined mesh are compared in Fig 5.2.4-6(a) and (b).

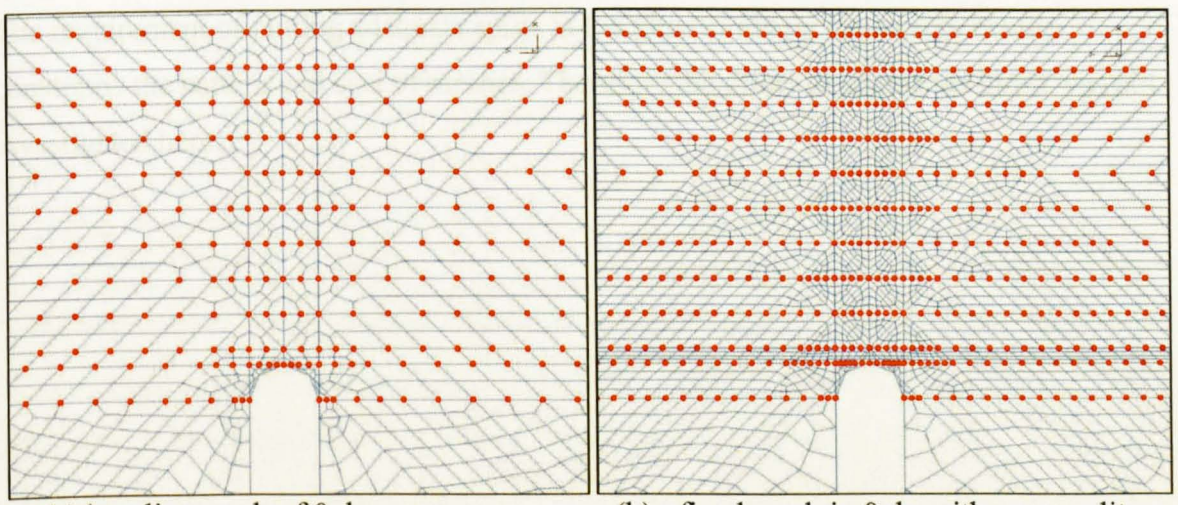

(a) baseline mesh of 0ply (b)refined mesh in 0ply with same splits

Fig 5.2.4-5 Comparison of the baseline mesh and the refined mesh around the notch with the same splits in 0 plies

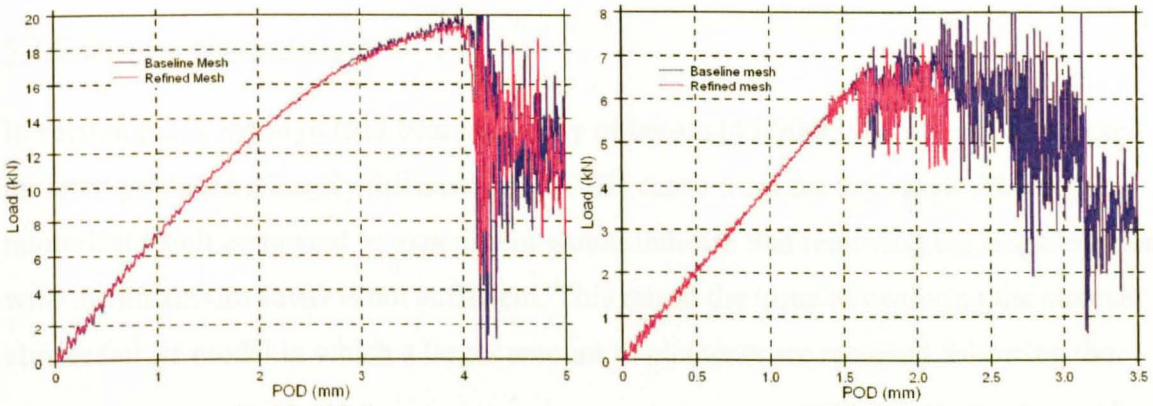

(a) $[0_4/90_4]_{2s}$ (b) $[0/90]_{4s}$

Fig 5.2.4-6 Comparison of Load-POD curves of the new refined mesh with the baseline meshes

The comparison in Fig 5.2.4-6 shows that the refined mesh has very little influence on the fibre pulling out failure of $[0_4/90_4]_{2s}$ lay-up, but initiated the fibre failure a bit earlier in $[0/90]_{4s}$ lay-up. The propagation load of $[0/90]_{4s}$ was slightly decreased as well with the refined mesh..

From above comparison of different pre-defined splits and mesh sizes, it can be concluded that the splits in 45/-45 plies, especially the one right across the notch tip, have a large influence on the failure of quasi-isotropic lay-ups. Location and number of splits in 0 plies have very little influence on the global failure of cross-ply lay-ups but obvious influence on the local fibre failure of this type of lay-ups. The split right across the notch tip is more important than splits at other locations.in 0 plies. The influence of mesh size is less important than the arrangement of splits in both ply-blocked and ply-dispersed lay-ups. The requirement of putting adequate splits in the plies to obtain reasonable results constrains the pattern and size of meshes. Therefore the effect of coarsened mesh was not investigated here.

5.2.5 Element cluster failure

In section 5.2.2, the high load bearing ability of lay-up $[45/90/45/0]_{4s}$ after fibre failure initiated produced a largely different Load-POD curve from the test result. The higher numerical result compared to experiment would indicate that removing the single element with the maximum stress is not sufficient. This raised the issue of exploring the element cluster failure model in which a larger amount of elements are removed following the initial failure point as determined by the Weibull integration $\sum_{i=1}^{TotalNoofSolidElements} V_i \left(\frac{\sigma_i}{\sigma_{unit}} \right)^m \geq 1$.

In order to achieve this it is necessary to determine which elements to remove once the Weibull integration has determined the overall point of failure. From the maximum elemental stress σ_{elem_max} and corresponding element volume V_{elem} when the Weibull integration criterion is satisfied in a loaded specimen, the survival probability of this element is:

$$P_{elem}(s) = \exp\left(-\left(\sigma_{elem\_max} / \sigma_o\right)^m V_{elem}\right) \qquad (5.2.5\text{-}1)$$

In contrast the survival probability of the entire specimen subject to a constant and uniform tensile stress, σ, would be:

$$P_{specimen}(s) = \exp\left(-\left(\sigma / \sigma_o\right)^m V_{specimen}\right) \qquad (5.2.5\text{-}2)$$

This denotes what can be described as an "average" failure stress, σ, for the specimen. To compare the point of failure of the specimen subject to a general load and a constant stress, we take them to have equal probablility of survival, $P_{specimen}(s) = P_{elem}(s)$. This defines a critical value of σ, denoted as σ_c, which is given by:

$$\sigma_c = \left(\frac{V_{elem}}{V_{specimen}} \right)^m \sigma_{elem\_max} \qquad (5.2.5\text{-}3)$$

Elements with stresses larger than σ_c would tend to be unstable and can be easily triggered by the elements with maximum stress to fail together. In this way, the cluster of failed elements to be removed can be determined when the Weibull integration criterion is satisfied.

A new model formulation to remove all elements with stresses large than σ_c when the Weibull criterion is satisfied was implemented in LS-Dyna and run on selected lay-ups;

$[45/90/45/0]_{4s}$, $[45/90/45/0]_{2s}$ and $[45_2/90_2/45_2/0_2]_s$. The obtained Load vs. POD curves are compared with test results and results of models in section 5.2.2 in Fig 5.5.1-1(a), (b) and (c). The cluster element failure models produced much sharper load drops after fibre failure initiated. This suggests that the cluster of failed fibres should be somewhere between elements with maximum stress and elements with stresses larger than σ_c and needs further investigation to figure out.

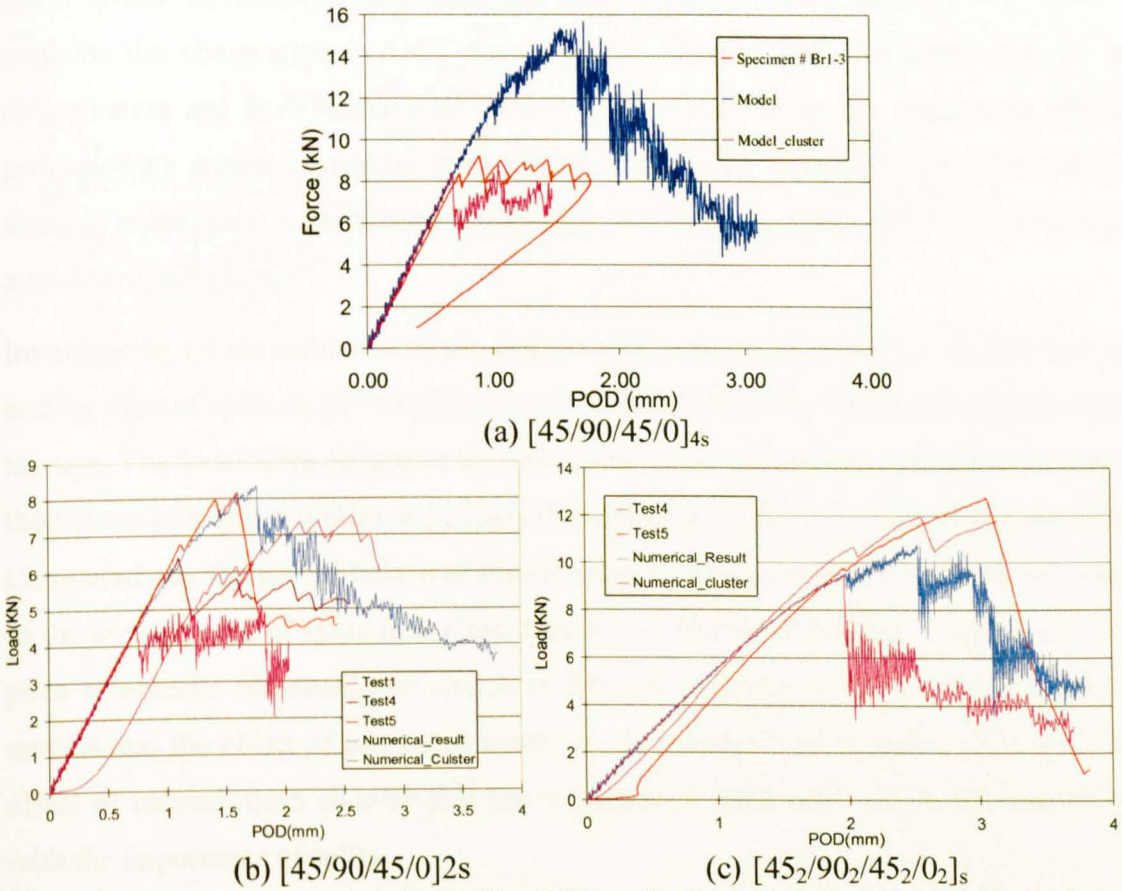

(a) $[45/90/45/0]_{4s}$

(b) [45/90/45/0]2s

(c) $[45_2/90_2/45_2/0_2]_s$

Fig 5.5.1-1 Failure curves using cluster fibre failure criterion and comparison with results from tests and the baseline model

5.2.6 Conclusion

The method to model delamination and splitting with interface elements and fibre failure using global Weibull failure criteria obtained very good results for most of the lay-ups from the OCT tests in four aspects: load vs. POD curves, surface failure appearance, delamination and splitting and fibre breakage In the one exceptional case of the $[45/90/45/0]_{4s}$ layup, the model could predict the fibre failure initiation point well but gave much higher failure propagation loads than the experiment. This suggests that a cluster of elements rather than the single maximum stressed element might fail and needs to be

removed after the Weibull criterion is satisfied. A statistical element cluster failure criterion which could determine the size of the cluster has been developed for this purpose.

The models showed that splitting near the notch can effectively reduce the stress concentration around the notch and prevent fibre failure in the early stages of loading. Splits occur more easily in the blocked ply specimens due to the thicker ply blocks. These splits spread the stress concentration and form a much larger damage process zone. This explains the observation in OCT tests that the blocked ply specimens tend to fail by delamination and have larger final failure loads. In dispersed ply specimens, splitting is prevented by greater constraint from neighbouring plies with different orientations, thus stress is more easily accumulated locally near the notch causing earlier fibre breakage and a more brittle failure.

Investigation on the influence of pre-defined splits and mesh size showed that the number and location of splits in 45/-45 plies have a large influence on the failure of quasi-isotropic lay-ups. The local fibre failure of dispersed and cross-ply lay-ups was also influenced by the pattern of splits in 0 plies, especially the existence of the split right across the notch tip. Comparatively the global failure of ply-blocked cross-ply lay-ups was much less sensitive to the arrangement of splits in 0 plies. Due to the request of putting adequate splits in the plies to achieve reasonable results, it is difficult to apply coarsened mesh in the OCT models and the effect of coarsened mesh was not studied in this thesis. The study on the effect of refined mesh showed that the influence of mesh size can be ignored compared with the importance of splits.

Chapter 6. Conclusions and Future Work

6.1 Conclusions

The major attempt of this thesis was to develop a general analysis technique to capture the most important modes of failure in a laminated composite and their interactions. This required the development and use interface elements and a progressive fibre-dominated element failure model and their combination.

Interface elements are widely used in modelling delamination and splitting problems in laminates. The form of interface elements could be a shell, a beam or an eight-node solid. In this thesis, the forms of discrete beam and eight-node solid element were adopted for the interface element and a concise bi-linear softening law for mixed mode failure was implemented. To achieve this aim, a pre-processing program to generate interface elements in laminates was developed first. This pre-processing program was used in all the modelling work in this thesis and proved its accuracy and reliability in producing appropriate interface elements at desired locations in a laminate. The embedded algorithm to calculate the effective area and orientation vectors of beam interface elements was verified as well.

The bi-linear softening law in interface elements was validated by modelling the standard Mode I fracture test of a Double Cantilever Beam (DCB) and Mode II test of End Notched Flexure(ENF). The excellent performance of interface elements was demonstrated in modelling dynamic transverse shear failure of single-lap specimens by reducing or eliminating the mesh dependency problems which solid element based models usually encounter in cases with high local stress concentrations.

Many publications on interface element formulations with mixed-mode loading consider the interaction between tensile and shear stress. Some include studies on the enhancing effect of compressive stress on shear strength, but few consider the influence of compressive strength on the Mode II fracture energy, G_{IIC}. A numerical investigation of the influence of through-thickness compressive stress on the Mode II damage evolution was carried out by modelling delamination in a single-lap shear specimen and cut-ply and

dropped-ply specimens, and revealed that the increase of G_{IIC} is related to the increased shear strength. The increase of shear strength is a linear function of the normal compressive stress, i.e. $\Delta S_{Shear\_n} = -\eta_f \sigma_{33}$ and the increase of G_{IIC} is a function of the compressive stress, the shear strength and the G_{IIC} :

$$\Delta G_{IIC} = G_{IIC}[-(2\eta_f / S_{Shear})\sigma_{33} + \eta_f(\sigma_{33} / S_{Shear})^2]$$

The new interface failure criterion based on the above understanding of the effect of compressive through-thickness stress on the delamination was implemented in finite element codes and produced much improved predictions of delamination in the presence of compressive stresses.

Brittle fibre tensile breakage is another major damage mode involved in laminate failure. The statistical strength in the fibre direction in laminates is largely influenced by the randomly distributed defects within the specimen, therefore is size dependent. Though various statistic fibre failure models were developed to account for this effect, they only achieved success in certain configurations of laminates and most of them only concerned with the global failure of a lamina or a laminate with special lay-ups due to the fibre breakage. Very little work has been done to analyze arbitrary configurations of fibre breaks including progressive fibre failure in a laminate. In this thesis, the unique advantage of finite element analysis in determining the complex stress and strain states in composites and calculating stress redistribution was utilized to implement a progressive statistic fibre-dominated element failure model which does not use ad hoc local load sharing rules as most other statistical fibre failure models do. The proposed progressive statistical fibre-dominated element failure model identifies the initiation of fibre tensile failure in a composite by a Weibull statistical criterion and removes only the element with the maximum longitudinal tensile stress in each step when the Weibull criterion is satisfied. This model can be applied in arbitrary configurations of a laminate with only the basic elastic properties and Weibull modulus m and characteristic strength σ_{unit} being provided.

Four point bending tests on 16ply, 32ply and 64ply unidirectional glass fibre laminates and six open-hole tests on carbon fibre/epoxy laminates with various quasi-isotropic lay-ups were selected to be modeled using this progressive fibre failure theory. The model could predict excellent fibre failure initiation strength for all the set-ups. The insufficiency of

four bending tests and open-hole tests is that the fibre failure was sudden and catastrophic, which gave little opportunity to study the influence of the sub-critical damage on the progression of fibre failure. To achieve the latter aim, Overheight Compact Tension (OCT) tests, originally devised by University of British Columbia, were conducted on eight different lay-ups of IM7/8552 carbon/epoxy laminates. In OCT tests, a stable process zone are formed ahead of the crack tip and sub-critical damage in the form of splitting and delamination are promoted, thus it is possible to investigate their interaction with progressive fibre failure.

OCT test results showed that lay-up and ply block thickness (stacking sequence of laminates) could significantly influence the failure modes of a laminate. In general dispersed plies within a laminate restrict splitting and delamination and promote fibre failure and crack growth through the whole thickness. Damage growth in such laminates is more localized. In contrast, blocked plies promote a larger amount of splitting and delamination and cause a larger process zone. When this process zone becomes so large that the specimen size is no longer sufficient, the specimen fails in a form of global collapse with the 0 plies pulling out of the specimens.

OCT tests on all the eight lay-ups were modelled using interface elements implemented in Umat42 and progressive fibre failure theory implemented in Umat44 in LS-Dyna. The simulation could well capture the progressive growth of splitting, delamination and fibre breakages within various laminates. The predicted Load vs. Pin Opening Displacement (POD) curves, final failure modes, and delamination within the specimens were in excellent accordance with experimental results.

The above modelling work and comparison with experimental results showed that the technique in this thesis to model stress and damage interaction in fibre reinforced composite laminates has been highly successful. The original objectives have thus been satisfied. The techniques is thus worth further application and verification in future modelling work of composite structures.

6.2 Future Work

Mesh dependency of progressive fibre dominated element failure theory in this thesis was briefly discussed in modelling the 32ply four point bending test. This is worth further investigation when being applied in more complex structures, especially the OCT specimens. To closely model the splitting behavior as seen in X-ray results within laminates, a very fine mesh was applied in modelling the OCT specimens in this thesis, which caused the simulations to be very time-consuming. For instance, the largest model for $[0/90]_{8s}$ lay-up has 231,936 solid elements and 337, 174 discrete beam interface elements, which took around 400 running hours for 1CPU on the Blue Crystal High Performance computer to reach the fibre failure initiation point and a further 300 hours to get a progressive failure result for the specimen. Though mesh dependency of the OCT models was discussed in Section 5.2.4 with refined meshes, the influence of coarsened mesh and how coarse the mesh could be to achieve the convergent results is more worth investigation for the concern of computing efficiency. If the progressive fibre dominated element failure theory proved to be much less mesh dependent, a coarser mesh could be applied in OCT specimens and obtain results much more quickly.

The implementation of progressive fibre dominated element failure theory in this thesis needs to integrate elemental Weibull survival probability through the whole model in each time step. In parallel computing, this is can only be realized by using 1CPU so far. When using multiple CPUs in BlueCrystal, the specimen would be divided into several parts accordingly and the integration only performed separately in each part instead of through the whole model. If the global integration problem using more than one CPU could be resolved by understanding the data communication mechanism of parallel computing, the advantage of high performance computers could be more efficiently utilized to improve the simulation speed greatly.

The predicted fibre pull-out POD value for lay-up $[0_4/90_4]_{2s}$ in OCT tests was much lower than experimental result. This might be improved by putting more potential 0° and 90° splits in the model, since it was evident in X-ray images that massive 0° and 90° splitting existed around the notch of lay-up $[0_4/90_4]_{2s}$ and it was proved that splits could help the

growth of delamination and increase the non-linearity behavior, hence increase the POD value to the fibre pull-out. This is worth further verifying in future work.

New techniques for creating mesh independent cracks within a laminate using eXtended Finite Element Method (XFEM)[215],[216],[217] or the phantom nodes method[218],[219] offer a potential solution to the required high split density. These have been shown to have capability for creating matrix cracks in arbitrary meshes and being coupled with cohesive zone models. Further work is required to fully demonstrate their robustness and application across a wider range of cases but initial results appear promising. Integration of techniques such as these with the work presented here would be useful step forward.

The predicted load bearing ability of the $[45/90/45/0]_{4s}$ lay-up from the initial model was much higher than the actual result in experiments after fibre failure initiated. The proposed element cluster failure model was in turn slightly lower and resulted in premature failure for other layups. It will be necessary to undertake further work to better understand the criterion which should be used to determine element removal after the initial failure point has been identified by the Weibull integration.

Appendix A Data Structure and Algorithms for Interface Elements Pre-processor

1. For Discrete Beam Interface Elements

1.1 Data structures

The file 'modules.for' lists all the data structures applied in the program. They are:

1 . type: node

real area

real coord(3)

This data structure is used to record global coordinates information of each node, and its effective area when forming the node of an discrete-beam interface element.

2. type: coord

real xvectors(3)

real vvectors(3)

This stores axial and transverse vectors of beam elements.

3. type: element

integer elem_no

integer nodes(8)

integer faces(6)

This records the serial number of the solid element in the model, serial numbers of its 8 nodes, and positions of its 6 faces in a ply (if faces(i)=0, the i-th face of the element is an outer face, if faces(i)=1, then the i-th face is an inner face).

4. type: interline

integer face_no

integer id_line(2)

This records the adjacent surface information of the edge of one surface. For instance, when interlines(3)%face_no=25, id_line(1)=4 and id_line(2)=2, it means that the 3rd edge of one surface is also the 4th edge of the 25th surface in the same ply, and the directions of this line in two adjacent surfaces are reverse. If id_line(2)=1, the two edges are in the same direction.

5. type: surface

integer interply_no

integer interface_no

integer id_elem

integer id_face

type(interline) interlines(4)

This reecords the information of interlaminae number, host element number of the outer face, its position in host element, and the adjacent surface information of its 4 edges. For instance, when

surfaces(5)%interply_no=11, interface_no=3, id_elem=36, id_face=4,

%interlines(1)%face_no=27, id_line(1)=3, id_line(2)=1

%interlines(2)%face_no=32, id_line(1)=4, id_line(2)=2

%interlines(3)%face_no=41, id_line(1)=2, id_line(2)=2

%interlines(4)%face_no=52, id_line(1)=1, id_line(2)=1

it means that the 5th surface of one ply is the 4th face of this ply's 36th elements, it has interface with the 3rd surface of the 11th ply. The 1st edge of this surface is also the 3rd edge of the 27th surface in the same ply, it has the same direction in two different surfaces. In the same sense, the 3rd edge of the surface is the 2nd edge of the 41st surface, its orientations in two surfaces are reverse.

6. type: beam

integer part_no

integer id_coord
real area
integer nodes(2)

This records the part number, local coordinate system number, effective area and component nodes of the discrete beam elements.

7. type: ply
integer no_elems
integer no_surfaces
integer no_beams
type(element) elements(200000)
type(surface) surfaces(200000)
type(beam) beams(200000)

This records the element, surface and beam information in each ply.

1.2 Algorithms

The maximum number of nodes and plies that the program can deal with are 9,000,000 and 30 respectively. Each laminate can at most have 200,000 elements, 200,000 surfaces and 200,000 beams. The user can adjust these limits in 'modules.for' according to the actual configuration of personal computer.

The main algorithms in the program are:

1.Matching outer faces of each ply:

After the program reads in the geometry data of the model, it begins to find out the outer faces of each ply. Ply by ply the program matches 6 faces of every element to faces of other elements in the same ply by comparing the node information of the face (if the face is triangular, the face is taken as a special quadrangular face, in which two nodes are coincident.).

One matrix, id_nodes(6,4)=[1 2 3 4
1 2 6 5
2 3 7 6
7 8 5 6
7 8 4 3
1 5 8 4]

is used to index serial numbers of the 4 nodes of the face in the element. For instance, id_nodes(4,3)=5 means that the 3rd node on the 4th face of the element is the 5th node of the element.

If one face in an element can find a matched face in another element, the corresponding element%faces(i) will be set to 1. When the matching operation finished, those faces with value of '0' are the outer faces of the ply.

2. Finding adjacent face and edge of the outer face

After step 1, the program starts to match 4 edges of every outer face with edges of other outer faces in the same ply by comparing node numbers of the edge.

The matrix: id_lines(4,2)=[1 2
2 3
3 4
4 1]

is used to index the serial numbers of two nodes of the edge in the surface. For instance, id_lines(3,1)=3 means that the 1st node of the 3rd edge is the 3rd node of the surface; id_lines(3,2)=4 means that the 2nd node of the 3rd edge is the 4th node of the surface.

If the i-th edge of one outer face shares the same edge with another outer face, its data structure surface%interlines(i)%face_no will record the face number of the matched face, surface%interlines(i)%interline(1) records matched edge number in another face, and

surface%interlines(i)%interline(2) records the edge orientation relative to itself(if their orientations are the same, =1; if their direction are reverse, =2). This step is mainly to provide essential information for calculation in the subroutine 'modify_node.for'.

3. Matching interfaces

In this step the program matches outer faces of each ply with outer faces of other plies by comparing their nodal coordinates. If the two nodes in two plies have the same serial number, then a new node is created using the same coordinates. One of the two plies will use the new node for its elements and the other ply still uses the old node in its elements. Elements that involve the new node will change their corresponding elements%node(8) information accordingly using the subroutine 'modify_node.for' of which the algorithm will be described in the next section. In this way the interface between two plies is separated. If 4 edges of one outer face in a ply match the 4 edges of an outer face in another ply, then the PID, face number and the edge information of the later ply are stored in the data structure, surfaces%interlines(4) of the former ply. The effective area of each node on the faces is also calculated by the subroutine 'area.for'(its algorithm will be described in section 6) and stored in the corresponding node%area.

When this process finished, all interfaces will be identified and separated.

4. Creating discrete beam thickness elements.

On the basis of step 3, discrete beam elements are created from the node in lower PID ply to its matched node in higher PID ply. The effective area of the beam is taken as the weight area of the node in the lower ply. The orientation vectors of the beam are calculated in 'beamvector.for', whose algorithm will be described in section 7. The part ID of beam elements is set to lower PID*100+ higher PID. For instance, a beam with the part ID '203' means that it's between the 2^{nd} ply and 3^{rd} ply.

5. Algorithm of 'modify_node.for'

One matrix: mat_line(4,4)=[4 2 2 1

1 2 3 1

2 2 4 1

3 2 1 1]

is used to index the position of a common node in two adjacent edges of one surface. For instance, to find the adjacent edge of the 2nd edge on its 1st node of one surface, we use mat_line(2,2*1-1)=mat_line(2,1)=1(adjacent edge no.) and mat_line(2,2*1)=mat_line(2,2)=2(adjacent node ID), which means that the 1st node of the 2rd edge is also the 2nd node of the 1st edge;

to find the adjacent edge of the 2nd edge on its 2nd node of the surface, we use mat_line(2,2*2-1)=mat_line(2,3)=3(adjacent edge no.) and mat_line(2,2*2)=mat_line(2,4)=1(adjacent node ID), which means that the 2nd node of the 2nd edge is the 1st node of the 3rd edge;

In Step 3, when the i-th node of the j-th edge on the m-th surface of one ply is found to have the same node number with one node on the ply numbered with a lower PID, this node will be re-numbered as node_no=1+total number of nodes.

a>.

The serial number of the element hosting the m-th surface is

elem_no=surfaces(m)%id_elem.

The serial number of the node on this element is indexed as

id_node=id_nodes(surfaces(m)%id_face, id_lines(j, i)), where:

id_nodes((6,4)=[1 2 3 4

1 2 6 5

2 3 7 6

7 8 5 6

7 8 4 3

1 5 8 4]

id_lines(4,2)=[1 2

2 3

3 4

4 1]

then the node information of this element can be modified as

elements(elem_no)%nodes(id_node)=node_no.

b>.

With id_line2=mat_line(j, 2*i-1) and id_node2=mat_line(j, 2*i), it can be found that the i-th node of the j-th edge is also the id_node2_th node of the id_line2_th edge on the m-th surface.

With face_no2= surfaces(m)%interlines(id_line2)%face_no, the surfaces(face_no2) is the adjacent surface on the id_line2_th edge of the m-th surface on the same ply.

The id_line2_th edge of the m-th surface is also the id_interline=surfaces(m)%interlines(id_line2)%id_line(1) _th edge of its adjacent surface.

The position of the i-th node of the j-th edge of the m-th surface on the id_interline_th edge of the face_no2_th surfaces is calculated as
id_internode= mod(id_node2*surfaces(face_no2)%interlines(id_line2)%id_line(2), 3)

For instance, if one node is the 2nd node of the 3rd edge of the 6th (m=6) surface,
surfaces(6)%interply_no=11, id_elem=43, id_face=5,
%interlines(1)%face_no=27, id_line(1)=3, id_line(2)=1
%interlines(2)%face_no=32, id_line(1)=4, id_line(2)=2
%interlines(3)%face_no=41, id_line(1)=2, id_line(2)=2
%interlines(4)%face_no=52, id_line(1)=1, id_line(2)=1

then the 6th surface of the ply is the 5th (surfaces(6)%id_face=5) face of its 43rd (elem_no=surfaces(6)%id_elem=43) element, the node is the 4th (id_lines(3,2)=4) node of the 6th surface, and the 6th (id_node=id_nodes(5, 4)=6) node of the 43rd element.

The 2nd node of the 3rd edge is also the 1st (id_node2=mat_line(3, 2*2)=1) node of the 4th (id_line2=mat_line(3, 2*2-1)=4) edge of the 6th surface. The adjacent surface on the 4th edge of the 6th surface is the 52nd (face_no2=surfaces(6)%interlines(4)%face_no=52) surface on the same ply. The 4th edge of the 6th surface is also the 1st (id_interline=surfaces(6)%interlines(4)%id_line(1)=1) edge of the 52nd surface, the edges in two surfaces have the same direction (surfaces(6)%interlines(4)%id_line(2)=1), i.e. their first node number and second node number are equal correspondingly.

Therefore, the 2nd node of the 3rd edge of the 6th surface is also the 1st (id_internode=mod(1*1,3)=1) node of the 1st (id_interline=1) edge of the 52nd (face_no2=52) surface on the same ply.

c>.

Then the number of the element hosting the adjacent surface of the m-th surface on its id_line2_th edge is

elem_no2=surfaces(face_no2)%id_elem

the number of the new node on this element is indexed as

id_node=id_nodes(surfaces(face_no2)%id_face, id_lines(id_interline, id_internode))

the node information of this element can be modified as

elements(elem_nos)%nodes(id_node)=node_no.

d>

Return to step b> to continue finding the adjacent surface of the face_no2_th surface and its host element and modify its node number as the new value, then the next surface and its host element...till the adjacent surface returns back to the m-th surface. In this way all elements that include the new node are modified, and the interface is separated.

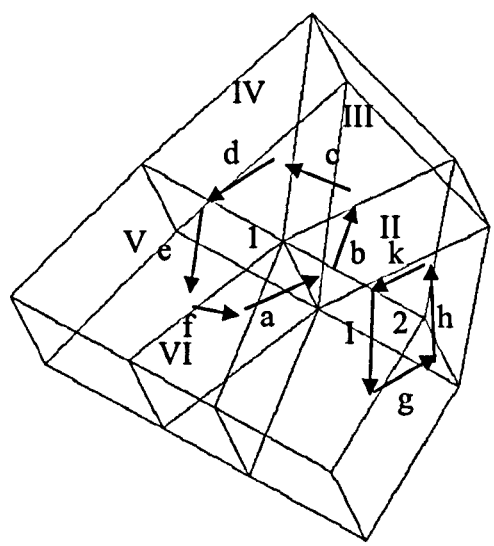

Fig A 1.2-1 Algorithm demonstration for 'modify_node.for'

To take the model in Fig 3.1-10 as an example, we assume that the loop begins from node 1 of line a. In step a>, the program modifies the node 1 on element I. Then in step b>, line b of element I is figured out and in step c>, element II is modified for its common edge with element I on line b. As the program continues, element III is modified for its common edge with element II on line c, so is element IV for common line d with element III, element V for common line e with element IV, element VI for common line f with element V. At last, when the loop reaches element I again all elements that involve the node 1 are modified and the loop finishes.

In the same sense, if the loop begins from node 2 of line g, then the loop is line g(element I)→line h(element II)→line K(element II, skip)→line b(element I)→finish.

6. Algorithm of 'area.for'

For a quadrangular mesh as shown in Fig A 1.2-11 (the triangular mesh can be taken as a special quadrangular mesh, in which the 3rd node is coincident with the 4th node) in the global coordinate system XYZ, its 4 nodes are:

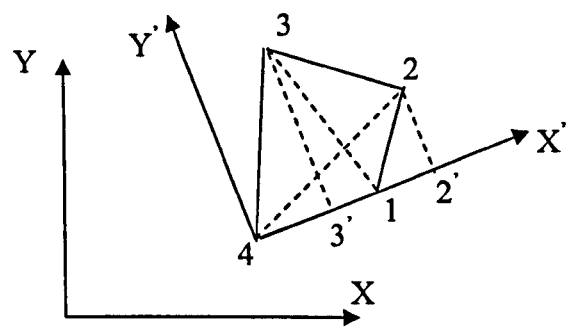

Fig A 1.2-2 Relationship of Local and Global coordinate systems

node1(x_1,y_1,z_1)
node2(x_2,y_2,z_2)
node3(x_3,y_3,z_3)
node4(x_4,y_4,z_4)

Node 4 is the origin of the local coordinate system X'Y'Z'. X' is from node 4 to node 1 and Y' is in the mesh plane and points to the side of node 2 and node 3.

Distances between two nodes of the mesh are:

d14(distance between node 1 and node 4)= $\sqrt{(x_1-x_4)^2+(y_1-y_4)^2+(z_1-z_4)^2}$

d24(distance between node 2 and node 4)= $\sqrt{(x_2-x_4)^2+(y_2-y_4)^2+(z_2-z_4)^2}$

d34(distance between node 3 and node 4)= $\sqrt{(x_3-x_4)^2+(y_3-y_4)^2+(z_3-z_4)^2}$

d21(distance between node 2 and node 1)= $\sqrt{(x_2-x_1)^2+(y_2-y_1)^2+(z_2-z_1)^2}$

d31(distance between node 3 and node 1)= $\sqrt{(x_3-x_1)^2+(y_3-y_1)^2+(z_3-z_1)^2}$

Local coordinates of the 4 nodes are calculated as the below:

node 4: ($x'_4=0$, $y'_4=0$, $z'_4=0$)

node 1: ($x'_1=d14$, $y'_1=0$, $z'_1=0$)

node 2: (x'_2, y'_2, $z'_2=0$)

node 3: (x'_3, y'_3, $z'_3=0$)

$$\begin{cases} d_{24}^2-(x_2')^2=d_{21}^2-(x_2'-x_1')^2 \\ d_{24}^2=(x_2')^2+(y_2')^2 \end{cases} \Rightarrow \begin{cases} x_2'=\dfrac{d_{24}^2-d_{21}^2+(x_1')^2}{2x_1'} \\ y_2'=\sqrt{d_{24}^2-(x_2')^2} \end{cases}$$

$$\begin{cases} d_{34}^2-(x_3')^2=d_{31}^2-(x_3'-x_1')^2 \\ d_{34}^2=(x_3')^2+(y_3')^2 \end{cases} \Rightarrow \begin{cases} x_3'=\dfrac{d_{34}^2-d_{31}^2+(x_1')^2}{2x_1'} \\ y_3'=\sqrt{d_{34}^2-(x_3')^2} \end{cases}$$

We assume that the shear stress distribution function on above mesh is S(x',y').

The total shear force SF on the mesh will be $SF=\int_A S(x',y')dx'dy'$, A is the area of the mesh.

We now need to determine a set of values of A_1, A_2, A_3 and A_4, which can satisfy the following equations:

$$\begin{cases} SF=\int_A S(x',y')dx'dy'=S(x_1',y_1')A_1+S(x_2',y_2')A_2+S(x_3',y_3')A_3+S(x_4',y_4')A_4 \\ A_1+A_2+A_3+A_4=A \end{cases}$$

Here, A_1, A_2, A_3 and A_4 are corresponding effective areas of node 1, node 2, node 3 and node 4.

In this program, Gauss interpolation formulae are applied to calculate the values of A_1, A_2, A_3 and A_4.

7. Algorithm for calculating beam orientation vectors

Fig A 1.2-3 (a) presents a typical outer surface mesh pattern on which a beam element need to be generated at the node O.

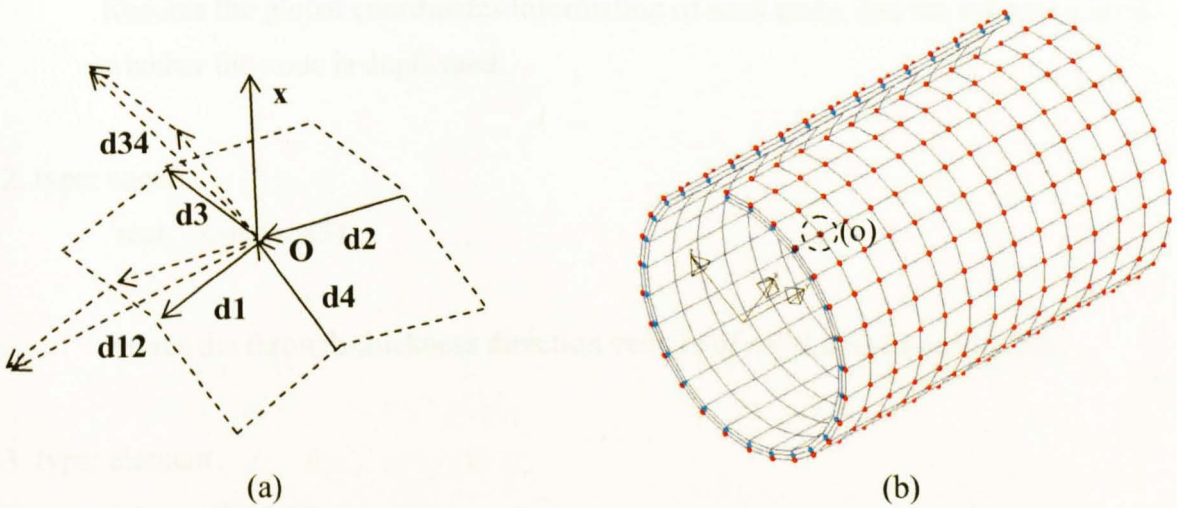

Fig A 1.2-3 Beam orientation vectors

From the stored information in step 3, the values of vector **d1**,**d2**,**d3**, **d4** can be calculated. Then the vector **d12**=**d1**+**d2** and vector **d34**=**d3**+**d4** are obtained.

The axial vector of the beam at node O, **x** , would be: **x**=**d12** × **d34**.

The transversal vector of the beam can be taken as **d12** or **d34**.

Fig A 1.2-3(b) demonstrates a local coordinate system for beam (o), which is obtained by 'beamvector.for'. The result shows that the beam orientation vectors calculated from this algorithm is reasonable.

2. For Solid Interface Elements

2.1 Data structures

The file 'modules.for' lists all the data structures applied in the program. They are:

1 . type: node

integer change

real coord(3)

Records the global coordinates information of each node, and the information on whether the node is duplicated.

2. type: coord

real xvectors(3)

Stores the through-thickness direction vectors of solid interface elements.

3. type: element

integer elem_no

integer nodes(8)

integer faces(6)

Similar to that in section 3.1

4. type: interline

integer face_no

integer id_line(2)

Similar to that in section 3.1

5. type: surface

integer interply_no

integer interface_no

integer id_elem

integer id_face

type(interline) interlines(4)

Similar to that in section 3.1

6. type: intsolid

integer part_no

integer nodes(8)

Records the part number and component nodes of the solid interface elements.

7. type: ply

integer no_elems

integer no_surfaces

integer no_intelems

type(element) elements(200000)

type(surface) surfaces(200000)

type(intsolid) intelems(200000)

Records the element, surface and solid interface information in each ply.

2.2 Algorithms

The maximum numbers of nodes and plies that the program can deal with are 9,000,000 and 30 respectively. Each laminate can at most have 200,000 elements, 200,000 surfaces and 200,000 beams. The user can adjust these limits in 'modules.for' according to their actual situation.

The main algorithms in the program are:

1. Matching outer faces of each ply:

Similar to step 1 in section 3.1.2.

2. Finding adjacent face and edge of the outer face

Similar to step 2 in section 3.1.2.

3. Matching interfaces

Similar to step 3 in section 3.1.2.

4. Creating solid interface elements.

On the basis of step 3, *SOLID interface elements are created by the four nodes in lower PID ply to and their matched four nodes in higher PID ply. The coordinates of the eight nodes composing the solid interface element are changed to:

X_new(higher PID)=**X**_old(higher PID)+TK*V_thickness;

X_new(lower PID)=**X**_old(lower PID)-TK*V_thickness;

In which, **X**_new is the new coordinate vectors, **X**_old is the original coordinate vectors, TK is the thickness of solid interface and V_thickness is the dimensional through-thickness direction vectors of the interface. V_thickness is calculated in 'intelemvector.for' with similar algorithm as that for **X** vectors in 'beamvector.for'.

The part ID is set to lower PID*100+ higher PID. For instance, a solid interface with the part ID '203' means that it's between the 2nd ply and 3rd ply.

Appendix B Input Cards for User Defined Materials in LS-Dyna

1. User Defined Material Input Card for Discrete Beam Interface Elements in Ls-Dyna

The material formulation for discrete beam interface elements was implemented in Ls-Dyna using user defined material 42(Mat42). The input card for Mat42 is as the below:

```
*MAT_USER_DEFINED_MATERIAL_MODELS
$ MID      RO      MT     LMC      NHV    IORTHO    IB    IG
     11 1.0E-4      42      11        5         0    11    11
      0       0       0       0        0
$  GIc     GIIc     SY1    SY12       EI       EII   alf
    0.2      1.0    60.0    90.0  1000000.0 1000000.0   1.0   0.0
$              f      BG
    0.0      0.0  1000.0
```

Where:

MID	material identification
RO	material mass density
MT	user material type.
LMC	length of material constant array.
NHV	number of history variables to be stored
IORTHO	set to 1 if the material is orthotropic, here is set to 0
IB	address of bulk modulus in material constants array
IG	address of shear modulus in material constants array

GIC	Mode I fracture energy.
GIIC	Mode II fracture energy
SY1	Mode I yield stress
SY12	Mode II yield stress
EI	Young's modulus

EII	Shear Modulus
alf	mix-mode factor of GIc and GIIc, here using 1
f	enhancing factor of through-thickness compressive stress on delamination
BG	Bulk and Shear modulus of interface elements BG is used for time step control

2. User Defined Material Input Card for Solid Interface Elements in Ls-Dyna

The material formulation for discrete beam interface elements was implemented in Ls-Dyna using user defined material 49(Mat49). The input card for Mat49 is as the below:

*MAT_USER_DEFINED_MATERIAL_MODELS

$ MID	RO	MT	LCM	NHV	IORTHO	IB	IG
12	1.0E-2	49	13	35	1	12	13
0	0	0	0	0			
$ AOPT	MAXC	XP	YP	ZP	A1	A2	A3
0.0	3.0	0.0	0.0	0.0	0.0	0.0	0.0
$ V1	V2	V3	D1	D2	D3		
0.0	0.0	0.0	0.0	0.0	0.0	0.0	
$ GIc	GIIc	Y1	Y12	EI	EII	alf	tk
0.225	0.87	94.0	75.0	800000.0	300000.0	0.0	1.0E-2
$		f	B	G			
0.0	0.0	0.79	1000.0	1000.0			

Where:

MID	material identification
RO	material mass density
MT	user material type.
LMC	length of material constant array.
NHV	number of history variables to be stored
IORTHO	set to 1 if the material is orthotropic, here is set to 1
IB	address of bulk modulus in material constants array

IG	address of shear modulus in material constants array

The meaning and set of
AOPT, MAXC, XP, YP, ZP, A1, A2, A3, V1, V2, V3, D1, D2, D3
are the same as those in Mat2, Mat21 and Mat22 in LS-Dyna.

GIC	Mode I fracture energy.
GIIC	Mode II fracture energy
SY1	Mode I yield stress
SY12	Mode II yield stress
EI	Young's modulus
EII	Shear Modulus
alf	mix-mode factor of GIc and GIIc, here using 1
tk	thickness of solid interface elements
f	enhancive factor of through-thickness compressive stress on delamination
B	Bulk modulus
G	Shear modulus
	B and G are used for time step control

3 User Defined Material Input Card for Solid Element in Chapter 5 in Ls-Dyna

The material formulation for solid elements introduced in Chapter 5, which considered non-linear shear behaviour, thermal stress and fibre dominated element failure criteria was implemented in Ls-Dyna using user defined material 44(Mat44). The input card for Mat44 is as the below:

Mat44 (for fibre dominated element failure under Weibull criteria)

*MAT_USER_DEFINED_MATERIAL_MODELS

$ MID	RO	MT	LCM	NHV	IORTHO	IB	IG
12	1.0E-2	44	18	19	1	13	13
0	0	0	0	0			
$ AOPT	MAXC	XP	YP	ZP	A1	A2	A3

	2.0	0.0	0.0	0.0	0.0	1.0	0.0	0.0
$	V1	V2	V3	D1	D2	D3		
	0.0	0.0	0.0	0.0	1.0	0.0	0.0	
$	E11	E22	E33	PR21	PR31	PR32	G12	G23
	43900.0	15400.0	15400.0	0.1052	0.1052	0.3	4340.0	2750.0
$	G31	AA	AB	AC	BG	PD	m	sigmau
	4340.0	0.0	3.0E-5	3.0E-5	100000.0	10.0	29.3	1976.0
$	n	p1	p2	p3	p4	p5	a01	a11
	6	0.02	0.05	0.08	0.12	0.3	0.7328	5653
$	a21	a02	a12	a22	a03	a13	a23	a04
	-1.14600	42.65	1646	-15330	66.14	567.3	-2896	89.88
$	a14	a24	a05	a15	a25	a06	a16	a26
	-34.76	939.1	89.89	-34.81	939.3	-4.098	560.2	0.0

Where:

MID	material identification
RO	material mass density
MT	user material type.
LMC	length of material constant array.
NHV	number of history variables to be stored and output
IORTHO	set to 1 if the material is orthotropic, here is set to 1
IB	address of bulk modulus in material constants array
IG	address of shear modulus in material constants array

The meaning and set of
AOPT, MAXC, XP, YP, ZP, A1, A2, A3, V1, V2, V3, D1, D2, D3
are the same as those of Mat2, Mat21 and Mat22 in Ls-Dyna.

The meaning and set of
E11, E22, E33, PR21, PR31, PR32, G12, G23, G31, AA, AB, AC
are the same as those of Mat2, Mat21 and Mat22 in Ls-Dyna as well.

BG Bulk and shear modulus

BG is used for time step control

PD identification of modeled part.
if the model is a half model(for symmetric case), then PD=2,
if the model is a one quarter model, PD=4
in the similar way, if the model is only 1/10 modeled, then PD=10
if the model is fully modeled, PD=1

m weibull modulus

sigmau unidirectional strength of a unit volume material

n number of piecewise strains

p1...pn-1 piecewise strains

a01, a11, a21 coefficients of 2^{nd} order polynomial interpolation in the first piece of strains.

...

a0n,a1n,a2n coefficients of 2^{nd} order polynomial interpolation in the n-th piece of strains.

The output history variables are:

hisv(1): elemental volume at time t

hisv(2): temperature at time t

hisv(3): original elemental volume at time t=0

hisv(4): shear strain(4) in local material coordinate system

hisv(5): shear strain(5) in local material coordinate system

hisv(6): shear strain(6) in local material coordinate system

hisv(7): Elemental failure flag: =1 failed; =0 unfailed

hisv(8): Global failure flag: =1 Weibull integration criterion satisfied; =0 unfailed

hisv(9): backup variable for debugging the program

hisv(10): elemental Weibull integration

hisv(11): Global Weibull integration at each time step

hisv(12): maximum elemental Weibull integration at each time step

hisv(13): maximum fibre direction elemental stress at each time step

hisv(14): X stress in local material system

hisv(15): Y stress in local material system

hisv(16): Z stress in local material system

hisv(17): XY shear stress in local material coordinate system

hisv(18): YZ shear stress in local material coordinate system

hisv(19): ZX shear stress in local material coordinate system

Appendix C OCT Test Results and C-scan, X-ray Scan Results

1. $[0/90]_{4S}$(2mm)

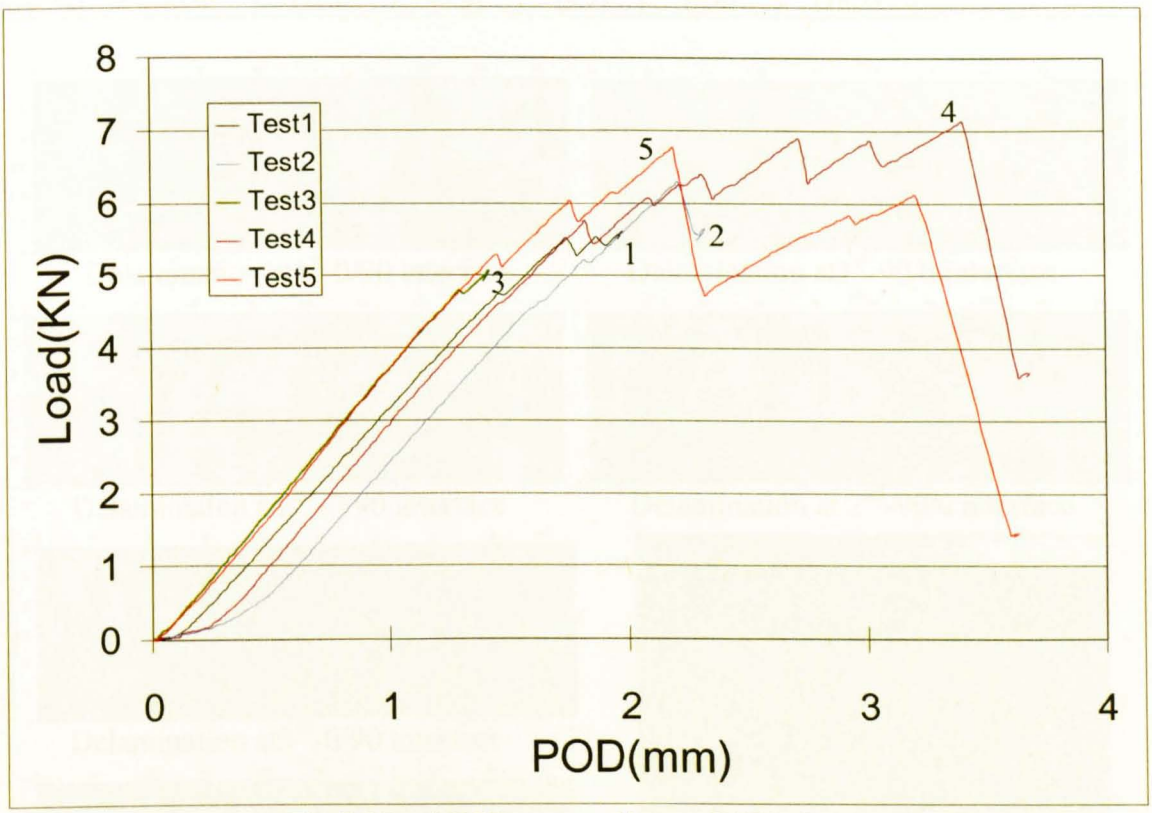

Fig C-0 Load-POD curves of lay-up $[0/90]_{4S}$(2mm)

Table C-1 Characterized load drops in OCT tests of lay-up $[0/90]_{4S}$(2mm)

$[0/90]_{4S}$ (2mm) Specimen No.	1st load drop		1st clear 0° splitting on surface		1st clear fibre breakage on surface		Unload
	Load (KN)	POD (mm)	Load (KN)	POD (mm)	Load (KN)	POD (mm)	
1	4.74	1.39	5.52	1.67			Unloaded after 0° splitting appearing on the surface and the load has two obvious dropdown
2	5.18	1.54	6.31	1.92			Unloaded after 0° splitting appearing on the surface and the load has a large dropdown
3	4.80	1.31					Unloaded after the 1st small load dropdown
4	4.68	1.30	5.75	1.66	7.12	3.23	Unloaded after the clear fibre breakage appearing on the

							surface and propagating towards the back side.
5	5.28	1.45	6.03	1.76	6.77	2.19	Unloaded after the fibre breakage propagating to the backside
Average (c.v.,%)	4.94 (6.9)	1.40 (10.0)	5.90 (6.9)	1.75 (9.7)	6.94 (2.6)	2.71 (19.2)	

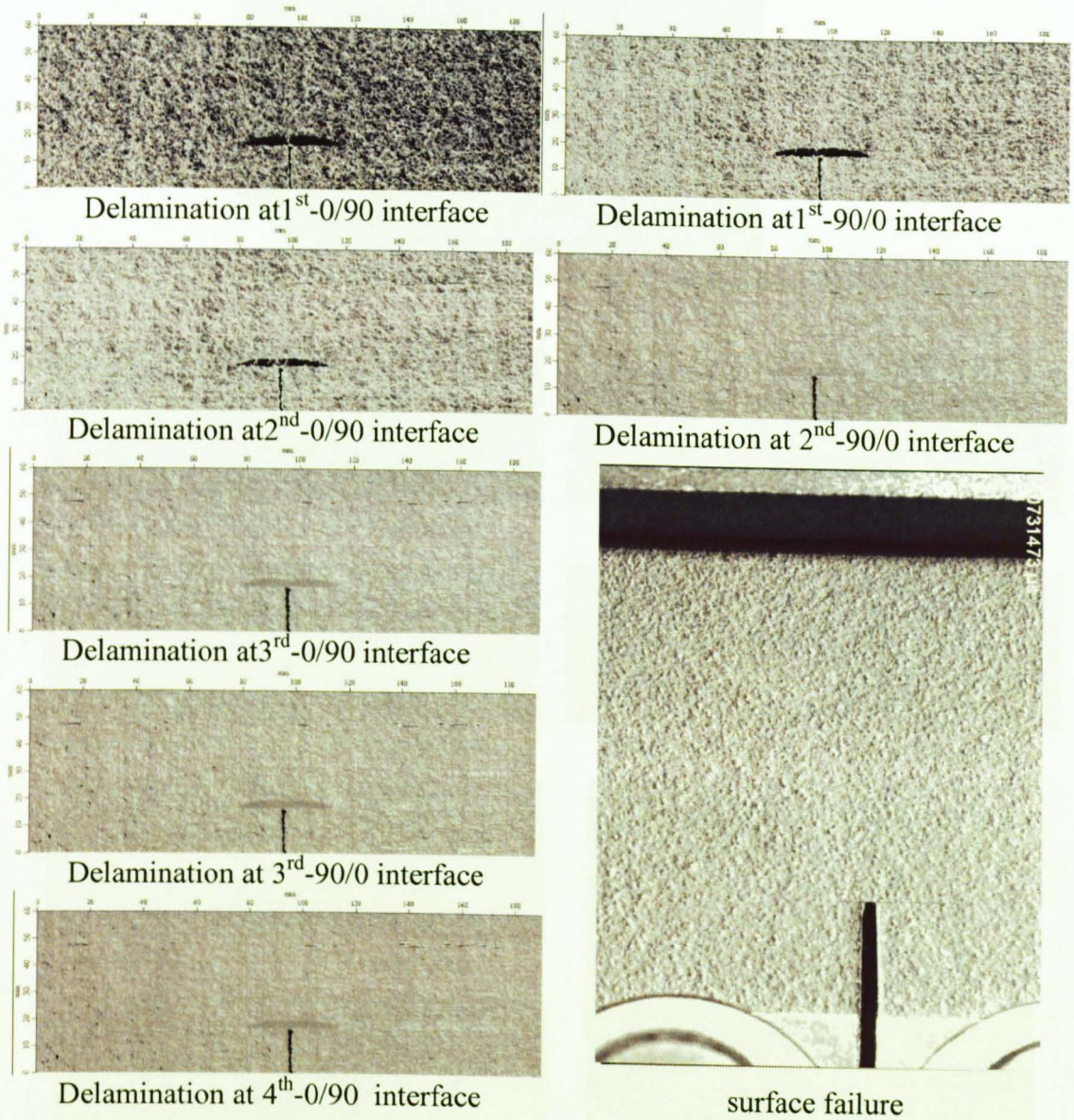

Fig C-1.1 C-scan results of test 1 and the surface failure

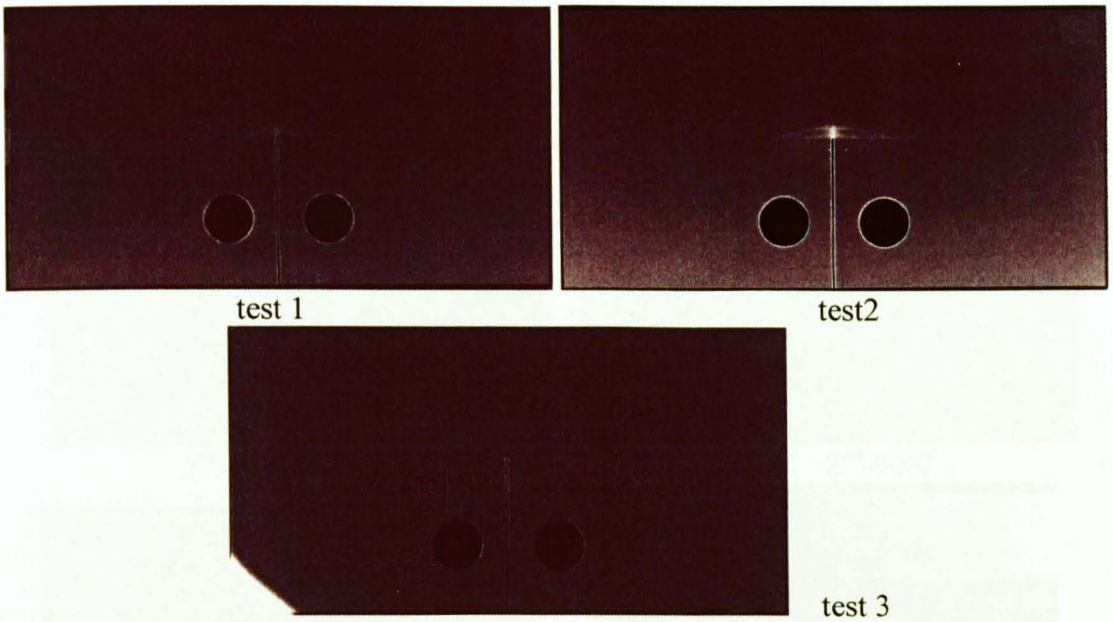

Fig C-1.2 X-ray scan results of test 1, test 2 and test 3

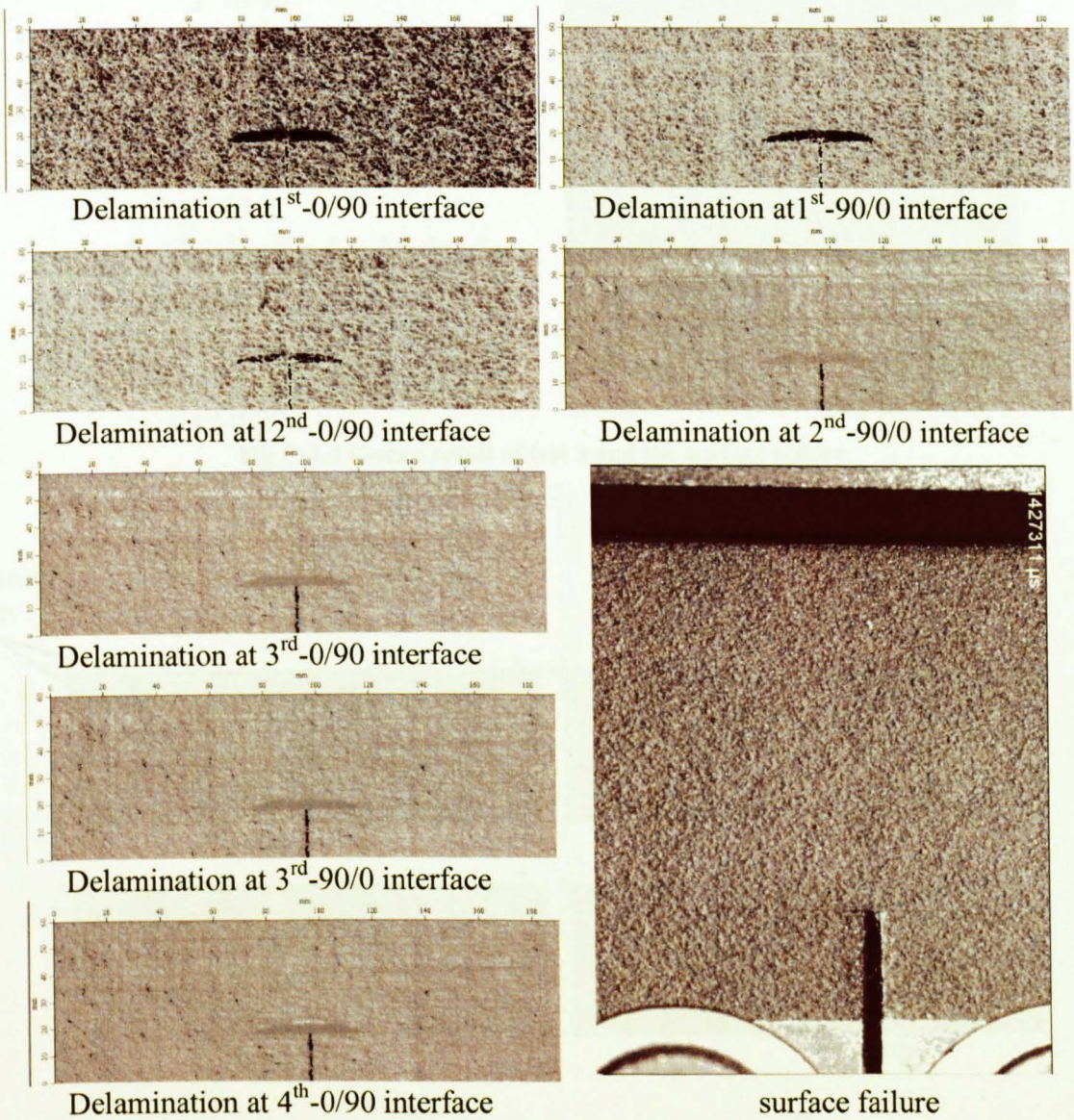

Fig C-1.3 C-scan result of test 2 and the surface failure

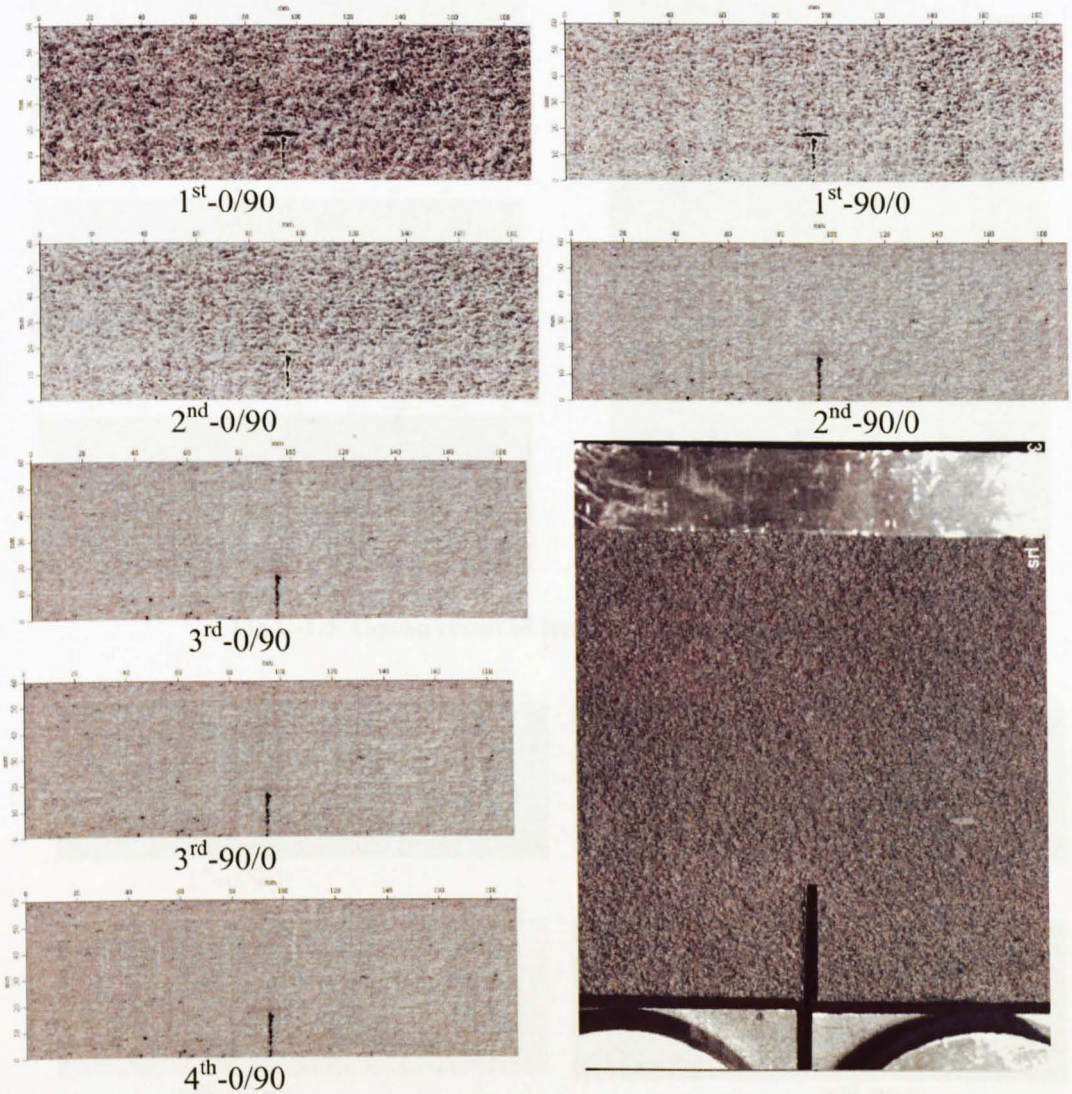

Fig C-1.4 C-scan result of test 3 and the surface failure

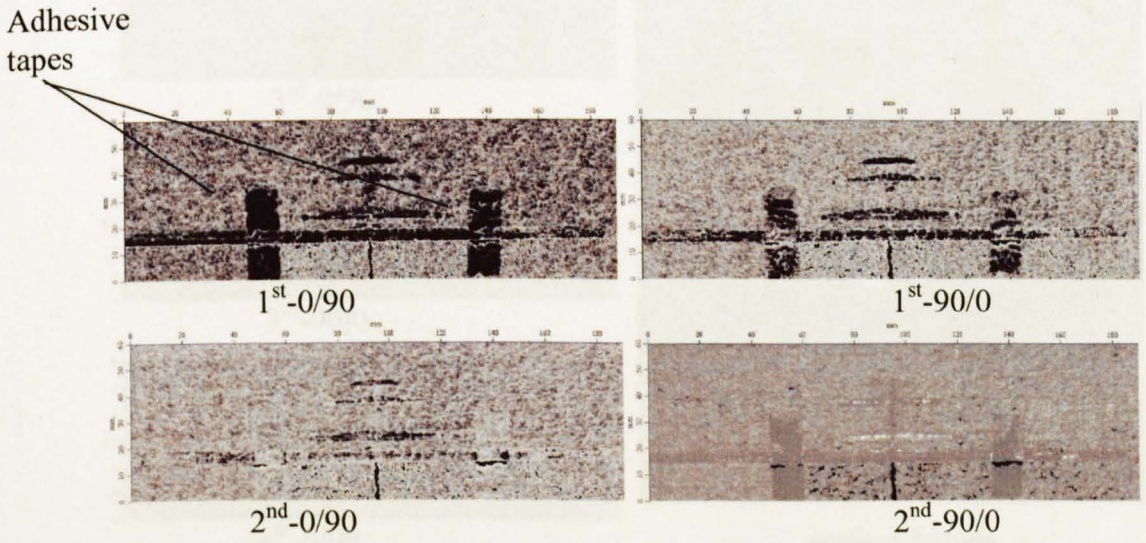

3rd-0/90

3rd-90/0

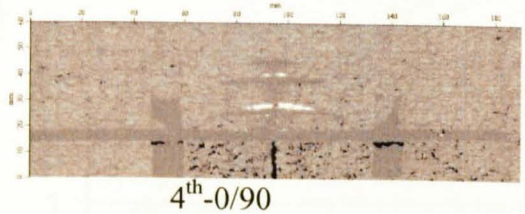

4th-0/90

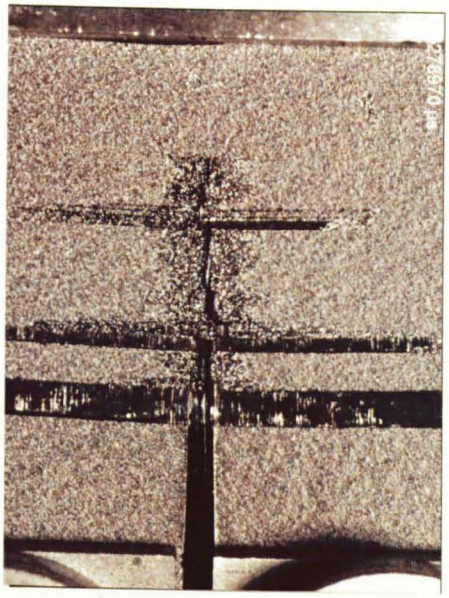

surface failure

Fig C-1.5 C-scan result of test 5 and the surface failure

1st-0/90

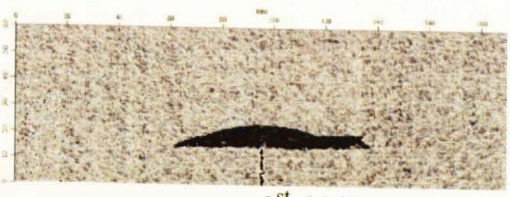

1st-90/0

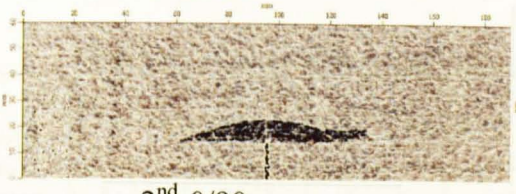

2nd-0/90

2nd-90/0

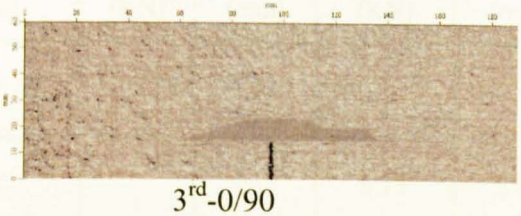

3rd-0/90

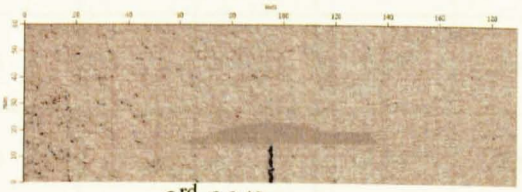

3rd-90/0

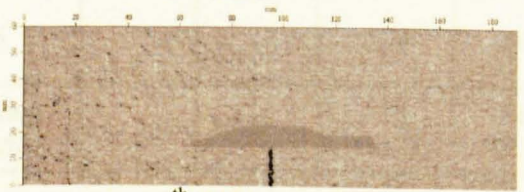

4th-0/90

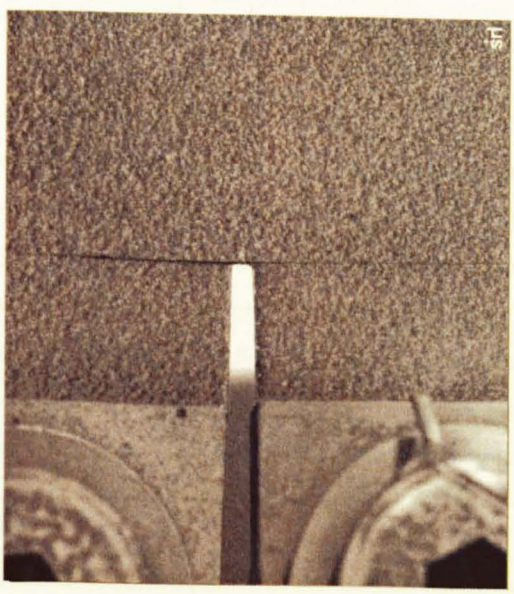

surface failure

Fig C-1.6 C-scan result of test 6 and the surface failure

2. $[0_2/90_2]_{2S}$ (2mm)

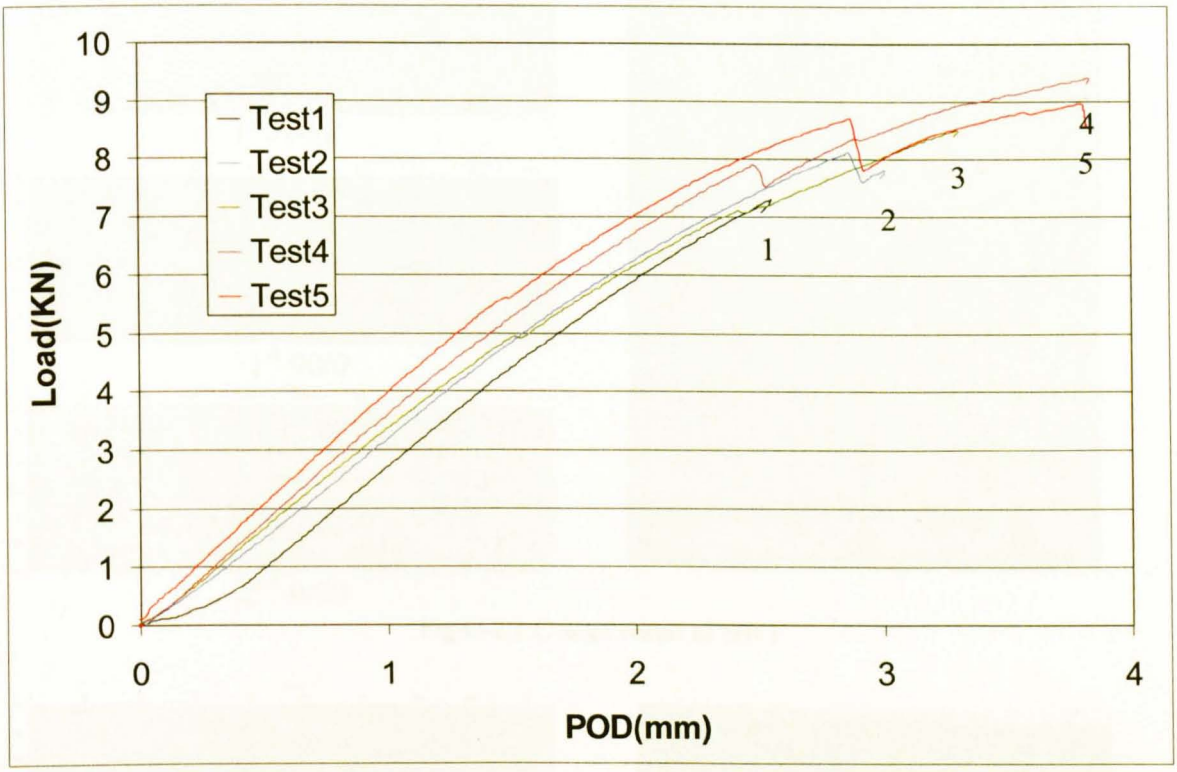

Fig C-2.0 Load-POD curves of lay-up $[0_2/90_2]_{2S}$ (2mm)

Table C-2.1 Characterized load drops in OCT tests of lay-up $[0_2/90_2]_{2S}$(2mm)

$[0_2/90_2]_{2S}$ (2mm) Specimen No.	1st interrupted		1st load drop		Final failure		Unload
	Load (KN)	POD (mm)	Load (KN)	POD (mm)	Load (KN)	POD (mm)	
1	7.32	2.32					Unloaded near and before the 1st load drop down.
2			8.13	2.86	7.76	3.00	Unloaded when the specimen began to warp
3			7.09	2.43	8.48	3.31	Unloaded when the specimen began to warp
4			7.84	2.50	9.39	3.84	Unloaded when the specimen began to warp
5			8.70	2.94	8.88	3.91	Unloaded when the specimen began to warp
Average (c.v,%.)			7.94 (10.7)	2.68 (9.7)			

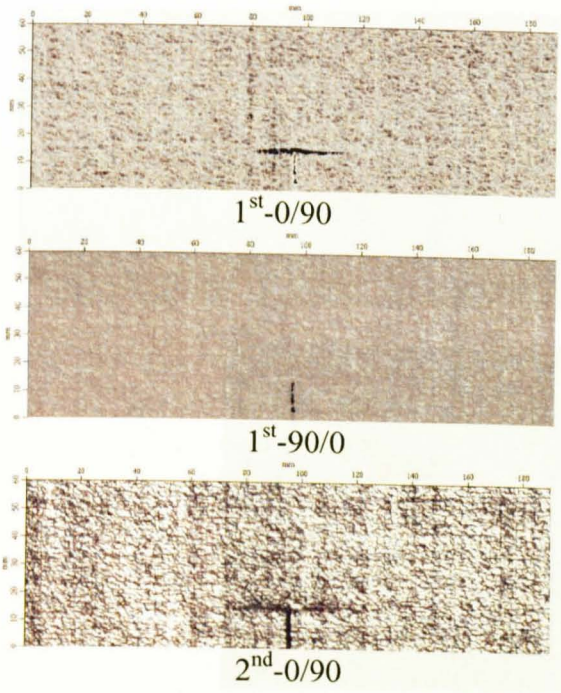

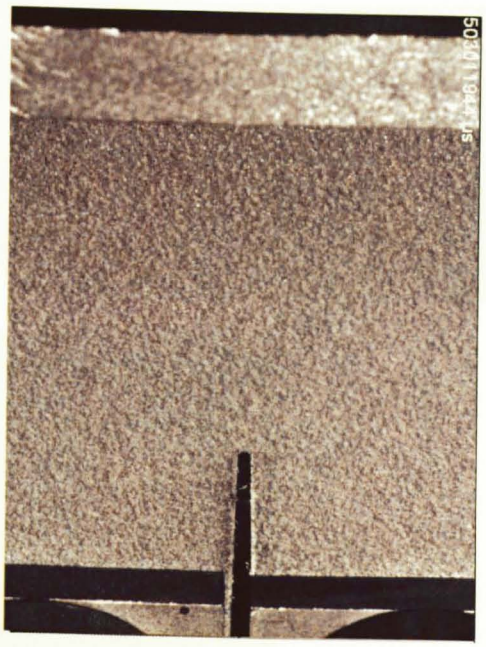

Fig C-2.1 C-scan result of test 1

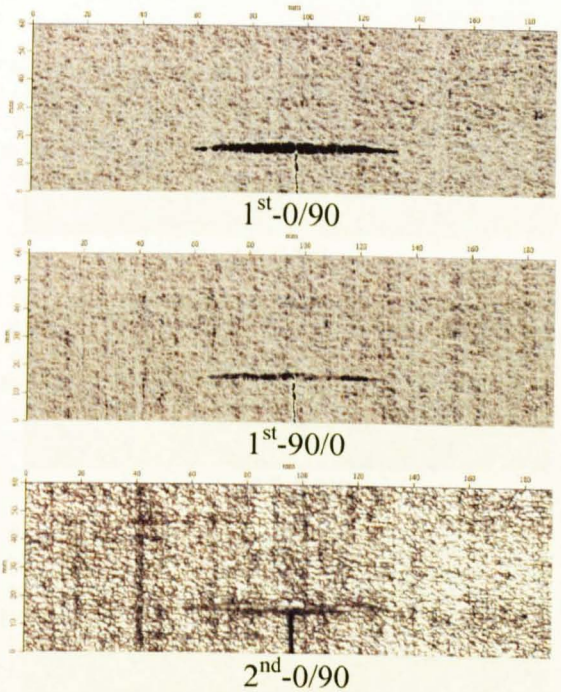

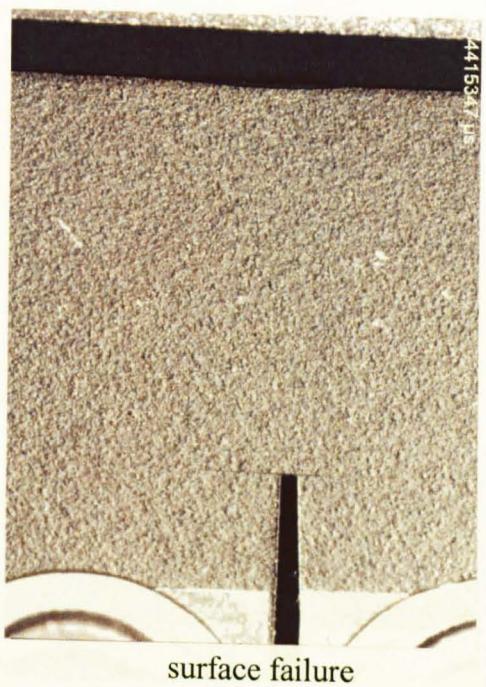

Fig C-2.2 C-scan result of test 2 and the surface failure

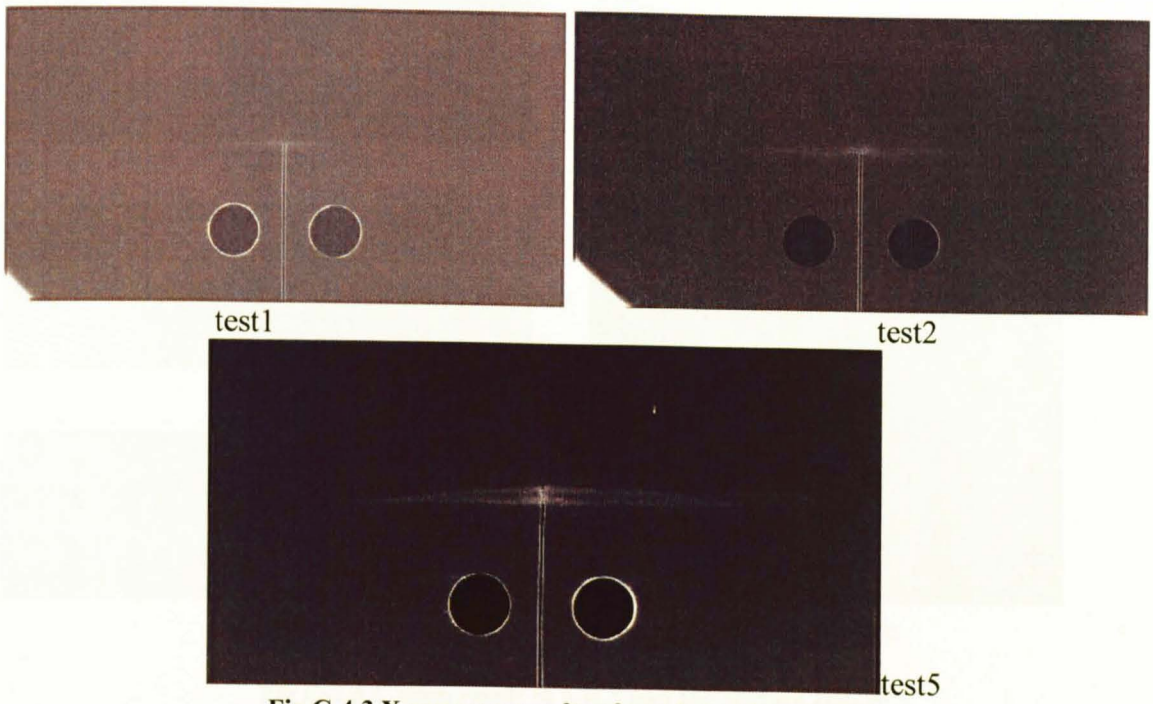

Fig C-4.3 X-ray scan results of test 1, test 2 and test 3

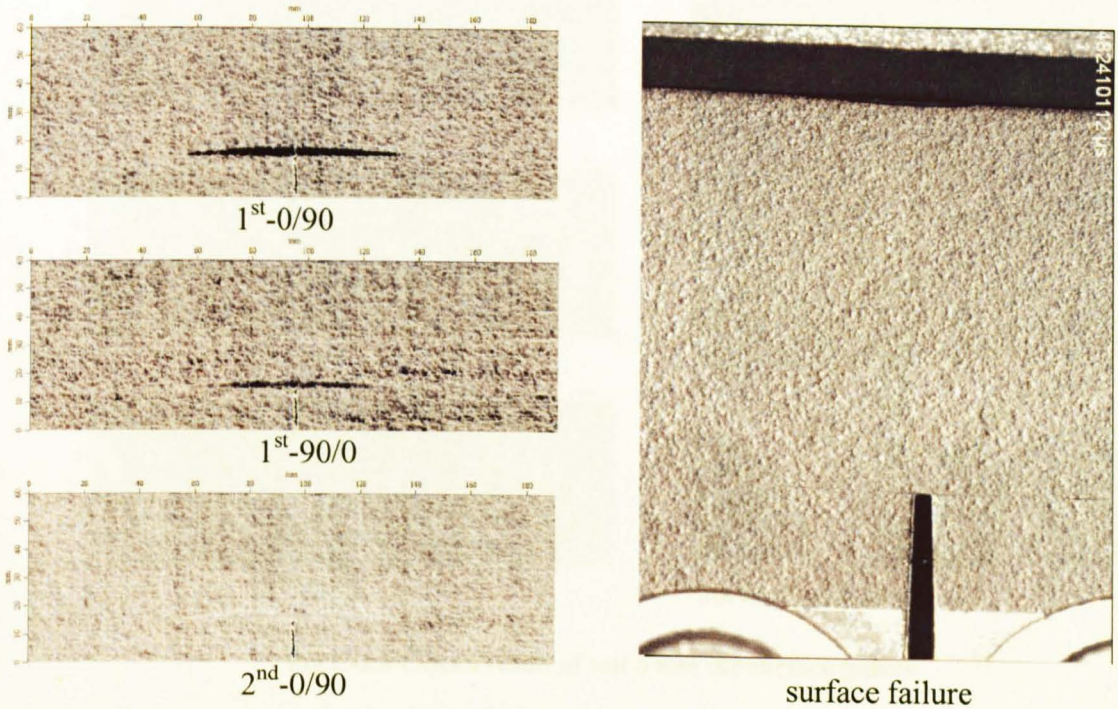

Fig C-2.4 C-scan result of test 3 and the surface failure

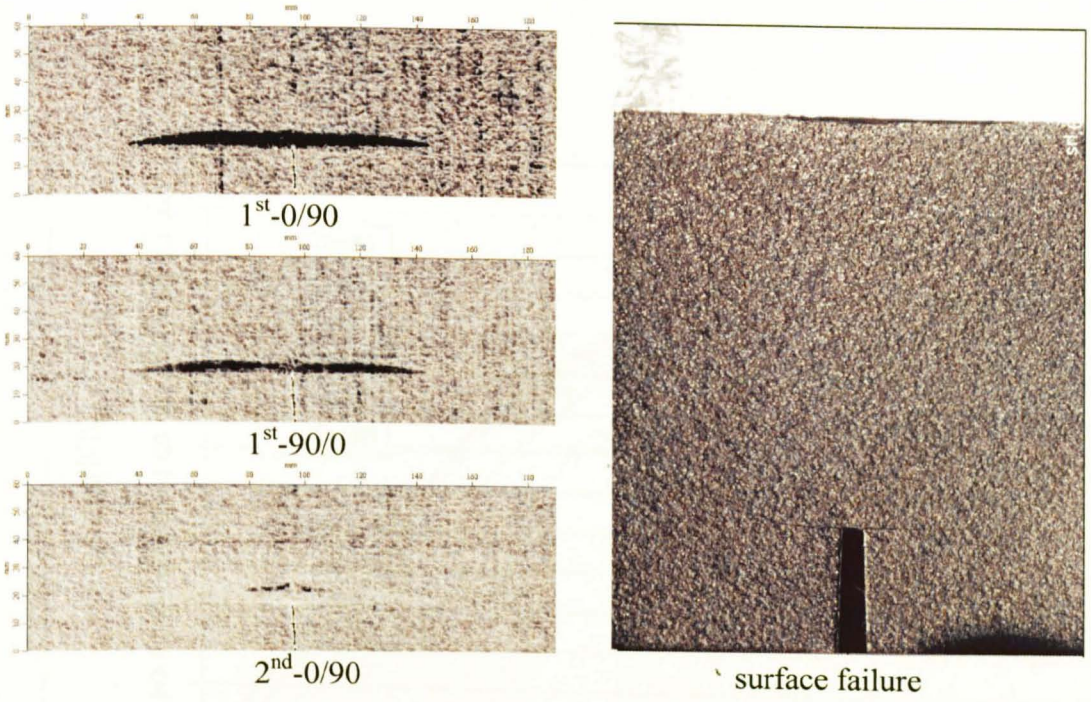

Fig C-2.5 C-scan result of test 5 and the surface failure

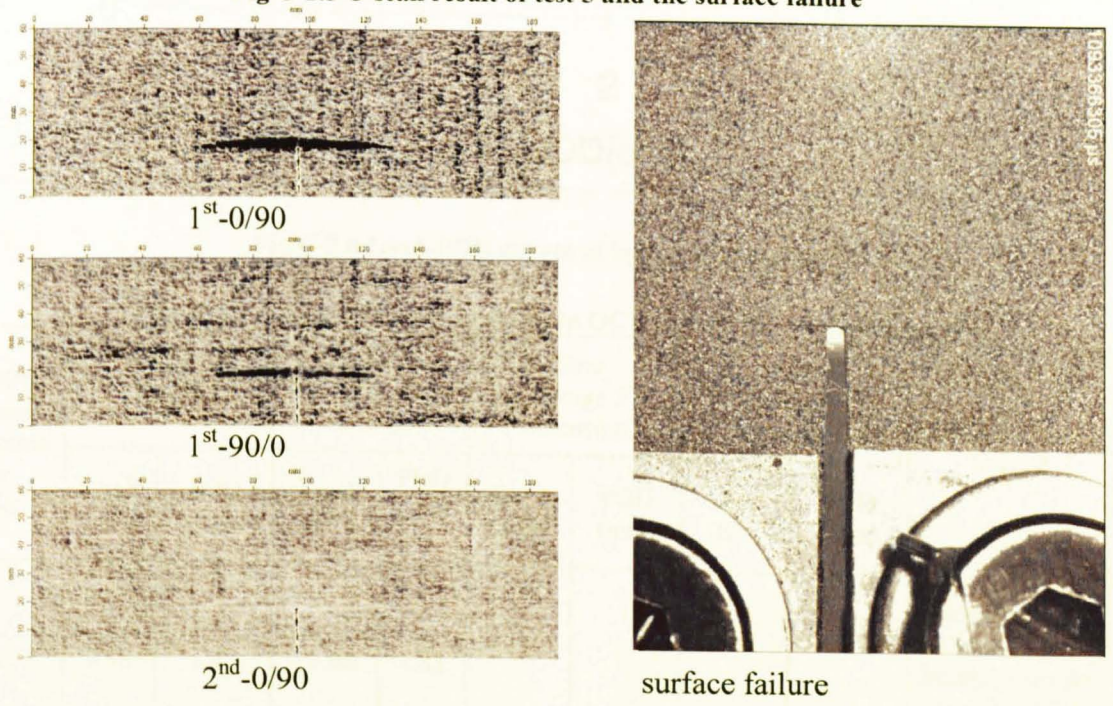

Fig C-2.6 C-scan result of test 6 and the surface failure

3. $[0/90]_{8S}$(4mm)

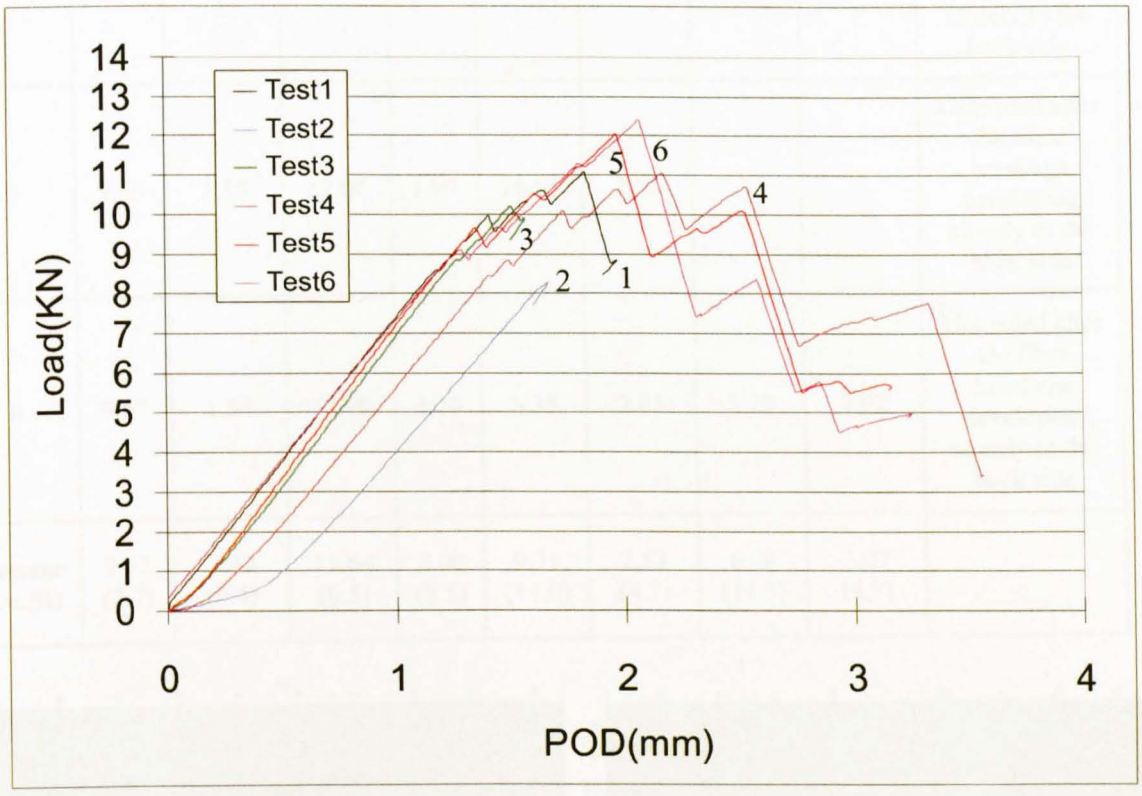

Fig C-3.0 Load-POD curves of lay-up $[0/90]_{8S}$(4mm)

Table C-3.1 Characterized load drops in OCT tests of lay-up $[0/90]_{8S}$(4mm)

$[0/90]_{8S}$ (4mm) Specimen No.	1st load drop		1st clear fibre breakage on surface		Fibre breakage 2nd extension		Fibre breakage 3rd extension		Unload
	Load (KN)	POD (mm)	Load (KN)	POD (mm)	Load (KN)	POD (mm)	Load (KN)	POD (mm)	
1	9.98	1.41	11.08	1.83					Unloaded after 1st clear fibre breakage on the surface and a large load drop
2	8.28	1.36* (before 1st load drop)							Unloaded near but before the 1st load drop.
3	10.19	1.51							Unloaded after the 1st small load dropdown

4	10.11	1.63	11.06	2.07	10.73	2.42	7.74	3.22	Unloaded after the fibre breakage developing closely to the back side
5	9.66	1.35	12.04	1.97	10.05	2.53			Unloaded after the fibre breakage developing closely to the back side
6	9.67	1.54	12.40	2.14	8.35	2.65	5.78	2.92	Unloaded after the fibre breakage developing closely to the back side
Average (c.v.,%)	9.92 (2.7)	1.49 (9.4)	11.64 (6.5)	2.00 (8.5)	9.71 (14.0)	2.53 (4.7)	6.76 (14.5)	3.07 (4.9)	

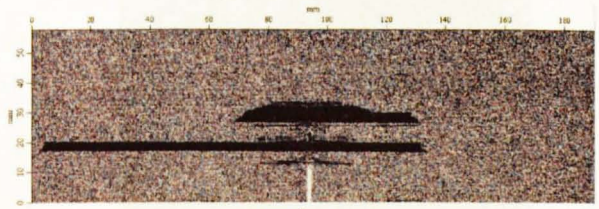

test1

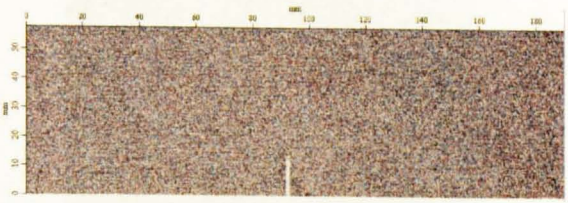

test2

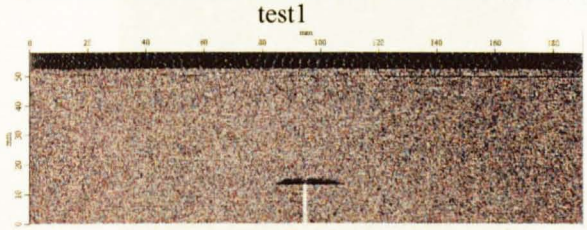

Test3

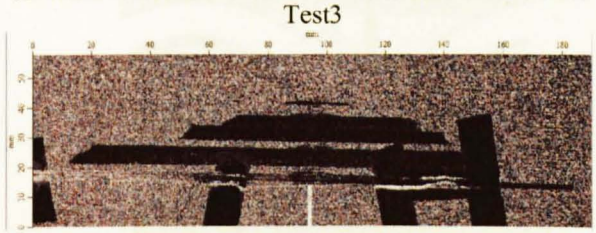

test4

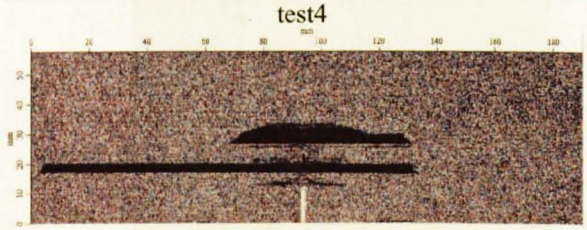

test5

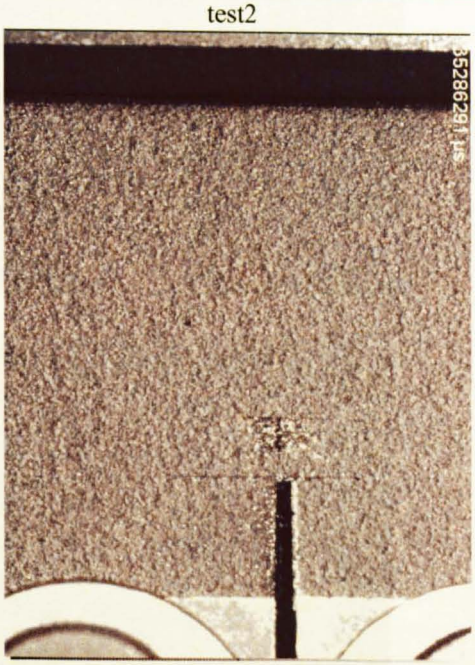

surface failure of test 1

Fig C-3.1 C-scan Result and the surface failure of test 1

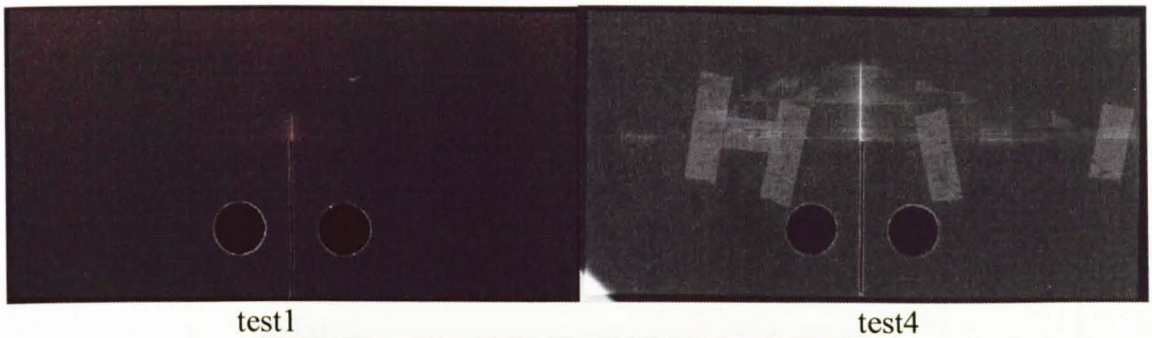

test1 test4

test 5

Fig C 3.2 X-ray results of test 1, 4 and 5

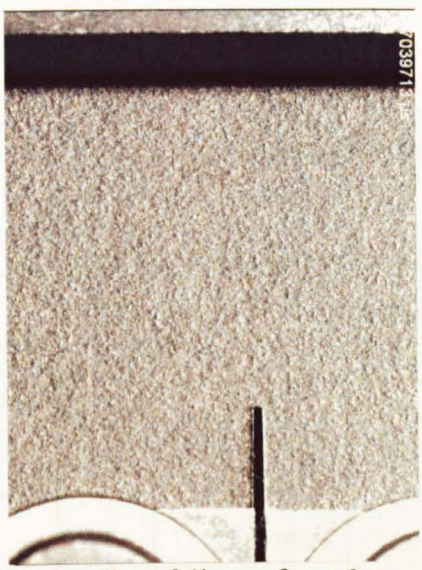

surface failure of test 2

surface failure of test 3

surface failure of test 5

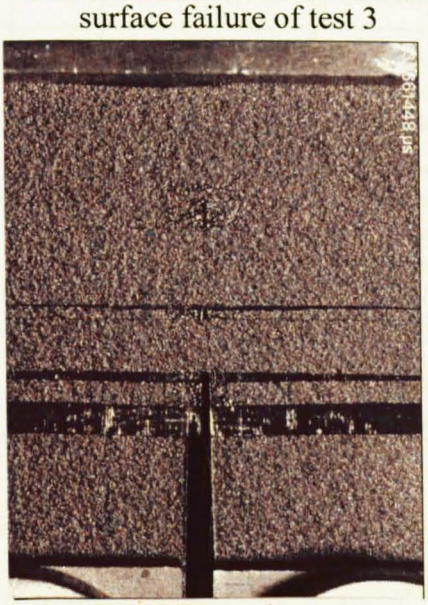

surface failure of test 4

Fig C-3.3 surface failure of test 2, 3, 4, 5

4. $[0_4/90_4]_{2S}$(4mm)

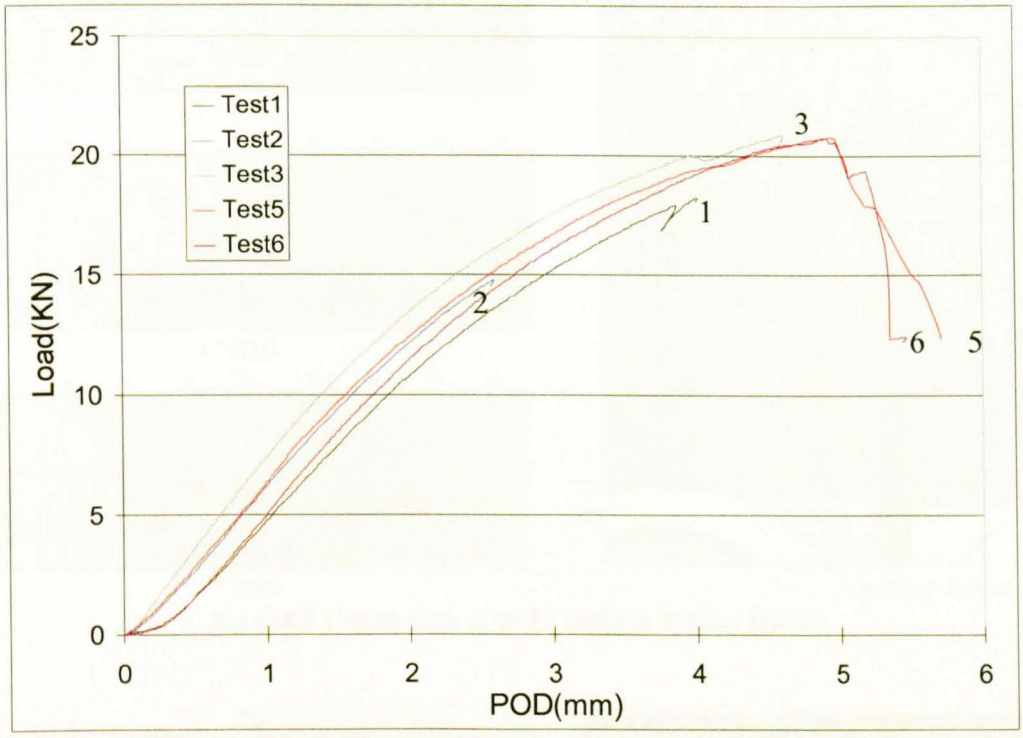

Fig C-4.0 Load-POD curves of lay-up $[0_4/90_4]_{2S}$(4mm)

Table C-4.1 Characterized load drops in OCT tests of lay-up $[0_4/90_4]_{2S}$ (4mm)

$[0_4/90_4]_{2S}$ (4mm) Specimen No.	1st interrupted load		2nd interrupted load		3rd interrupted load		Final failure		Unload
	Load (KN)	POD (mm)	Load (KN)	POD (mm)	Load (KN)	POD (mm)	Load (KN)	POD (mm)	
1			18.24	3.84					Unloaded close to the final failure
2	14.64	2.59							Unloaded when the specimen has plastic deformation
3					20.80	4.61			Unloaded very close to the final failure
5							20.74	4.98	Unloaded after part of the 0° surface separated
6							20.75	4.73	Unloaded after part of the 0° surface separated
Average (c.v.,%)							20.74 (0.05)	4.86 (2.7)	

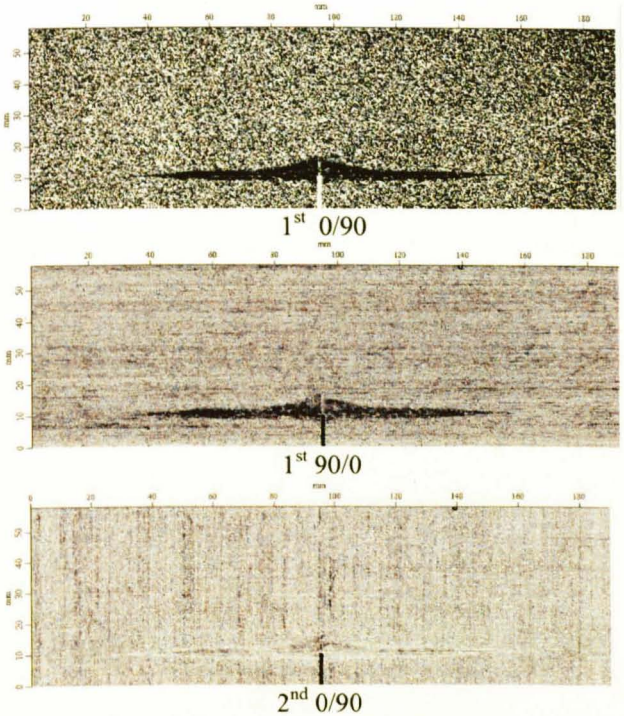

surface failure

Fig C-4.1 C-scan data of test 1 and the surface failure

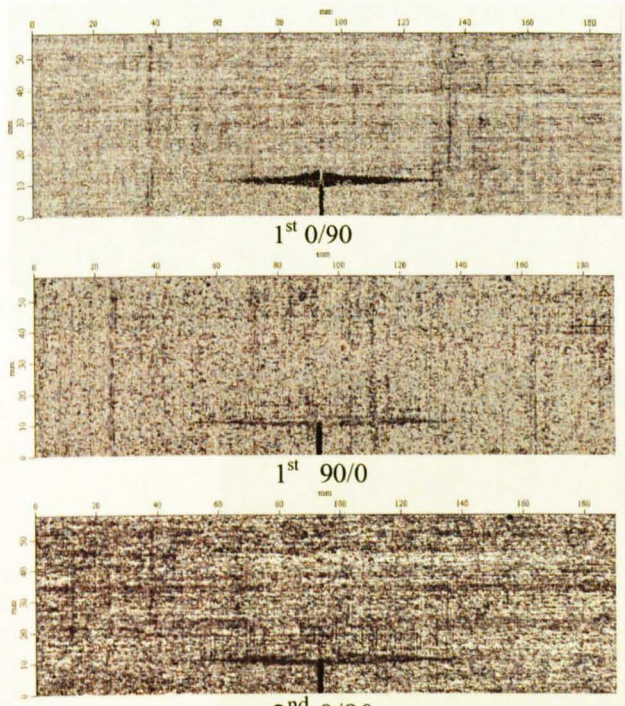

surface failure

Fig C-4.2 C-scan data of test 2 and the surface failure

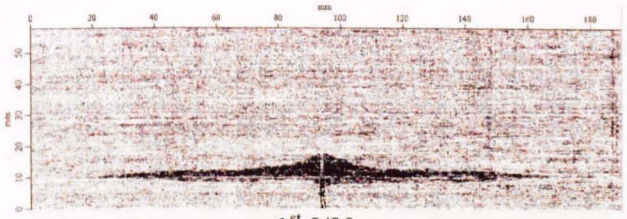

1st 0/90

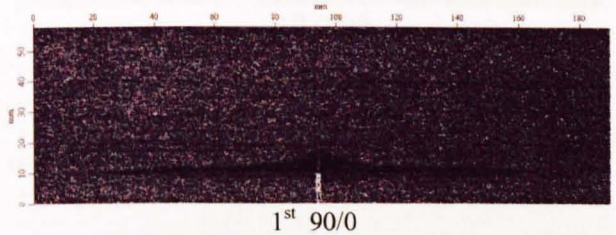

1st 90/0

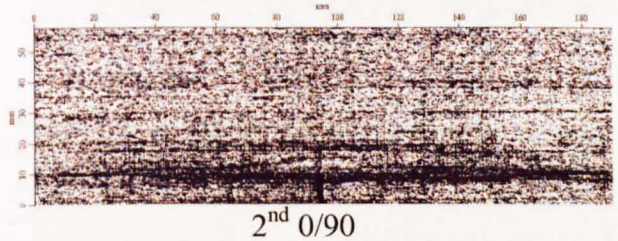

2nd 0/90

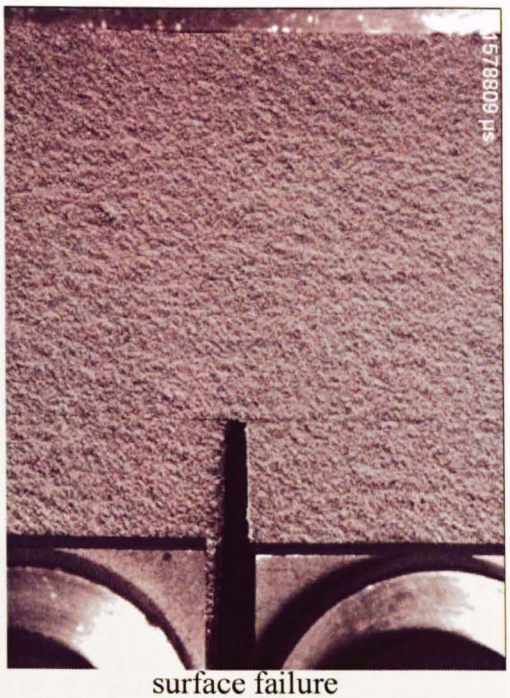

surface failure

FigC-4.3 C-scan data of test 3 and the surface failure

test 1

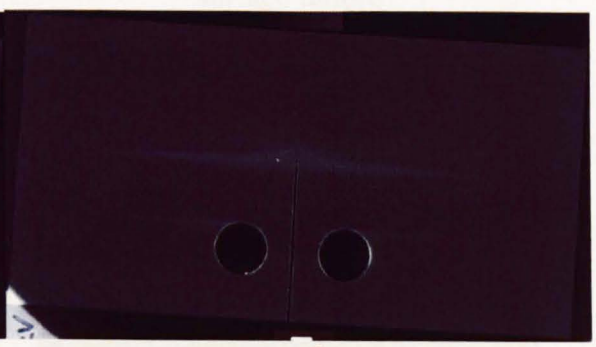

test 2

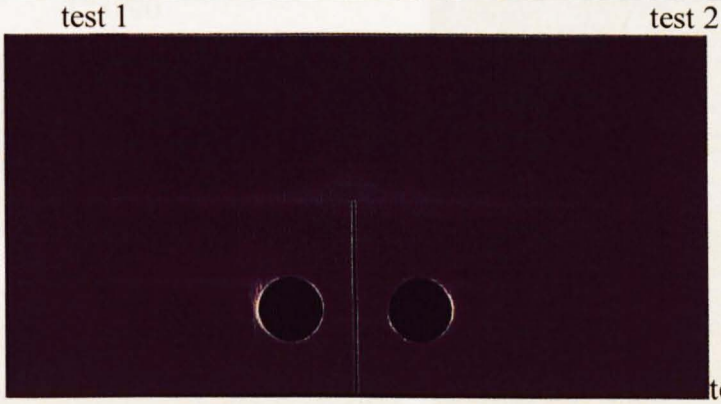

test 3

FigC-4-4 X-ray results of test 1, 2 and 3

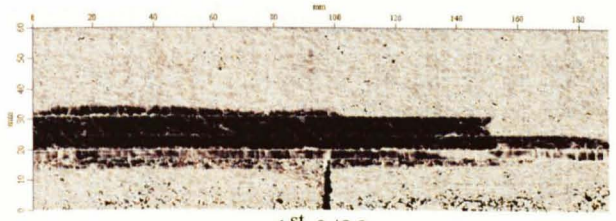

1st 0/90

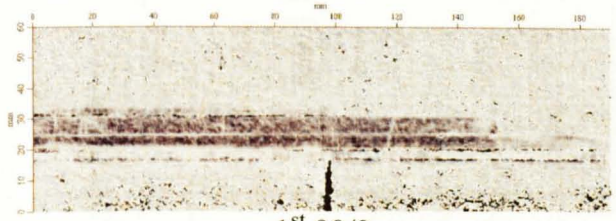

1st 90/0

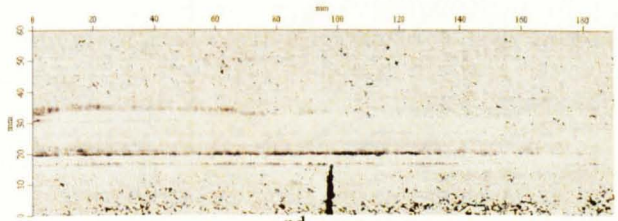

2nd 0/90

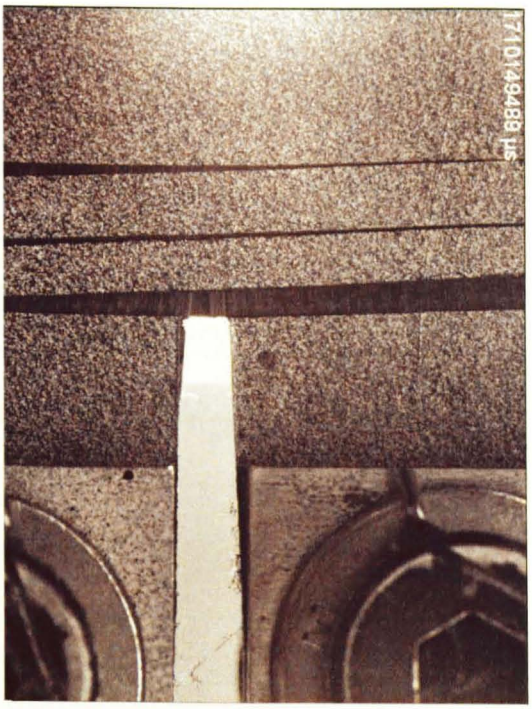

surface failure

Fig C-4.5 C-scan data of test 4 and the surface failure

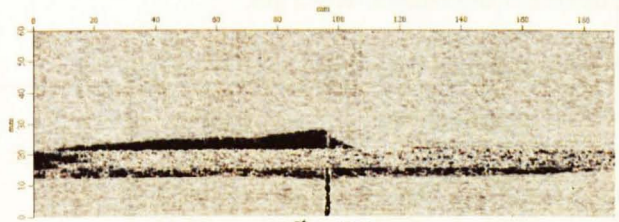

1st 0/90

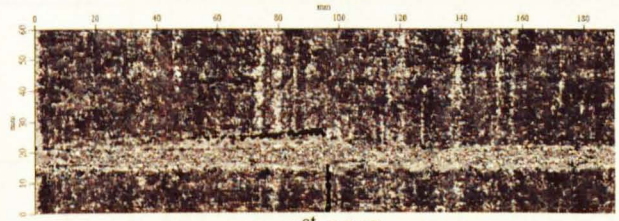

1st 90/0

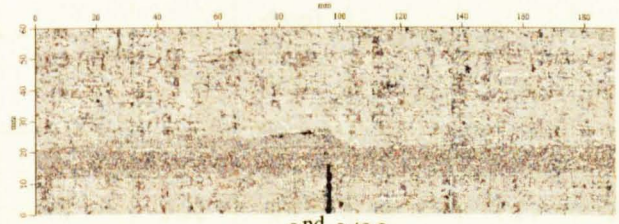

2nd 0/90

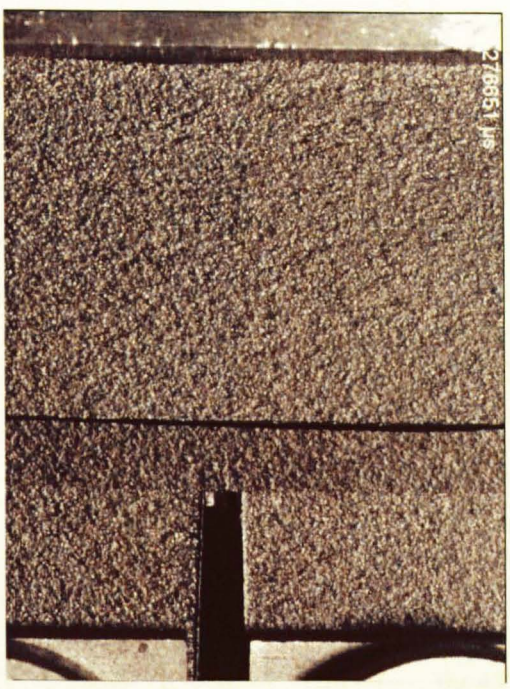

surface failure

Fig C-4.6 C-scan data of test 6 and the surface failure

5 $[45/90/135/90]_{2S}$ (2mm)

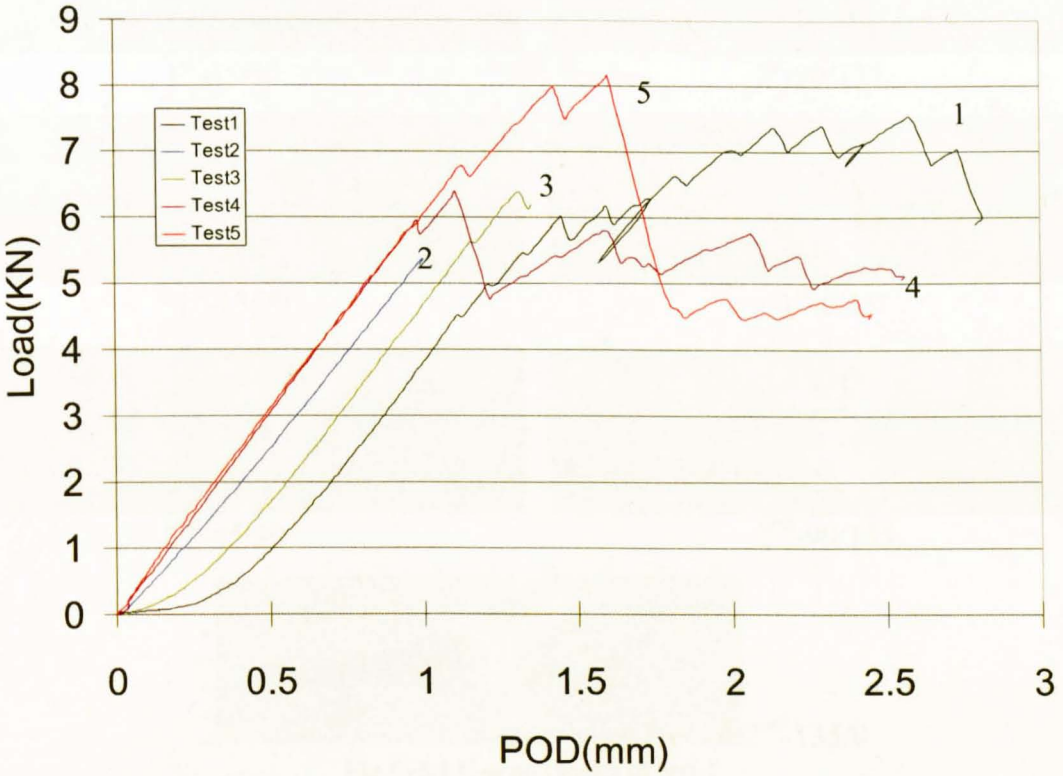

Fig C-5.0- Load-POD curves of lay-up $[45/90/135/90]_{2S}$ (2mm)

Table C-5.1 Characterized load drops in OCT tests of lay-up $[45/90/135/90]_{2S}$(2mm)

Specimen No.	1st load drop		2nd load drop		3rd load drop		Final failure		Unload
	Load (KN)	POD (mm)	Load (KN)	POD (mm)	Load (KN)	POD (mm)	Load (KN)	POD (mm)	
1	6.01	1.07	6.17	1.22	7.04	1.62	7.00	1.78	Unloaded after part of the 45° surface being separated
2	5.37	1.00* (before 1st load drop)							Unloaded near but before the 1st load drop
3	5.68	0.93	6.36	1.09					Unloaded after 2nd load drop
4	5.95	0.98	6.38	1.11	5.77	1.60	5.20	1.78	Unloaded after part of the 45° surface being separated
5	6.76	1.13	7.97	1.43	8.16	1.60	4.50	1.86	Unloaded after part of the 45° surface being separated
Average (c.v., %)	6.10 (10.8)	1.03 (9.7)	6.72 (18.6)	1.21 (18.2)	6.99 (17.4)	1.61 (0.6)	5.57 (25.7)	1.81 (2.8)	

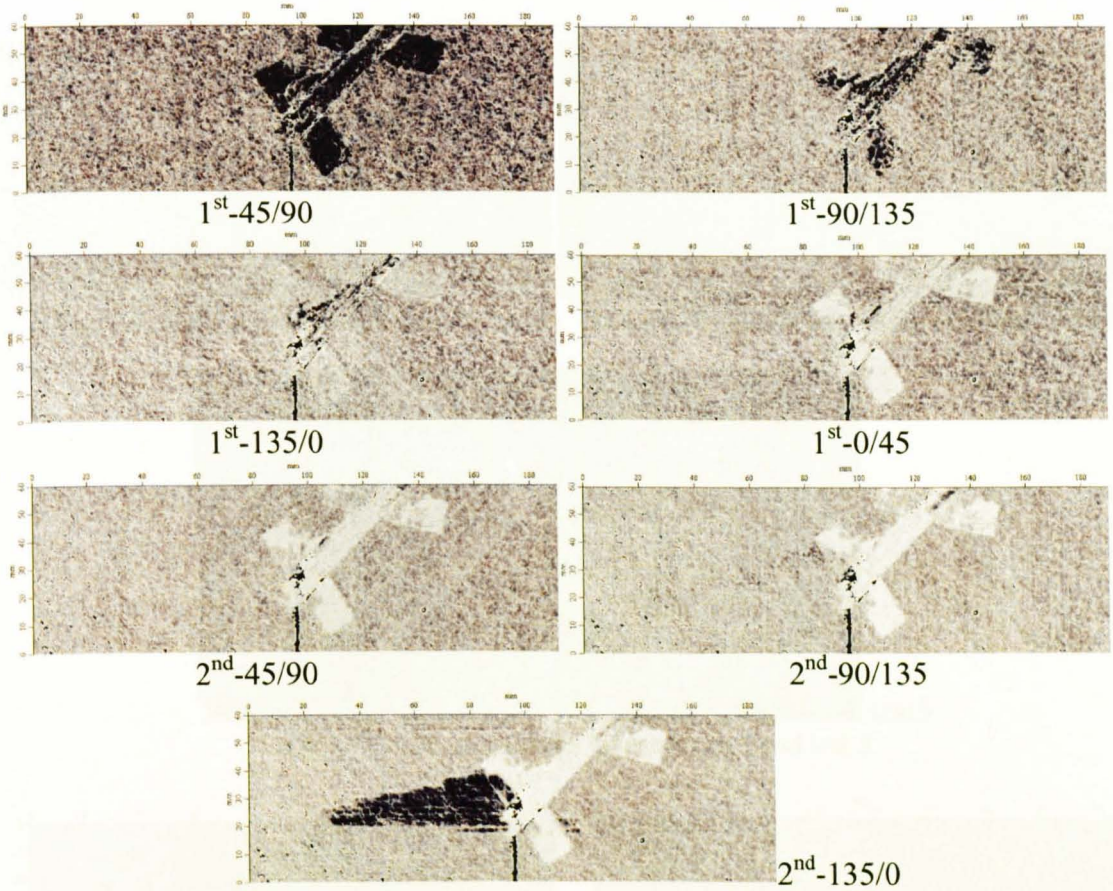

Fig C-5.1 C-scan results of test 1

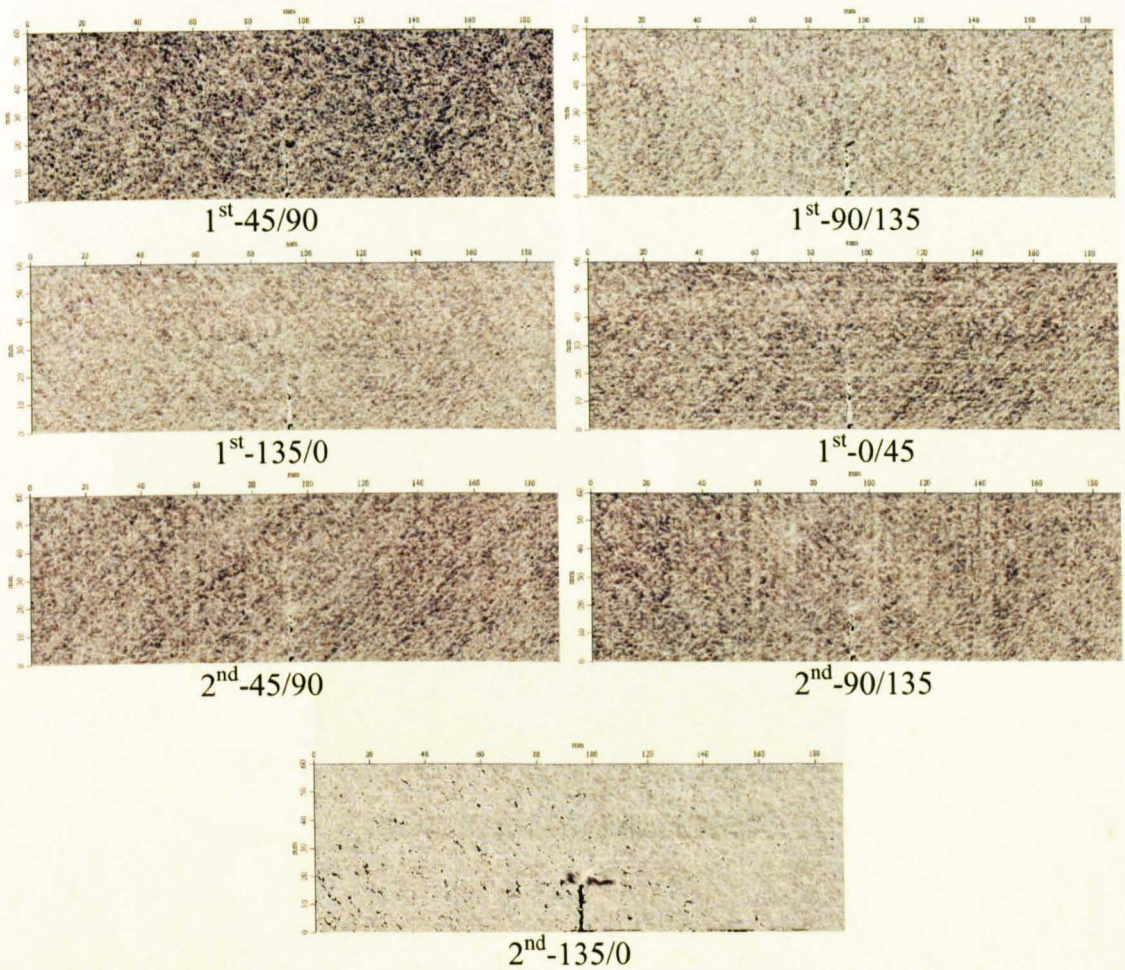

Fig C-5.2 C-scan results of test 2

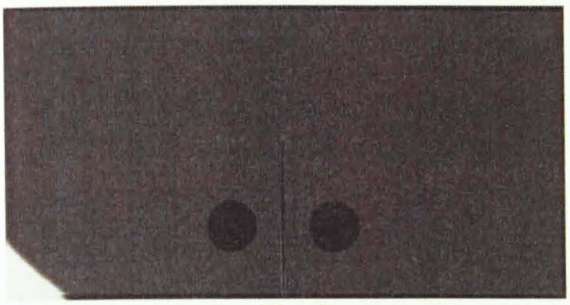

Test2

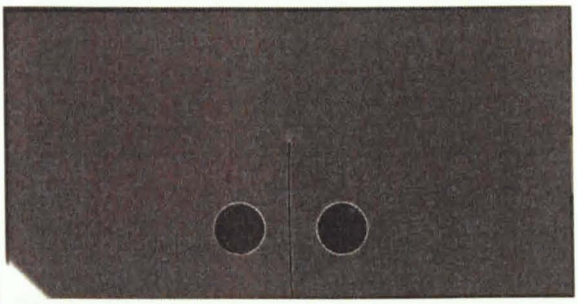

test3

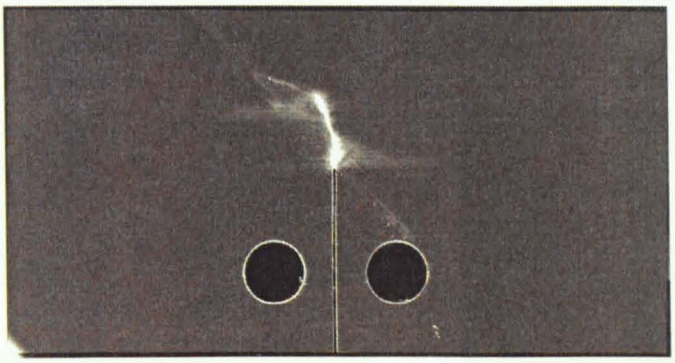

test5

Fig C-2.3 X-ray scan results of test 2, test 3 and test 5

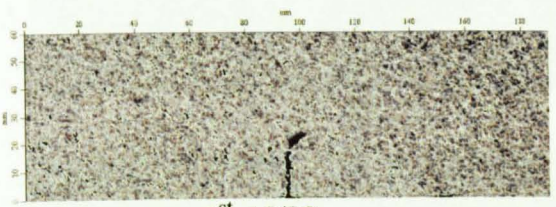

1^{st}-45/90

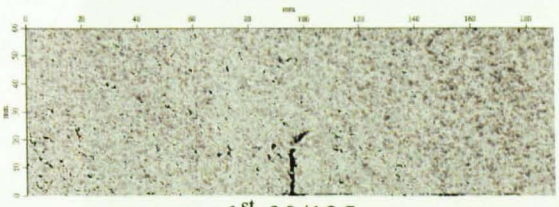

1^{st}-90/135

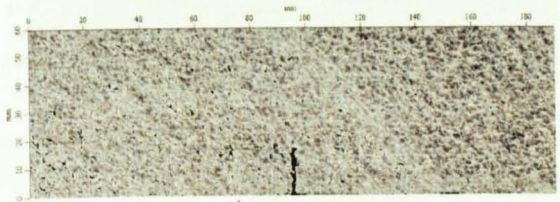

1^{st}-135/0

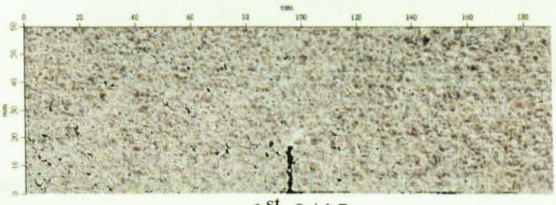

1^{st}-0/45

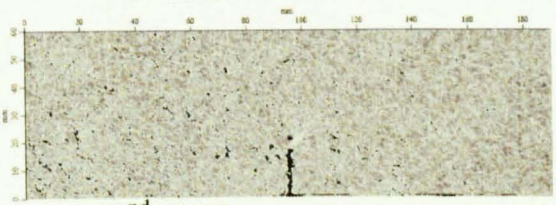

2^{nd}-45/90

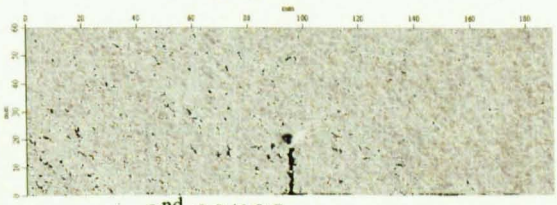

2^{nd}-90/135

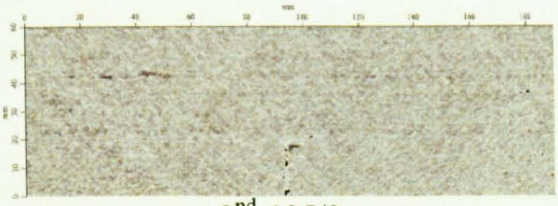

2^{nd}-135/0

Fig C-5.4 C-scan results of test 3

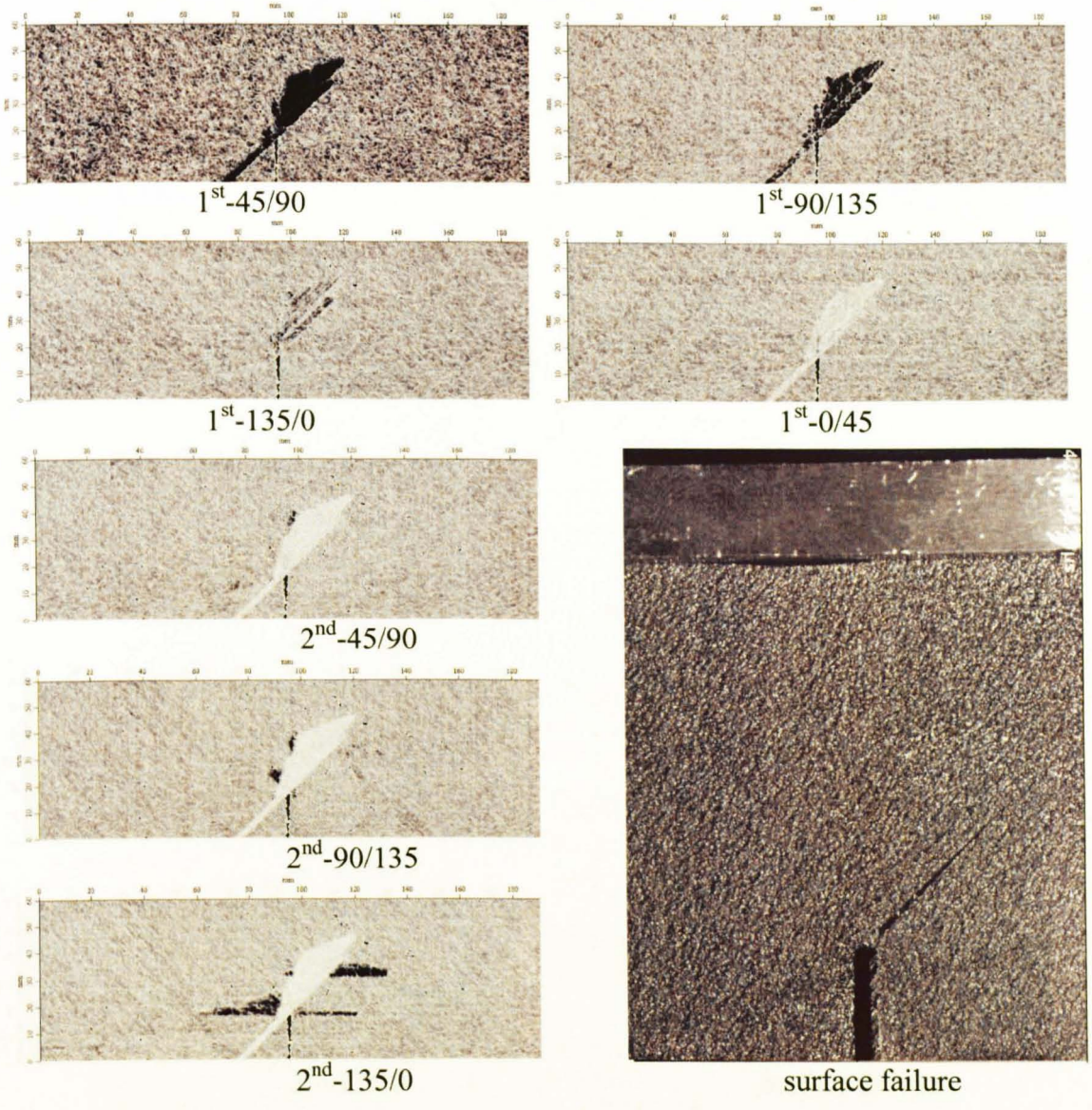

Fig C-5.5 C-scan results of test 5 and the surface failure

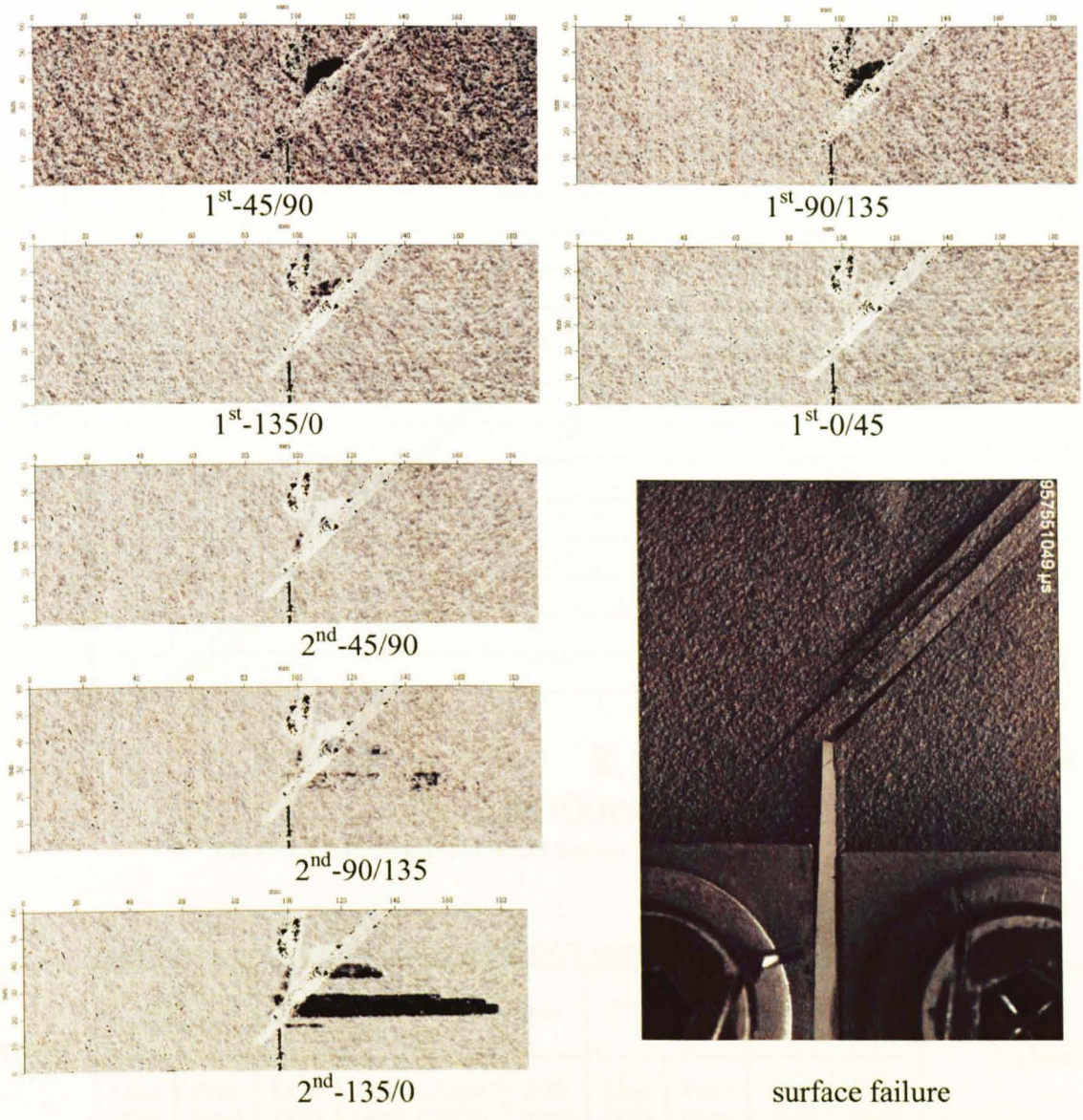

Fig C-5.6 C-scan results of test 6 and the surface failure

6. $[45_2/90_2/135_2/0_2]s$ (2mm)

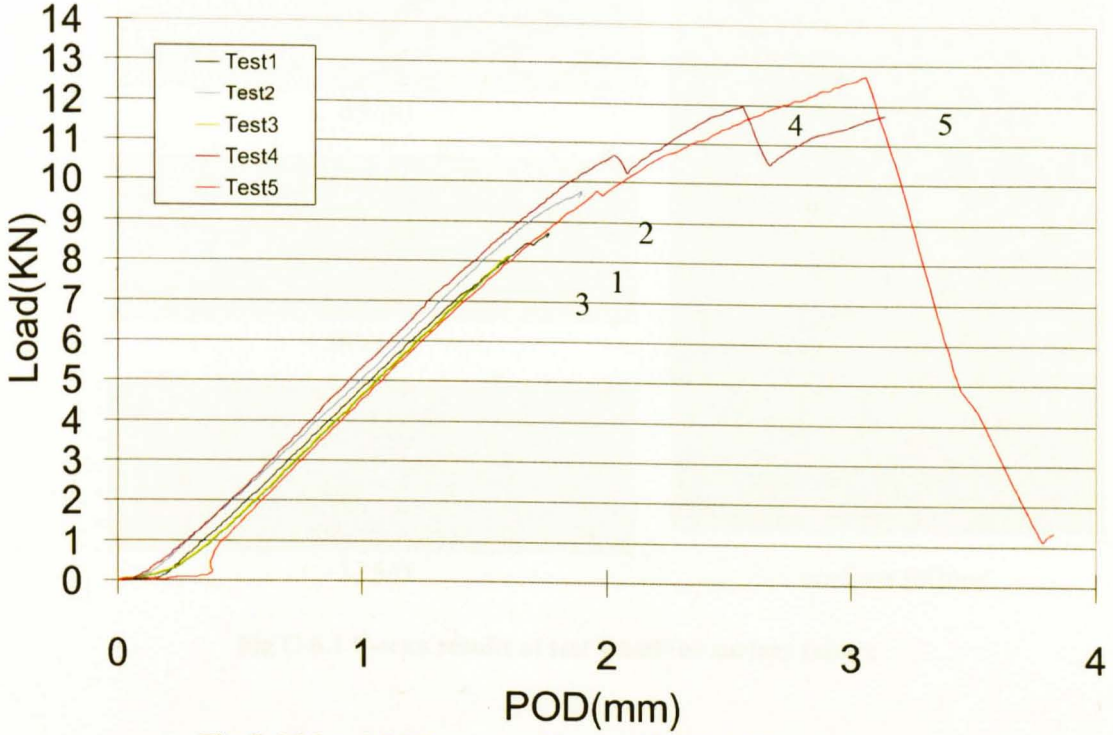

Fig C-6.0 Load-POD curves of lay-up $[45_2/90_2/135_2/0_2]s$ (2mm)

Table C6.1 Characterized load drops in OCT tests of lay-up $[45_2/90_2/135_2/0_2]s$ (2mm)

Specimen No.	1st interrupted		2nd interrupted		1st load drop		2nd load drop		Final failure		Unload
	Load (KN)	POD (mm)	Load (kN)	POD (mm)	Load (KN)	POD (mm)	Load (KN)	POD (mm)	Load (KN)	POD (mm)	
1					10.45	2.11					Unloaded after the 1st load dropdown with 45° splitting appearing on the surface
2			9.74	1.79							Unloaded near and before the 1st load drop
3	8.25	1.50									Unloaded after the specimen started to have plastic deformation
4					10.69	2.03	11.97	2.55	11.76	3.13	Unloaded after the failure developing to back side and causing crush
5					9.77	1.82			12.73	2.91	Unloaded after the failure developing to back side and causing crush
Average (c.v.,%)					10.30 (5.1)	1.99 (8.5)			12.24 (4.0)	3.02 (3.6)	

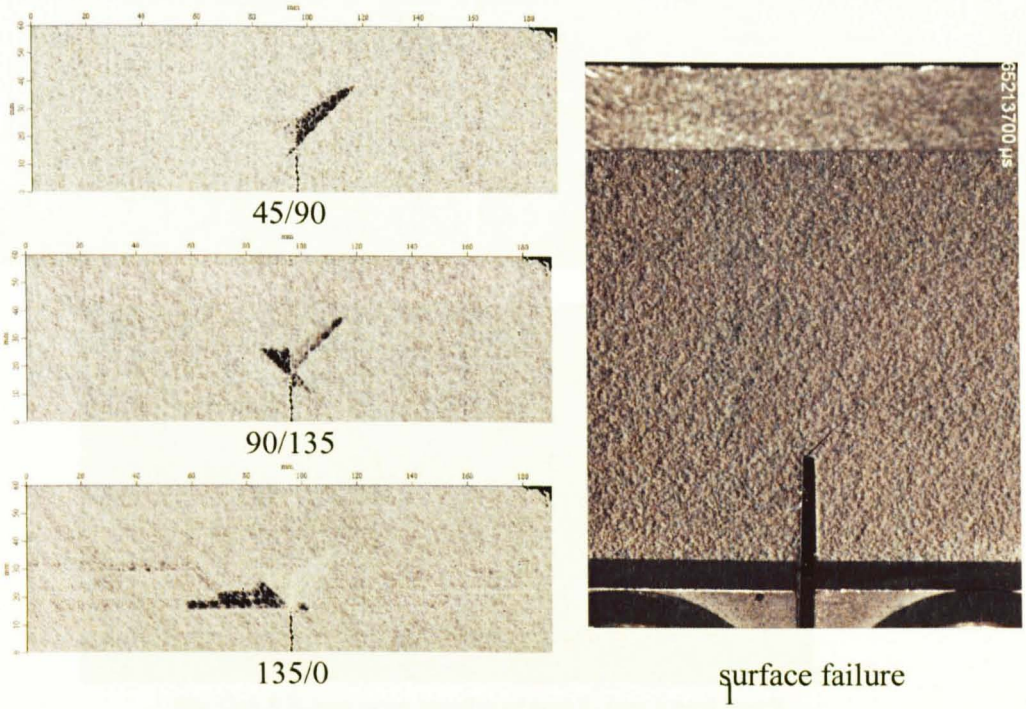

Fig C-6.1 C-scan results of test 1 and the surface failure

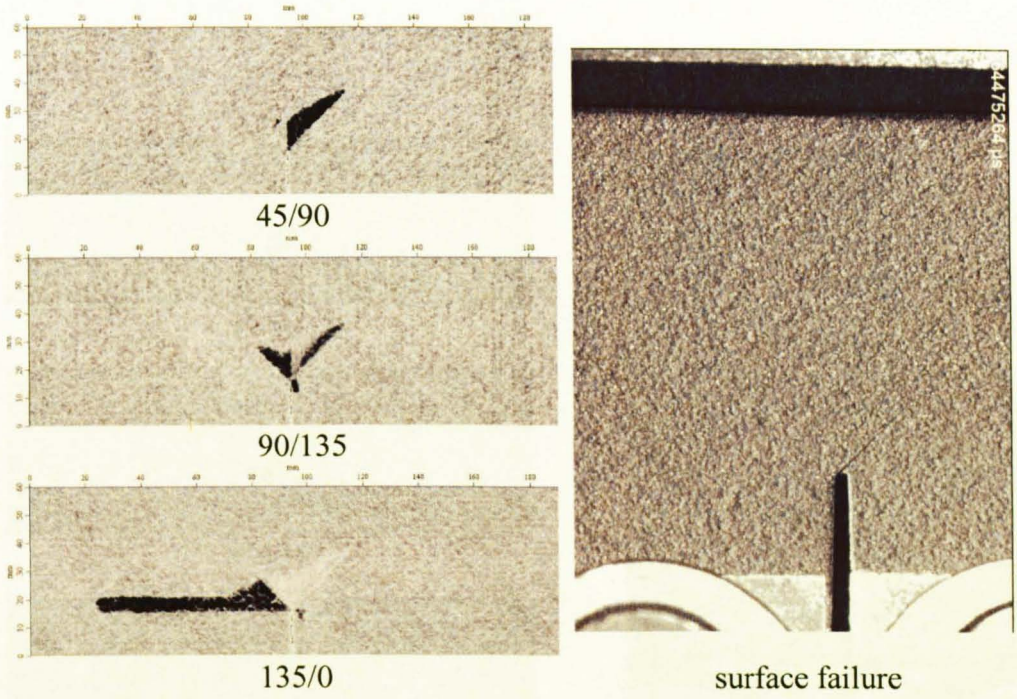

Fig C-6.2 C-scan results of test 2 and the surface failure

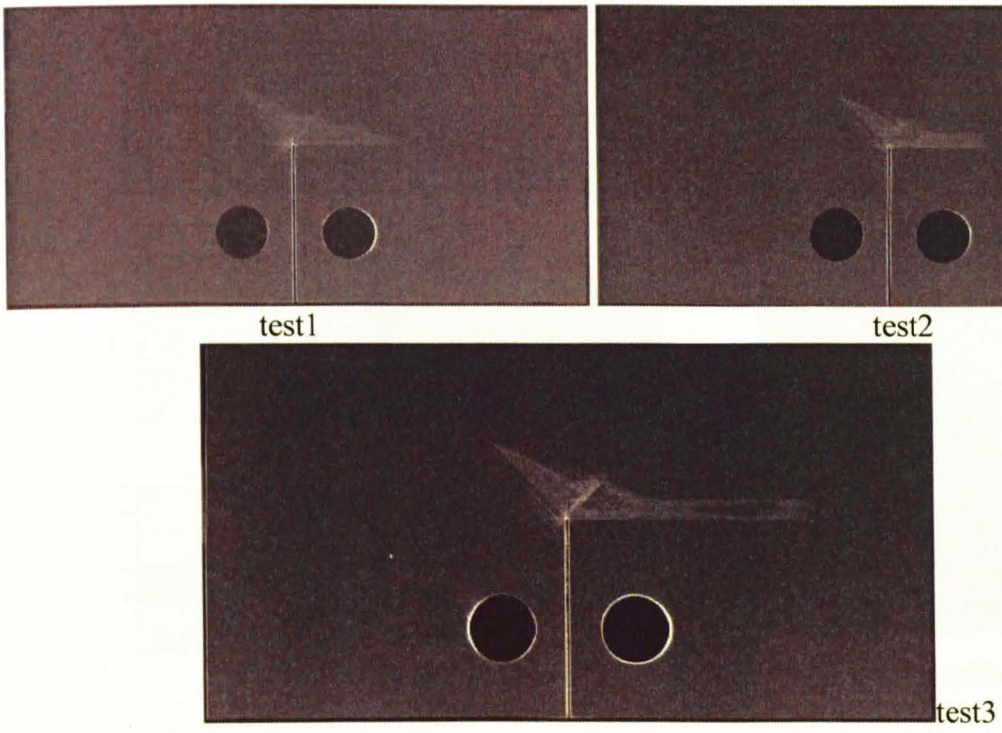

Fig C-6.3 X-ray scan results of test 1, test 2 and test 3

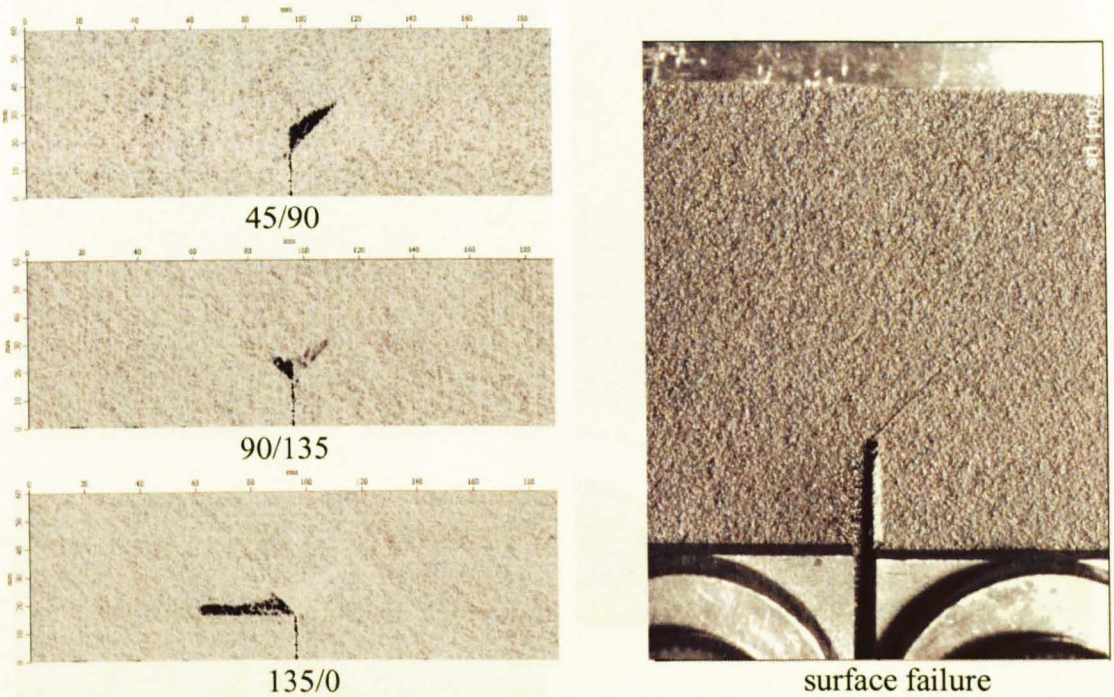

Fig C-6.4 C-scan results of test 3 and the surface failure

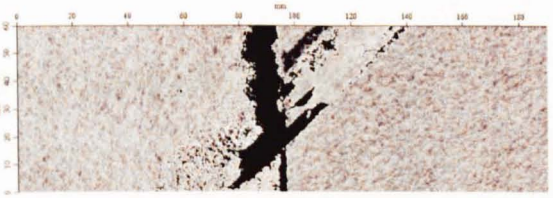

45/90

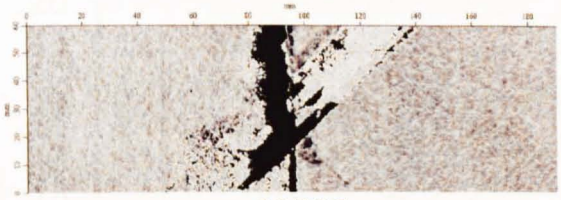

90/135

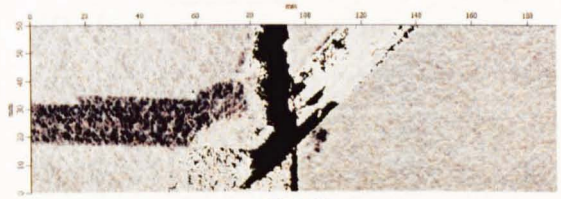

135/0

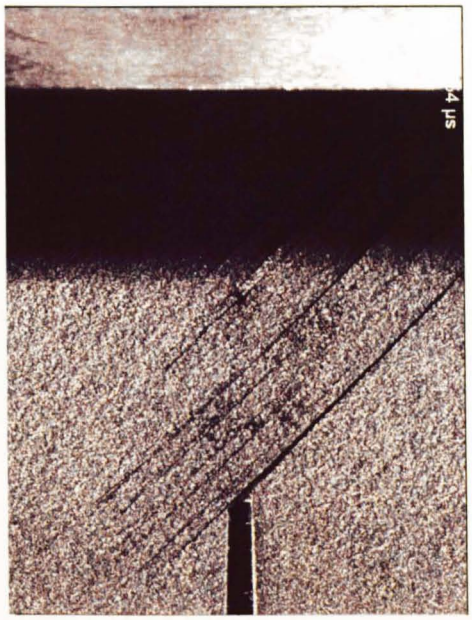

surface failure

Fig C-6..5 C-scan results of test 5 and the surface failure

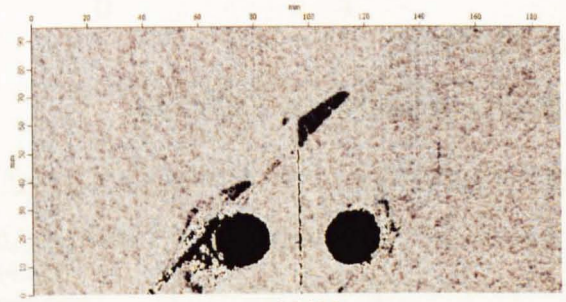

45/90

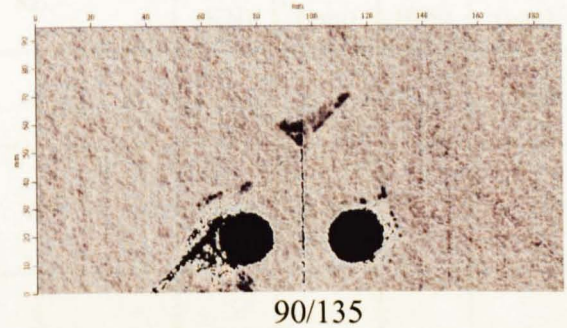

90/135

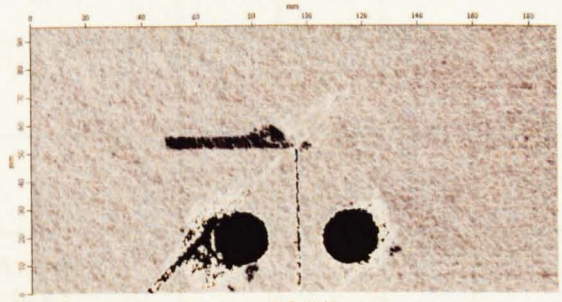

135/0

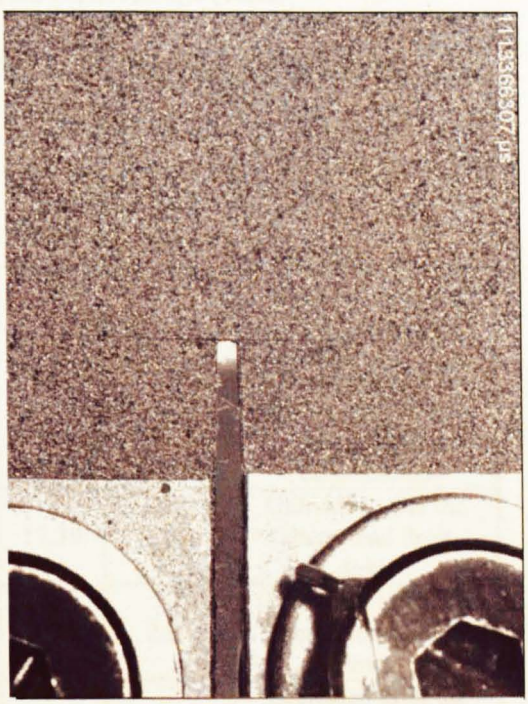

surface failure

Fig C-6.6 C-scan results of test 6 and the surface failure

7. $[45_4/90_4/135_4/90_4]s$ (4mm)

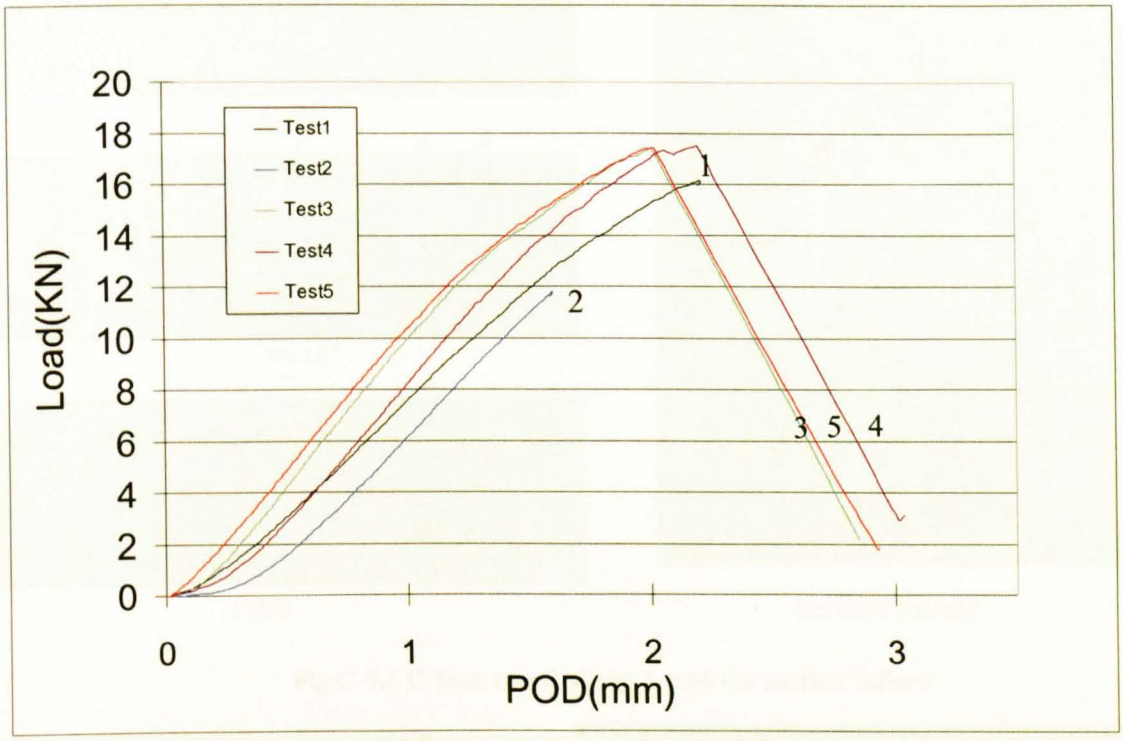

Fig C-7..0 Load-POD curves of lay-up $[45_4/90_4/135_4/90_4]s$ (4mm)

Table C-7.1 Characterized load drops in OCT tests of lay-up $[45_4/90_4/135_4/90_4]s$ (4mm)

$[45_4/90_4/135_4/90_4]s$ (4mm) Specimen No.	1st interrupted		2nd interrupted		Final failure		Unload
	Load (KN)	POD (mm)	Load (KN)	POD (mm)	Load (KN)	POD (mm)	
1			16.14	1.74			Unloaded near the final failure
2	11.78	1.16					Unloaded when the specimen started to have plastic deformation
3					17.39	2.01	Unloaded after the sharp load drop down
4					17.46	2.00	Unloaded after the sharp load drop down
5					17.39	2.02	Unloaded after the sharp load drop down
Average (c.v.)					17.41 (0.2%)	2.01 (0.5%)	

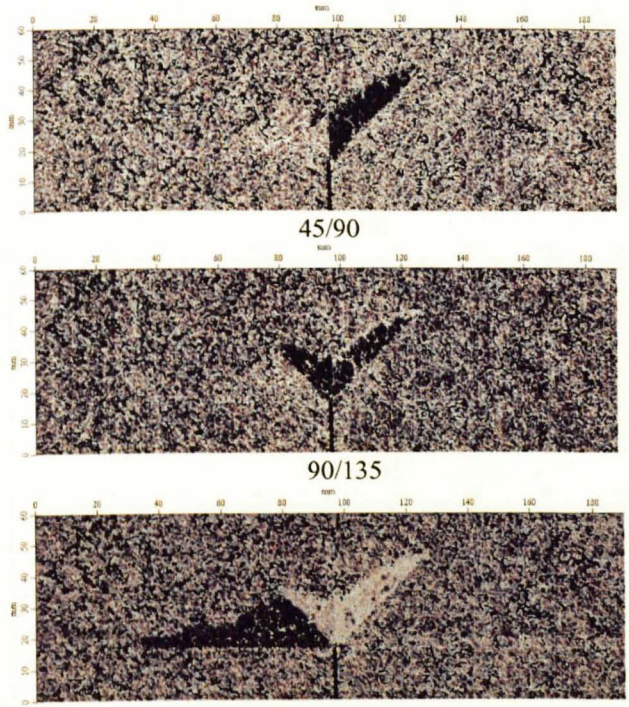

surface failure

Fig C-7.1 C-scan result of test 1 and the surface failure

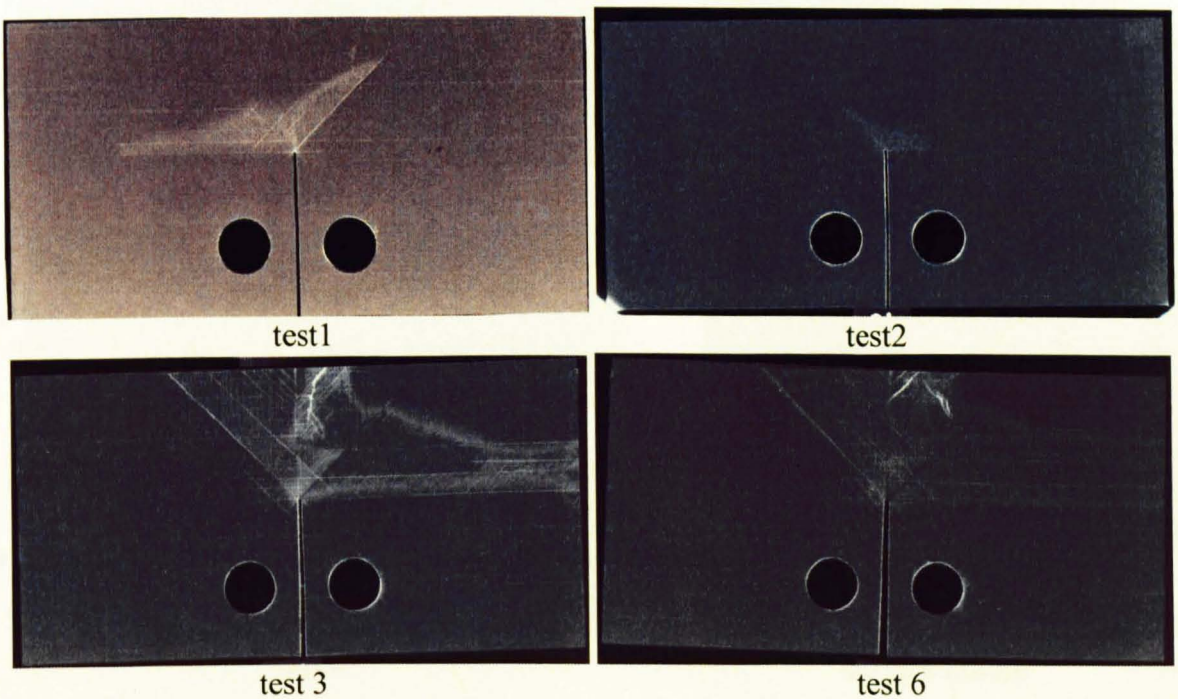

Fig C-7.2 X-ray scan results of test 1 and test 3

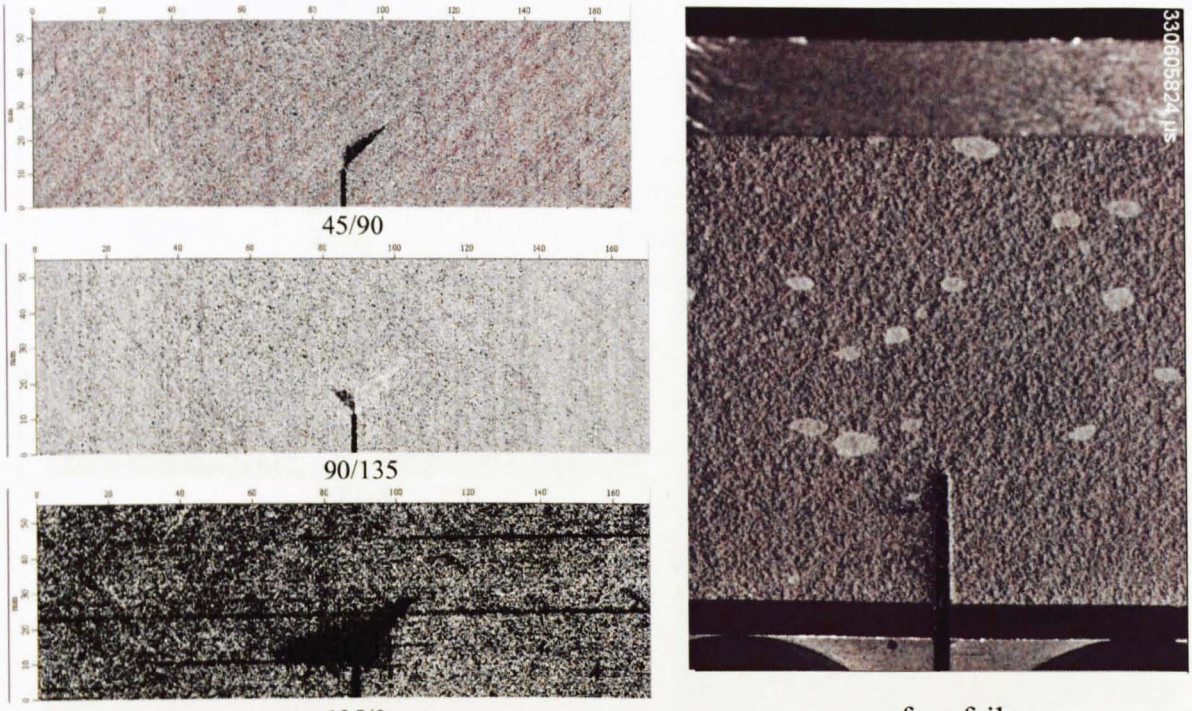

Fig C-7.3 C-scan result of test 2 and the surface failure

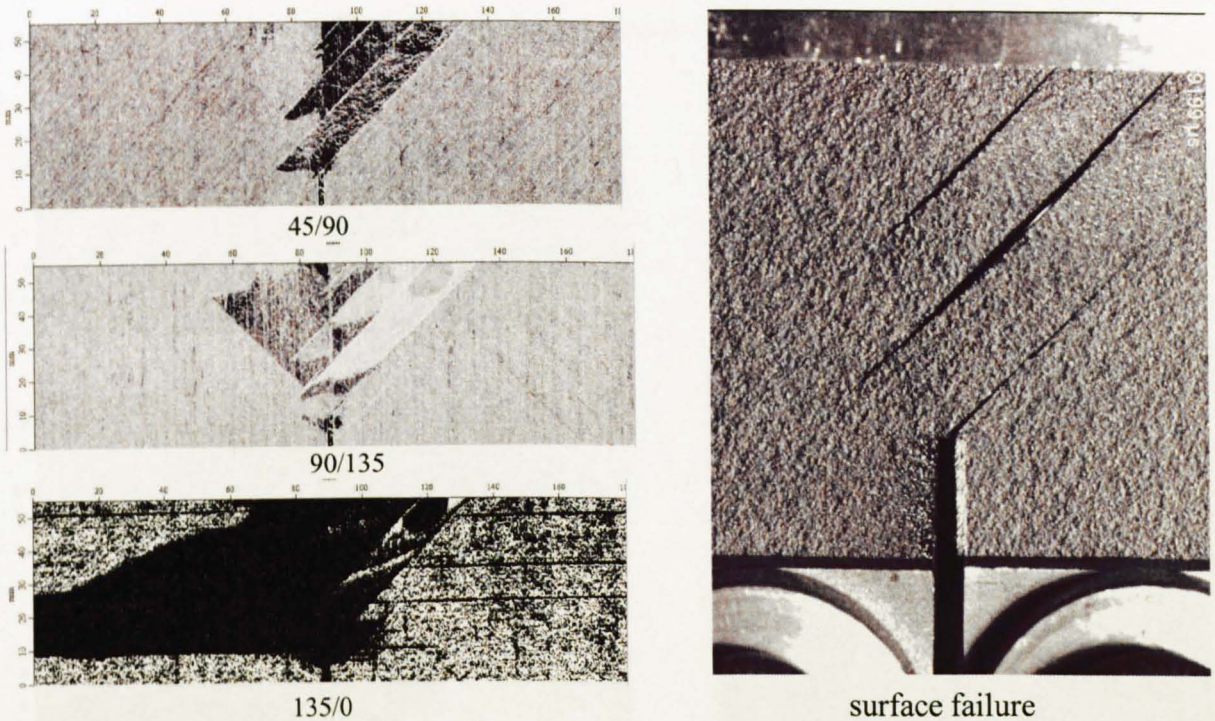

Fig C-7.4 C-scan result of test 3 and the surface failure

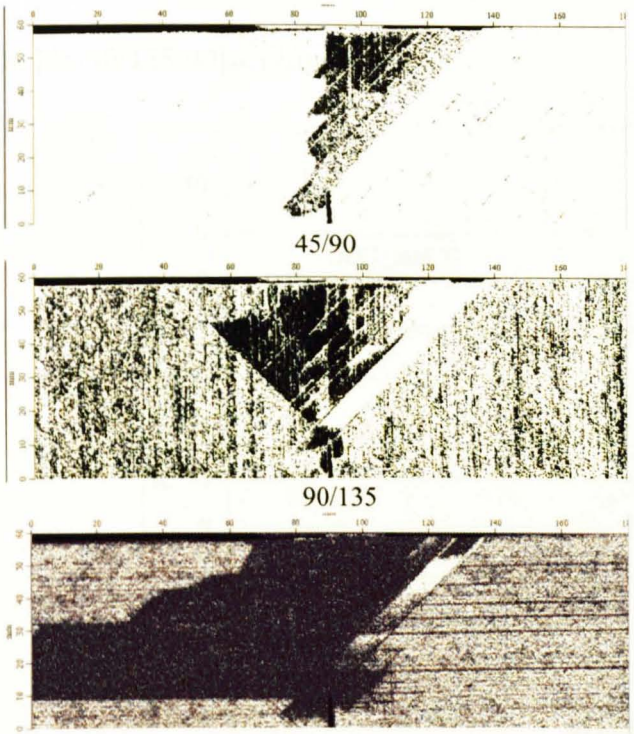

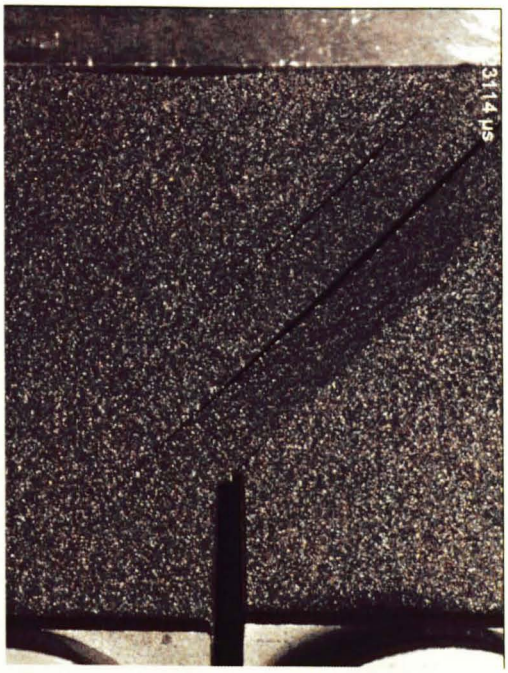

surface failure

Fig C-7.5 C-scan result of test 5 and the surface failure

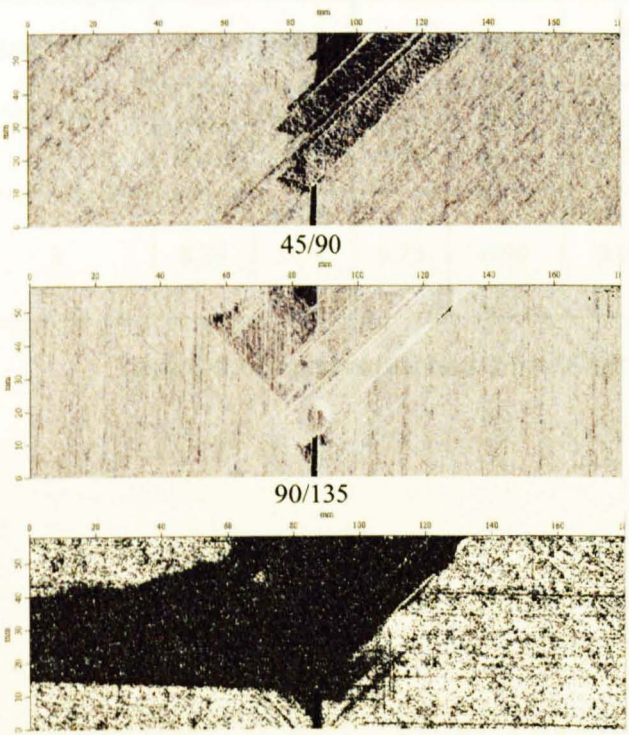

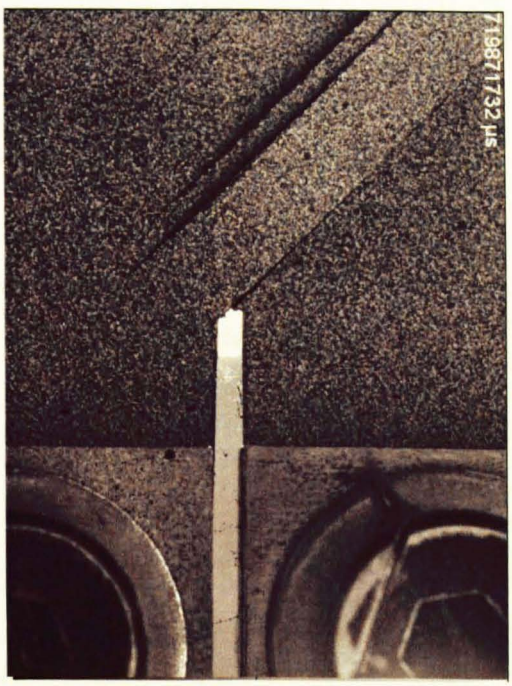

surface failure

Fig C7.6 C-scan result of test 6 and the surface failure

8. $[45/90/135/90]_{4S}$ (4mm)

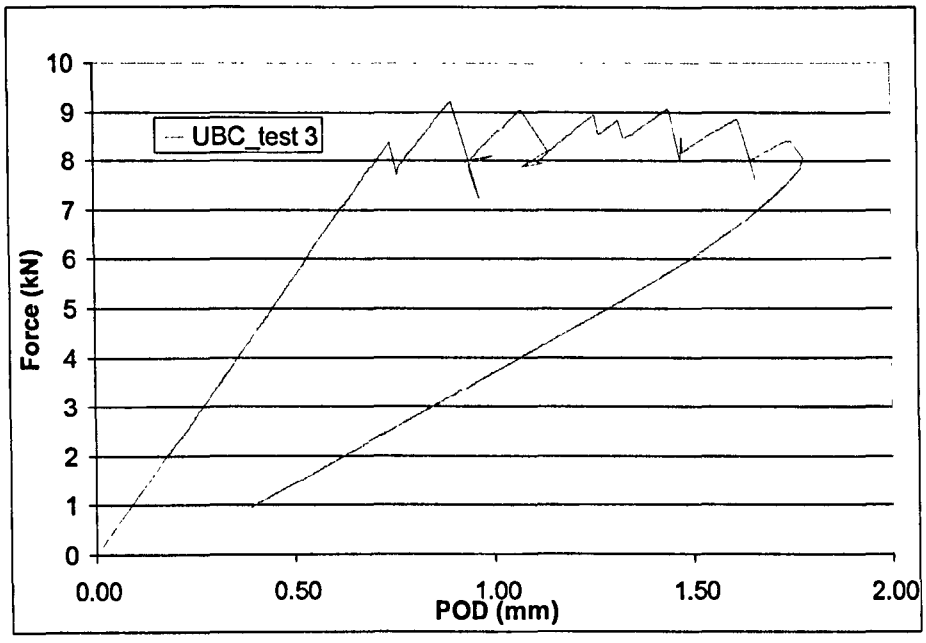

Fig C-8.0 Load-POD curves of lay-up $[45/90/135/90]_{4S}$ (4mm) from UBC

$[45/90/135/0]_{4S}$ (2mm) Specimen No.	1st load drop		2nd load drop		3rd load drop		Final failure		Unload
	Load (KN)	POD (mm)	Load (KN)	POD (mm)	Load (KN)	POD (mm)	Load (KN)	POD (mm)	
3	8.39	0.74	9.23	0.90	9.05	1.07	8.41	1.75	Unloaded after stable failure propagation

Table C-8.1 Characterized load drops in OCT tests of lay-up $[45/90/135/90]_{4s}$ (4mm)

References

1 Isaac MD, Ori Ishai. *Engineering Mechanics of Composite Materials.* Oxford University Press. Second Edition.

2 Paris F. *A study of failure criteria of fibrous composite materials.* NASA/CR-2001-210661

3 Hinton MJ, Soden PD. *Predicting failure in composite laminates: The background to the exercise.* Composites Science and Technology, v 58, n 7, 1998, p 1001-1010

4 Hoffman O. *The brittle strength of orthotropic materials.* Journal of Composite Materials 1967, P1-200.

5 Tsai, SW, Wu EM. *A general theory of strength for anisotropic materials.* Journal of Composite Materialss 1971, 5, p 58-80.

6 Di Sciuva M, Icardi U; Villani M. *Failure analysis of composite laminates under large deflection.* Composite Structures, v 40, n 3-4, Dec 3-4, 1997, p 239-255

7 Huybrechts S, Maji A, Lao J, Wegner P, Meink T. *Validation of the quadratic composite failure criteria with out-of-plane shear terms.* Journal of Composite Materials, v 36, n 15, 2002, p 1879-1888

8Gamble K, Pilling M, Wilson A. *An automatednitiation and growth of damage in carbon-fibre composite materials.* Composite Structures, v 32, n 1-4, 1995, p 265-274

9 Padhi GS, Shenoi RA, Moy SSJ, Hawkins GL. *Progressive failure and ultimate collapse of laminated composite plates in bending.* Composite Structures, v 40, n 3-4, Dec 3-4, 1997, p 277-291.

10 Liu KS, Tsai SW. *Progressive quadratic failure criterion for a laminate.* Composites Science and Technology, v 58, n 7, Jul, 1998, p 1023-1032

11 Naik GN, Murty AV, Krishna. *Failure mechanism-based approach for design of composite laminates.* Composite Structures, v 45, n 1, May, 1999, p 71-80

12 Zywicz E. *On the equivalence of stress- and strain-based failure criteria in elastic media.* European Journal of Mechanics, A/Solids, v 18, n 3, 1999, p 391-398

13 Hashin Z. *Failure criteria for unidirectional fibre composites.* ASME Journal of Applied Mechanics. 1980, 47, 329-334.

14 Sun CT, Quinn BJ, Oplinger DW. *Comparative Evaluation of Failure Analysis Methods for Composite Laminates.* DOT/FAA/AR-95/109.

15 Paris F, Correa E, Canas J. *Micromechanical view of failure of the matrix in fibrous composite materials.* Composites Science and Technology, v 63, n 7, May, 2003, p 1041-1052

16 Puck A, Schu" rmann, H. *Failure Analysis of FRP Laminates by Means of Physically Based Phenomenological Models.* Composites Science and Technology, 58: 1045–1067.

17 Dávila CG, Camanho PP, Rose CA.*Failure criteria for FRP laminates.* Journal of Composite Materials, v 39, n 4, 2005, p 323-345.

18 Cuntze RG, Freund A. *The predictive capability of failure mode concept-based strength criteria for multidirectional laminates.* Composites Science and Technology, v 64, n 3-4, March, 2004, p 343-377

19 Cuntze RG. *The predictive capability of failure mode concept-based strength criteria for multi-directional laminates-part B.* Composites Science and Technology, v 64, n 3-4, March, 2004, p 487-516

20 Hart-Smith LJ. *Should Fibrous Composite Failure Modes Be Interacted or Superimposed?* Composites, v. 24, n 1, 1993, p 53–55.

21 Soden PD, Hinton M.J, Kaddour AS. *Comparison of the predictive capabilities of current failure theories for composite laminates.* Composites Science and Technology, v 58, n 7, Jul, 1998, p 1225-1254

22 Hinton M.J, Kaddour AS, Soden PD. *A comparison of the predictive capabilities of current failure theories for composite laminates, judged against experimental evidence.* Composites Science and Technology, v 62, n 12-13 SPECIAL ISSUE, 2002, p 1725-1797

23 Kaddour AS, Hinton MJ, Soden PD. *A comparison of the predictive capabilities of current failure theories for composite laminates: Additional contributions.* Composites Science and Technology, v 64, n 3-4, March, 2004, p 449-476

24 Hinton MJ, Kaddour AS, Soden PD. *A further assessment of the predictive capabilities of current failure theories for composite laminates: Comparison with experimental evidence.* Composites Science and Technology, v 64, n 3-4, March, 2004, p 549-588

25 Hinton MJ, Kaddour AS, Soden PD. *Evaluation of failure prediction in composite laminates: Background to 'part B' of the exercise.* Composites Science and Technology, v 62, n 12-13 SPECIAL ISSUE, 2002, p 1481-1488

26 Hinton MJ, Kaddour AS, Soden PD. *Evaluation of failure prediction in composite laminates: Background to 'part C' of the exercise.* Composites Science and Technology, v 64, n 3-4, March, 2004, p 321-327

27 Bailey JE, Curtis PT, Parvisi A., *On the transverse cracking and longitudinal splitting of glass and carbon fibre reinforced epoxy cross ply laminates and the effect of Poisson and thermally generated strain.* Proc. R.Soc. Lond., 1979, A366, 599±623.

28 Flaggs DL, Kural MH. *Experimental determination of the in-situ transverse laminate strength in graphite epoxy laminates.* Journal of Composite Materials., 1982, 16,103±116.

29 Rotem A, Hashin Z. *Failure modes of angle ply laminates.* Journal of Composite Materials., 1975, 9, 191±206.

30 Hart-Smith LJ. *Predictions of the original and truncated maximum-strain failure models for certain fibrous composite laminates.* Composites Science and Technology., 1998, 58(7),1151.

31 Hart-Smith LJ. *Predictions of a generalized maximum shear-stress failure criterion for certain fibrous composite laminates.* Composites Science and Technology., 1998, 58(7),1179.

32 Sun CT, Tao JX. *Prediction of failure envelopesand stress/strain behaviour of composite laminates.* Composites Science and Technology., 1998, 58(7), 1125.

33 Rotem A, Hashin Z. *Failure modes of angle ply laminates.* Journal of Composite Materials., 1975, 9, 191-206.

34 Petit PH, Waddoups ME. *A method of predicting the nonlinear behavior of laminated composites.* Journal of Composite Materials, 3: 2–19.

35 Vaziri R, Olson MD, Anderson DL. *A plasticity-based constitutive model for fibre-reinforced composite laminates.* Journal of Composite Materials, 25: 512–535.

36 Lin,WP, Hu HT. *Parametric study on the failure of fiber-reinforced composite laminates under biaxial tensile load.* Journal of Composite Materials, v 36, n 12, 2002, p 1481-1503

37 Li Sg, Zou Z, Reid SR. *A continuum damage model for delaminations in laminated composites.* Journal of the Mechanics and Physics of Solids, v 51, n 2, February, 2003, p 333-356

38 Liu S. *Quasi-impact damage initiation and growth of thick-section and toughened composite material.l.*International Journal of Solids and Structures. 31, 3079–3098.

39 Zou Z, Reid SR, Li S, Soden PD. *Modelling interlaminar and intralaminar damage in filament wound pipes under quasi-static indentation.* Journal of Composite Materials. 36, 477–499.

40 Krueger, R, O'Brien TK. *A Shell/3DModeling Technique for the Analysis of Delaminated Composite Laminates.* Composites-Part A, v 32, 2001, p 25-44.

41 Li J, Sen JK. *Analysis of Frame-to-Skin Joint Pull-Off Tests and Prediction of the Delamination Failure.* 42nd AIAA/ASME/ASCE/AHS/ASC Structures, Structural Dynamics and Materials Conference, 2000, Seattle, WA, U.S.A.

42 Li J. *Three-Dimensional Effects in the Prediction of Flange Delamination in Composite Skin-Stringer Pull-Off Specimens.* 15th Conference of the American Society for Composites , 2000, Texas, U.S.A.: 983-990.

43 Krueger R, Cvitkovich MK, O'Brien TK, Minguet PJ. *Testing and Analysis of Composite Skin/Stringer Debonding Under Multi-Axial Loading.* Journal of Composite Materialss, v 34, n15, 2000, p 1263-1300.

44 Köning M, Krueger R, Rinderknecht S. *Numerical Simulation of Delamination Buckling and Growth.* Proceedings of the 10th International Conference on Composite Materials (ICCM-10), 1995, Whistler, Canada.

45 Krueger R. *A Shell/3D Modeling Technique for Delamination in Composite Laminates.* Proceedings of the 14th Conference of the American Society for Composites, 1999, Ohio, U.S.A.: 843-852.

46 Krueger R, Minguet PJ, O'Brien TK. *A Method for Calculating Strain Energy Release Rates in Preliminary Design of Composite Skin/Stringer Debonding Under Multi-Axial Loading.* NASA TM-1999-209365.

47 Rybicki EF, Kanninen MF. *A Finite Element Calculation of Stress Intensity Factors by a Modified Crack Closure Integral.* Engineering Fracture Mechanics, v 9, 1977, p 931-938.

48 Kreuger R, Minguet PJ, O'Brien TK, *A method for calculating strain energy release rates in preliminary design of composite skin/stringer debonding under multiaxial loading.* Composite structures: theory and practice, ASTM STP 1383, American Society for Testing and Materials, West Conshohocken, PA (2000), pp. 105–128.

49 Kreuger R, Paris IL, O'Brien TK, Minguet PJ. *Fatigue life methodology for bonded composite skin/stringer configurations.* Journal of Composites Technology and Research 24 (2002) (2), p 308–331.

50 Krueger R. *A Shell/3D Modeling Technique for the analysis of delaminated composite laminates.* NASA Technical Memorandum, NASA/TM-2000-210287, June; 2000.

51 Hibbitt, Karlsson, and Sorensen Inc., ABAQUS Version 6.3-3; 2003.

52 Irwin GR.. *Analysis of stresses and strains near the end of a crack transversing a plate.* Journal of Applied Mechanics. 24, 361–366.

53 Ribicki EF, Kanninen MF. *A finite element calculation of stress intensity factors by a modified crack closure integral.* Engineering Fracture mechanics. 9, 931–938.

54 Zou Z, Reid SR, Soden PD, Li S. *Mode separation of energy release rate for delamination in composite laminates using sublaminates.* International Journal of Solids and Structures. 38, 2597–2613.

55 Rinderknecht S, Kröplin B. *Calculation of Delamination Growth With Fracture and Damage Mechanics.Recent Developments in Finite Element Analysis*, CIMNE. 1994, Barcelona, Spain.

56 Rice JR. *A path independent integral and the approximate analysis of strain concentration by notches and cracks.* Journal of Applied Mechanics. 35, 379–386.

57 Hellen TK. *On the method of the virtual crack extension. International Journal for Numerical Methods in Engineering.* 9, 187–207.

58 Parks DM. *A stiffness derivative finite element technique for determination of crack tip stress intensity factors.* International Journal of Fracture. 10, 487–502.

59 Geubelle PH, Baylor JS. *Impact-induced delamination of composites: a 2D simulation.* Composites Part B 29B, p589–602.

60 Petrossian Z, Wisnom MR. *Prediction of delamination initiation and growth from discontinuous plies using interface elements.* Composites Part A 29A, p503–515.

61 Pinho ST, Camanho PP, de Moura MF. *Numerical simulation of the crushing process of composite materials.* International Journal of Crashworthiness, 9(3), 2004, p 263–76.

62 Pinho ST, Iannucci L, Robinson P. *Formulation and implementation of decohesion elements in an explicit finite element code.* Composites: Part A, v37, 2006, p778–789

63 Yang B, Ravi-Chandar K. *Antiplane shear crack growth under quasi-static loading in damaging material.* International Journal of Solids and Structures. 35, p 3695–3715.

64 Needleman A. T*he effect of bond strength and loading rate on the conditions governing the attainment of intersonic crack growth along interfaces.* Journal of Mechanics and Physics of Solids 47, p 2411–2449.

65 Espinosa HD, Dwivedi SD, Lu HC. *Modelling impact induced delamination of woven fibre reinforced composites with contact/cohesive laws.* Computer Methods in Applied Mechanics and Engineering. 183, p 259–290.

66 Mohammed I, Liechti KM. *Cohesive zone modelling of crack nucleation at bimaterial corners.* Journal of Mechanics and Physics of Solids 48, p 735–764.

67 Pandol A, Guduru PR, Ortiz M, Rosakis AJ. *Three dimensional cohesive-element analysis and experiments of dynamic fracture in C300 steel.* International Journal of Solids and Structures. 37, p 3733–3760.

68 Rahul-Kumar P, Jagota A, Bennison SJ, Saigal S. *Interfacial failure in a compressive shear strength test of glass/polymer laminates.* International Journal of Solids and Structures. 37, p 7281–7305.

69 Chen C, Fleck NA, Lu TJ. *The mode I crack growth resistance of metallic foams.* Journal of the Mechanics and Physics of Solids 49, p 231–259.

70 Liechti KM, Wu JD. *Mixed-mode, time-dependent rubber/metal debonding.* Journal of Mechanics and Physics of Solids 49, p 1039–1072.

71 Dudgale DS. *Yielding of Steel Sheets Containing Slits.* Journal of Mechanics and Physics of Solids, v 8, 1960, p 100-104.

72 Barenblatt GI. *Mathematical Theory of EquilibriumCracks in Brittle Failure. Advances in Applied Mechanics*, v 7, 1962.

73 Camanho PP, Dávila CG, Ambur DR. *Numerical Simulation of Delamination Growth in Composite Materials.* NASA-TP-211041, 2001.

74 De Moura MF, Gonçalves JP, Marques AT, PT de Castro. *Modeling Compression Failure After Low Velocity Impact on Laminated Composites Using Interface Elements.* Journal of Composite Materialss, v 31, 1997, p 1462-1479.

75 Reddy Jr, ED, Mello FJ, Guess TR. *Modeling the Initiation and Growth of Delaminations in Composite Structures.* Journal of Composite Materialss, v 31, 1997, p 812-831.

76 Chen J, Crisfield MA, Kinloch AJ, Busso EP, Matthews FL, Qiu Y. *Predicting Progressive Delamination of Composite Material Specimens Via Interface Elements.* Mechanics of Composite Materials and Structures, v 6, 1999, p 301-317.

77 Petrossian Z, Wisnom MR. *Prediction of Delamination Initiation and Growth From Discontinuous Plies Using Interface Elements.* Composites-Part A, v 29, 1998, p 503-515.

78 Cui W, Wisnom MR. *A Combined Stress-Based and Fracture Mechanics-Based Model for Predicting Delamination in Composites.* Composites, v 24, 1993, p 467-474.

79 Shahwan KW, Waas AW. *Non-Self-Similar Decohesion Along a Finite Interface of Unilaterally Constrained Delaminations.* Proceedings of the Royal Society of London 453, 1997, p 515-550.

80 Needleman A. *A continuum model for void nucleation by inclusion debonding.* Journal of Applied Mechanics. 54, 1987,p 525–531.

81 Xu XP, Needleman A. *Numerical simulation of fast crack growth in brittle solids.* Journal of the Mechanics and Physics of Solids 42, 1994, p1397–1434.

82 Reedy ED, Mello FJ, Guess TR. *Modelling the initiation and growth of delaminations in composite structures.* Journal of Composite Materials. 31, 1997,p 812–831.

83 Mi Y, Crisfield MA, Davies GAO. *Progressive delamination using interface elements.* Journal of Composite Materials. 32, 1998,p 1246–1272.

84 Tvergaard V, Hutchinson JW. *The relation between crack growth resistance and fracture process parameters in elastic–plastic solids.* Journal of Mechanics and Physics of Solids 40, 1992, p 1377–1397.

[85] Crisfield, M. A.; H. B. Hellweg; G. A. O. Davies. *Failure Analysis of Composite Structures Using Interface Elements.* Proceedings of the NAFEMS Conference on Application of Finite Elements to Composite Materials, Vol. 1-4, London, U.K., 1997.

86 Li SG, Zou Z, Reid SR. *A continuum damage model for delaminations in laminated composites.* Journal of the Mechanics and Physics of Solids, v 51, n 2, February, 2003, p 333-356

87 Brewer JC, Lagace PA. Quadratic stress criterion for initiation of delamination. *Journal of Composite Materialss* 1988;122:1141-55.

88 Camanho PP, Matthews FL. *Delamination Onset Prediction in Mechanically Fastened Joints in Composite Laminates.* Journal of Composite Materialss, v 33, 1999, p 906–927.

89 Da' vila CG, Johnson ER. *Analysis of Delamination Initiation in Postbuckled Dropped-Ply Laminates.* AIAA Journal, v 31, 1993, p 721–727.

90 Mohammadi S, Owen DRJ, Peric D. *A Combined Finite/Discrete Element Algorithm for Delamination Analysis of Composites.* Finite Elements in Analysis and Design, v 28, 1998, p 321–336.

91 Sun CT, Quinn BJ, Oplinger DW. *Comparative Evaluation of Failure Analysis Methods for Composite Laminates.* DOT/FAA/AR-95/109, 1996.

92 Puck A, Schu" rmann H. *Failure Analysis of FRP Laminates by Means of Physically Based Phenomenological Models.* Composites Science and Technology, v 58, 1998, p 1045–1067.

93 Hou JP, Petrinic N, Ruiz C. *A delamination criterion for laminated composites under low-velocity impact.* Composites Science and Technology, v 61, n 14, November, 2001, p 2069-2074.

94 Christensen RM, Deteresa SJ. *Delamination failure investigation for out-of-plane loading in laminates.* Journal of Composite Materials, v 38, n 24, 2004, p 2231-2238

95 Blackman B, Kinloch AJ. *Determination of the Mode I Adhesive Fracture Energy GIc of Structural Adhesives Using the Double Cantilever Beam (DCB) Specimen and Tapered DCB Specimens.* version 97–04.

96 ASTM D5528-94a. *Standard test method for mode I interlaminar fracture toughness of unidirectional polymer matrix composites.*

97 AECMA Aerospace series. Carbon Fibre Reinforced Plastics. *Determination of InterlaminarFracture Toughness Energy Mode I-GIc (prEN6033) and Mode II-GIIc (prEN6034)*, 12, 1995.

98 Davies P,Blackman BRK, Brunner AJ. *Standard test methods for delamination resistance of composite materials: current status.* Applied Composite Materials, v 5, n 6, 1998, p 345-364

99 *Determination of the Mode II delamination resistance of unidirectional fibre-reinforced polymer laminates using the End Loaded Split Specimen(ELS).* Version 99-06-03

100 ASTM D 6671/D 6671M-06. *Standard test method for mixed mode I-mode II interlaminar fracture toughness of unidirectional fibre reinforced polymer matrix composites..*

101 Lee SM. An Edge Crack Torsion *Method for Mode III Delamination Fracture Testing.* Journal of Composites Technology & Research, v 15, 1993, p 193-201.

102 James GR. *Characterization of the Edge Crack Torsion (ECT) Test for Mode III Fracture Toughness Measurement of Laminated Composites.* NASA/TM-2004-213269.

103 Camanho PP, Dávila CG, Ambur DR. *Numerical Simulation of Delamination Growth in Composite Materials.* NASA-TP-211041, 2001.

104 Reeder JR. *A Bilinear Failure Criterion for Mixed-Mode Delamination. Composite Materials:Testing and Design*, ASTM STP 1206, American Society for Testing and Materials, 1993.

105 Reeder JR. *An Evaluation of Mixed-Mode Delamination Failure Criteria.* NASA TM 104210,1992.

106 Wu EM, Reuter Jr. RC. *Crack extension in fiberglass reinforced plastics.* T & AM Report No. 275, University of Illinois, 1965.

107 Johnson WS, Mangalgiri PD. *Influence on the Resin on Interlaminar Mixed-Mode Fracture. Toughened Composites*, ASTM STP 937, Norman J. Johnston, Ed., American Society for Testing and Materials,Philadelphia, PA, 1987, pp. 295-315.

108 Donaldson SL. *Fracture Toughness Testing of Graphite/Epoxy and Graphite/PEEK Composites.* Composites, April 1985, pp.103-109.

109 Spencer B, Barnby JT. *The Effects of Notch and Fibre Angles on Crack Propagation in Fibre-Reinforced Polymers.* Journal of Material Science, Vol. 11, 1976, pp. 83-88.

110 Jurf RA, Pipes RB. *Interlaminar Fracture of Composite Materials.* Journal of Composite Materialss, v 16, September 1982, pp.386-394.

111 Mall S, Kochhar NK. *Criterion for Mixed-Mode Fracture in Composite Bonded Joints.* NASA CR 178112, May 1986.

112 Whitcomb JD. *Analysis of Instability-Related Growth of a Through-Width Delamination.* NASA TM 86301,September 1984.

113 Ashizawa M. *Faster interlaminar fracture of a compressively loaded composite containing a defect.* Paper presented at the Fifth DOD/NASA Conference on Fibrous Composites in Structural Design, New Orleans, LA,Jan. 1981. (Available as Douglas Paper No. 6994.)

114 Donaldson SL. *The Effect of Interlaminar Fracture Properties on the Delamination Buckling of Composite Laminates.* Composite Science and Technology, Vol. 28, 1987, pp. 33-44.

115 Hashemi S, Kinloch AJ, Williams JG. *Mechanics and Mechanisms of Delamination in a Poly(ether sulphone)-Fibre Composite.* Composites Science and Technology, Vol. 37, 1990, pp. 429-462.

116 Yan XQ, Du SY, Wang, D. *An Engineering Method of Determining The Delamination Fracture Toughness of Composite Laminates.* Engineering Fracture Mechanics, Vol. 39, No. 4, 1991, pp 623-627.

117 Hahn HT. *A Mixed-Mode Fracture Criterion for Composite Materials.* Composites Technology Review, v 5, Spring, 1983, p. 26-29.

118 Hahn HT, Johannesson T. *A Correlation Between Fracture Energy and Fracture Morphology in Mixed-Mode Fracture of Composites.* ICM 4, v 1, 1983, pp. 431-438.

119 White SR. *Mixed-Mode Interlaminar Fracture of Graphite/Epoxy Composites.* Master Thesis,Washington University, Saint Louis, Missouri, May, 1987.

120 Hashemi S, Kinloch AJ, Williams JG. *Interlaminar Fracture of Composite Materials.* 6th ICCM & 2nd ECCM Conference Proceedings, Elsevier Applied Science, London, Vol. 3, July 1987, pp. 3.254-3.264.

121 Williams JG. *The Fracture Mechanics of Delamination Tests. Journal of Strain Analysis,* v 24, No 3.1989.

122 Hashemi S, Kinloch AJ, Williams JG. *The Effects of Geometry, Rate and Temperature on the Mode I,Mode II and Mixed-Mode I/II Interlaminar Fracture of Carbon-Fibre/ Poly(ether-ether ketone) Composite.* Journal of Composite Materialss, v 24, September 1990, pp. 918-956.

123 Hashemi S, Kinloch AJ, Williams G. *Mixed-Mode Fracture in Fiber-Polymer Composite laminates.* Composite Materials: Fatigue and Fracture, v 3, ASTM STP 1110, T. K. O'Brien, Ed., American Society for Testing and Materials, Philadelphia, 1991, pp. 143-168.

124 Benzeggagh ML, Kenane M. *Measurement of Mixed-Mode Delamination Fracture Toughness of Unidirectional Glass/Epoxy Composites With Mixed-Mode Bending Apparatus,* Composites Science and Technology, v 56, 1996, p 439–449.

125 Kim BW, Mayer AH. *Influence of fiber direction and mixed-mode ration on delamination fracture toughness of carbon/epoxy laminates.* Composites Science and Technology, v 63, n 5, April, 2003, p 695-713

126 Piotr Czarnocki. *Bulking delamination hazard in a case of composite structures of gliders and uavs.* UAV-NET meeting 7 Paris, 16-17 June, 2003.

127 Cui W, Wisnom MR, Jones, M.I. *Effect of through thickness tensile and compressive stresses on delamination propagation fracture energy.* Journal of Composites Technology & Research, v 16, n 4, Oct, 1994, p 329-335.

128 Wisnom MR. *Size effects in the testing of fibre-composite materials.* Composites Science and Technology 59, 1999. 1937-1957.

129 Morton J. *Scaling of impact-loaded carbon-fiber composites.* AIAA , 26 (1988) 989-94.

130 Kellas S, Johnson DP, Morton J and Jackson KE. *Scaling effects in sublaminate-scaled composite laminates.* 34th AIAA/ASME/ASCE/AHS/ASC Structures, Structural Dynamics and Mater. Conf. AIAA/ASME Adaptive Structures Forum, 19-22 April 1993, La Jolla, CA, Part 6, pp. 3715-25, 1993.

131 Awerbuch J, Madhukar MS. *Notched strength of composite laminates: predictions and experiments – a review.* Journal of Reinforced Plastics and Composites 1985(4), P 3–159.

132 Lagace), Brewer J and Kassapoglou C. *The effect of thickness on interlaminar stresses and delamination in straight edged laminates.* Journal of Com. Technol. Res., 9(1987) 81-7.

133 Wang ASD. *Fracture mechanics of sublamiate cracks in composite materials.* Composites Technology Review, 6(2)(1984) 45-62.

134 Kellas S and Morton J. *Strength scaling in fibre composites.* AIAA J, 30(1992) 1074-80.

135 Wisnom MR, Atkinson JW. *Reduction in tensile and flexural strength of unidirectional glass fibre-epoxy with increasing specimen size.* Composite Structures, v 38, n 1-4, May-Aug, 1997, p 405-411

136 Sutherland LS, Shenoi RA,Lewis SM. *Size and scale effects in composites: I. Literature review.* Composiites Science and Technology, v 59, n 2, 1999, p 209-220.

137 Wisnom MR. *Relationship between strength variability and size effect in unidirectional carbon fibre/epoxy.* Composites,1991;22(1): p 47.

138 Weibull W. *A statistical distribution function of wide applicability.* Journal of Applied Mechanics 18 (1951), pp. 293–297.

139 Hedgepeth JM, Dyke PV. *Local stress concentrations in imperfect filamentary composite materials.* Journal of Composites Material. 1 (1967), pp. 294–309.

9 I.J. Beyerlein, Phoenix SL. *Stress concentrations around multiple fiber breaks in an elastic matrix with local yielding or debonding using quadratic influence superposition.* Journal of Mechanics and Physics of Solids, 44 (1997), pp. 1997–2039.

140 Beyerlein I.J, Phoenix SL., *Stress concentrations around multiple fiber breaks in an elastic matrix with local yielding or debonding using quadratic influence superposition.* Journal of Mechanics and Physics of Solids, 44 (1997), pp. 1997–2039.

141 Phoenix SL. *Statistical scaling relationships and size effects in the strength and creep rupture of fibrous composites. Workshop on Scaling Effects in Composite Materials and Structures*, NASA Conference Publication 3271, July 1994,; 219-242.

142 Gurvich MR, Pipes RB. *Strength size effect of laminated composites.* Composites Science and Technology, 1995; 55: 93-105.

143 Curtin WA. *Tensile strength of fibre reinforced composites III. Beyond the traditional Weibull model for fibre strengths.* Journal of Composite Materials, 2000; 34:1301-1332.

144 Okabe T, Takeda N. *Size effect on tensile strength of unidirectional CRFP composites-experimen and simulation.* Composites Science and Technology, 2002,; 62: 2053-2064.

145 Taibei A, Sun J. *Statistical size effect of laminated composite materials.* Composite Structures 1999; 46: 209-16.

146 Harlow DG, Phoenix SL. 1978a. *The chain of bundles probability model for the strength of fibrous materials I: analysis and conjectures.* Journal of Composite Materials 12, 314-334.

147 Kortschot MT and Beaumont PWR. *Damage mechanics of composite materials: I—Measurements of damage and strength.* Composites Science and Technology, 39 (4),1990, P 289-290.

148 Kortschot MT and Beaumont PWR. *Damage mechanics of composite materials: II—a damaged-based notched strength model.* Composites Science and Technology, 39 (4), 1990,p 303-326

149 Kortschot MT and Beaumont PWR. *Damage mechanics of composite materials. III: Prediction of damage growth and notched strength.* Composites Science and Technology, 40 (2), 1991, p 147-165.

150 Kortschot MT and Beaumont PWR. *Damage mechanics of composite materials. IV: The effect of lay-up on damage growth and notched strength.* Composites Science and Technology, 40 (2), 1991, p 167-169.

151 Dong L, Harding J. *A single-lap shear specimen for determining the effect of strain rate on the interlaminar shear strength of carbon-fibre reinforced laminates.* Composites 1994;25:129-38.

152 Jiang WG,Hallett SR, Green BG, Wisnom MR. *A concise interface constitutive law for analysis of delamination and splitting in composite materials and its application to scaled notched tensile specimens.* International Journal for Numerical Methods in Engineering, v 69, n 9, 2007, p 1982-1995.

153 Williams JG, Hadavinia H. *Analytical solutions for cohesive zone models.* Journal of the Mechanics and Physics of Solids 50 (2002), pp. 809–825

154 Silvestre TP, Lorenzo Iannucci and Paul Robinson. *Modelling delamination in an explicit FE code using 3D decohesion elements.* Comptest 2004, Bristol. 2004.

155 LS-Dyna Keyword User's Manual - Version 971, Livermore Software Technology Corporation (LSTC), 2007

156 Turon A, Dávila CG, Camanho PP, Costa J. *An Engineering Solution for using Coarse Meshes in the Simulation of Delamination With Cohesive Zone Models.* NASA/TM-2005-213547

157 Christensen M, Deteresa J. *Delamination failure investigation for out-of-plane loading in laminates.* Journal of Composite Materialss 2004;38: 2231-2238.

158 Deteresa J, Freeman C, Groves E. T*he effects of through-thickness compression on the interlaminar shear response of laminated fiber composites.* Journal of Composite Materialss 2004;38: 681-697.

159 Hart-Smith LJ. *Should Fibrous Composite Failure Modes Be Interacted or Superimposed? Composites* 1993;24:53–55.

160 Hart-Smith LJ. *Predictions of the original and truncated maximum-strain failure models for certain fibrous composite laminates.* Composites Science and Technology., 1998;58:1151.

161 Hart-Smith LJ. *Predictions of a generalized maximum shear-stress failure criterion for certain fibrous composite laminates.* Composites Science and Technology. 1998;58:1179.

162 Sun CT, Tao JX. *Prediction of failure envelopesand stress/strain behaviour of composite laminates.* Composites Science and Technology. 1998;58:1125.

163 Rotem A. *Prediction of laminate failure with the Rotem failure criterion.* Composites Science and Technology. 1998;58:1083.

164 Cui W, Wisnom MR, Jones MI. *Effect of through thickness tensile and compressive stresses on delamination propagation fracture energy.* Journal of Composites Technology & Research, JCTRER 1994;16:329-335.

165 Wisnom MR, LI DS. *Modelling damage initiation and propagration in composites using interface elements.* CADCOMP 1994.

166 Shi YB, Hull D, Price JN. *Mode II fracture of +θ/-θ angled laminate interfaces.* Composites Science and Technology 1993; 47:173-184

167 Wisnom MR, Chang FK. *Modelling of splitting and delamination in notched cross-ply laminates.* Composites Science and Technology 2000;60:2849-2856.

168 Hou JP, Petrinic N, Ruiz C. *A delamination criterion for laminated composites under low-velocity impact.* Composites Science and Technology 2001;61:2069-2074.

169 Xiao JR, Gillespie JWJ. *A Phenomenological Mohr--Coulomb Failure Criterion for Composite Laminates under Interlaminar Shear and Compression.* Journal of Composite Materialss 2007; 41: 1295-1309.

170 Dong L, Harding J. *A single-lap shear specimen for determining the effect of strain rate on the interlaminar shear strength of carbon-fibre reinforced laminates.* Composites 1994;25:129-38.

171 Hallett SR, Ruiz C, Harding J. *The effect of strain rate on the interlaminar shear strength of a carbon/epoxy cross-ply laminate: comparison between experiment and numerical prediction.* Composites Science and Technology 1999;59:749-758.

172 Brewer JC, Lagace PA. *Quadratic stress criterion for initiation of delamination.* Journal of Composite Materialss 1988;122:1141-55.

173 LS-Dyna Keyword User's Manual - Version 971, Livermore Software Technology Corporation (LSTC), 2007

174 Shi YB, Hull D, Price JN. *Mode II fracture of +θ/-θ angled laminate interfaces.* Composites Science and Technology 1993; 47:173-184.

175 Czarnocki P. *Bulking delamination hazard in a case of composite structures of gliders and uavs.* UAV-NET meeting 7 Paris, 16-17 June, 2003.

176 Wisnom MR, Chang FK. *Modelling of splitting and delamination in notched cross-ply laminates.* Composites Science and Technology 2000;60:2849-2856.

177 Hou JP, Petrinic N, Ruiz C. *A delamination criterion for laminated composites under low-velocity impact.* Composites Science and Technology 2001;61:2069-2074.

178 Hedgepeth JM, Dyke PVan. *Local stress concentrations in imperfect filamentary composite materials.* Journal of Composite Materials. 1 (1967), pp. 294–309.

179 Beyerlein I.J, Phoenix SL. *Stress concentrations around multiple fiber breaks in an elastic matrix with local yielding or debonding using quadratic influence superposition.* Journal of the Mechanics and Physics of Solids 44 (1997), pp. 1997–2039.

180 Weibull W. *A statistical distribution function of wide applicability.* Journal of Applied Mechanics 18 (1951), pp. 293–297.

181 Weibull W. *A statistical theory of the strength of materials.* Ingeniourswetenscapsakademien Handlingar 1939; 151: 1-29.

182 Kellas S, Morton J. *Strength scaling in fibre composites.* AIAA J 1992; 30(4):1074-80.

183 R. Moreton, The *effect of gauge length on the tensile strength of R.A.E. carbon fibres.* Fibre Science and Technology 1 (1969), p. 273. Abstract | PDF (445 K) | View Record in Scopus | Cited By in Scopus (9)

184 W.J. Padgett, S.D. Durham and A.M. Mason, *Weibull analysis of the strength of carbon fibres using linear and power law models for the length effect.* Composite Materials 29 14 (1995), p. 1875.

185 Wisnom MR. *Relationship between strength variability and size effect in unidirectional Carbon fibre/epoxy.* Composites, 1991; 22:47-52.

186 Phoenix SL. *Statistical scaling relationships and size effects in the strength and creep rupture of fibrous composites.* Workshop on Scaling Effects in Composite Materials and Structures, NASA Conference Publication 3271, July 1994,; 219-242.

187 Gurvich MR, Pipes RB. *Strength size effect of laminated composites.* Composites Science and Technology, 1995; 55: 93-105.

188 Curtin WA. *Tensile strength of fibre reinforced composites III. Beyond the traditional Weibull model for fibre strengths.* Journal of Composite Materials, 2000; 34:1301-1332.

189 Okabe T, Takeda N. *Size effect on tensile strength of unidirectional CRFP composites-experimen and simulation.* Composites Science and Technology, 2002,; 62: 2053-2064.

190 Taibei A, Sun J. *Statistical size effect of laminated composite materials.* Composite Structures 1999; 46: 209-16.

191 Harlow DG, Phoenix SL. 1978a. *The chain of bundles probability model for the strength of fibrous materials I: analysis and conjectures.* Journal of Composite Materials 12, 314-334.

192 J.O. Hallquist, LS-DYNA3D theoretical manual, Livermore Software Technology Corporation (1994).

193 Bathe KJ, Wilson EL. *Numerical methods in finite element analysis.* Prentice-Hall, Inc., Englewood Cliffs (NJ) (1976).

194 Jiang WG, Hallet SR and Wisnom MR. *Scaling effects in notched composites(SINCS)* Report No.6: Finite Element Modelling Report. Jan 2006

195 Hallett SR, Green BG, Jiang w-G and Wisnom MR. *An Experimental and Numerical Investigation into the Damage Mechanisms in Notched Composites.*, Composites Part A, In press

196 Hallett SR, Wisnom MR. *Numerical investigation of progressive damage and the effect of layup in notched tensile tests.* Journal of Composite Materials 40, 2006, p1229-1245.

197 Benjamin GG. *The effect of size on the tensile strength of composite laminates containing circular holes.* Ph.d Thesis, 2006.

198 Hexcel 8552 epoxy matrix product datasheet. Pdf download from: htt;://www.hexcelcomposites.com/Markets/Products/Prepregs/PrepregDownld.html.

199 Wisnom MR, Atkinson JW. *Reduction in tensile and flexural strength of unidirectional glass fibre-epoxy with increasing specimen size.* Composite Structures, v 38, n 1-4, May-Aug, 1997, p 405-411

200 Hallett SR, Jiang WG, Khan B and Wisnom MR, *Modelling the interaction between matrix cracks and delamination damage in scaled quasi-isotropic specimens.* Composites Science and Technology, 2008. **68**(1): p. 80-89.

201 Kortschot MT and Beaumont PWR, *Damage Mechanics of Composite-Materials .1. Measurements of Damage and Strength.* Composites Science and Technology, 1990. **39**(4): p. 289-301.

202 Hallett SR and Wisnom MR, Experimental investigation of progressive damage and the effect of layup in notched tensile tests. Journal of Composite Materials, 2006. **40**(2): p. 119-141.

203 Lagace P, *Notch sensitivity and stacking sequence of laminated composites,* in *Composite materials: testing and design (seventh conference), ASTM STP 893*, J. M. Whitney, Editor: Philadelphia. 1986, p. 161–76.

204 Walsh TJ and Ochoa OO, *Composites with multiple cutouts.* Composite Structures, 1993. **24**(2): p. 117-124.

205 Johnson WS and Treasurer P, *Radiographic investigation of the effects of ply modification on damage development in laminates containing circular holes.* Journal of Composite Materials, 2008. **42**(20): p. 2143-2161.

206 Moffat AJ, Wright P, Buffiere JY, Sinclair I and Spearing SM, *Micromechanisms of damage in 0 degrees splits in a [90/0](s) composite material using synchrotron radiation computed tomography.* Scripta Materialia, 2008. **59**(10): p. 1043-1046.

207 Wright P, Fu X, Sinclair I and Spearing SM, *Ultra high resolution computed tomography of damage in notched carbon fiber-epoxy composites.* Journal of Composite Materials, 2008. **42**(19): p. 1993-2002.

208 Hallett SR, Green, B.G., Jiang, W.G., and Wisnom, M.R., *An Experimental and numerical investigation into the damage mechanisms in notched composites.* Composites Part A, 2009. 40(5): p.613-624.

209 Green BG, Wisnom MR and Hallett SR. *An experimental investigation into the tensile strength scaling of notched composites.* Composites Part a, 2007. **38**(3): p. 867-878.

210 Jose S, Ramesh Kumar R, Jana MK and Venkateswara Rao G, *Intralaminar fracture toughness of a cross-ply laminate and its constituent sub-laminates.* Composites Science and Technology, 2001. **61**(8): p. 1115-1122.

211 Pinho ST, Robinson P and Iannucci L, *Fracture toughness of the tensile and compressive fibre failure modes in laminated composites.* Composites Science and Technology, 2006. **66**(13): p. 2069-2079.

212 Cowley KD and Beaumont PWR. *The interlaminar and intralaminar fracture toughness of carbon-fibre/polymer composites: The effect of temperature.* Composites Science and Technology, 1997. **57**(11): p. 1433-1444.

213 Kongshavn I and Poursartip A. *Experimental investigation of a strain-softening approach to predicting failure in notched fibre-reinforced composite laminates.* Composites Science and Technology, 1999. **59**(1): p. 29-40.

214 Davis manual - LaVision StrainMaster Brochure, 2007

215 T Belytschko, YY Lu and L Gu. *Element-Free Galerkin Methods.* International Journal for Numerical Methods in Engineering, 1994 37: p229-256.

216 T Belytschko and M Tabbara.*Dynamic Fracture Using Element-Free Galerkin Methods.* International Journal for Numerical Methods in Engineering, 1996 39: p923-938.

217 DBP Huynh, T Belytschko, *The extended finite element method for fracture in composite materials.* International Journal for Numerical Methods in Engineering, 2009 77(2):p214-239

218 Iarve EV. *Mesh independent modelling of cracks by using higher order shape functions.* International Journal of Numerical Method in Engineering 2003 56(6): p 869–882

219 van der Meer FP, Sluys LJ. *A phantom node formulation with mixed mode cohesive law for splitting in laminates.* International Journal of Fracture, 2009 158(2): p 107-124